Modelling and Simulation of Coupled Thermal-Hydraulic-Mechanical Processes in Geothermal Extraction
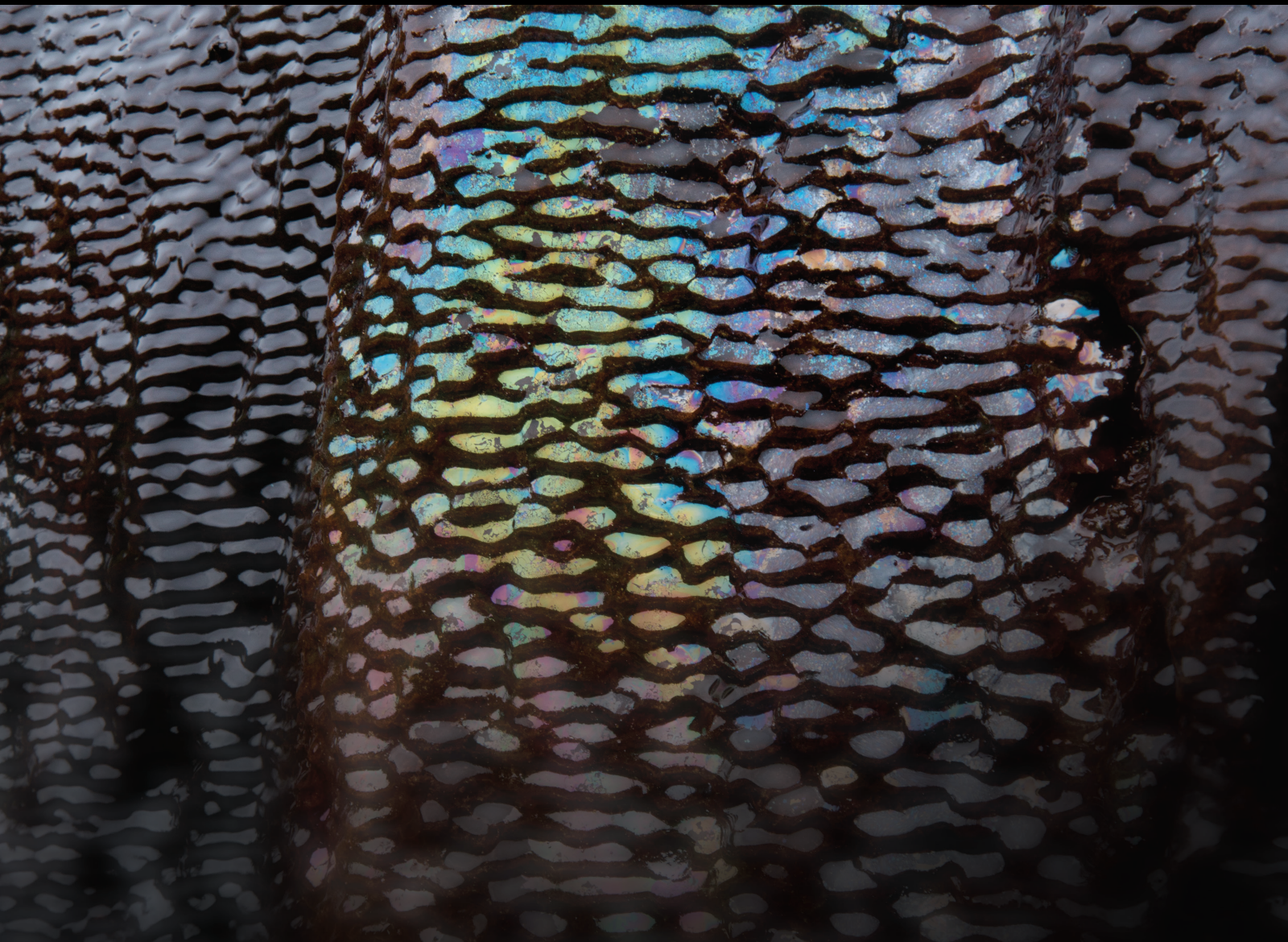
Lead Guest Editor: Tianran Ma
Guest Editors: Hao Xu, Weijun Shen, and Jiehao Wang

Modelling and Simulation of Coupled Thermal-Hydraulic-Mechanical Processes in Geothermal Extraction

Modelling and Simulation of Coupled Thermal-Hydraulic-Mechanical Processes in Geothermal Extraction

Lead Guest Editor: Tianran Ma
Guest Editors: Hao Xu, Weijun Shen, and Jiehao Wang

Bisheng Wu iD, China
Da-yang Xuan iD, China
Yi Xue iD, China
HE YONGLIANG, China
Fan Yang iD, China
Zhenyuan Yin iD, China
Sohrab Zendehboudi, Canada
Zhixiong Zeng iD, Hong Kong
Yuanyuan Zha iD, China
Keni Zhang, China
Mingjie Zhang iD, China
Rongqing Zhang, China
Xianwei Zhang iD, China
Ye Zhang iD, USA
Zetian Zhang iD, China
Ling-Li Zhou iD, Ireland
Yingfang Zhou iD, United Kingdom
Daoyi Zhu iD, China
Quanle Zou, China
Martina Zucchi, Italy

Contents

WILEY | Hindawi

Research Article

Present-Day In Situ Stress Analysis in Shale Reservoir of Haiba Block, Southern Sichuan Basin, South China

Wei Guo,[1] Wei Ju,[2] Majia Zheng,[3] Weijun Shen [ID],[4,5] Jian Zhang,[6] Pingping Liang,[1] Shengyu Wang,[2] and Haohao Hu[2]

[1]*Research Institute of Petroleum Exploration and Development, PetroChina, Beijing 100083, China*
[2]*School of Resources and Geosciences, China University of Mining and Technology, Xuzhou 221116, China*
[3]*PetroChina Southwest Oil and Gasfield Company, Chengdu 610000, China*
[4]*Key Laboratory for Mechanics in Fluid Solid Coupling Systems, Institute of Mechanics, Chinese Academy of Sciences, Beijing 100190, China*
[5]*School of Engineering Science, University of Chinese Academy of Sciences, Beijing 100049, China*
[6]*Shale Gas Institute, PetroChina Southwest Oil and Gasfield Company, Chengdu 610051, China*

Correspondence should be addressed to Weijun Shen; wjshen763@imech.ac.cn

Natural gas from shale gas reservoirs has been an important contributor for reserve growth, deliverability construction, and profits growth in natural gas industry in the world. Hydraulic fracturing is commonly required in the shale gas commercial development, and thus understanding the present-day in situ stress field is greatly significant for the hydraulic fracturing and efficient development in shale gas reservoirs. However, there are no systematic investigations on the present-day in situ stress field in the Haiba Block from the Sichuan Basin, South China. In this study, the present-day in situ stress orientations and magnitudes in shale reservoir of Haiba Block are investigated based on the well interpretations from borehole image log and geomechanical modeling. Then, the effects of stresses on hydraulic fracturing, horizontal wells, and natural fracture reactivation were discussed. The results indicate that the horizontal maximum principal stress (S_{Hmax}) orientation is mainly in the NE-SW-trending, NW-SE-trending, and WNW-ESE-trending in the Haiba Block. The magnitudes of horizontal maximum and minimum principal stresses are 13.5 MPa~85.5 MPa and 2.8 MPa~31.6 MPa, respectively. In the Haiba Block, the differential stress is generally low in the northern part, which indicates that complex hydraulic fracture networks may be produced. While the natural fractures are generally stable under the present-day in situ stress field. When the increase of pore pressure gradient is about 30 KPa/m, nearly all natural fractures in the Longmaxi Formation may be reactivated. The results can provide the insights into a better understanding of the present-day in situ stress distribution so as to optimize perforation orientation, hydraulic fracturing design, and enhance gas production in shale gas reservoirs.

1. Introduction

With the deepening development of hydrocarbon exploration and development, unconventional hydrocarbon resources indicate the great effects on global energy structure, and among them, shale gas is an important and realistic alternative one [1–4]. Shale gas in the United States has been economical to produce for several years [5, 6]. According to a survey from the U.S. Energy Information Administration (EIA), nearly 75 percent of natural gas in the United States came from shale gas reservoirs in 2019 [7]. Shale gas resources are rich in China, and the EIA has showed that the technically recoverable shale gas reserves in China are $36.08 \times 10^{12}\,m^3$, which are the largest reserves in the world [8]. Therefore, speeding up the exploration and development of shale gas reservoirs is of greatly strategic significance for ensuring energy security and optimizing energy structure of natural gas in China.
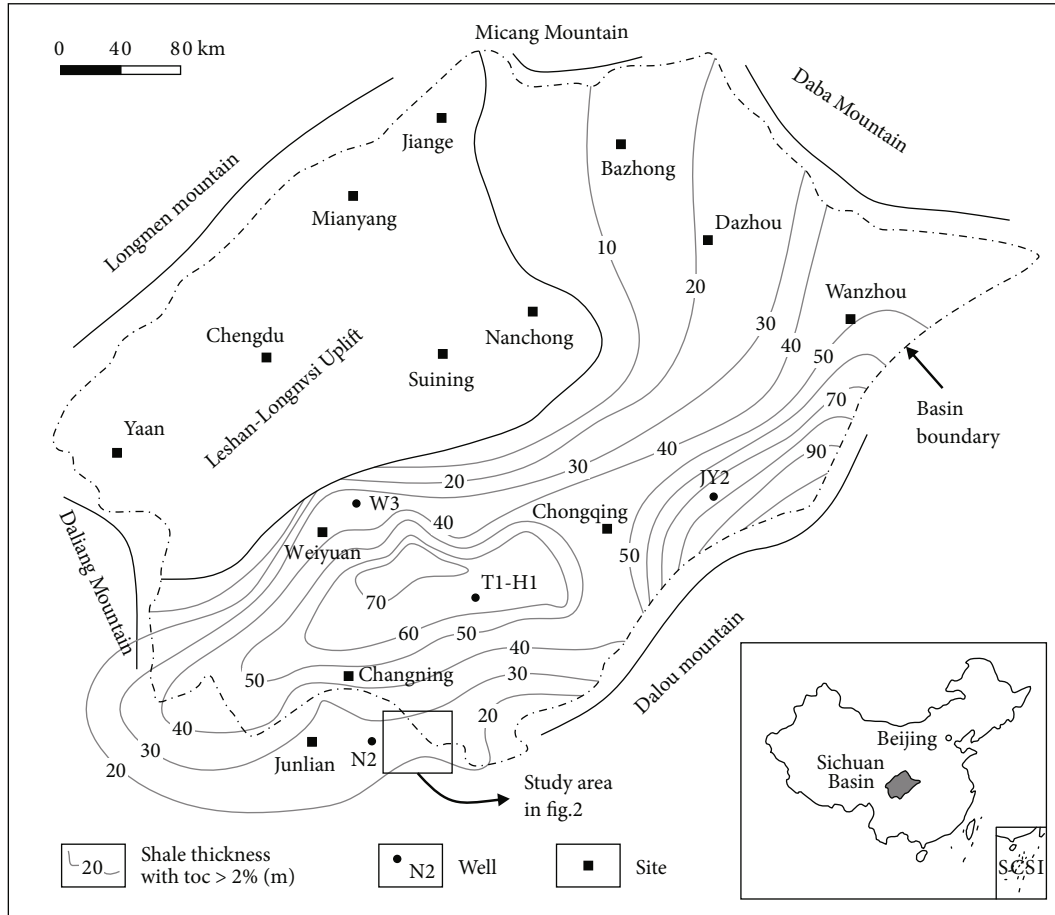
Figure 1: Geographic location and characteristics in the southern Sichuan Basin, China [17].

There are widely distributed marine shale gas resources in China, and shale gas exploration and development have achieved the remarkable success in the Sichuan Basin of China [9]. Within the basin, the Silurian Longmaxi Formation and Ordovician Wufeng Formation are characterized by the thick organic-rich shales and high thermal maturity. They are viewed as the most significant target layers for shale gas development, and the intensive exploration and exploitation are going currently [10–12]. Commonly, shale gas reservoirs are characterized by low porosity and low permeability, and the reservoir properties make the gas flow in shale pores difficult. The ability to economically produce natural gas from unconventional shale gas reservoirs has been made possible through the application of hydraulic fracturing and horizontal well drilling [6]. Knowledge of the present-day in situ stress state will help guide hydraulic fracturing design and greatly improve shale gas reservoir management [13, 14]. Consequently, understanding the present-day in situ stress distribution in shale gas reservoirs is essential to determine the mechanical characteristics of shale so as to provide the theoretical reference for hydraulic fracturing design and optimized perforation orientation in the shale gas exploitation and development.

In a sedimentary basin, the present-day in situ stress state may change both laterally and vertically. Generally, the description of present-day in situ stress state is based on vertical stress (S_v) magnitude, horizontal maximum principal stress (S_{Hmax}) magnitude, horizontal minimum principal stress (S_{hmin}) magnitude, and the orientation of S_{Hmax} [15]. According to the categorization from Jones [16], there exist three types of stress regime based on stress magnitude, including normal faulting stress regime ($S_v > S_{Hmax} > S_{hmin}$), strike-slip faulting stress regime ($S_{Hmax} > S_v > S_{hmin}$), and reverse faulting stress regime ($S_{Hmax} > S_{hmin} > S_v$). However, the Haiba Block of southern Sichuan Basin is a new shale gas exploration and development block in the Sichuan Basin, South China. Currently, there are few studies on the measured present-day in situ stress data and the scattered distributions, and a detailed understanding of the present-day in situ stress distribution in the shale gas reservoirs is lacking, which cannot support the further shale gas development. Hence, it is extremely necessary to understand in situ stress distribution so as to optimize perforation orientation and ultimately, hence, field production in shale gas reservoirs.

In this study, the present-day in situ stress states of the Haiba Block from the Sichuan Basin, South China were conducted using the finite element (FE) numerical simulations. The S_{Hmax} orientation was interpreted, and then the present-day in situ stress distribution in the Haiba Block was quantitatively delineated. Furthermore, the effects of stresses on hydraulic fracturing, horizontal wells, and natural
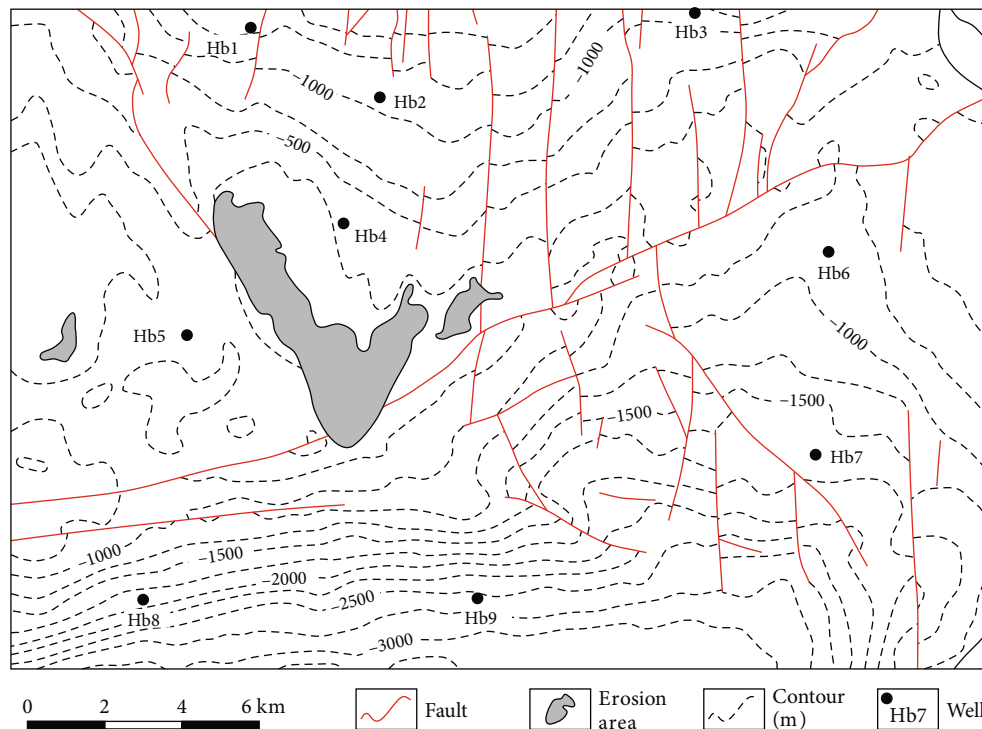
FIGURE 2: Structural framework of Haiba Block in the southern Sichuan Basin, China (The contours indicate the burial depth of bottom Wufeng Formation—Lower Silurian Longmaxi Formation).

fracture reactivation were analyzed to implicate gas production in shale gas reservoirs.

2. Geological Setting

The Sichuan Basin, a multiple-cycle diamond-shaped sedimentary basin, is located in the southwestern China, which is illustrated in Figure 1. The Basin covers an area of over $18 \times 104\,km^2$, which is an important area for shale gas commercial production in southern China [10, 17]. The Haiba Block is located in the southern portion of Sichuan Basin, which mainly includes the Haiba anticline, Yunshanba syncline, and Hualang syncline. The high-quality shale target is mainly developed in the Long 1 subformation, which is with a buried depth of 3000 m. During the past long geological evolution, the Haiba Block experienced the multiple phases of tectonic activities, and which resulted in a series of well-developed faults as shown in Figure 2.

In the Haiba Block, the Wufeng Formation and Longmaxi Formation are the most important layers for shale gas development, whose lithology is characterized by black carbonaceous/silty shale and mudstone as illustrated in Figure 3. The Longmaxi Formation can be divided into two subformation (Long 1 and Long 2), and Long 1 subformation is further divided into two segments: Long 1^1 and Long 1^2 from bottom to top. Burial depths of the Wufeng Formation are distributed from 600 m to 1500 m as shown in Figure 2. The thickness of Wufeng Formation and Longmaxi Formation is generally stable within the Haiba Block, which varies in the intervals of $4 \sim 15$ m and $200 \sim 250$ m, respectively. As shown in Figure 3, the experiment results

show that the porosity of Wufeng-Longmaxi Formations varies between 2.78% and 7.89% with an average of 4.7%, and the TOC ranges from 1.02% to 6.06% with an average of 3.0%. The well tests indicate that the Wufeng Formation and Longmaxi Formation Long 1^1 segment is the target production layer for shale gas of the Haiba Block in the southern Sichuan Basin, South China.

3. Interpretation of the S_{Hmax} Orientation

In general, wellbore breakouts (WBs), drilling-induced tensile fractures (DITFs), earthquake focal mechanisms, in situ stress measurements, etc., could be used as the important stress indicators to determine the S_{Hmax} orientation [18, 19]. Commonly, both WBs and DITFs could be detected from the borehole image log, as illustrated in Figure 4. The WBs orientation indicates the azimuth of S_{hmin}, perpendicular to the S_{Hmax} orientation [13, 20]. However, the directions of the DITFs are indicative of the S_{Hmax} orientations [21]. In borehole image log, the DITFs usually appear in two different patterns. One pattern is the symmetrically aligned fractures parallel or subparallel to borehole axis on the opposite sides of the borehole wall, as shown in Figure 4(a). The other pattern is the en echelon fractures around the borehole showing traces 180° apart, as illustrated in Figure 4(b). The WBs are commonly shown as broad, parallel conductive zones separated by approximately 180° in borehole image log, which are shown in Figure 4(c).

In this study, based on available data in the Haiba Block, the interpretations of the S_{Hmax} orientation are mainly carried out in wells Hb1, Hb2, Hb3, Hb4, Hb5, and Hb7 from
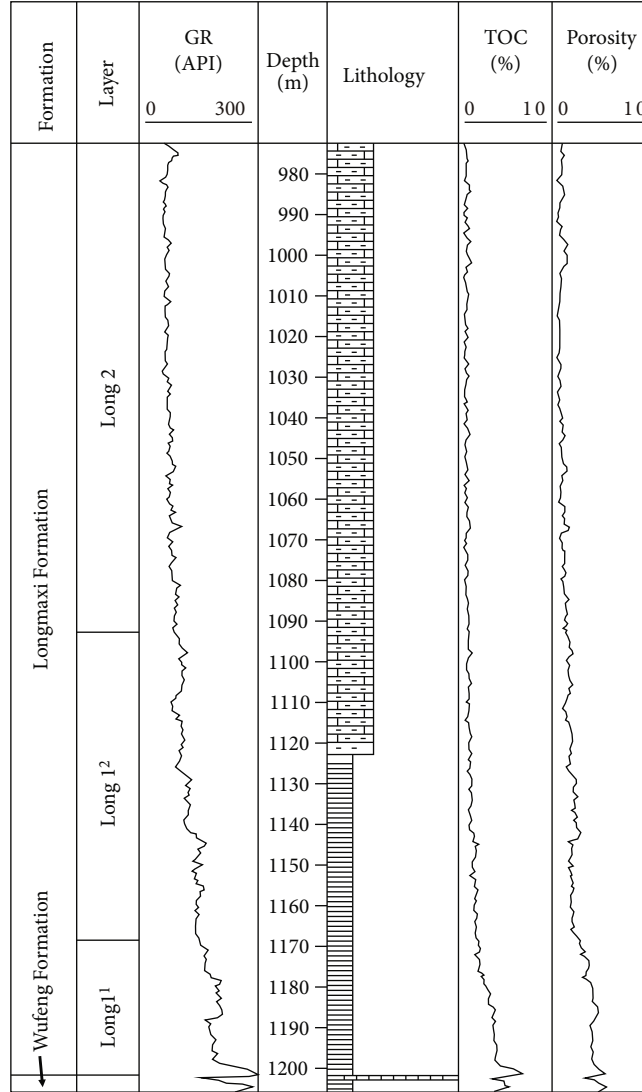
FIGURE 3: Typical lithological system of the Wufeng Formation and Longmaxi Formation in the Haiba Block (Well Hb3).

the stress indicators of WBs and DITFs, separately. The results show that the S_{Hmax} orientations in the Wufeng-Longmaxi Formations of Haiba Block mainly indicate the NE-SW-trending, NW-SE-trending, and WNW-ESE-trending as illustrated in Figure 5. According to the tectonic analysis in a larger scale, the NE-SW-trending may be a regional S_{Hmax} orientation. The NW-SE-trending and WNW-ESE-trending are the local S_{Hmax} orientations. The development of faults and natural fractures, lateral lithology differences, etc., could function as the important factors influencing variations of the S_{Hmax} orientations in the Haiba Block.

4. Present-Day In Situ Stress Prediction

In the Haiba Block, the measured in situ stress magnitudes are few and widely spread. Consequently, the overall characteristics of present-day stress distribution in the Haiba Block cannot be fully understood. In this study, the detailed in situ stress distributions in the Haiba shale reservoirs are delin-

eated according to the finite element (FE) numerical method. Generally, the basic principles and procedures for the FE stress simulation are as follows: (1) a complete geological model is established and further discretized into a finite number of elements connected by the nodes; (2) the corresponding rock mechanics parameters are assigned to those elements divided; (3) the continuous stress function and strain function of the geological body are transformed into a field function for solving finite points, which is used by the following:

$$\sigma = \left[\sigma_x \, \sigma_y \, \sigma_z \, \tau_{xy} \, \tau_{yz} \, \tau_{zx}\right]^T, \tag{1}$$

$$\varepsilon = \left[\varepsilon_x \, \varepsilon_y \, \varepsilon_z \, \gamma_{xy} \, \gamma_{yz} \, \gamma_{zx}\right]^T, \tag{2}$$

$$\sigma = D\varepsilon, \tag{3}$$

$$[P] = [K][\delta], \tag{4}$$

Well Hb2   Well Hb3   Well Hb7

(a)   (b)   (c)
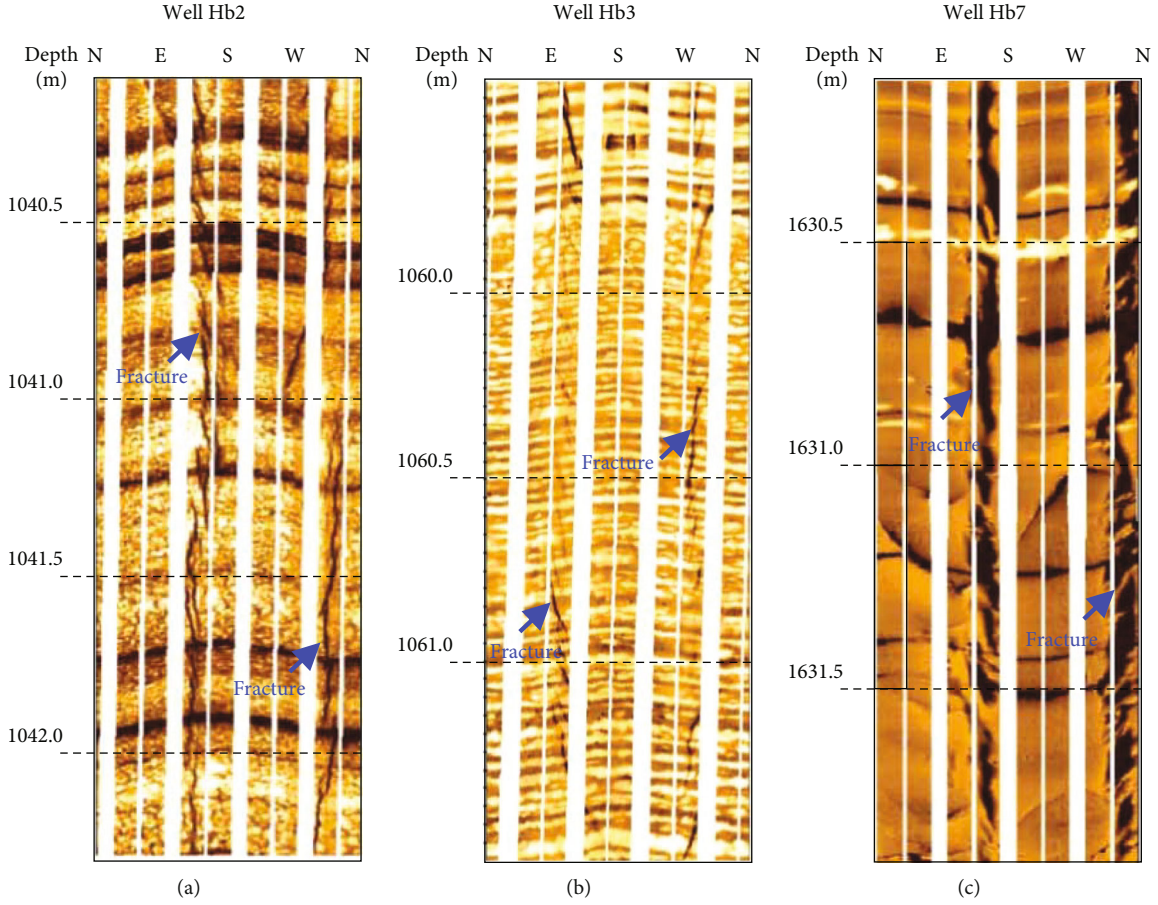
FIGURE 4: Borehole image logs showing drilling-induced tensile fractures (DITFs) and wellbore breakouts (WBs) in the Haiba Block.

where σ is the stress; ε is the strain; D is the elastic matrix; $[P]$ is the integral nodal load matrix; $[K]$ is the integral stiffness matrix; and $[\delta]$ is the nodal displacement matrix for the integral structure of the examined elemental array.

By solving the linear equation, the nodal displacement, strain, and stress of each individual element in the structure can be determined [22].

Generally, the fracture closure pressure (P_c) is indicative of the S_{hmin} magnitude at the test depth, which can be described as follows [23, 24],

$$S_{hmin} = P_c, \tag{5}$$

According to the previous studies [25], the S_{Hmax} magnitude is generally calculated and expressed as follows:

$$S_{hmax} = 3S_{hmin} - P_f - P_o + T, \tag{6}$$

where P_f is the formation break-down pressure; P_o is the pore pressure; and T is the tensile strength of the rock.

4.1. Geological Model Setup. The accuracy of the geological model directly determines the credibility of the in situ stress simulation results [26, 27]. In this study, the Silurian Longmaxi Formation of Haiba Block, southern Sichuan Basin, South China is selected for the model setup and further
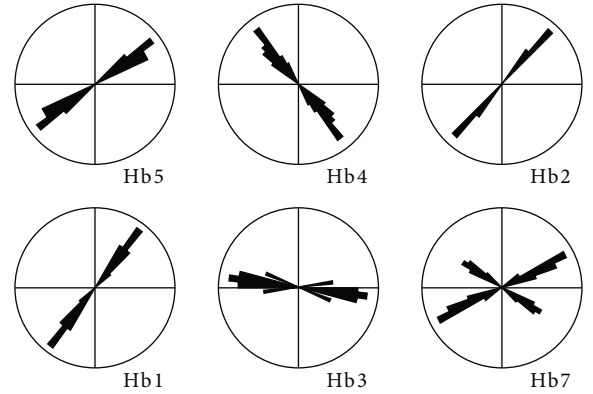
FIGURE 5: The S_{Hmax} orientations interpreted from drilling-induced tensile fractures (DITFs) and wellbore breakouts (WBs) in the Haiba Block.

stress analysis. The initial three-dimensional (3D) geometric model is constructed based on the structural and sedimentary conditions in the Haiba Block as shown in Figure 6. According to the principals of the finite element method, the faults are generally represented by the zones inside the model [28], which is illustrated in Figure 6(a). Consequently, the constructed 3D geometric model contains different zones representing the geological units, namely, the Longmaxi Formation and faults.

(a)   (b)
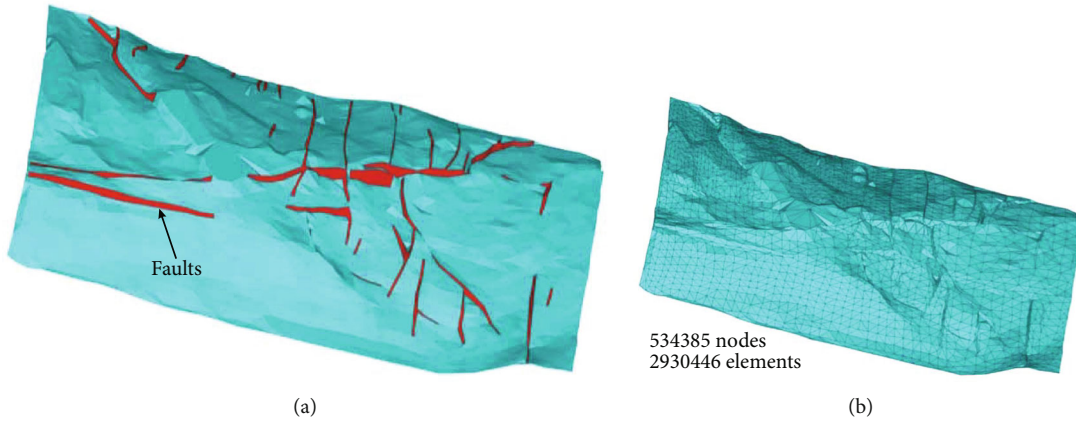
FIGURE 6: Geometry (a) and meshing results (b) of the initial Haiba 3D model.

TABLE 1: Reservoir rock mechanics parameters used in this study.

Unit	Density ρ (kg/m^3)	Young's modulus E (GPa)	Poisson's ratio μ
Target layer	2500	25.0	0.23
Fault zone	1750	17.5	0.25
Nested model	2550	27.0	0.25
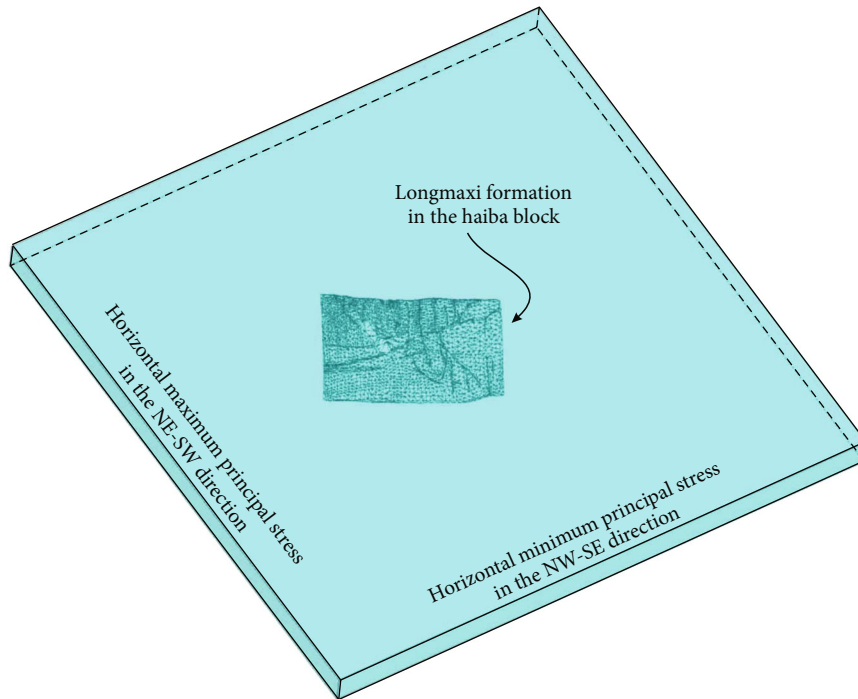
FIGURE 7: Simplified nested model of the Longmaxi Formation in the Haiba Block.

In the following, the reservoir properties are assigned to these different units to make into the geological model. In this study, the mechanical parameters of the target layer (Longmaxi Formation) are determined by the rock mechanics experiments. They are the average values obtained from 20 samples, and the rock mechanics parameters used in this study are listed in Table 1. In addition, the faults are developed in the study area, and their distribution can largely influence the in situ stresses. However, within the FE model, the mechanics parameters for fault zones are unavailable from the laboratory experiments. As to this question, the faults in the FE models are generally defined as the weakness zones with their Young's moduli lower than the corresponding sedimentary layer. The Young's modulus ratio between

(a)

(b)
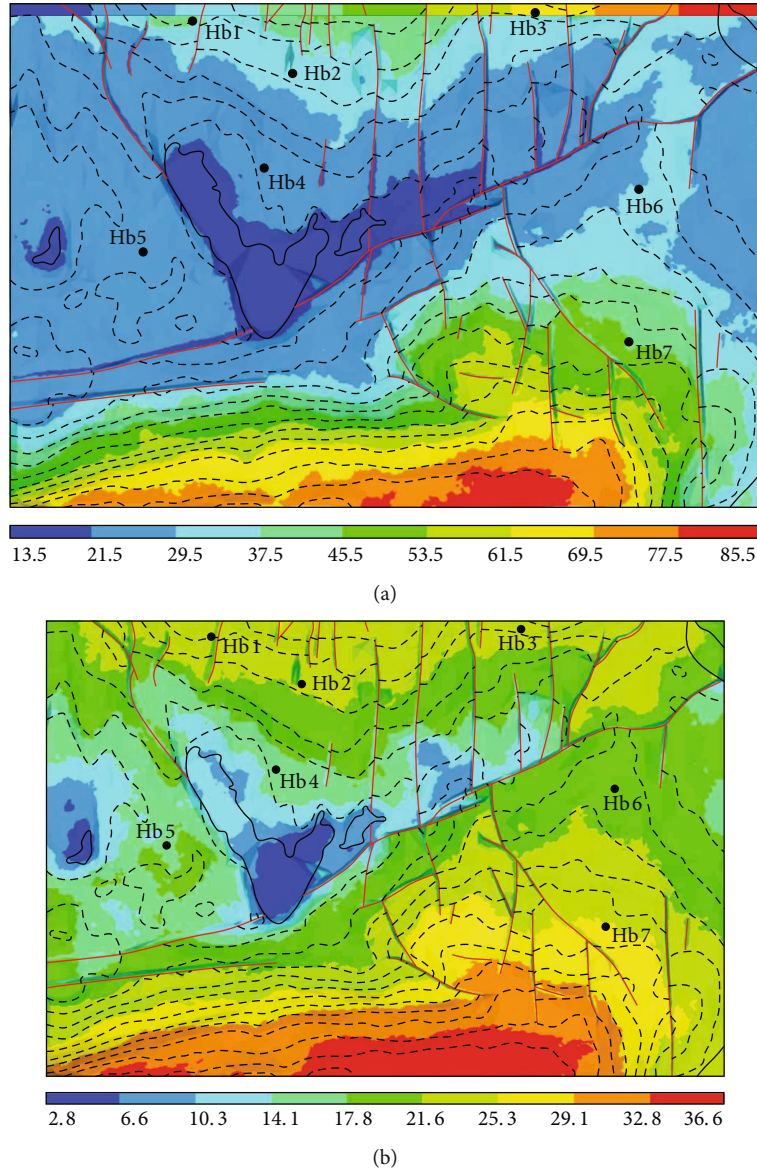
FIGURE 8: The calculated S_{Hmax} (a) and S_{hmin} (b) magnitudes in the Longmaxi Formation of Haiba Block (compressive stresses are considered as positive and tensile stresses are negative).

fault zone and sedimentary layer is commonly between 0.5 and 0.7 [26, 29], and a ratio of 0.7 is used in this study. All faults and sedimentary layers in this model are meshed or discretized using primarily three-nodel triangular elements. After the meshing, approximately 534385 nodes and 2930446 elements are produced within the FE model as illustrated in Figure 6(b).

4.2. Boundary Conditions. In this study, the boundary conditions are difficult to determine and apply because there is no clear geological boundary to demarcate the Haiba Block from the rest parts of Sichuan Basin. To solve this problem and facilitate the applying forces, the Haiba Block is nested within a larger rectangular parallelepiped approximately 5 times of the study area, as illustrated in Figure 7. Vertically, the entire geological model is subjected to the gravity loading

$(g = 9.8\,m/s^2)$, which can be directly and automatically applied in the finite element software. Laterally, according to the measured stress data and several attempts, the stress magnitudes of approximately $S_{Hmax} = 32\,MPa$ and $S_{hmin} = 27\,MPa$ are used in the NE-SW direction and NW-SE direction of the nested model, respectively. In addition, some appropriate displacement constraints are applied to the geological model so as to prevent it from the rotation and rigid displacement. The top of the model is set as a free surface, and the bottom is vertically fixed. In the numerical analysis, the stress symbols are defined based on the following rules that compressive stresses are positive and tensile stresses are negative. In the following, the node displacement is taken as the objective function to build the multivariate equations, and the stress and strain values in each element body are calculated [27].

TABLE 2: Error analysis of the measured and calculated stress results from numerical simulation.

Well	Measured S_{Hmax} (MPa)	Calculated S_{Hmax} (GPa)	Error (%)	Measured S_{hmin} (MPa)	Calculated S_{hmin} (MPa)	Error (%)
Hb1	38.6	39.6	2.59	24.7	23.1	6.48
Hb2	30.1	32.6	8.31	19.7	21.5	9.14
Hb3	35.9	37.9	5.57	22.5	23.9	6.22
Hb4	14.7	22.1	50.34	11.1	14.5	30.63
Hb7	53.1	49.5	6.78	30.3	26.8	11.55

0.9   6.2   11.5   16.8   22.1   27.4   32.7   38.0   43.3   48.6
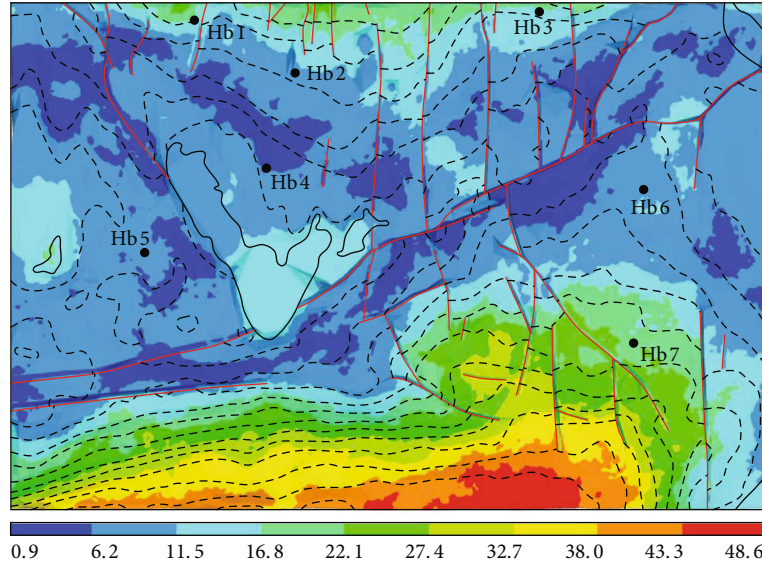
FIGURE 9: Differential stress in the Longmaxi Formation of Haiba Block Stress (unit: MPa).

4.3. Results and Error Analysis. In the Longmaxi Formation of Haiba Block, southern Sichuan Basin, the S_{Hmax} values range from 13.5 MPa to 85.5 MPa as illustrated in Figure 8(a), and the S_{hmin} values are between 2.8 MPa and 36.6 MPa as shown in Figure 8(b), both of which are the indicative of compression. The calculated results indicate that the stress distributions in the study area are greatly depth- and fault-controlled, i.e., faults and burial depth greatly influence the present-day stress distribution. The lower stress magnitudes are mainly distributed in regions around wells Hsb5-Hb6 and fault zones.

In order to verify the credibility of the calculated stress results shown in Figure 8, and the error analysis is described based on the following:

$$r = \frac{|d1 - d2|}{d2} \times 100\%, \tag{7}$$

where r is the error between the calculated and measured stress values and $d1$ and $d2$ are the calculated and measured stress values, respectively.

In this study, the errors between the measured and calculated stress magnitudes are low, and they are generally less than 12% except Well Hb4, which is listed in Table 2. It implies that this modeling results are believable, and there are two reasons for the relatively high error between the measured and calculated stress values in Well Hb4. One rea-

son is that the error calculated based on Equation (4) may be larger when the absolute stress magnitudes are relatively low. The other reason is that Well Hb4 is located around the erosion areas, and the erosion effects on stress magnitude are not taken into account in the simulation process. In general, the predicted stress distribution shown in Figure 8 may provide the geological references for further shale gas exploration and development.

5. Implications for Shale Gas Production

5.1. Effects of Stresses on Hydraulic Fracturing and Horizontal Wells. The growth in shale gas production in the United States and other countries has been a direct consequence of utilizing hydraulic fracturing and drilling horizontal wells, which creates a complex fracture network allowing for the gas improvement during well performance [30, 31]. And thus the hydraulic fracturing and horizontal wells are required in the commercial development of shale gas. The present-day in situ stress state indicates the critical effects on hydraulic fracturing operations and horizontal well drillings.

Differential stress is an important factor during the hydraulic fracturing design, and the lower differential stress magnitude commonly results in complex fracture networks [32, 33]. In this study, based on the present-day stress prediction results, differential stress magnitudes in the Longmaxi Formation of Haiba Block vary between 0.9 MPa and 48.6 MPa, which are mainly controlled by the burial depth
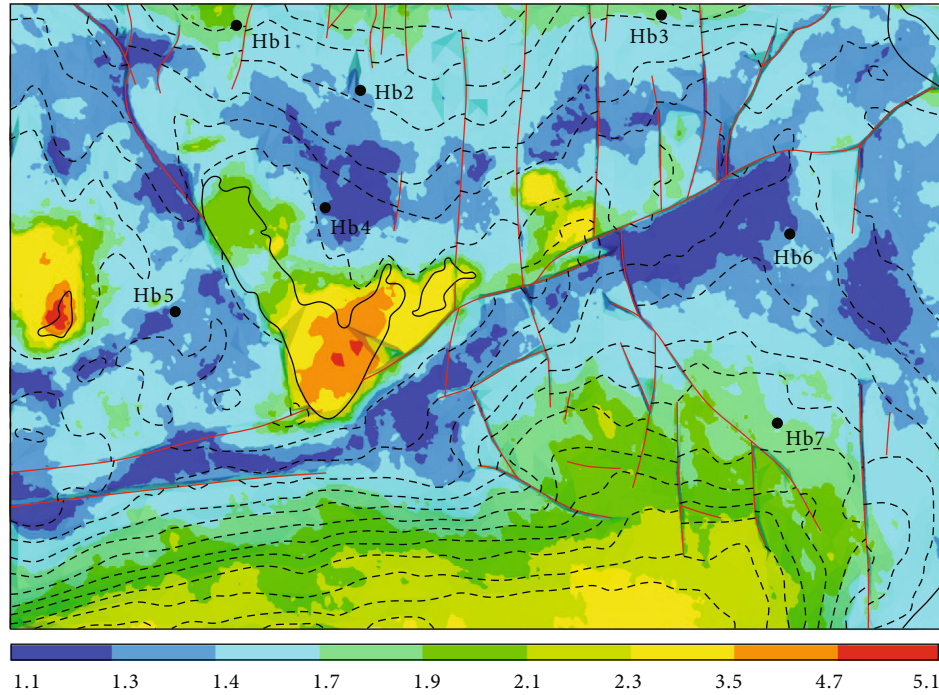
FIGURE 10: Distribution of the unequilibrium tectonic indicator (K) in the Longmaxi Formation of Haiba Block.
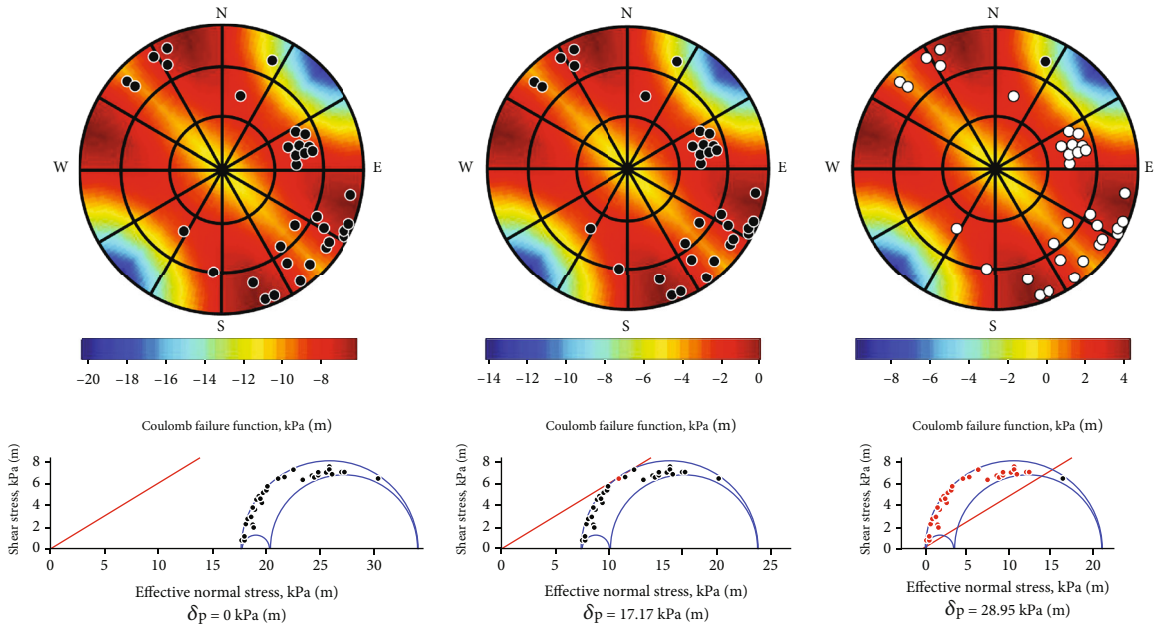
FIGURE 11: Lower hemisphere stereonet plots and Mohr's circles analyzing natural fracture reactivation risks in Well Hb2 of Haiba Block.

as illustrated in Figure 9. In the northern part (structurally high areas), differential stress magnitudes are generally low, and they are less than 11.5 MPa. However, with the increasing burial depth in the southern part, differential stress magnitudes are high, and they are generally higher than 22.1 MPa. Consequently, it can be deduced that the complex hydraulic fracture networks will be produced in the northern part of Haiba Block.

The unequilibrium tectonic indicator (K), a ratio between S_{Hmax} magnitude and S_{hmin} magnitude, is a signifi-

cant factor in hydraulic fracturing design [27]. In this study, the K value ranges between 1.1 and 5.1 in the Longmaxi Fromation as shown in Figure 10. Based on the results both in Figures 9 and 10, the areas with low differential stress and K are the engineering sweet spots for subsequent shale gas development in the Haiba Block. In addition, drilling horizontal well is the other important and critical technique for shale gas production. Commonly, a newly generated hydraulic fracture generally propagates along the path that requires the minimum force [30, 34]. Therefore, in the Longmaxi

shale reservoir of Haiba Block, horizontal wells are better drilled parallel to the S_{hmin} direction as shown in Figure 5.

5.2. Effects of Stresses on Natural Fracture Reactivation. In general, during the hydraulic fracturing within shale gas reservoir, fluids are injected into the target subsurface reservoir rocks, resulting in geomechanically-induced effects, such as natural fracture reactivation [3, 34]. In this study, the reactivation risk plots are introduced to analyze natural fracture reactivations, which use the Mohr's circle criterion [35]. Natural fractures within the Longmaxi Formation of Well Hb2 are selected as the example for analysis. The plots are shown in Figure 11 with warm and cold colors, which indicate higher and lower fracture reactivation risk, respectively.

In the Haiba Block, initially, the failure line (red line) is far from Mohr's circle, which indicates all natural fractures are stable under the present stress field. When fluids are injected into the target shale gas reservoir, the Mohr's circle moves left as illustrated in Figure 11, which increases the reactivation risk for natural fractures. Fractures are in their critical state when the failure line rightly gets into contact with the Mohr's circle. In this study, based on the modeling analysis, when the pore pressure gradient caused by fluid injection increases 28.95 kPa/m, nearly all natural fractures in the Longmaxi Formation of Well Hb2 are reactivated as shown in Figure 11. The fracture orientations are plotted as the pole of planes with different colors representing the relative ease of fracture susceptibility as the amount of pore pressure increase required to reactivate a fracture. The red colors show the highest likelihood of the fracture reactivation, while the blue colors indicate the least likelihood of reactivation for all possible fractures in the present-day stress state. The black and white dots in the stereonet plots are normal and critically stressed natural fractures, respectively. In the Mohr circles, the black and red dots are normal and critically stressed natural fractures, and the δp indicates the pore pressure increases.

6. Conclusions

Accurate knowledge of the present-day in situ stress field can help shale gas exploration and development of the Haiba Block in the Sichuan Basin, South China. In this study, the present-day in situ stress distribution and orientations are analyzed based on the numerical simulation and interpretations from borehole image log. And then the effects of stresses on hydraulic fracturing, horizontal wells, and natural fracture reactivation were discussed to illustrate gas production in shale gas reservoirs. The main conclusions are as follows. (1) The S_{Hmax} orientations in the Wufeng-Longmaxi shale reservoirs of Haiba Block are mainly the NE-SW-trending, NW-SE-trending, and WNW-ESE-trending, and the NE-SW-trending is the regional S_{Hmax} direction. In the Longmaxi Formation, the S_{Hmax} values range from 13.5 MPa to 85.5 MPa, while the S_{hmin} values are between 2.8 MPa and 36.6 MPa, and they are indicative of the compression. The distributions of stress magnitudes in the study area are greatly depth- and fault-controlled, and the deeper depths (e.g., the southern part of Haiba Block) indicate the

larger in situ stress magnitudes. (2) In the Haiba Block, the differential stress is generally low in the northern part and high in southern part, which indicates that the complex hydraulic fracture networks will be produced in the northern part of Haiba Block. In addition, based on natural fracture reactivation analysis, all natural fractures are initially stable under the present-day stress field. When the increase of pore pressure gradient is approximately 30 kPa/m, nearly all natural fractures in the Longmaxi Formation will be reactivated.

Data Availability

The data used to support the findings of this study are included within the article.

Conflicts of Interest

The authors declared no potential conflicts of interest with respect to the research, authorship, and publication of this article.

Acknowledgments

References

[1] D. M. Jarvie, R. J. Hill, T. E. Ruble, and R. M. Pollastro, "Unconventional shale-gas systems: the Mississippian Barnett Shale of North-Central Texas as one model for thermogenic shale-gas assessment," *AAPG Bulletin*, vol. 91, no. 4, pp. 475–499, 2007.

[2] W. J. Shen, T. R. Ma, X. Z. Li, B. Sun, Y. Hu, and J. Xu, "Fully coupled modeling of two-phase fluid flow and geomechanics in ultra-deep natural gas reservoirs," *Physics of Fluids*, vol. 34, no. 4, article 043101, 2022.

[3] W. Ju, X. B. Niu, S. B. Feng et al., "Present-day in-situs stress field within the Yanchang Formation tight oil reservoir of Ordos Basin, Central China," *Journal of Petroleum Science and Engineering*, vol. 187, article 106809, 2020.

[4] W. J. Shen, X. Z. Li, T. R. Ma, J. Cai, X. Lu, and S. Zhou, "High-pressure methane adsorption behavior on deep shales: experiments and modeling," *Physics of Fluids*, vol. 33, no. 6, article 063103, 2021.

[5] K. A. Bowker, "Barnett shale gas production, Fort Worth Basin: issues and discussion," *AAPG Bulletin*, vol. 91, no. 4, pp. 523–533, 2007.

[6] D. Rahm, "Regulating hydraulic fracturing in shale gas plays: the case of Texas," *Energy Policy*, vol. 39, no. 5, pp. 2974–2981, 2011.

[7] X. H. Ma, W. J. Shen, X. Z. Li, Y. Hu, X. Liu, and X. Lu, "Experimental investigation on water adsorption and desorption isotherms of the Longmaxi shale in the Sichuan Basin, China," *Scientific Reports*, vol. 10, no. 1, p. 13434, 2020.

[8] X. Z. Li, Z. H. Guo, Y. Hu et al., "High-quality development of ultra-deep large gas fields in China: challenges, strategies and

proposals," *Natural Gas Industry*, vol. 7, no. 5, pp. 505–513, 2020.

[9] X. L. Tang, Z. X. Jiang, S. Jiang et al., "Characteristics, capability, and origin of shale gas desorption of the Longmaxi Formation in the southeastern Sichuan Basin, China," *Scientific Reports*, vol. 9, no. 1, p. 1035, 2019.

[10] C. N. Zou, Z. Yang, J. X. Dai et al., "The characteristics and significance of conventional and unconventional Sinian-Silurian gas systems in the Sichuan Basin, Central China," *Marine and Petroleum Geology*, vol. 64, pp. 386–402, 2015.

[11] W. Ju, J. L. Wang, H. H. Fang, Y. Gong, and S. Zhang, "Paleostress reconstructions and stress regimes in the Nanchuan region of Sichuan Basin, South China: implications for hydrocarbon exploration," *Geosciences Journal*, vol. 21, no. 4, pp. 553–564, 2017.

[12] W. J. Shen, X. Z. Li, Y. M. Xu, Y. Sun, and W. Huang, "Gas flow behavior of nanoscale pores in shale gas reservoirs," *Energies*, vol. 10, no. 6, p. 751, 2017.

[13] M. D. Zoback, C. A. Barton, M. Brudy et al., "Determination of stress orientation and magnitude in deep wells," *International Journal of Rock Mechanics and Mining Sciences*, vol. 40, no. 7-8, pp. 1049–1076, 2003.

[14] M. Tingay, R. R. Hillis, C. K. Morley, R. C. King, R. E. Swarbrick, and A. R. Damit, "Present-day stress and neotectonics of Brunei: implications for petroleum exploration and production," *AAPG Bulletin*, vol. 93, no. 1, pp. 75–100, 2009.

[15] M. Rajabi, M. Tingay, and O. Heidbach, "The present-day state of tectonic stress in the Darling Basin, Australia: implications for exploration and production," *Marine and Petroleum Geology*, vol. 77, pp. 776–790, 2016.

[16] O. Jones, "The Dynamics of faulting and dyke formation: with applications to Britain," *Nature*, vol. 149, no. 3789, pp. 651-652, 1942.

[17] Q. Z. Guan, D. Z. Dong, S. F. Wang et al., "Preliminary study on shale gas microreservoir characteristics of the lower Silurian Longmaxi Formation in the southern Sichuan Basin, China," *Journal of Natural Gas Science and Engineering*, vol. 31, pp. 382–395, 2016.

[18] O. Heidbach, M. Tingay, A. Barth, J. Reinecker, D. Kurfeß, and B. Müller, "Global crustal stress pattern based on the World Stress Map database release 2008," *Tectonophysics*, vol. 482, no. 1-4, pp. 3–15, 2010.

[19] W. Ju, Z. L. Li, W. F. Sun, and H. Xu, "In-situ stress orientations in the Xiagou tight oil reservoir of Qingxi oilfield, Jiuxi Basin, Northwestern China," *Marine and Petroleum Geology*, vol. 98, pp. 258–269, 2018.

[20] J. D. O. Williams, M. W. Fellgett, A. Kingdon, and J. P. Williamson, "In-situ stress orientations in the UK Southern North Sea: regional trends, deviations and detachment of the post-Zechstein stress field," *Marine and Petroleum Geology*, vol. 67, pp. 769–784, 2015.

[21] M. Sandiford, M. Wallace, and D. Coblentz, "Origin of the in situ stress field in South-Eastern Australia," *Basin Research*, vol. 16, no. 3, pp. 325–338, 2004.

[22] W. Zeng, W. Ding, J. Zhang et al., "Fracture development in Paleozoic shale of Chongqing area (South China). Part two: numerical simulation of tectonic stress field and prediction of fractures distribution," *Journal of Asian Earth Sciences*, vol. 75, pp. 267–279, 2013.

[23] A. J. White, M. O. Traugott, and R. E. Swarbrick, "The use of leak-off tests as means of predicting minimumin-situstress," *Petroleum Geoscience*, vol. 8, no. 2, pp. 189–193, 2002.

[24] R. Liu, J. Z. Liu, W. L. Zhu et al., "In situ stress analysis in the Yinggehai Basin, northwestern South China Sea: implication for the pore pressure-stress coupling process," *Marine and Petroleum Geology*, vol. 77, pp. 341–352, 2016.

[25] M. K. Hubbert and D. G. Willis, "Mechanics of hydraulic fracturing," *AIME Petroleum Transactions*, vol. 210, no. 1, pp. 153–168, 1957.

[26] W. Ju and W. F. Sun, "Tectonic fractures in the lower Cretaceous Xiagou Formation of Qingxi oilfield, Jiuxi Basin, NW China. Part two: numerical simulation of tectonic stress field and prediction of tectonic fractures," *Journal of Petroleum Science and Engineering*, vol. 146, pp. 626–636, 2016.

[27] J. S. Liu, H. M. Yang, X. F. Wu, and Y. Liu, "The in situ stress field and microscale controlling factors in the Ordos Basin, Central China," *International Journal of Rock Mechanics and Mining Sciences*, vol. 135, no. 7, article 104482, 2020.

[28] K. Fischer and A. Henk, "A workflow for building and calibrating 3-D geomechanical models–a case study for a gas reservoir in the North German Basin," *Solid Earth*, vol. 4, no. 2, pp. 347–355, 2013.

[29] K. Jiu, W. L. Ding, W. H. Huang, S. You, Y. Zhang, and W. Zeng, "Simulation of paleotectonic stress fields within Paleogene shale reservoirs and prediction of favorable zones for fracture development within the Zhanhua depression, Bohai Bay Basin, East China," *Journal of Petroleum Science and Engineering*, vol. 110, pp. 119–131, 2013.

[30] A. Kingdon, M. W. Fellgett, and J. D. O. Williams, "Use of borehole imaging to improve understanding of the in-situ stress orientation of central and Northern England and its implications for unconventional hydrocarbon resources," *Marine and Petroleum Geology*, vol. 73, pp. 1–20, 2016.

[31] M. H. Rmmay and A. A. Awotunde, "Stochastic optimization of hydraulic fracture and horizontal well parameters in shale gas reservoirs," *Journal of Natural Gas Science and Engineering*, vol. 36, pp. 71–78, 2016.

[32] A. N. Dehghan, K. Goshtasbi, K. Ahangari, and Y. Jin, "Experimental investigation of hydraulic fracture propagation in fractured blocks," *Bulletin of Engineering Geology and the Environment*, vol. 74, no. 3, pp. 887–895, 2015.

[33] Y. S. Zhang, J. C. Zhang, B. Yuan, and S. Yin, "In-situ stresses controlling hydraulic fracture propagation and fracture breakdown pressure," *Journal of Petroleum Science and Engineering*, vol. 164, pp. 164–173, 2018.

[34] S. Reynolds, R. Hillis, and E. Paraschivoiu, "In situ stress field, fault reactivation and seal integrity in the Bight Basin, South Australia," *Exploration Geophysics*, vol. 34, no. 3, pp. 174–181, 2003.

[35] S. D. Mildren, R. R. Hillis, and J. Kaldi, "alibrating predictions of fault seal reactivation in the Timor Sea," *Journal of the Australian Petroleum Production & Exploration Association*, vol. 42, no. 1, pp. 187–202, 2002.

WILEY | Hindawi

Research Article

Influence Research for Softening and Swelling of Weakly Cemented Soft Rock on the Stability of Surrounding Rock in Roadway

Yan Li ⓘ, Chao Ma ⓘ, Lianying Zhang ⓘ, and Bing Li ⓘ

Xuzhou University of Technology, Xuzhou 221000, China

Correspondence should be addressed to Chao Ma; mbqq2008@126.com

In order to study the influence of the softening and swelling of weakly cemented soft rock on the stability of roadway surrounding rock, based on the background of the general return airway in the south wing of Yuwu coal mine, 4 different schemes are designed according to whether the softening or swelling effect of weak cemented soft rock is considered. Based on the numerical simulation program, FLAC^{3D} was used to analyze the distribution characteristics of the shear stress, displacement, and plastic zone of the surrounding rock of the roadway under these 4 designs. On this basis, in view of the geological conditions of the roadway, a new type of "grouting + anchor cable mesh + bottom arch" combined support plan is proposed. The research results show that, under the conventional anchor-net-cable-spraying support scheme, the surrounding rock of the roadway can remain stable without considering the softening and expansion of the weakly cemented soft rock in contact with water and its maximum displacement and plastic zone depth are only 66.9 mm and 2.8 m. When considering the softening and swelling of weakly cemented soft rock roadways, due to the synergistic effect of the two, the maximum displacement of the surrounding rock of the roadway and the depth of the plastic zone will reach 517.4 mm and 6.7 m, respectively, which will continue to increase with excavating along the roadway and lead to ultimately destabilization and destruction. After adopting the combined support of "grouting + anchor cable mesh + bottom arch," the maximum displacement of the surrounding rock of the roadway and the depth of the plastic zone will be reduced by 77.1% ~ 92.0% and 18.7% ~ 72.4%, respectively, and they will basically remain stable after excavation of 5 days.

1. Introduction

Weakly cemented soft rock, such as carbonaceous mudstone, mudstone, and silty mudstone, is distributed widely in the top and floor of coal seams in central and western China under the influence of geological tectonics [1–4]. Because the low strength, loose cementation, and poor performance of this rock, especially water, will result in softening and expansion, it is always sustainable growth and serious deformation of surrounding rock when tunneling in weak cemented soft rock roadway, drenched by water, leading to some accidents, including the floor heave, roof caving, and collapse, which seriously restrains efficient coal mine production safety [5–9].

Aiming at the stability control problem of surrounding rock in weakly cemented soft rock roadway under the condition of abundant water, Zhao et al. [10], Li et al. [11], Zhang et al. [12], and Liu et al. [13] carried out some experimental researches on the hydrodynamic characteristics of weakly cemented soft rock and obtained the variation rules of softening, expansion, and deformation parameters of weakly cemented soft rock with its water content or immersion time. Combining numerical simulation and field measurement, Jing and Chen [14], Zhu et al. [15, 16], Hu et al. [17], and Hu [18] analyzed the deformation and failure characteristics of surrounding rock of water-rich and weakly cemented soft rock roadway. Some supporting schemes, such as "bolt and cable combined support," "two layers of steel mesh sandwiching concrete shotcrete layer + anchor cable grouting," and "steel mesh roof protection + long and short anchor cable + channel steel beam," have been put forward and achieved good application effect. However, the

above research results rarely show the combination of laboratory test results and practical engineering practice, resulting in the fact that the influence mechanism of water softening and expansion of weakly cemented soft rock on deformation and failure of roadway surrounding rock is not very clear. Therefore, in this paper, based on the background of the general return airway in the south wing of Yuwu coal mine, a trilinear strain-softening model is introduced to change the strength and volume parameters of weakly cemented soft rock before and after flooding to reflect its water-softening and expansion characteristics. On this basis, numerical software FLAC^{3D} is used to analyze the distribution characteristics of the shear stress, displacement, and plastic zone of the surrounding rock of the roadway under four conditions, which are designed according to whether the softening or swelling effect of weak cemented soft rock is considered. In addition, a new type of "grouting + anchor cable mesh + bottom arch" combined support plan is proposed.

2. Engineering Situation

Yuwu Coal Industry Co. LTD is located 23 km southwest of Lu 'an Mining Group in the north of Houzhuang Village, about 35 km away from Changzhi City and 11 km away from Changcun Coal Mine. The general situation of its south wing return airway is shown in Figure 1. The cross section of the total return airway in the south wing of Yuwu Coal Industry Co. LTD is 5.2 m wide and 4.4 m high, and the buried depth is 1.55 m. The vertical and horizontal stresses are 12.8 MPa and 19.2 MPa, respectively. According to the surrounding borehole bar chart, the strata on top and bottom mainly consist of coal rock, mudstone, sandy mudstone, and medium and fine sandstone, shown in Figure 2. Among them, mudstone and sandy mudstone are weakly cemented soft rock, which is easy to sliming and expansion in the water, while the fractures of medium and fine sandstones are highly developed and water-rich.

The original support scheme of the roadway is designed as the combined support of bolt mesh cable and shotcrete, shown in Figure 3. The row distance between the left rebar bolts in the roof is 800 mm × 800 mm, with the diameter of 22 mm and the length of 2500 mm. The roof prestressed steel strand anchor cables are arranged in three-flowers distribution, with row spacing of 2400 mm × 2400 mm, diameter of 17.8 mm, and the length of 6300 mm. The roof and two sides of the roadway are supported by metal mesh shotcrete with 100 mm thick, while C25 plain concrete with 200 mm thick is used to support to bottom of the roadway. However, it is found that a large number of fracture channels in roof and floor of roadway after excavation for a period of time, due to excavation damage in weakly cemented soft rock, result in adjacent fracture water in fine sand strata flowing into it, which causing liming and expansion. In addition, instability of large deformation occurred, such as roof subsidence, intensive floor heave, anchor bolt fracture, and pallet drops, leading to serious threats to stability control of surrounding rock of roadway.
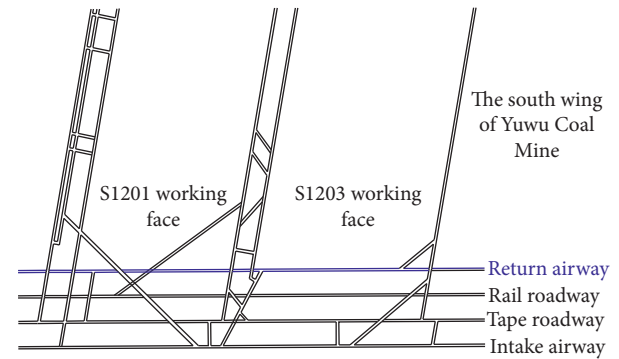
Figure 1: General situation of south wing return airway of Yuwu coal mine.
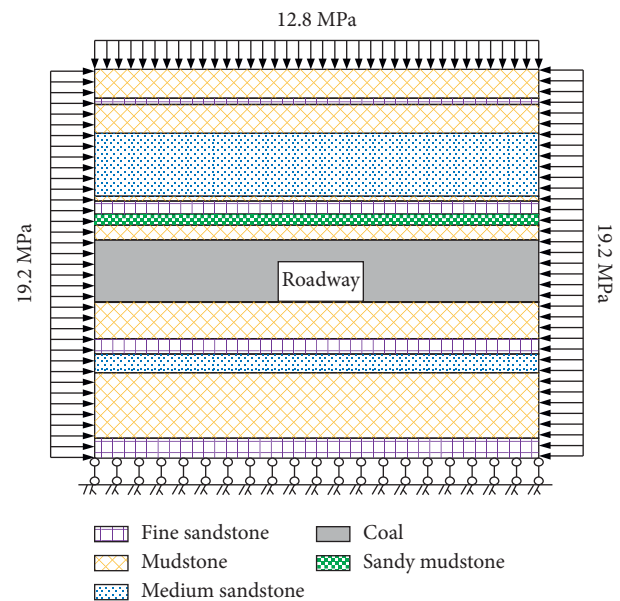
Figure 2: Geological section of the south wing general return airway.

3. Numerical Simulation Scheme Design

3.1. Numerical Model Establishment of Excavation of the Roadway. According to Saint Venant's principle, the width and height of the numerical model are more than 5 times the size of the roadway, and numerical software FLAC^{3D} is used to establish numerical model (shown in Figure 4) for the total return airway in the south wing of Yuwu in order to reduce the influence of setting boundary condition on deformation and failure of surrounding rock in roadway. The width, height, and length of the model are 45.2 m, 38.5 m, and 45.0 m, respectively, including 153000 elements and 161874 modes. For the mechanical boundary condition, the bottom surface in the model is fixed, and 19.2 MPa horizontal force is applied to around model, while 12.8 MPa vertical force is applied on the top surface. For the permeable boundary condition, the top surface is set as the permeable boundary, and the remaining surfaces are set as the impervious boundary. In the simulation of excavation roadway, each tunneling
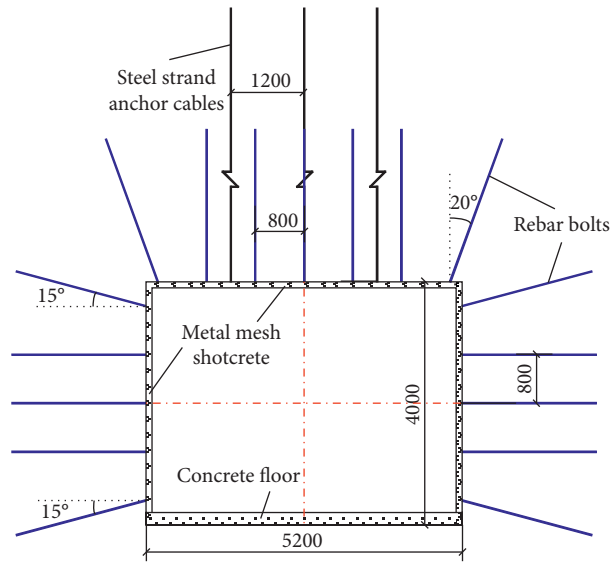
FIGURE 3: The support of anchor-net-cable-spraying for the south wing general return air tunnel.

— Stress measuring line

∘ Displacement measuring point

(a)   (b)
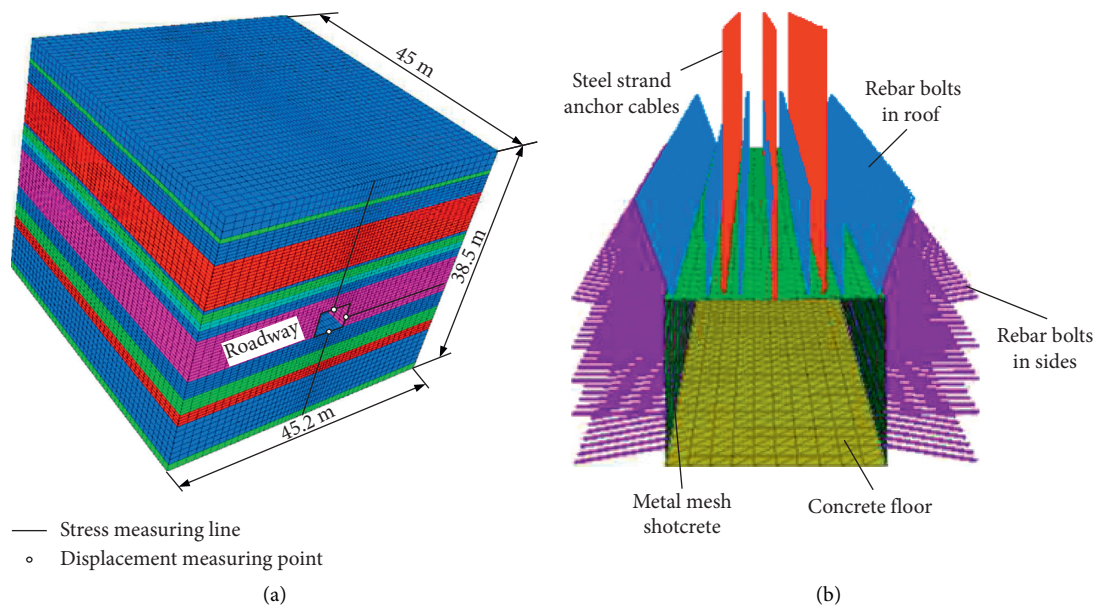
FIGURE 4: Numerical model of roadway excavation. (a) Grid model. (b) Supporting structure.

distance is 3 m, while anchor bolt and cable are simulated by cable element (with elastic modulus of 210 GPa, anchor agent cohesion of 5.0 MPa, internal friction angle of 33°, contact surface stiffness of 1000 GPa, and tensile strength of 360 MPa). Shell elements are used to simulate metal mesh shotcrete (with elastic modulus of 28 GPa and Poisson's ratio of 0.25) and concrete floor (with elastic modulus of 30 GPa and Poisson's ratio of 0.2). Besides, a measuring point and a measuring line are arranged on the top, bottom, and two sides of the initial driving face of roadway, respectively (shown in Figure 4(a)), in order to further study and analyze the stress and displacement variation characteristics of surrounding rock.

3.2. Determination of Mechanical Parameters of Surrounding Rock in the Roadway. In recent years, the trilinear strain softening model (shown in Figure 5) has been widely applied in numerical simulation of mine engineering, due to its simple parameter setting and its ability to reflect the strength variation characteristics of rock [19, 20]. Before reaching the ultimate bearing capacity, the rock is in the elastic stage OA, in which the stress σ and volume strain ε_v increase and decrease linearly with the increase of strain ε, respectively. At this stage, the cohesion c and the internal friction angle φ remain unchanged with initial value c_0 and φ_0, respectively. Over the ultimate bearing capacity, rocks start to produce plastic strain and enter into softening stage AB, in which the
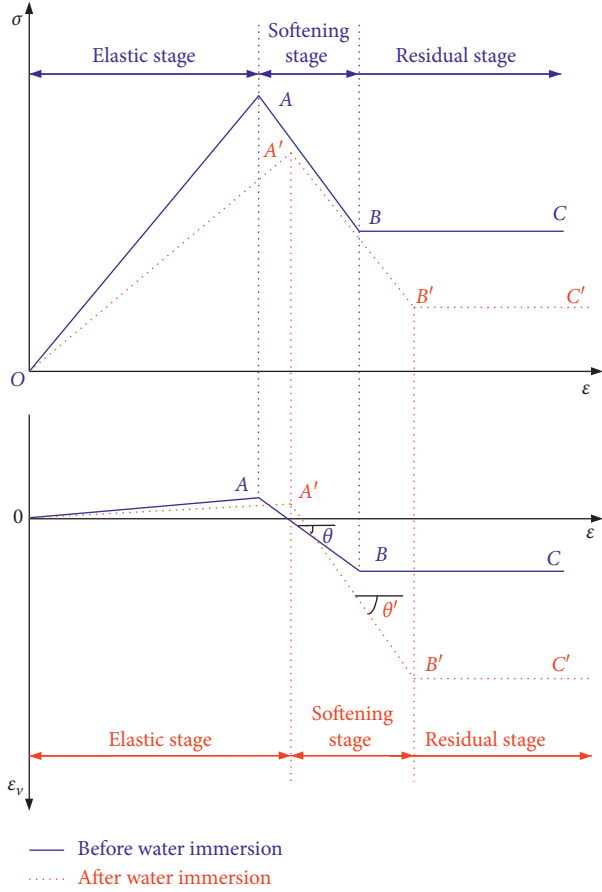
Figure 5: Changes of strength and volumetric strain with strain of weakly cemented soft rock before and after water absorption.

stress σ decreases rapidly with the increase of strain, while volume strain ε_v increases rapidly in the form of relationship shown in equation (1). At this point, the cohesion c and the internal friction angle φ gradually reduce to residual value of c_r and φ_r, respectively. The rocks will enter the residual stage BC upon the plastic strain increasing to s certain value. In the stage BC, both the stress σ and the volume strain ε_v will stop increasing with an increase in strain, while the cohesion c and the internal friction angle φ gradually keep the value of c_r and φ_r, respectively.

$$\varepsilon_v = \left(\frac{2 \sin \theta}{1 - \sin \theta} \right) \varepsilon_p, \tag{1}$$

where ε_v, θ, and ε_p are volume strain, dilatancy angle, and plastic strain, respectively.

For the rocks with good water stability, such as medium sandstone, fine sandstone, and coal rock, the variation characteristics of strength and volume strain before and after water absorption are not obvious, while, for weakly cemented mudstone and sandy mudstone (shown in Figure 5), water has limited influence on strength and volume strain (the strength only decreases by 15% ~ 20% after water immersion [13]), due to its complete structure and low permeability in the elastic stage. However, because of the cementing and expansion of clay minerals around the

through-crack, the attenuation range of strength and volume strain will increase significantly in the strain softening stage, which is indirectly reflected by the decrease of residual cohesion c_r and internal friction angle φ_r and the increase of dilatancy angle θ [17–19]. According to the indoor test results of rock [10, 12, 20–24], the mechanical parameters, used in simulation, of different surrounding rocks in the total return airway in the south wing are shown in Table 1.

3.3. Numerical Simulation Scheme Design. In order to study the influence of the softening and swelling of weakly cemented soft rock on the stability of roadway surrounding rock, based on the background of engineering, 4 different schemes are designed as follows:

(1) Scheme 1: the mechanical parameters of sandy mudstone and mudstone before water absorption are used, regardless of water softening and expansion;

(2) Scheme 2: only considering water softening, the mechanical parameters of sandy mudstone and mudstone after water absorption are used, regardless of variation of dilatancy angle.

(3) Scheme 3: only considering expansion, the mechanical parameters of sandy mudstone and mudstone before water absorption are used, and the variation of dilatancy angle is considered.

(4) Scheme 4: considering water softening and expansion, the mechanical parameters of sandy mudstone and mudstone after water absorption are used.

4. Numerical Results Analysis

4.1. Influence of Softening and Expansion on Stress of Surrounding Rock in the Roadway. After finishing the excavation, maximum shear stress distribution curves of surrounding rock of weakly cemented soft rock in roadway under different numerical simulation schemes are shown in Figure 6. Since the stress of surrounding rock is redistributed after excavation, the shear stress is highly centralized in the roadway surface. The rock shear failure will occur when shear stress exceeds the shear strength of rocks, leading to reduce in carrying capacity. The high shear stress will distribute in depth of the surrounding rock and gradually attenuates, and the maximum is located in a certain distance away from the roadway surface. At the position where the maximum shear stress is concentrated, the surrounding rock in the surface is at the state of plastic failure, and the more serious the failure degree, the smaller the shear stress. However, the surrounding rock from the maximum shear stress concentration position to the depth is in an elastic state, and the farther away from the roadway surface, the smaller shear stress, which finally reduces to initial stress state.

It can be seen from Figure 6 that, without considering the softening and expansion of weakly cemented soft rock (Scheme 1), the maximum shear stress concentration values of roof, floor, and two sides are 9.1 MPa, 11.2 MPa, and 6.7 MPa, respectively, which are located at the distance of

TABLE 1: Mechanical parameters of surrounding rock of roadway.

Rock types	Density (kg/m³)	Elasticity modulus/ GPa	Poisson's ratio	Prepeak cohesion/ MPa	Prepeak internal friction angle/°	Residual cohesion/ MPa	Residual internal friction angle/°	Tensile strength/ MPa	Dilatancy angle/°
Sandy mudstone	2280	4.1 (3.3)	0.28	1.64 (1.39)	31 (30)	1.0 (0.4)	28 (25)	1.2 (1.0)	6 (45)
Mudstone	2150	3.7 (3.0)	0.30	2.05 (1.74)	30(29)	1.2 (0.5)	26(24)	1.6 (1.4)	5 (55)
Fine sandstone	2600	6.5	0.23	1.96	35	0.6	32	1.6	12
Medium sandstone	2510	5.9	0.25	1.78	34	0.5	31	1.5	10
Siltstone	2480	5.0	0.24	1.82	34	0.6	31	1.4	11
Coal mine	1450	2.4	0.28	1.42	31	0.6	30	1.0	7

Note. The number in the bracket is the corresponding parameter value of soft rock after water absorption.

(a)

(b)

(c)
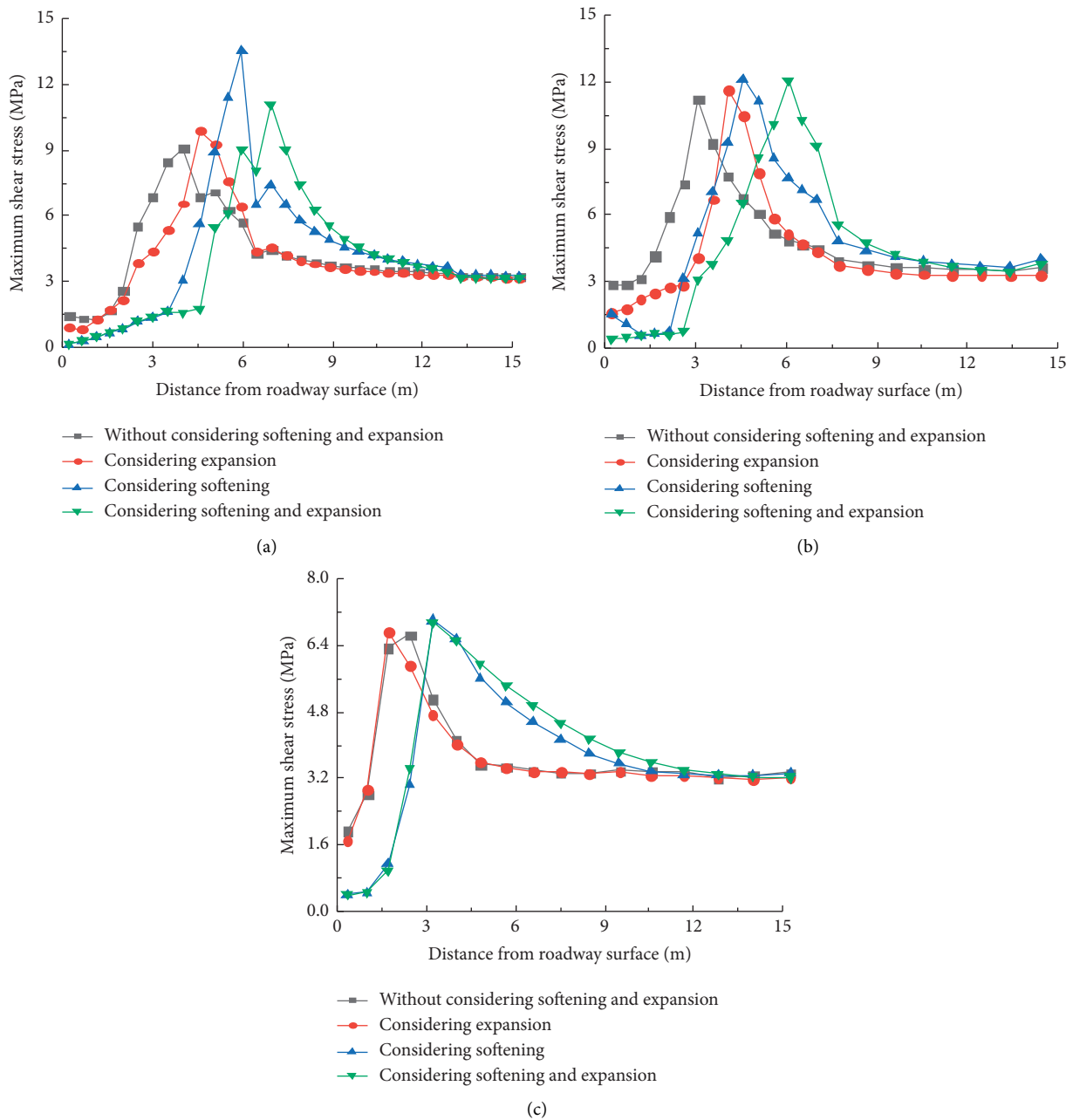
FIGURE 6: Maximum shear stress distribution curves of weakly cemented soft rock in the roadway under different simulation schemes. (a) Roof. (b) Floor. (c) Two sides.

4.0 m, 3.1 m, and 2.4 m from roadway surface. And the surrounding rock, which are in the range of plastic failure, remains the maximum shear stress of 1.3 MPa ~ 2.8 MPa. Compared with Scheme 1, under the condition of Scheme 2 (that is, considering water softening), the maximum shear stress concentration values of surrounding rock have smaller changes, but their locations on roof and floor are 0.5 m and 1.0 m far away from the roadway, while they remain unchanged in the two sides of roadway. When only considering expansion (Scheme 3) or both water softening and expansion (Scheme 4), the maximum shear stress of surrounding rock at the range of plastic failure directly reduces to 0.3 MPa. And the concentration positions of the maximum shear stress in roof, floor, and two sides are about 2.0 m ~ 3.0 m, 1.5 m ~ 3.0 m, and 0.8 m away from the roadway, respectively. This indicates that the softening and expansion, especially softening, of weakly cemented soft rock will reduce the carrying capacity of shallow surrounding rock and increase the degree of failure, resulting in the significant increase of surrounding rock loose zone and the decline of carrying capacity or local failure in supporting structure.

4.2. Influence of Softening and Expansion on Deformation of Surrounding Rock in the Roadway

4.2.1. Vertical Displacement. Figure 7 shows the vertical displacement distributions of surrounding rock of weakly cemented soft rock in roadway after finishing the excavation under different numerical simulation schemes. Under the condition of Scheme 1, the vertical displacement of surrounding rock mainly occurs in the shallow area of 2 m at the roof and floor. The maximum vertical displacement is at the center of roof and floor of roadway, which are 66.9 m and 30.9 mm, respectively, while the vertical displacement in the depth or two sides of roadway decreases rapidly to 0. It is indicated that the conventional bolt-net cable shotcrete support technology can effectively ensure the safety of weakly cemented soft rock in roadway without considering water (no softening and expansion). Under the conditions of Schemes 2 to 4, the locations of the maximum vertical displacement of surrounding rock are still at the center of roof and floor, which are 162.0 mm and 254.3 mm, respectively, improved by 142.2% and 723.0% compared with those in Scheme 1. The maximum vertical displacements at the center of roof and floor are 253.1 mm and 96.9 mm under Scheme 3, improved by 278.3% and 213.6%, respectively. For Scheme 4, the maximum vertical displacements of surrounding rock are 517.4 mm and 496.2 mm in the center of roof and floor, respectively, which are increased by 673.4% and 1505.8%. Moreover, considering the expansion of soft rock, the attenuation rate of vertical displacement of surrounding rock will significantly slow down with the increase of depth, leading to a great displacement at 2 m away from the roadway surface and a larger loosening range of surrounding rock. Therefore, it can be seen that the softening of soft rock is the main reason for roof subsidence, while the floor heave is mainly related to expansion. Considering both

softening and expansion, these two will cause obvious synergistic effect, resulting to displacement damage, such as sharp increase in vertical displacement of roof and floor, roof caving, and floor heave.

4.2.2. Horizontal Displacement. The horizontal displacement distributions of surrounding rock of weakly cemented soft rock in roadway after finishing the excavation under different numerical simulation schemes are shown in Figure 8. Under the condition of Scheme 1, the horizontal displacement of surrounding rock is mainly produced in the top with depth of 1.5 m and two sides of roadway. The maximum horizontal displacement is at the center of the surface of the two sides, of which the value is 40.4 mm, indicating that the surrounding rock of the two sides in roadway can keep stability under the conventional bolt-net cable shotcrete support. Compared with Scheme 1, under the condition of Scheme 2, the maximum horizontal displacement of surrounding rock only increases by 1.7 mm at two sides, while that increases significantly in the top with 1.5 depth and floor, especially near the corner of roadway, where the value increases directly to 32.0 mm.

In the case of Scheme 3, the horizontal displacement distribution law of surrounding rock is the same as that in Scheme 1, but the maximum horizontal displacement at the center of two sides in roadway is 153.0 mm, which is 3.8 times that in Scheme 1. However, the horizontal displacement of surrounding rock in roadway increases significantly in top and floor with depth of 3.0 m and two sides, of which the maximums are 206.6 mm and 141.4 mm, under the condition of Scheme 4. The above results show that the expansion of weakly cemented soft rock around the roadway has a limited influence on horizontal displacement of two sides, while the softening will weaken greatly the bearing arch action of the surrounding rock, leading to serious horizontal displacement of two sides. When both the softening and expansion occur, the horizontal displacement of two sides will further increase due to the coupling effect, resulting in accidents, such as bulging and wall caving.

4.2.3. Maximum Displacement of the Roadway Surface over Time. Figure 9 shows the displacement variation curve of measured points in surrounding rock during excavation of roadway. It is can be seen that, regardless of softening and expansion, the displacements of surrounding rock at roof, floor, and two sides of roadway are always small (the maximum is less than 70 mm), which keep the constants after excavating forward 9 m. This indicates that the supporting structure and surrounding rock have formed an effective bearing system, which can restrain effectively the deformation extension of surrounding rock in roadway. Under the condition of considering expansion, the maximum displacement of surrounding rock at two sides keeps unchanged, but that at roof and floor increases to 250 mm, which remains roughly stable after excavating forward 21 m, while, considering softening, the maximum displacements at roof, floor, and two sides are 2-3 times higher than that of
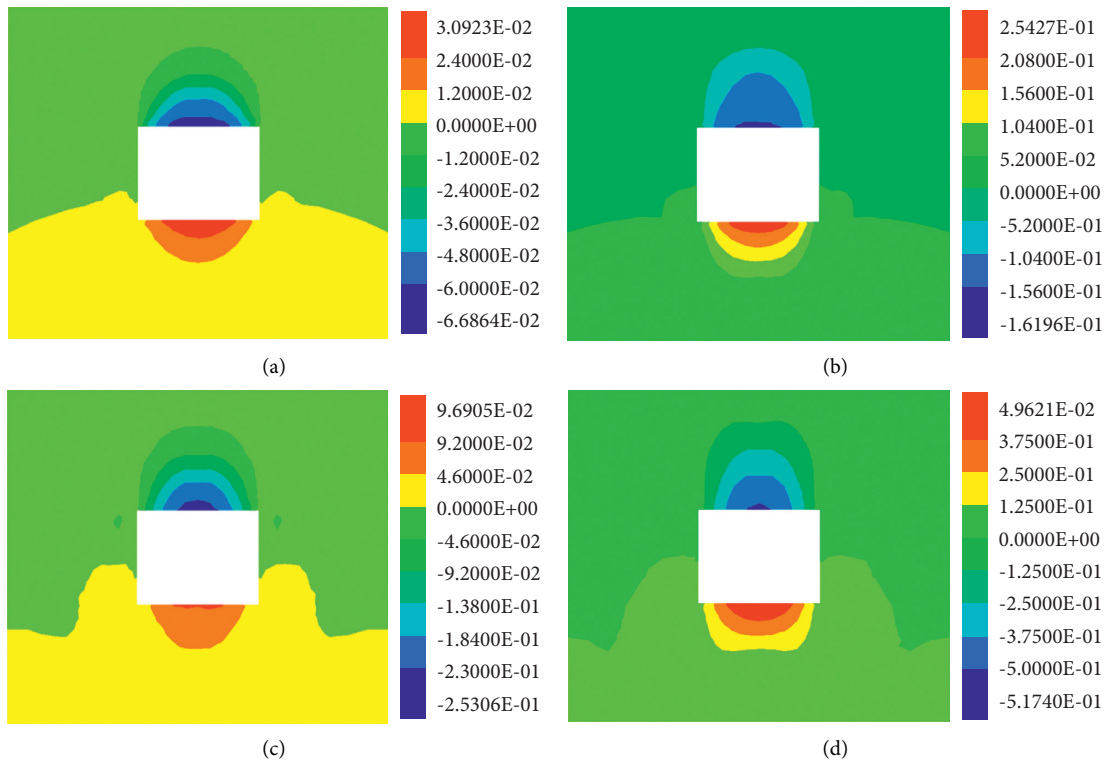
FIGURE 7: Vertical displacement distributions of surrounding rock of weakly cemented soft rock in the roadway under different simulation schemes. (a) Without softening and expansion. (b) With expansion. (c) With softening. (d) With softening and expansion.
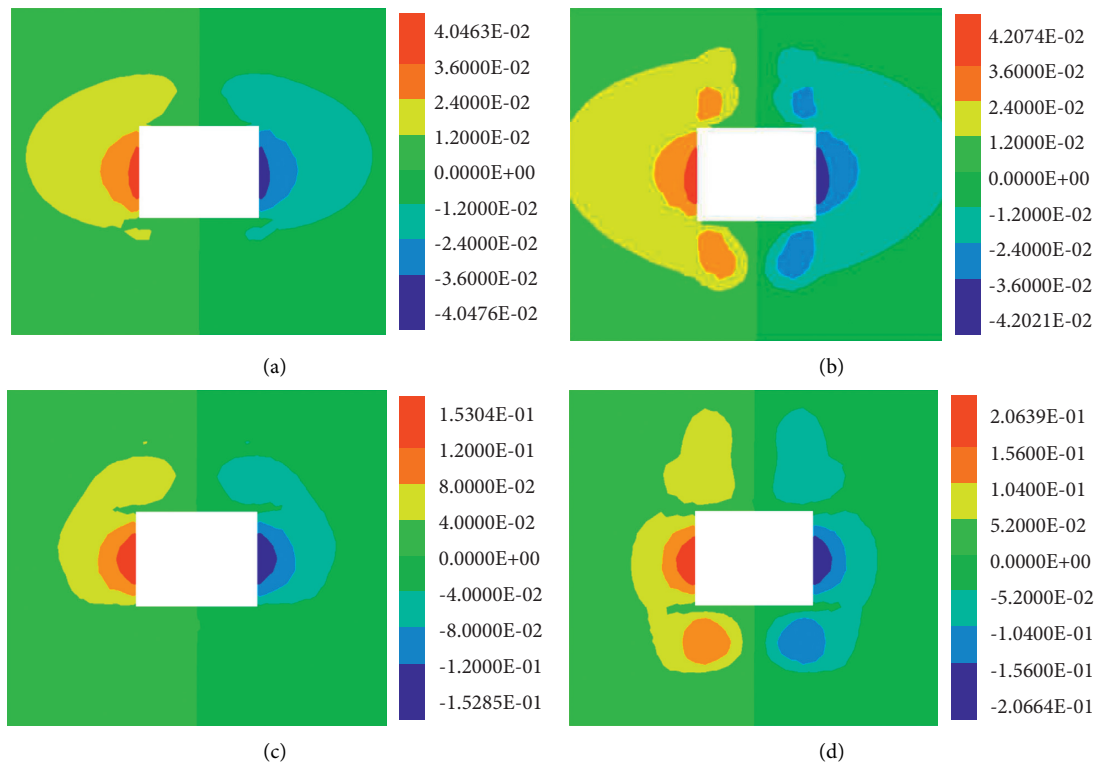
FIGURE 8: Horizontal displacement distributions of surrounding rock of weakly cemented soft rock in the roadway under different simulation schemes. (a) Without softening and expansion. (b) With expansion. (c) With softening. (d) With softening and expansion.

(a)

(b)

(c)
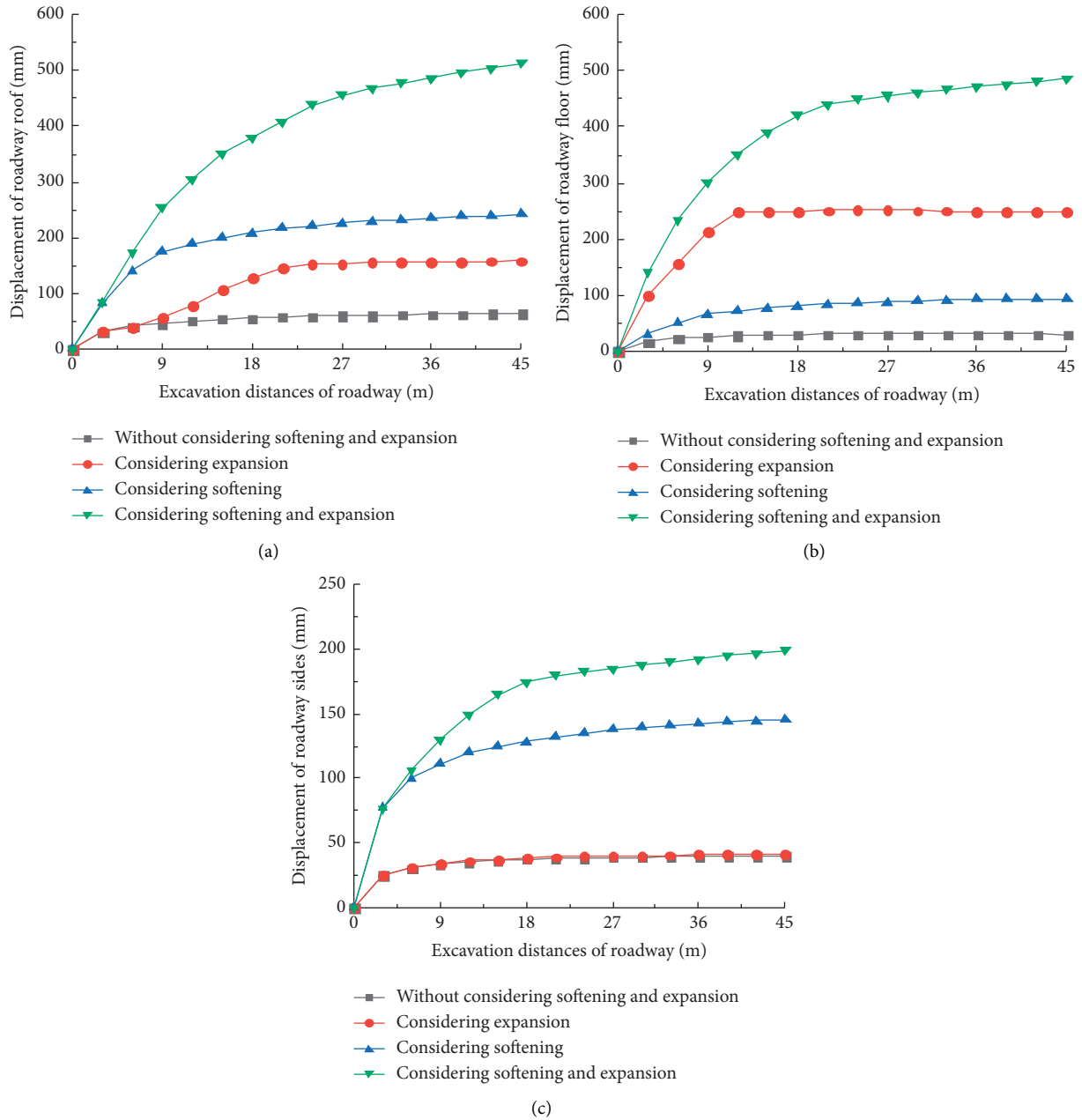
FIGURE 9: Change curves of surface displacement of weakly cemented soft rock in the roadway under different schemes. (a) Roadway roof. (b) Roadway floor. (c) Roadway sides.

Scheme 1, which still increase gradually with the increase of excavation distances after excavating forward 21 m. Compared with Scheme 1, the maximum displacements at roof, floor, and two sides increase by 7 times, 15 times, and 4 times under the condition of considering both softening and expansion, which continue to increase with excavating, leading to large deformation instability of roadway. Therefore, it is necessary to consider the effect of softening and expansion of weakly cemented soft rock on the stability of surrounding rock and supporting structure when tunneling in water-rich and weakly cemented soft rock stratum, in order to avoid serious economic losses caused by roadway repair or instability.

4.3. Influence of Softening and Expansion on Failure of the Surrounding Rock in the Roadway.
The distributions of plastic zone for surrounding rock of weakly cemented soft rock in roadway after finishing the excavation under different numerical simulation schemes are shown in Figure 10. Regardless of softening and expansion, the failure depths of plastic zones of surrounding rock in roof, floor, and two sides are 2.7 m, 2.8 m, and 2.0 m, respectively, and these plastic zones are not cut-through, indicating that the surrounding rock is at the effective supporting range by existed support of anchor cable. Under the condition of considering expansion, the failure depth of plastic zone in two sides of surrounding rock is
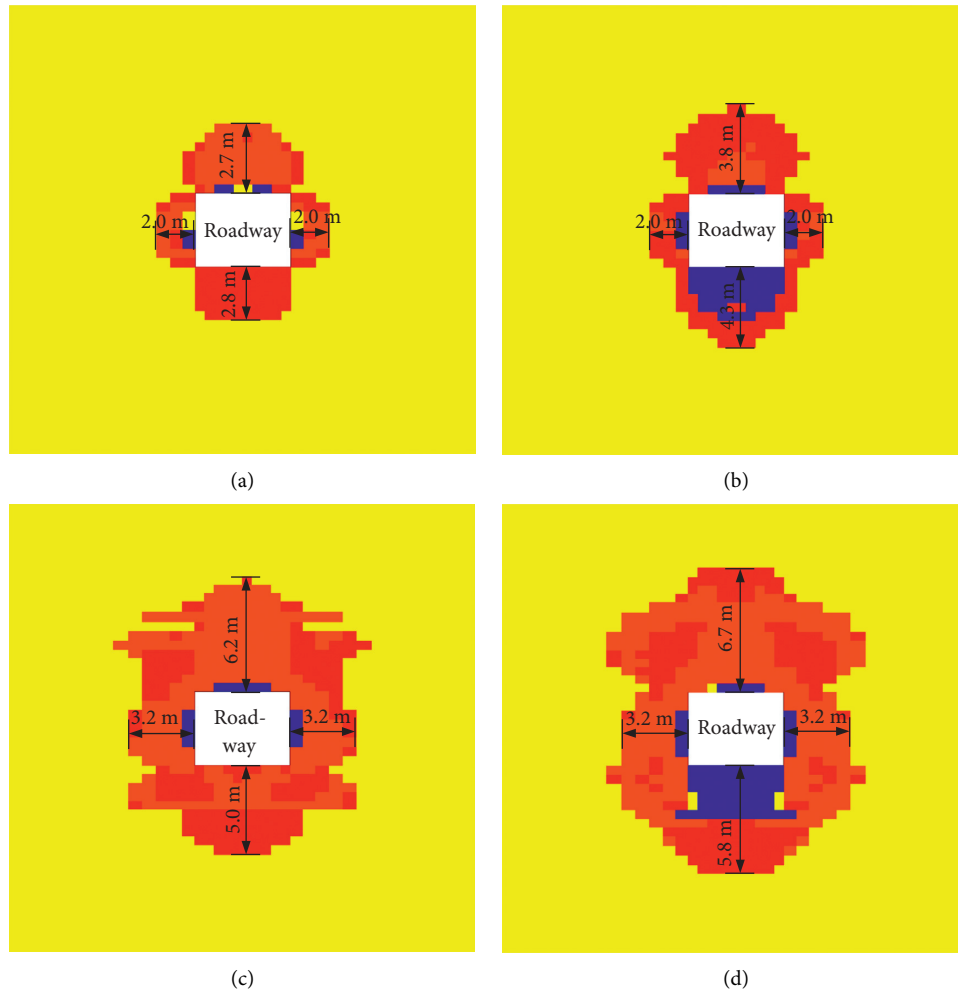
FIGURE 10: Distribution of plastic zone of weakly cemented soft rock roadway surrounding rock under different simulation schemes (red: shear failure, blue: shear-tension failure). (a) Scheme 1: without softening and expansion. (b) Scheme 2: with expansion. (c) Scheme 3: with softening. (d) Scheme 4: with softening and expansion.

still 2.0 m, but that in roof and floor extends to 3.85 m and 4.36 m, respectively. This indicates that the expansion of weakly cemented soft rock stratum affects the bearing capacity of support structure in two sides, but it will seriously affect the interaction and bearing capacity of the supporting and itself. When the softening is considered, the failure depths of plastic zones in roof, floor, and two sides are 6.2 m, 5.0 m, and 3.2 m, respectively. And these plastic zones are cut-through, indicating that it is difficult for the surrounding rock of roadway to form an effective bearing arch system, leading to a large increase in the stress of the existing supporting structure and a greater probability of failure. With considering softening and expanding of weakly cemented soft rock, the plastic failure range in roof and floor further increases to 6.7 m and 5.8 m, resulting in weakening in the bearing capacity of surrounding rock and exacerbating roadway deformation.

5. Studying on Supporting Countermeasures of Weakly Cemented Soft Rock in the Roadway

5.1. Design of the New Supporting Scheme. It can be seen from the above that the original supporting scheme of the total return airway in the south wing of Yuwu can effectively suppress its deformation and failure expansion to ensure the safety of roadway. However, under the condition of water, the shallow strata with weakly cemented soft rock of roadway will produce water fracture channel due to shear stress concentration, of which large amounts of clay minerals cement and expand, leading to great increase in scope and degree of damage of surrounding rock in roadway. The large deformation sustains increase to ultimate failure destruction of supporting structure and instability of roadway. It can be concluded that the key to stability control of the surrounding rock with water-rich and weakly cemented soft rock in roadway is to reduce the failure range and degree of
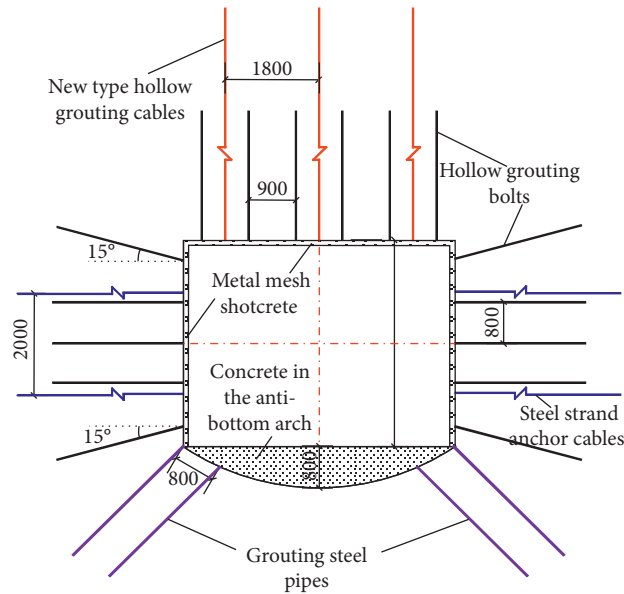
FIGURE 11: "Grouting + anchor cable mesh + bottom arch" combined support scheme for weakly cemented and soft rock in the roadway.

weakly cemented soft rock, and to prevent the fissure water in the fine sandstone around the roadway from penetrating into the roadway through the water-conducting fissure of the weakly cemented soft rock. Therefore, a new combined support scheme of "Grouting + anchor cable mesh + bottom arch" is put forward for total return airway in the south wing of Yuwu, as shown in Figure 11:

(1) Grouting and water plugging of surrounding rock. Since the bolt body of the hollow anchor bolt adopts a hollow design, the hole in the bolt body is used as a high-pressure wind and water channel and a grouting channel. Compared with a solid bolt body, the hollow bolt body design can obtain better rigidity and shear strength. Therefore, the screw steel bolts in the roof and two sides of roadway in original support scheme are changed into hollow grouting bolts with $\Phi 20\,mm \times 2500\,mm$, of which the row spacing is 800 mm, but that in roof and two sides is 900 mm and 800 mm, respectively. The anchor cables in roof of roadway are changed into new hollow grouting anchor cable with $\Phi 22\,mm \times 8000\,mm$ and row spacing 1800 mm × 1600 mm. Two grouting steel pipes, with $\Phi 32\,mm \times 3000\,mm$ and row spacing 800 mm × 800 mm, are arranged at the bottom of both sides of the roadway, respectively. The grouting materials is Malisan cement slurry, and the grouting pressure is 1.0 ~ 3.0 MPa.

(2) Strengthen support of anchor cable in two sides. Two prestressed steel strand anchor cables, with $\Phi 17.8\,mm \times 2000\,mm$, row spacing ,2000 mm ×1600 mm, and preload not less than 110 kN, are added between the two sides of hollow grouting anchor bolts.

(3) Closed roadway surface with metal mesh shotcrete. A layer of 50 mm thick concrete is initially sprayed on the roof and two sides of the roadway. In addition, a metal mesh with size of 100 mm × 100 mm is laid. After the completion of the construction of anchor and cable, another layer of 50 mm thick concrete is sprayed.

(4) Overbreak and backfilled of the bottom arch. The bottom of the roadway is overdug to from an antibottom arch with the height of 800 mm, and C25 plain concrete is backfilled in the antibottom arch.

5.2. Effect Analysis of Engineering Application. Based on the numerical simulation of Scheme 4, the excavation process of roadway under the combined support scheme of "grouting + anchor cable mesh + bottom arch" is simulated again (during the simulation, the cohesion of the rock in the grouting reinforcement range was increased by 1.2 times, the internal friction angle was increased by 0.5°, and the permeability coefficient was reduced by 20 times), and the displacement and plastic zone distribution after the excavation of surrounding rock in roadway with weakly cemented soft rock are shown in Figure 12. It can be seen that the maximum displacement of surrounding rock under the new support scheme still appears at the center of the roof, floor, and two sides of roadway, but the values reduce to 41.4 mm, 31.9 mm, and 47.3 mm, respectively, which are 92.0%, 93.6%, and 77.1% lower than those under the condition of Scheme 4. Under the new support scheme, the depth of plastic zone of surrounding rock in roof, floor, and two sides is 2.7 m, 1.6 m, and 2.6 m, respectively, which are reduced by 59.7%, 72.4%, and 18.7% compared with Scheme 4. It can be concluded that the combined support scheme of "grouting + anchor cable mesh + bottom arch" can significantly reduce the softening and expansion of weakly cemented soft rock and ensure the safe tunneling and normal use of weakly cemented soft rock in roadway.
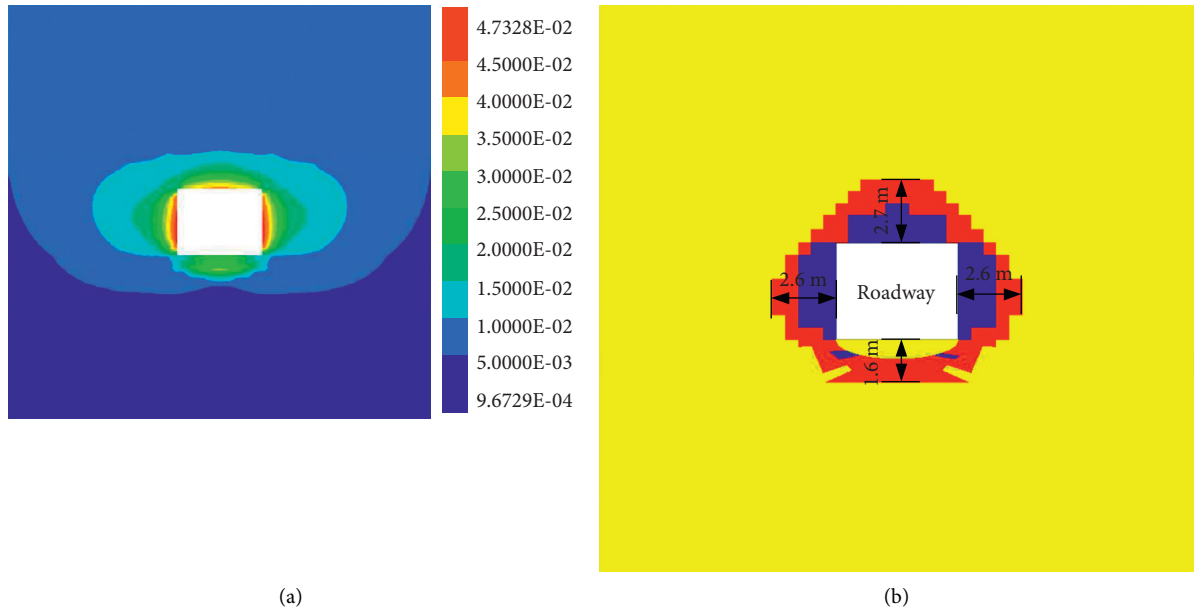
FIGURE 12: Numerical calculation results of displacement and plastic zone of surrounding rock in roadway with weak cemented soft rock roadway under new support scheme. (a) Displacement. (b) Plastic zone.
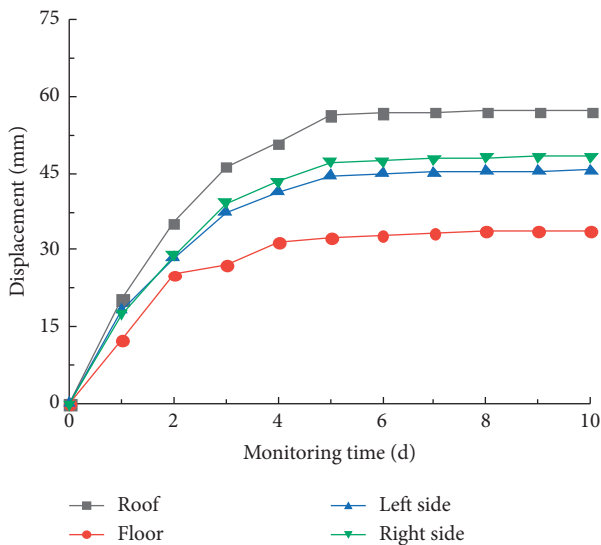
FIGURE 13: Monitoring curves of surrounding rock displacement of roadway under the new support scheme.

(4) In order to further study the stability of surrounding rock in roadway under the combined support scheme of "grouting + anchor cable mesh + bottom arch," the displacement of excavation section in the actual roadway is monitored. The displacement of the actual roadway over time is shown in Figure 13. It can be seen that the displacements of roof, floor, and two sides in roadway remain at stable values of 57.2 mm, 33.9 mm, and 48.4 mm, respectively, after excavation of 5 days under the combined support of "grouting + anchor cable mesh + bottom arch." This measured data is similar to the numerical simulation results in this paper, further indicating that the combined support of "grouting + anchor cable mesh + bottom arch" can effectively control the stability of surrounding rock with weakly cemented soft rock in roadway, which is more scientific and reasonable.

6. Conclusions

(1) Under the condition of considering softening and expansion, the maximum shear stress of surrounding rock in the plastic failure range of roadway directly reduces to 0.3 MPa, and its concentration position at roof, floor, and two sides is about 3.0 m and 0.8 m outward, respectively, compared with those in the non-water environment.

(2) The maximum displacements of surrounding rock with weakly cemented soft rock in roof, floor, and two sides of roadway are 66.9 m, 30.9 mm, and 40.4 mm, respectively, in anhydrous environment. However, in the water-rich environment, due to the obvious synergistic effect of softening and expansion of weakly cemented soft rock, these values increase to 517.4 mm, 496.2 mm, and 206.6 mm, respectively, which continue to increase with tunneling of roadway.

(3) Considering the influence of softening and expansion of weakly cemented soft rock, the depths of plastic failure zones of the roof, floor, and two sides are 6.8 m, 5.8 m, and 3.2 m, respectively, which are 2.5, 2.1, and 1.6 times those under anhydrous environment.

(4) Compared with the conventional bolt mesh cable shotcrete support, the maximum displacements of roof, floor, and two sides with weakly cemented soft rock decrease by 92.0%, 93.6%, and 77.1% under the combined support scheme of "grouting + anchor cable mesh + bottom arch," respectively, and the depths of the plastic zone are reduced by 59.7%, 72.4%, and 18.7%.

Data Availability

The data used to support the findings of this study are included within the article.

Conflicts of Interest

The authors declare that they have no conflicts of interest.

Acknowledgments

References

[1] X. Zhang, L. I. Jun, J. Liu, and W. Peng, "Research on deformation characteristics of strong expansive soft rock roadway and its control strategy," *Journal of China University of Mining & Technology*, vol. 46, no. 3, pp. 494–500, 2017.

[2] G. Zhang, G. Guo, and Y. Lv, "Study on the strata movement rule of the ultrathick and weak cementation overburden in deep mining by similar material simulation: a case study in China," *Mathematical Problems in Engineering*, vol. 2020, Article ID 7356740, 21 pages, 2020.

[3] L. I. Qing, J. Hou, T. Han, W. Xu, Z. Zhou, and M. Dong, "Research on deformation mechanism and support technology of coal roadway with weakly cemented rock strata in Yangjiacun mine," *Coal Engineering*, vol. 48, no. 07, pp. 40–43, 2016.

[4] B. Luo, Y. Sun, Z. Xu et al., "Damage characteristics and mechanism of the 2017 groundwater inrush accident that occurred at dongyu coalmine in Taiyuan, Shanxi, China," *Water*, vol. 13, no. 3, p. 368, 2021.

[5] B. Liang, Q. Cao, J. Wang, and L. Jiang, "Experimental study on slaking characteristics of feeble disintegration soft rock in drying-wetting cycle," *China Safety Science Journal*, vol. 27, no. 8, pp. 91–96, 2017.

[6] Q. Meng, J. Wang, L. Han, W. Sun, W. Qiao, and G. Wang, "Physical and mechanical properties and constitutive model of very weakly cemented rock," *Rock and Soil Mechanics*, vol. 41, no. S1, pp. 19–29, 2020.

[7] B. Wang, "Calculation analysis on water swelling deformation of road in soft rock," *China Coal*, vol. 37, no. 05, pp. 58–60+93, 2011.

[8] Y. Xue, J. Liu, P. G. Ranjith, Z. Zhang, F. Gao, and S. Wang, "Experimental investigation on the nonlinear characteristics of energy evolution and failure characteristics of coal under different gas pressures," *Bulletin of Engineering Geology and the Environment*, vol. 81, no. 1, p. 38, 2022.

[9] Y. Xue, J. Liu, X. Liang, S. Wang, and Z. Ma, "Ecological risk assessment of soil and water loss by thermal enhanced methane recovery: numerical study using two-phase flow simulation," *Journal of Cleaner Production*, vol. 334, Article ID 130183, 2022.

[10] W. Zhao, W. Liang, M. Xu, and B. Liu, "Stability analysis of roadway in weakly consolidated formation based on clay mineral content," *Safety In Coal Mines*, vol. 51, no. 12, pp. 277–282, 2020.

[11] Y. Li, S. Wang, J. Zou, H. Wang, H. Li, and N. Wu, "Correlation research between shear strength and moisture content of swelling mudstone," *Science Technology and Engineering*, vol. 21, no. 7, pp. 2857–2864, 2021.

[12] J. Zhang, S. Cheng, H. Wang, Z. Gao, F. Zhou, and H. Zhou, "Experiment of microstructure and hydrologic characteristics of weakly cemented soft rocks in western China," *Coal Geology & Exploration*, vol. 48, no. 03, pp. 116–121, 2020.

[13] J. Liu, H. Jing, B. Meng, L. Wang, X. Zhang, and J. Yang, "Research on the effect of moisture content on the creep behavior of weakly cemented soft rock and its fractional-order model," *Rock and Soil Mechanics*, vol. 41, no. 08, pp. 2609–2618, 2020.

[14] L. Jing and S. Chen, "Composite support technology and monitoring analysis of water-rich soft rock roadway," *Safety In Coal Mines*, vol. 49, no. 08, pp. 231–233+238, 2018.

[15] X. Zhu, Z. Yang, Z. Pan, J. Zhao, and Z. Yang, "Full anchored cable support technology for dynamic pressure roadway with weakly cemented water-rich roof," *Coal Technology*, vol. 39, no. 03, pp. 26–30, 2020.

[16] X. Zhu, Z. Yang, H. Zhong, and J. Zhao, "Deformation characteristics and control technology of surrounding rock in retaining roadway with weak cemented water rich roof," *China Energy and Environmental Protection*, vol. 41, no. 11, pp. 167–170+174, 2019.

[17] G. Zhu, S. Li, J. Bai, X. Wang, and Y. Bai, "Study on rational support technology of mine weakly consolidated watery roadway," *Coal Science and Technology*, vol. 44, no. 03, pp. 7–11, 2016.

[18] Y. Hu, "Study on roof-fall mechanism and supporting countermeasure of rich water soft rock roadway," *Coal Mining Technology*, vol. 23, no. 03, pp. 63–66, 2018.

[19] C. Sun, S. Zhang, B. Jia, and Z. Wu, "Physical and numerical model tests on post-peak mechanical properties of granite," *Chinese Journal of Geotechnical Engineering*, vol. 37, no. 05, pp. 847–852, 2015.

[20] W. Jing, W. Xue, and Z. Yao, "Variation of the internal friction angle and cohesion of the plastic softening zone rock in roadway surrounding rock," *Journal of China Coal Society*, vol. 43, no. 08, pp. 2203–2210, 2018.

[21] X. Ma, S. Zhang, and X. Ma, "Experimental study on water principle characteristics of Neogene weak cementation rock," *Yellow River*, vol. 38, no. 05, pp. 125–127+142, 2016.

[22] L. Wang and Z. Li, "Triaxial compression test analysis of weakly cemented mudstone in West China," *Journal of Yangtze River Scientific Research Institute*, vol. 33, no. 08, pp. 86–90+95, 2016.

[23] G. Liu and L. I. Ming, "Experimental study of coal rock uniaxial and triaxial compression," *Safety In Coal Mines*, vol. 44, no. 07, pp. 4–6, 2013.

[24] J. Liu, Y. Xue, Q. Zhang, H. Wang, and S. Wang, "Coupled thermo-hydro-mechanical modelling for geothermal doublet system with 3D fractal fracture," *Applied Thermal Engineering*, vol. 200, Article ID 117716, 2022.

WILEY | Hindawi

Research Article

Total Seepage Resistance Model of Water-Displacing Diffusion of Slurry in Series and Parallel Fractures

Yang Hu [ID],[1] **Junhe Xie** [ID],[2] **Jian Ge** [ID],[3] **and Gang Liu** [ID][3]

[1]*School of Resources and Civil Engineering, Suzhou University, Suzhou 234000, Anhui, China*
[2]*School of Mechanics and Civil Engineering, China University of Mining & Technology, Xuzhou, Jiangsu 221116, China*
[3]*Renlou Coal Mine, Anhui Hengyuan Coal and Electricity Group Company Limited, Huaibei 235123, China*

Correspondence should be addressed to Yang Hu; hyhyc2012@126.com

With the increase in mining depth, potential water inrush in the limestone-fractured aquifers of Taiyuan formation and Ordovician formation becomes seriously threatened to the mining process. Grouting reinforcement, as a common prevention method, has been widely used in mine water inrush prevention. In this paper, a model of "seepage resistance" is proposed for the slurry diffusion in a single fracture and the theoretical expression on the seepage resistance corresponding to slurry with different flow patterns is conducted. The total seepage resistance model of water-displacing diffusion by slurry in series and parallel fractures is established. With the Lagrange interfacial tracing method, the control equations of water-displacing diffusion by slurry in fracture networks are derived, which get mutually validated with the theoretical results.

1. Introduction

The total coal reserves are abundant in China which accounted for 94% of total primary energy sources and about one-seventh of the world's total proven coal reserves. Although the proportion of total coal consumption in China's total disposable energy consumption has decreased in recent years, the current situation of coal-based energy structure in China will not change in the short term [1]. With the exhaustion of mining of shallow coal resources, the mining of deep coal resources has become normal. However, potential water inrush in the limestone-fractured aquifers of Taiyuan formation and Ordovician formation becomes seriously threatened to the process of mining deep coal resources [2]. According to incomplete statistics, the reserves of the North China type coal field threatened by the fractured aquifers of Taiyuan formation and Ordovician formation in the mining process are as high as 10 billion tons [3]. For the mining of coal resources under loose aquifers, the gangue waste filling-mining method is usually used to reduce the development height of water-conducting fracture zone, so as to improve the upper mining limit and reduce the waste of coal

resources. At the same time, in order to liberate a large number of coal resources threatened by confined fractured aquifers, the grouting reconstruction technology for the fractured aquifers is mainly adopted to prevent water inrush from the floor of coalbed in the mining process [4–7], which can not only displace the water in the fractured aquifer but also greatly increase the strength of the fractured rock masses after the fractures are blocked; thus, the purpose of turning the fractured aquifer into a relatively watertight layer is achieved.

In recent years, according to research on the diffusion mechanism of slurry in fractured rock masses by theoretical analysis, numerical simulation, laboratory test, and other research methods, many scholars at home and abroad have achieved many fruitful research results [8–17]. El Tani and Stille [18] derived the expression of the relationship between grouting time and diffusion range of slurry when Newtonian and Bingham slurry diffused in canal fractures and parallel plate fractures under the conditions of constant pressure grouting and constant flow grouting, which can provide a reference for grouting design of fractured rock mass. Mohajerani et al. [19] designed the slurry pressure display

calculation program (EGFP) for calculating the diffusion distance of slurry with different flow patterns (Newtonian slurry, Bingham slurry, and power-law slurry) in fractured rock mass. According to the analysis of the calculation examples using EGFP, it can be seen that the largest advantage of this method is high calculation efficiency. Liu and Sun [20] developed a grouting simulator considering the coupling effect between the slurry and rock, to calculate the fracture initiation, propagation, deformation of solids, and the flow process of slurry in the fracture. This method takes into account not only the fluid-solid coupling effect in the flow process of slurry but also factors such as hardening of slurry and evolution of fracture grid. Jin et al. [21] adopted the method of orthogonal experiment to analyze the diffusion effect of chemical slurry in the fracture under the condition of dynamic water; the results show that the water-plugging rate is positively correlated with the fracture roughness coefficient JRC but negatively correlated with slurry gel time, initial water flow rate, and fracture opening, and the curve of water flow rate and seepage pressure can be divided into three forms. The research results can provide certain reference for fracture grouting in rock mass. Hao et al. [22] studied the diffusion mechanism of self-expanding polyurethane slurry in fractures by laboratory tests and established a density model of the diffusion of polyurethane slurry in fractures by fitting the experimental data obtained. Chen et al. [13] used the coupling of finite element method (FEM) and volume of fluid (VOF) method to simulate the fracture of grouting process. In this method, the coupling effect of water and slurry two-phase fluid flow, stress distribution, and mesh cell damage is considered; in addition, the hardening process of slurry in soil is described by Young's modulus and viscosity which change with time. Finally, some examples of fracture grouting are simulated, and the effectiveness of the method is verified under the premise that the results obtained are similar to the experimental results.

The previous research mainly focuses on exploring the diffusion mechanism of slurry in non-water-filled fractured rock mass, but there are few research studies on the two-phase flow problem of water-displacing diffusion of slurry in the water-filled fractured structure. Since the existence of water in the fracture and the size of water pressure will change the diffusion state of slurry and the herringbone fracture structure is the basic component unit of the relatively complex discrete fracture network, it is necessary to further explore the diffusion mechanism of slurry in series and parallel structures such as herringbone fractures, so as to lay a foundation for the research on the water-displacing diffusion mechanism of slurry in complex fracture networks and finally achieve the purpose of choosing reasonable grouting parameters and ensuring the safety of mining.

2. Analysis of the Water-Displacing Mechanism in a Single Fracture

Exploring the mechanism of water-displacing diffusion of slurry in a single fracture is the basis of studying water-displacing diffusion of slurry in fracture networks, and also,

the pure cement slurry often used in the project site can be divided into power-law slurry ($0.5 < W/C < 0.7$), Bingham slurry ($0.7 < W/C < 1.0$), and Newtonian slurry ($W/C > 2.0$) [23]. In this section, theoretical analysis will be adopted to systematically analyze the changing law of the inflow flow rate along with the grouting time in the process of water-displacing diffusion of slurry in a single fracture with different flow patterns under constant pressure grouting.

2.1. Basic Assumptions. In the process of water-displacing diffusion of slurry in single fracture, the basic assumption is as follows:

(1) The slurry is an isotropic homogeneous fluid and incompressible

(2) The slurry has laminar flow in the process of water-displacing diffusion

(3) Slurry and water are incompatible, and water is completely displaced by slurry

(4) The fracture is saturated with water at the initial stage, and the slurry and water only diffuse in the fracture

(5) The velocity of slurry at the upper and lower surface of the fracture is 0, and the trace length of the fracture is the limit water-displacing diffusion distance of slurry

2.2. Theoretical Model. The schematic diagram of the water-displacing diffusion of each flow pattern of the slurry and the stress on the corresponding slurry microelement in a single fracture are shown in Figure 1. As shown in Figure 1, the equivalent hydraulic gap width of the fracture is b, the trace length is L, the grouting pressure is P_1, and the hydrostatic pressure is P_w.

According to the force balance of the slurry microelement along the x-axis, it can be seen that

$$P \cdot 2y - (P + dP) \cdot 2y - 2\tau dx = 0. \tag{1}$$

The rheological equation of Bingham slurry can be expressed as

$$\tau = \tau_0 + \mu_g \left(-\frac{du}{dy} \right), \tag{2}$$

where μ_g is the plastic viscosity of Bingham slurry; τ is the shear stress; and τ_0 is the yield stress of Bingham slurry.

From (1) and (2), we obtained

$$\frac{du}{dy} = \frac{1}{\mu_g} \left(\tau_0 + y \frac{dp}{dx} \right). \tag{3}$$

From the velocity boundary conditions of the flow core and nonflow core areas, it can be seen that

$$\left. \begin{aligned} u_{y=b/2} &= 0, \quad h_0 \le |y| \le \frac{b}{2} \\ u_{y=h_0} &= u, \quad -h_0 \le y \le h_0 \end{aligned} \right\}. \tag{4}$$
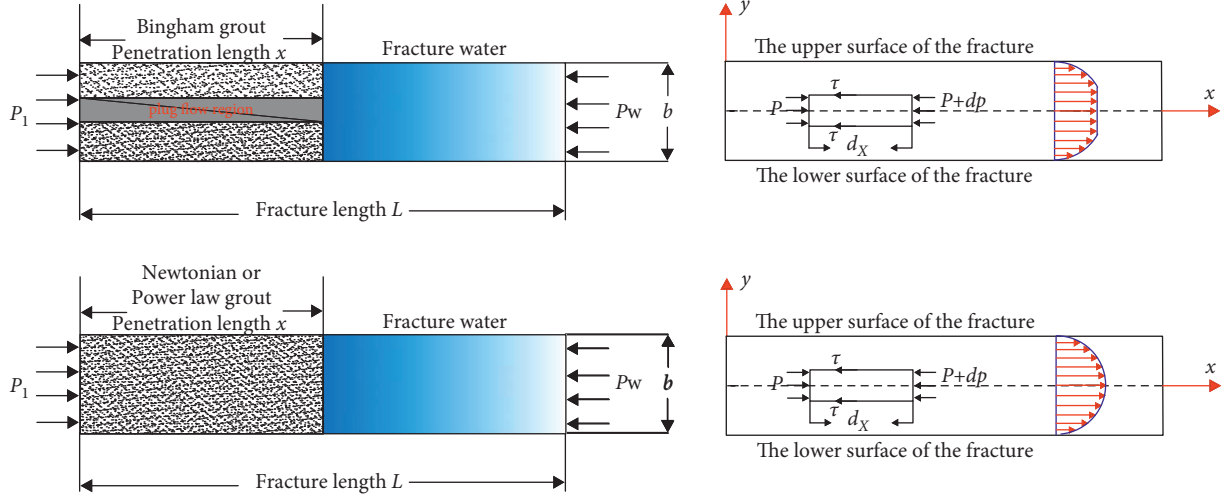
FIGURE 1: Sketch map of water-displacing diffusion by different types of slurry in a single fracture.

By introducing (4) into (3), we obtain the velocity distribution:

$$
u_g = \begin{cases}
\dfrac{1}{\mu_g}\left[\tau_0\left(|y| - \dfrac{b}{2}\right) + \dfrac{dp}{dx}\left(\dfrac{y^2}{2} - \dfrac{b^2}{8}\right)\right], & h_0 \le |y| \le \dfrac{b}{2}, \\[3mm]
\dfrac{1}{\mu_g}\left[\tau_0\left(h_0 - \dfrac{b}{2}\right) + \dfrac{dp}{dx}\left(\dfrac{h_0^2}{2} - \dfrac{b^2}{8}\right)\right], & -h_0 \le y \le h_0.
\end{cases}
\tag{5}
$$

According to the axisymmetric relation, the average velocity of the slurry can be given by

$$
\overline{u_g} = \frac{1}{b}\int_{-b/2}^{b/2} u\,dy = \frac{2}{b}\int_0^{b/2} u\,dy.
\tag{6}
$$

By introducing (5) into (6), we obtain

$$
\overline{u_g} = -\frac{b^2}{12\mu_g}\left[1 - \frac{3h}{b} + \frac{4h^3}{b^3}\right]\frac{dp}{dx}.
\tag{7}
$$

The starting pressure gradient of Bingham fluid and the height of flow core area (h) relation expression are as follows:

$$
\begin{cases}
\lambda = \dfrac{2\tau_0}{b}, \\[3mm]
h = \dfrac{\tau_0}{-(dp/dx)}.
\end{cases}
\tag{8}
$$

By introducing (8) into (7) and since λ is far less than dp/dx, ignoring an infinitesimal of higher order, the average slurry velocity can be calculated as

$$
\overline{u_g} = -\frac{b^2}{12\mu_g}\left[1 - \frac{3h}{b}\right]\frac{\partial p}{\partial x}.
\tag{9}
$$

The expression of flow rate q of Bingham slurry in the fracture is

$$
q = -\frac{b^3 w}{12\mu_g}\left[1 - \frac{3h}{b}\right]\frac{\partial p}{\partial x},
\tag{10}
$$

where w is the fracture thickness.

The rheological equation of power-law slurry can be expressed as follows:

$$
\tau = c\left(-\frac{du}{dy}\right)^n,
\tag{11}
$$

where c is the consistency coefficient of power-law slurry and n is the rheological index.

By introducing (10) into (1) and integrating, we obtain

$$
u = \left(\frac{1}{c}\right)^{1/n}\left(\frac{dp}{dx}\right)^{1/n}\left(\frac{n}{n+1}\right)|y|^{n+1/n} + A.
\tag{12}
$$

It can be known from the hypothesis that $u_{\pm b/2} = 0$; then, by introducing it into (12), the following equation can be obtained:

$$
u_g = \left(\frac{1}{c}\right)^{1/n}\left(\frac{dp}{dx}\right)^{1/n}\left(\frac{n}{n+1}\right)\left[|y|^{n+1/n} - \left(\frac{b}{2}\right)^{n+1/n}\right].
\tag{13}
$$

According to the axisymmetric relation, the average velocity of the slurry can be given by

$$
\overline{u_g} = \frac{1}{b}\int_{-b/2}^{b/2} u\,dy == \frac{2}{b}\int_0^{b/2} u\,dy.
\tag{14}
$$

By introducing (13) into (14), we obtain

$$
\overline{u_g} = \frac{-n}{2n+1}\left(\frac{1}{2^{n+1}c}\frac{dp}{dx}\right)^{1/n}b^{n+1/n}.
\tag{15}
$$

From the generalized Darcy's Law satisfied by power-law slurry, it can be observed that

$$
\overline{u_g} = -\frac{k_g}{\mu_g}\frac{\partial p}{\partial x}.
\tag{16}
$$

The equivalent apparent viscosity of power-law slurry in a single smooth fracture is given by

$$\mu_g = c\overline{\gamma}^{n-1}. \tag{17}$$

The average shear rate can be expressed as

$$\overline{\gamma} = \frac{1}{b} \int_{-b/2}^{b/2} \left(\frac{y}{c} \frac{dp}{dx} \right)^{1/n} dy. \tag{18}$$

Simultaneously, from (17) and (18), it can be obtained that

$$\mu_g = c \left[\left(\frac{n}{1+n} \right) \left(\frac{b}{2c} \frac{dp}{dx} \right)^{1/n} \right]^{n-1}. \tag{19}$$

The expression of the inflow flow q of power-law slurry in the fracture is

$$q = \frac{wb^3}{4\mu_g} \left(\frac{1}{1+n} \right)^{n-1} \frac{n^n}{2n+1}. \tag{20}$$

3. Analysis of the Water-Displacing Mechanism in Fracture Networks

3.1. The Model of Slurry (Water) Diffusion Seepage Resistance in a Single Fracture. In the process of constant pressure grouting in the fracture network, with the increase in the diffusion range of slurry, the flow of slurry inflow in the fracture network will continuously decrease, which is similar to the principle that the current value will continuously decrease when the total resistance of the constant-voltage circuit system increases with time. Based on this, the concept of resistance in the circuit was introduced into the water-displacing diffusion of slurry in the fracture network and the expressions of the resistance of different flow patterns of slurry and water in the diffusion process in a single fracture were analyzed, and then, the expressions of the total resistance of the fracture system at different grouting moments were obtained.

The flow of different patterns of slurry and water in series and parallel fracture structures under constant pressure is taken as the research model, and its schematic diagram is shown in Figure 2. L_1 and L_2 are the horizontal projection length of two series fractures; Δp_1 and Δp are the pressure difference at their inlet and outlet, respectively; and b_1 and b_2 are their equivalent hydraulic gap widths.

Taking the water-displacing diffusion process of Bingham slurry in the series structural fractures (as shown in Figure 2(a)) as the research object, when the water in the fracture system is completely displaced by Bingham slurry, the flow rate of Bingham slurry in the fractures of b_1 and b_2 at this moment can be expressed as follows:

$$q_1 = \frac{b_1^3 \Delta p_1 \cos \alpha_1 w_1}{12\mu_g L_1} \left[1 - \frac{3\tau_0}{b_1 (\Delta p_1 \cos \alpha_1 / L_1)} \right], \tag{21}$$

$$q_2 = \frac{b_2^3 \Delta p_2 \cos \alpha_2 w_2}{12\mu_g L_2} \left[1 - \frac{3\tau_0}{b_2 (\Delta p_2 \cos \alpha_2 / L_2)} \right]. \tag{22}$$

According to the expression of the total differential pressure Δp in the fracture network and the conservation of slurry flow at the serial fracture joints, it can be seen that

$$\begin{cases} \Delta p = \Delta p_1 + \Delta p_2, \\ q_1 = q_2. \end{cases} \tag{23}$$

From (21), (22), and (23), the following formula can be obtained:

$$\Delta p = \frac{12\mu_g L_1}{b_1^3 \cos \alpha_1 w_1 [1 - 3\tau_0/b_1 (\Delta p_1 \cos \alpha_1/L_1)]} q_1 + \frac{12\mu_g L_2}{b_2^3 \cos \alpha_2 w_2 [1 - 3\tau_0/b_2 (\Delta p_2 \cos \alpha_2/L_2)]} q_2. \tag{24}$$

Similarly, when the slurry-water interface is at the entrance of the fractures in series structure, the water flow rate in the fractures of b_1 and b_2 can be expressed as follows:

$$q_1 = \frac{b_1^3 w_1 \Delta p_1 \cos \alpha_1}{12\mu_w L_1}, \tag{25}$$

$$q_2 = \frac{b_2^3 w_2 \Delta p_2 \cos \alpha_2}{12\mu_w L_2}. \tag{26}$$

Simultaneously, from (25), (26), and (27), it can be obtained that

$$\Delta p = \frac{12\mu_w L_1}{b_1^3 w_1 \cos \alpha_1} q_1 + \frac{12\mu_w L_2}{b_2^3 w_2 \cos \alpha_2} q_2. \tag{27}$$

When the water in the parallel fracture (as shown in Figure 2(b)) is completely displaced by Bingham slurry, the relationship between the total slurry inflow q of the parallel fracture system and the flow rates q_1 and q_2 of the two branches of fractures can be obtained as follows:

$$q = q_1 + q_2. \tag{28}$$

Simultaneously, from (21), (22), and (30), it can be obtained that

$$q = \frac{\Delta p}{12\mu_g L_1/b_1^3 \cos \alpha_1 w_1 [1 - 3\tau_0/b_1 (\Delta p_1 \cos \alpha_1/L_1)]} + \frac{\Delta p}{12\mu_g L_2/b_2^3 \cos \alpha_2 w_2 [1 - 3\tau_0/b_2 (\Delta p_2 \cos \alpha_2/L_2)]}. \tag{29}$$

Similarly, at the initial moment of grouting, the total water flow rate in the parallel fracture system can be expressed as follows:

$$q = \frac{\Delta p}{12\mu_w L_1/b_1^3 w_1 \cos \alpha_1} + \frac{\Delta p}{12\mu_w L_2/b_2^3 w_2 \cos \alpha_2}. \tag{30}$$

By comparing equations (24), (29), (27), and (30), it can be found that the pressure difference Δp between the inlet and outlet of the fractured structure of different flow patterns is similar to the pressure difference in the circuit

(a)

(b)
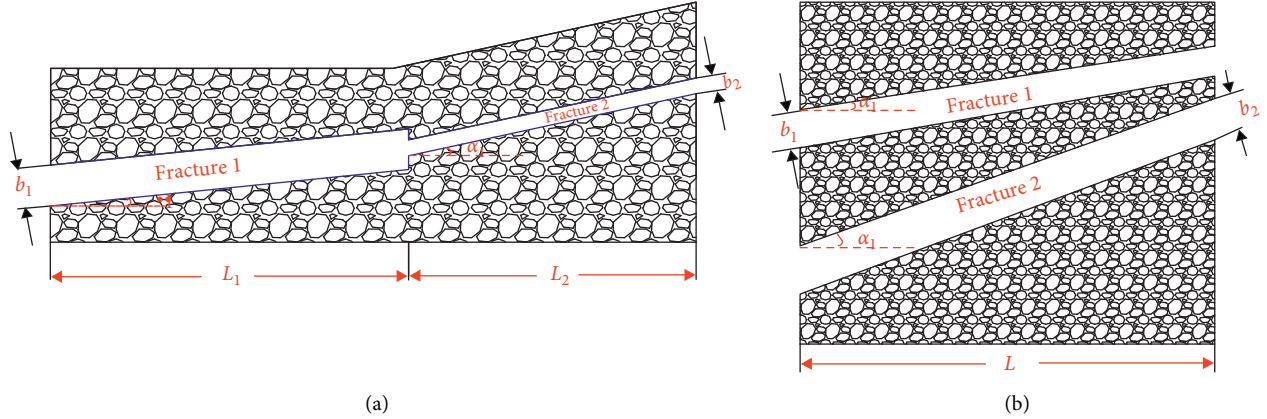
FIGURE 2: Schematic diagram of the fracture in tandem structure. (a) Series fracture structure. (b) Parallel fracture structure.

system and the flow rate q is similar to the current. Based on this, the corresponding resistance expression can be obtained, which is called seepage resistance. For the corresponding seepage resistance of Bingham slurry, power-law slurry, Newtonian slurry, and water diffusion in a single fracture, we call them, respectively, as Bingham slurry seepage resistance, power-law slurry seepage resistance, Newtonian slurry seepage resistance, and aqueous phase seepage resistance and they are, respectively, represented by R_{Bg}, R_{Mg}, R_{Ng}, and R_w. The expression of seepage resistance of different flow patterns of fluids can be obtained from the formula deduced, as shown in Table 1.

3.2. Total Seepage Resistance Model of Water-Displacing Diffusion of Slurry. When the slurry displaces water and diffuses in the fracture network system, the seepage resistance in the whole system will constantly change with the continuous increase in the diffusion range of slurry. Under the constant pressure difference (voltage) of the system, the flow rate (current) of the slurry will constantly change. Therefore, for the fracture network with the series and parallel form, the series and parallel relation of slurry seepage resistance and water phase seepage resistance can be used to represent the total seepage resistance of the system during the process of water-displacing diffusion of slurry, and then, the change of slurry flow (slurry pressure) of the corresponding system at different slurry diffusion positions under the condition of constant pressure (constant flow rate) grouting is obtained, so as to provide certain theoretical reference for the selection of grouting parameters. Earlier, we proposed the concept of total seepage resistance model of water-displacing diffusion of slurry in the fracture network structure. Next, the total seepage resistance method of the system will be used to analyze the variation rule of the inflow flow of the system in the process of water-displacing diffusion of slurry in the herringbone fracture with series and parallel structure under the condition of constant pressure grouting. The selected herringbone fracture structure schematic diagram is shown in Figure 3, and the corresponding parameters are shown in Table 2.

In Table 2, b_1, b_2, and b_3 are equivalent hydraulic gap width values of fracture 1, fracture 2, and fracture 3, respectively, and p_1 and p_2 are slurry pressure and hydrostatic pressure, respectively. The changes of total seepage resistance and corresponding slurry flow in the system under the condition of constant pressure grouting and water-displacing diffusion of slurry in the model in Figure 3 were analyzed based on Bingham slurry with different yield stress values τ_0 and power-law slurry with different rheological index values n as the research objects.

The viscosity of Bingham slurry is $\mu_g = 0.01$ Pa·s, and yield stress τ_0 is 1 Pa, 2 Pa, and 3 Pa, respectively; then, the slurry enters the herringbone fracture system from the injection end, the total seepage resistance of the system changes constantly, and the slurry flow rate changes constantly under the condition that the pressure difference of the system is constant. When the water-displacing diffusion of slurry occurs along the horizontal direction of distance $L_x < 10$ m, the expression of the total seepage resistance R of the system is as shown in

$$R = R_{g1} + R_{w1} + \frac{R_{w2}R_{w3}}{R_{w2} + R_{w3}}, \tag{31}$$

where R_{g1} is the corresponding slurry seepage resistance when the water-displacing diffusion distance of slurry is L_x and R_{w1} is the seepage resistance of the water phase in the horizontal main fracture. R_{w2} and R_{w3} are the corresponding aqueous phase seepage resistance of the secondary fractures, respectively, and the expressions of the seepage resistance of the slurry and the aqueous phase are shown in Figure 1.

According to the pressure continuity conditions at the slurry-water interface and the conservation conditions of system flow, it can be observed that

$$\frac{\Delta p_1}{R_{g1}} = \frac{\Delta p}{R}, \tag{32}$$

where $\triangle p$ represents the total pressure difference of the fracture system and $\triangle p_1$ represents the difference between the slurry-water interface pressure and grouting pressure at the slurry diffusion position.

TABLE 1: Expressions of seepage resistance for fluids with different flow patterns.

Bingham slurry seepage resistance R_{Bg} (N·s·m^{-5})	Power-law slurry seepage resistance R_{Mg} (N·s·m^{-5})	Newtonian slurry seepage resistance R_{Ng} (N·s·m^{-5})	Aqueous phase seepage resistance R_w (N·s·m^{-5})
$12\mu_g L_x / b^3 w \cos\alpha [1 - 3\tau_0 / b(\Delta p \cos\alpha / L_x)]$	$4\mu_g L_x / b^3 w \cos\alpha (1/1+n)^{n-1} n^n / 2n + 1$	$12\mu_g L_x / b^3 w \cos\alpha$	$12\mu_w L_x / b^3 w \cos\alpha$
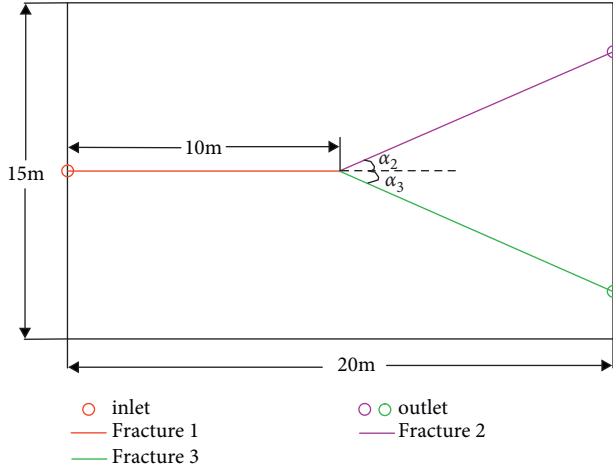
FIGURE 3: The herringbone fracture structure schematic diagram.

TABLE 2: Parameters of water-displacing grouting in the herringbone fracture.

L_1 (m)	b_1 (mm)	b_2 (mm)	b_3 (mm)	α_2 (°)	α_3 (°)	p_1 (MPa)	p_2 (MPa)
10	0.8	1.0	1.0	30	30	0.25	0.1

Simultaneously, equations (31) and (32), combined with the expressions of the seepage resistance of Bingham slurry and water phase in Table 1, can be used to obtain the values of the total seepage resistance R and the inflow flow q of the corresponding system at this position. Similarly, by the same serial-parallel relation, the value of the total seepage resistance R and the inflow flow q of the system can be obtained when the water-displacing diffusion distance of the slurry is along the horizontal direction $L_x > 10$ m.

As shown in Figure 4, with the increase in water-displacing diffusion distance of slurry in the herringbone fracture, the total system seepage resistance increases; when the water-displacing diffusion distance of slurry is small, different seepage resistance yield stress values corresponding to the system total resistance were similar. With the increase in water-displacing diffusion distance of slurry, the total seepage resistance of the slurry system with a higher yield stress value and difference value increases. As shown in Figure 4, when the horizontal diffusion distance of slurry is 13 m, the total seepage resistance R (as shown in point A in Figure 4) of the Bingham slurry system whose yield stress $\tau_0 = 3$ Pa is approximately 6×10^{10} N·s·m^{-5} and the corresponding slope was a straight line as the growth rate at this point approached infinity.

As shown in Figure 5, when the horizontal diffusion distance of slurry is 13 m, the flow (as shown in point A in Figure 5) of the Bingham slurry system whose yield stress

$\tau_0 = 3$ Pa is close to 0 m^3/s, the flow of slurry with different yield stress values decreases with the increase in water-displacing diffusion distance, and the reduction rate decreases continuously. When the diffusion distance of slurry is the same, the flow of the slurry with higher yield stress is smaller and the difference increases with the increase in the diffusion distance.

The above analysis shows that, in the case of constant pressure grouting, the total seepage resistance of the system increases with the increase in the slurry diffusion distance, and when the slurry diffusion distance is the same, the larger the yield stress is, the greater the total seepage resistance of the slurry corresponding system is, the smaller the slurry flow rate is, and the more difficult the water-displacing diffusion of slurry is.

4. Verification of the Total Seepage Resistance Model of Water-Displacing Diffusion of Slurry

In order to verify the correctness of the theoretical model of total seepage resistance of the system, the numerical simulation method was used to analyze the variation rules of the slurry-water interface pressure and the flow of slurry inflow at different diffusion positions during the water-displacing diffusion process of the Bingham slurry in the series and parallel fracture structure under the condition of constant pressure grouting, so as to verify the theoretical results mutually.

The Lagrange interface tracking method was used to track the moving distance of the abrupt interface. The process of water-displacing diffusion of slurry was regarded as piston displacement. Putting the calculation area for Ω, slurry area for Ω_g, and water area for Ω_w, the two-phase function $S(x, t)$ expression is

$$\begin{cases} S(x,t) = 1, & x \in \Omega^g, \\ S(x,t) = 0, & x \in \Omega^w. \end{cases} \tag{33}$$

For one-dimensional flows, the Lagrange interface tracking control equation is

$$\frac{\partial S(x,t)}{\partial t} + u(s) \cdot \nabla S(x,t) = 0, \tag{34}$$

where $u(s)$ is the velocity of slurry or water.

According to Darcy's Law, the expression is obtained as follows:

$$u(s) = \frac{-K(s)}{\mu(s)} \frac{\partial p}{\partial x}, \tag{35}$$
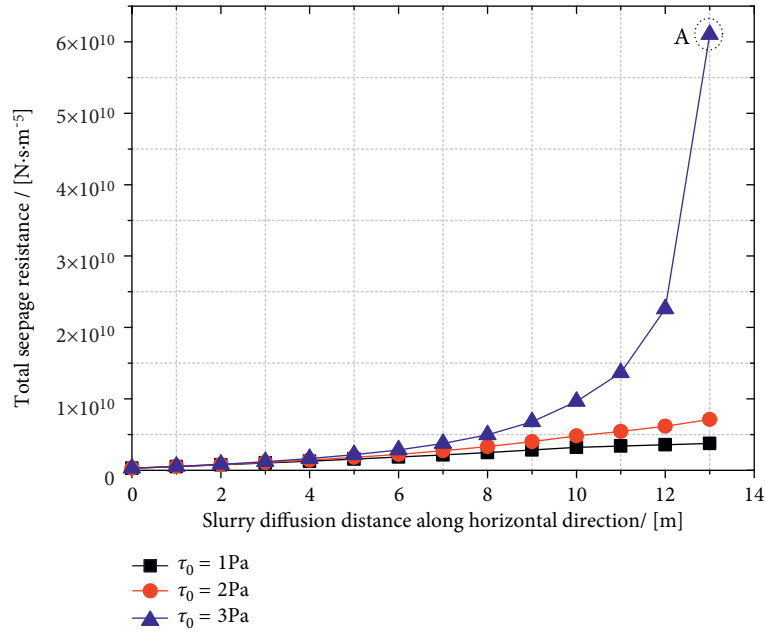
FIGURE 4: Relationship between the total seepage resistance of the system and the water-displacing diffusion distance of slurry (different yield stress values).
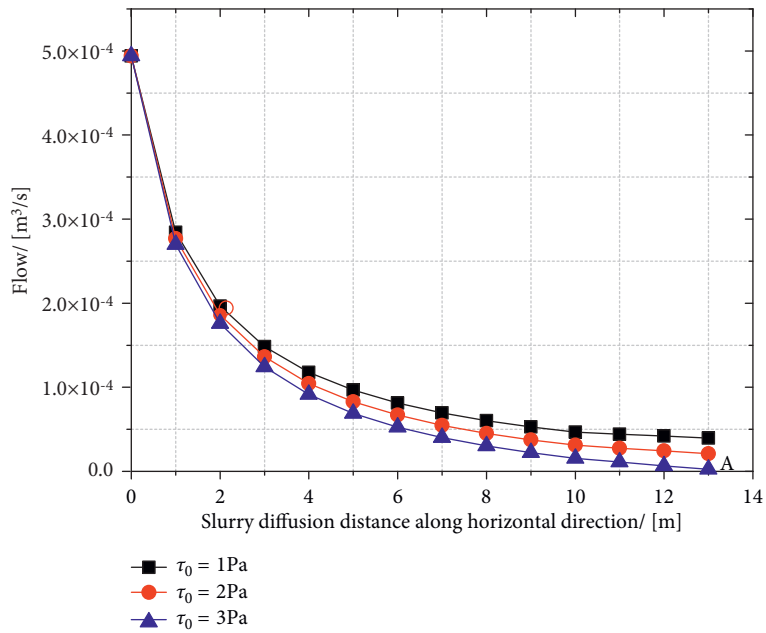
FIGURE 5: Relationship between system flow rate and slurry displacement diffusion distance (different yield stress values).

where $\mu(s)$ is the viscosity value of aqueous phase or slurry phase and $K(s)$ is the phase permeability.

The continuity equation of passive single-phase fluid flow in a single fracture is as follows:

$$\frac{\partial \rho}{\partial t} + \nabla \cdot (\rho u) = 0. \tag{36}$$

For incompressible fluid, (36) can be rewritten as

$$\nabla \cdot (u) = 0. \tag{37}$$

Therefore, the continuity equation of incompressible two-phase fluid flow in a single fracture can be written as follows:

$$\frac{\partial}{\partial x} \frac{K(s)}{\mu(s)} \frac{\partial p}{\partial x} = 0. \tag{38}$$

For the water-displacing diffusion of slurry in the fracture network structure, the overall mass conservation equation of the system can be expressed as

$$\int \frac{\partial}{\partial x} \frac{K(s)}{\mu(s)} \frac{\partial p}{\partial x} \, dx = 0. \tag{39}$$

Equations (5)–(1) can be rewritten as

$$\sum \frac{K(s)}{\mu(s)} \frac{\partial p}{\partial x} = 0. \tag{40}$$

In the process of water-displacing diffusion of Bingham slurry, the corresponding phase permeability $K(s)$ is expressed as

$$K_s = \begin{cases} \dfrac{b^2}{12} \left[1 + \dfrac{3\tau_0}{b\left(dp_g/dx\right)} \right], & s = 1, \\[3mm] \dfrac{b^2}{12}, & s = 0, \end{cases} \tag{41}$$

where τ_0 is the yield stress and b is the equivalent hydraulic gap width of the fracture.

In the process of water-displacing diffusion of power-law slurry, the corresponding phase permeability $K(s)$ can be expressed as

$$K_s = \begin{cases} \dfrac{b^2}{4} \left(\dfrac{1}{1+n} \right)^{n-1} \dfrac{n^n}{2n+1}, & s = 1, \\[3mm] \dfrac{b^2}{12}, & s = 0, \end{cases} \tag{42}$$

where n is the rheological index and b is the equivalent hydraulic gap width of the fracture.

From the previous paragraphs, equations (33), (34), (35), (40), and (41) are the numerical control equations of water-displacing diffusion of Bingham slurry in fracture network. Equations (33), (34), (35), (40), and (41) are the numerical control equations of water-displacing diffusion of power-law slurry in fracture network. By using COMSOL Multiphysics numerical software of low-dimensional PDE module, the control equations are defined directly on all of the fracture networks, and at the same time, in order to prevent the mutation of the phase function s between 0 and 1 from the reduction in the convergence of the partial differential equation, the phase function s was defined in the form of step function (step(s)), so that it could smoothly transition between 0 and 1. The parameter position of the step function was 2.5×10^{-5}, the size of the transition zone was 5×10^{-5}, and the order of continuous derivative was 2.

The Lagrange interface tracking method is adopted to track the interface. The expression corresponding to the change in the position of the slurry-water interface with time can be expressed as [24]

$$\xi(x)_{n+1} = \xi(x)_n + u_n \Delta t, \tag{43}$$

where $\xi(x)_n$ is the position of the slurry-water interface of the time step; $\xi(x)_{n+1}$ is the slurry-water interface location of the next step; u_n is the interface velocity of slurry and water corresponding to the time step; and Δt is the calculation time step.

To maintain the stability of the calculation, the calculated time step Δt should also satisfy the following relation [25]:

$$\Delta t = \min\left(\frac{\Delta x}{u}, \frac{\Delta l}{u} \right), \tag{44}$$

where Δx is the shortest fracture length and Δl is the shortest distance between adjacent nodes in the fracture network structure. We use COMSOL Multiphysics numerical software to define the above governing equations and compare the numerical results with the theoretical results in order to verify the correctness of the theoretical model. In the calculation, the form function is Lagrange type and the order of corresponding element is 2. The initial value and boundary conditions of the numerical solution are as follows: at the initial moment, the fracture network is saturated with water, that is, when $t = 0$, $s = 0$, and each inlet of the linear source is Dirichlet pressure boundary conditions. In other words, for the whole model, when $x = 0$, $s = 1$ and $P = P_1$. The outlet of the model is the boundary of flux source and Dirichlet pressure, that is, when $x = L$, $P = P_w$ and $\partial S/\partial x = 0$. The numerical model and grid division of water-displacing diffusion of slurry in fractures are shown in Figure 6. The length and width of the model are 20 m and 15 m, respectively. Assuming that Bingham slurry viscosity value $\mu_g = 0.01$ Pa·s, yield stress value of slurry $\tau_0 = 1$ Pa, and the rest of the parameters are as shown in Table 2, the diffusion range of water-displacing diffusion of slurry with the change in the relationship with grouting time is as shown in Figure 7.

As shown in Figure 7, with the increase in grouting time, the diffusion range of water-displacing diffusion of slurry increases continuously, but the growth rate of diffusion range of slurry decreases continuously within the same time interval. The above results show that, in the process of constant pressure grouting, with the increase in grouting time, the advance velocity of slurry-water interface decreases continuously, that is, the inflow flow decreases continuously and the difficulty of water-displacing diffusion of slurry increases continuously. If the above phenomenon is explained by the concept of total seepage resistance of the system, it can be understood that the total seepage resistance of the system keeps increasing with the continuous increase in the diffusion range of water-displacing mechanism. Therefore, under the condition of constant pressure grouting, the value of slurry flow will keep decreasing.

A monitoring line was arranged along the horizontal direction of the model to monitor the position of the slurry-water interface at different times, as well as the numerical values of the slurry-water interface pressure and slurry flow at different times, and the numerical solution was compared with the theoretical solution. The results are shown in Figure 8.

As shown in Figure 8, with the increase in the diffusion range of slurry, the interface pressure of slurry and the value of system slurry flow continuously decrease. It can be seen from the comparison between the theoretical solution and the numerical solution in Figure 8(a) that the difference between theoretical solution and the numerical solution of
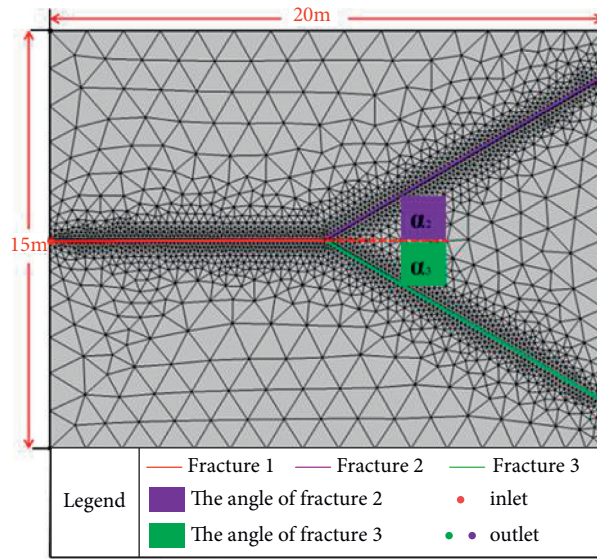
FIGURE 6: The numerical model and grid division of water-displacing diffusion of slurry in fractures.
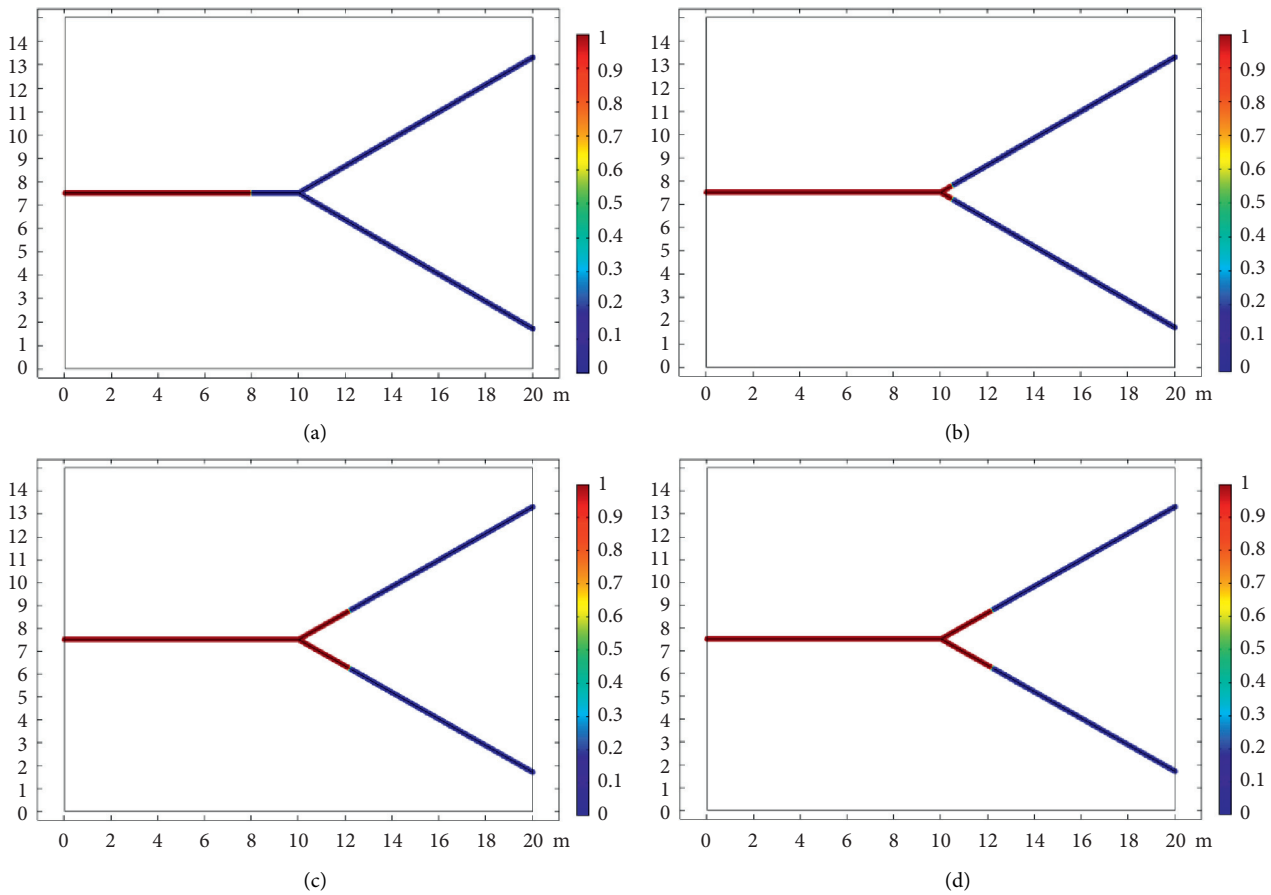
FIGURE 7: Relationship between diffusion range of water-displacing diffusion of slurry and grouting time. (a) $t = 50$ s. (b) $t = 100$ s. (c) $t = 150$ s. (d) $t = 200$ s.

the slurry-water interface pressure obtained at different diffusion distances is small and so is the difference between the theoretical solution and the numerical solution corresponding to the pressure drop of slurry. Therefore, under the same other conditions, the obtained difference of the slurry flow of the system is also small. Through the above
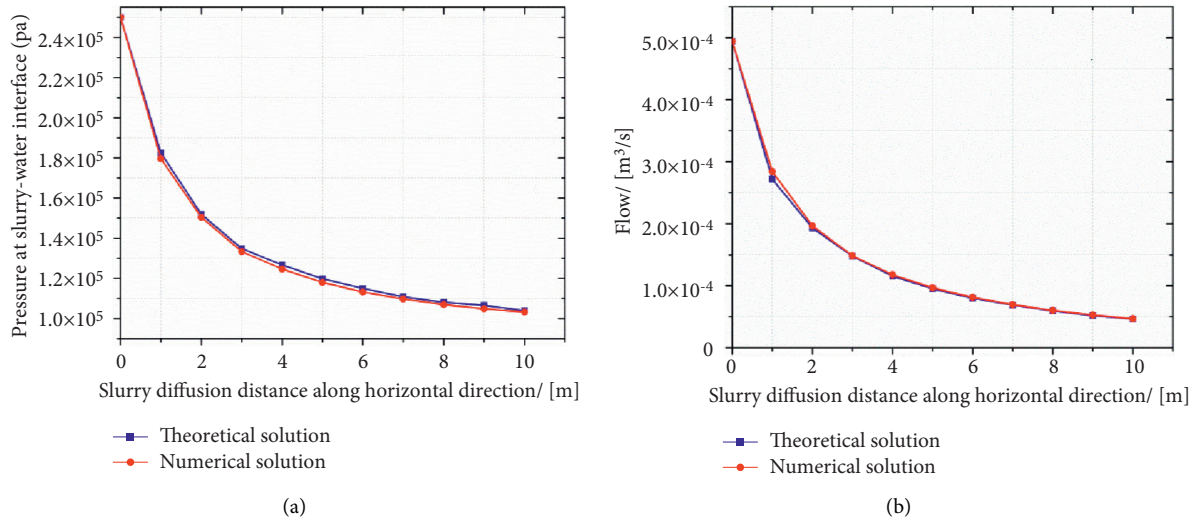
Figure 8: Comparison of numerical results and theoretical results. (a) Pressure of the slurry-water interface. (b) The value of system slurry flow.

analysis, it can be seen that the pressure of slurry-water interface and the inlet flow value of the system obtained by using the theoretical model of total seepage resistance of the system are basically the same as using the numerical solution; that is, the numerical results and the theoretical results are mutually verified.

5. Conclusions

(1) On the basis of reasonable assumptions, the theoretical model of water-displacing diffusion of slurry of different flow patterns in a single crack under constant pressure was established; on this basis, the concept of seepage resistance of each flow pattern of the slurry when diffusion occurs in a single fracture is put forward and the expression of corresponding seepage resistance is derived.

(2) Based on the concept of seepage resistance of each flow pattern of slurry diffusion in a single fracture and combined with the relationship between series and parallel fractures, the concept of the total seepage resistance model of the corresponding system of water-displacing diffusion of slurry in a fracture network structure with series and parallel combination is proposed, meanwhile, taking the herringbone fracture with a series and parallel structure as the research object for example analysis to analyze the change rules of total seepage resistance and slurry flow in the corresponding system with Bingham slurry with different yield stress values at different diffusion locations. The results show the following: for Bingham slurry with different yield stress values τ_0 of 1 Pa, 2 Pa, and 3 Pa, respectively, when the slurry diffusion distance along the horizontal direction is 13 m, the total seepage resistance R of the corresponding system increases from 3.04×10^8 N·s·m^{-5} at the initial time of grouting to 3.78×10^9 N·s·m^{-5}, 7.12×10^9 N·s·m^{-5}, and

6.1×10^{10} N·s·m^{-5}, respectively, and the slurry flow q decreases from 4.93×10^{-4} m^3/s at the initial time of grouting to 3.97×10^{-5} m^3/s, 2.11×10^{-5} m^3/s, and 2.47×10^{-6} m^3/s, respectively.

(3) The numerical control equations of water-displacing diffusion of different flow patterns of slurry in the fracture network were established, and the numerical analysis of water-displacing diffusion process of Bingham slurry in herringbone fracture structure is carried out. On the basis of mutual verification between theoretical and numerical conclusions, the correctness of the total seepage resistance model of water-displacing diffusion of slurry in the fracture network is verified. Based on the analysis of the diffusion law of different flow patterns in series and parallel fractures, the concept and expression of seepage resistance in the process of slurry flooding and diffusion in fractures are derived, which can be observed as the theory of slurry flooding and diffusion in complex fracture networks. The analysis provides a certain reference, and the related research results can provide theoretical support for the selection of grouting parameters during grouting in fractured aquifers.

Data Availability

The data used to support the findings of this study are available from the first author upon request.

Conflicts of Interest

The authors declare that they have no conflicts of interest.

Acknowledgments

References

[1] Y. Hu, W. Liu, T. Ma, R. Yang, and D. Liang, "Analysis on the stability of the inclined water-resisting roof layer while mining under the confined aquifer," *Geotechnical and Geological Engineering*, vol. 37, no. 2, pp. 995–1006, 2019.

[2] Z. Liu, *Rock Mass Fluid-Stress Coupling Process and Coal Seam Floor Water Inrush Mechanism Study*, China Coal Research Institute, Beijing, China, 2014.

[3] A. Li, *Water Inrush Mechanism on Seepage and Stress Coupling Damage of Coal Floor under Water Pressure and its Engineering Application*, Xian University of Science and Technology, Xian, China, 2012.

[4] X. Shi, S. Zhu, and W. Zhang, "Study on the mechanisms and prevention of water inrush events in a deeply buried high-pressure coal seam—a case study of the Chensilou coal mine in China," *Arabian Journal of Geosciences*, vol. 12, pp. 1–12, 2019.

[5] H. Li, H. Bai, J. Wu et al., "Mechanism of water inrush driven by grouting and control measures—a case study of Chensilou mine, China," *Arabian Journal of Geosciences*, vol. 10, pp. 1–10, 2017.

[6] S. N. Dong, "Some key scientific problems on water hazards frequently happened in China's coal mines," *Journal of China Coal Society*, vol. 35, pp. 66–71, 2010.

[7] S. N. W. H. Dong and W. Z. Zhang, "Udgement criteria with utilization and grouting reconstruction of top Ordovician limestone and floor damage depth in North China coal field," *Journal of China Coal Society*, vol. 44, pp. 2216–2226, 2019.

[8] S. Li, D. Pan, Z. Xu, P. Lin, and Y. Zhang, "Numerical simulation of dynamic water grouting using quick-setting slurry in rock fracture: the Sequential Diffusion and Solidification (SDS) method," *Computers and Geotechnics*, vol. 122, Article ID 103497, 2020.

[9] F. Xiao, J. Shang, and Z. Zhao, "DDA based grouting prediction and linkage between fracture aperture distribution and grouting characteristics," *Computers and Geotechnics*, vol. 112, pp. 350–369, 2019.

[10] W. Mu, L. Li, T. Yang, G. Yu, and Y. Han, "Numerical investigation on a grouting mechanism with slurry-rock coupling and shear displacement in a single rough fracture," *Bulletin of Engineering Geology and the Environment*, vol. 78, no. 8, pp. 6159–6177, 2019.

[11] L. Zou, U. Håkansson, and V. Cvetkovic, "Yield-power-law fluid propagation in water-saturated fracture networks with application to rock grouting," *Tunnelling and Underground Space Technology*, vol. 95, Article ID 103170, 2020.

[12] W. Zhang, S. Li, J. Wei et al., "Grouting rock fractures with cement and sodium silicate grout," *Carbonates and Evaporites*, vol. 33, no. 2, pp. 211–222, 2018.

[13] T.-L. Chen, L.-Y. Zhang, and D.-L. Zhang, "An FEM/VOF hybrid formulation for fracture grouting modelling," *Computers and Geotechnics*, vol. 58, pp. 14–27, 2014.

[14] P. Li, Q. S. Zhang, S. C. Li, and X. Zhang, "Time-dependent empirical model for fracture propagation in soil grouting," *Tunnelling and Underground Space Technology*, vol. 94, Article ID 103130, 2019.

[15] T. Ma, K. Zhang, W. Shen, C. Guo, and H. Xu, "Discontinuous and continuous Galerkin methods for compressible single-phase and two-phase flow in fractured porous media," *Advances in Water Resources*, vol. 156, Article ID 104039, 2021.

[16] W. Shen, X. Li, T. Ma, J. Cai, X. Lu, and S. Zhou, "High-pressure methane adsorption behavior on deep shales: experiments and modeling," *Physics of Fluids*, vol. 33, no. 6, Article ID 063103, 2021.

[17] R. Wang, Y. F. Dafalias, P. Fu, and J.-M. Zhang, "Fabric evolution and dilatancy within anisotropic critical state theory guided and validated by DEM." *International Journal of Solids and Structures*, vol. 188-189, pp. 210–222, 2020.

[18] M. El Tani and H. Stille, "Grout spread and injection period of silica solution and cement mix in rock fractures," *Rock Mechanics and Rock Engineering*, vol. 50, no. 9, pp. 2365–2380, 2017.

[19] S. Mohajerani, A. Baghbanan, R. Bagherpour, and H. Hashemolhosseini, "Grout penetration in fractured rock mass using a new developed explicit algorithm," *International Journal of Rock Mechanics and Mining Sciences*, vol. 80, pp. 412–417, 2015.

[20] Q. Liu and L. Sun, "Simulation of coupled hydro-mechanical interactions during grouting process in fractured media based on the combined finite-discrete element method," *Tunnelling and Underground Space Technology*, vol. 84, pp. 472–486, 2019.

[21] L. Jin, W. Sui, and J. Xiong, "Experimental investigation on chemical grouting in a permeated fracture replica with different roughness," *Applied Sciences*, vol. 9, no. 13, p. 2762, 2019.

[22] M. Hao, F. Wang, X. Li, B. Zhang, and Y. Zhong, "Numerical and experimental studies of diffusion law of grouting with expansible polymer," *Journal of Materials in Civil Engineering*, vol. 30, Article ID 04017290, 2018.

[23] W. Ruan, "Research on diffusion of grouting and basic properties of grouts," *Chinese Journal of Geotechnical Engineering*, vol. 27, pp. 69–73, 2005.

[24] G. W. Ma, H. D. Wang, L. F. Fan, and B. Wang, "Simulation of two-phase flow in horizontal fracture networks with numerical manifold method," *Advances in Water Resources*, vol. 108, pp. 293–309, 2017.

[25] L. Zou, U. Håkansson, and V. Cvetkovic, "Cement grout propagation in two-dimensional fracture networks: impact of structure and hydraulic variability," *International Journal of Rock Mechanics and Mining Sciences*, vol. 115, pp. 1–10, 2019.

WILEY | Hindawi

Research Article

Research on the Technology of Small Coal Pillars of Gob-Side Entry Retained in Deep Mines Based on the Roof Cutting for Pressure Unloading in the Lower Key Stratum

Yongjie Yang [iD][1] **and Yang Zhang** [iD][2]

[1]*Shandong University of Science and Technology, Qingdao 266590, China*
[2]*China University of Mining and Technology-Beijing, Beijing 100083, China*

Correspondence should be addressed to Yang Zhang; zhangyang57653@163.com

With the mining depth getting deeper and deeper, surrounding rock control technology has become a difficult issue in the development of modern mining, especially the mining roadways affected by mining. It is very difficult to control the surrounding rock due to the intense mining of the last working faces. In order to alleviate the impact of dynamic pressure on the gob-side entry retained, solve the ventilation difficulties caused by the commonly used method of the gob-side entry retained without leaving coal pillars, and solve the disadvantages of the inability to effectively isolate water and harmful gases, this paper proposes a small coal pillar gob-side entry retained technology based on the key stratum, that is, cutting the key stratum above the top plate, transferring lateral support pressure from the workings further up the seam to the depths of the coal seam, and then protecting gob-side entry retained method. In the final method of precracking and cutting joints by blasting with D-type polytunnel, we directionally cut the lower key stratum above the roadway in the designed direction and position. The theoretical analysis, numerical simulation and field test, and the method of the blasting broken roof pressure release effect are analyzed. Compared to the unloaded pressure method, the relatively complete direct roof is conducive to the maintenance of the surrounding rock on the gob-side entry retained. At the same time, the pressure relief caused by the fracture of the lower key stratum of the coal roof significantly improves the stress environment. The stress is no longer concentrated on the small coal pillars and the gob-side entry retained, and the required roadway support strength is greatly reduced and no longer needs to carry out the construction of roadside support system. This technology reduces labor intensity and production costs.

1. Introduction

When shallow coal resources become increasingly depleted, mining depths are increasing year on year. The coal seam conditions are becoming increasingly complex, and problems such as rock burst are a serious threat to mining safety. At the same time, the problem of mining succession tension is also becoming increasingly prominent, restricting the safe and efficient production of the mine. We have to adopt the gob-side entry retained to solve these problems, such as difficulties in ventilating the back hole in deep seam and high gas mines and the tension in the mining succession [1, 2].

The gob-side entry retained technology has the advantage of increasing the recovery rate of coal resources and achieving Y-shaped ventilation [3]. However, the current technique of the gob-side entry retained without coal pillar. It cannot effectively solve technical problems such as ventilation difficulties, air leakage from mining areas, and support difficulties in deep thick coal seam high gas mines. In recent years, academician He et al. proposed the roof cutting and pressure releasing automatically form a no-pillar entry mining technology [4–7]. But cutting technology of the gob-side entry retained requires superstrong support roadway, which is difficult and costly to support. And it is difficult to block

the harmful gas in the alley side barrier system. In addition, with the increase of mining depth, the roof cutting and pressure releasing automatically formed entry mining technology is influenced by high pressure. According to the statistical results, roof cutting and pressure releasing automatically formed entry technology is less applied under the condition that the depth of the well exceeds 650 m, and the top-cutting effect is not good [8].

Now, many experts and scholars at home and abroad on deep high stress entry surrounding rock deformation mechanism and stability problem have carried out a number of studies. Chen et al. [9] deep cut along the empty entry support difficult problem, by building control roof, lateral pressure, dynamic pressure resistance, and protection of coal for coordinated control. Yang et al. [10] for composite roof gob-side entry retained for filling body of inward problems build the mechanics model and obtained the displacement expression, and shear bolts are presented in this paper, as well as additional entry control scheme of the isolated column. Wu et al. [11] aiming at the gob-side entry retained the easy occurrence of delamination failure and divided the deformation and failure forms of the roof of deep well gob-side entry retained into four types; "more supporting structure" is put forward at the same time, the reasonable control of the roof abscission layer. Through practical engineering practice, Zhang et al. [12] and others found that the deformation of deep gob-side entry retained entry was mainly concentrated during mining and retained entry in working face and proposed to adopt the whole process support of roof support and retained entry with anchor, net, and cable combined with single hydraulic prop and build the wall by pumping and filling paste material, which can realize retained entry under the mining depth of kilometers. Zheng et al. [13] put forward subsection gob-side entry retained technology for deep high gas mines, aiming to solve the same problem and realize coal and gas comining. Hua et al. [14] took the deep well gob-side entry retained of Guqiao Coal Mine in Huainan as the engineering background and studied the evolution mechanism of floor heave of deep well gob-side entry retained. It is found that the phenomenon of entry floor heave is obvious during the first mining to the second mining. Xingen et al. [15] analyzed the stress state of hydraulic support and the deformation mechanism of roof of retreat channel according to statics theory and energy theory. Then, according to the geological conditions of the working face, the cutting design of the roof of the retracement trough is determined, and the cutting effect is analyzed by numerical simulation.

The No. 201 working face in Gaojiapu Coal Mine is a typical deep mining face with large mining height, which adopts double entry layout. In order to alleviate the problem of tight replacement, the headentry (No. 201 working face) is reserved as the tailentry in the No. 202 working face. Under the influence of high ground pressure and mining, the effect of retained entry is poor, and the entry roof fall and side slope appear. Under this background, a method of deep mine small coal pillar gob-side entry retained based on broken roof pressure relief is proposed; that is, the lower part key stratum above the entry roof is cut off while the direct roof is relatively intact. In this paper, the working principle

and test effect of this technology are studied and analyzed by various means, and the stress distribution state and surrounding rock failure law of broken roof pressure relief gob-side entry retained are obtained, thus verifying the feasibility of the gob-side entry retained method of small coal pillars in deep wells based on broken roof pressure relief key stratum The research results can provide useful reference for entry stability control under similar conditions.

2. Based on the Principle of Small Coal Pillar Gob-Side Entry Retained in Deep Mine with Broken Roof and Pressure Relief in the Lower Part of Coal Seam Roof Key Stratum

Academician Song Zhenqi of Shandong University of Science and Technology put forward the theory of transfer rock beam, which regards each group of rock strata moving at the same time (or nearly moving at the same time) as a moving whole, called "transfer rock beam" or "transfer rock beam" for short; that is, when the working face is excavated, the supporting pressure in the stope roof is transferred in a relatively complete rock body, as shown in Figure 1. In this paper, the technical method of roof breaking and pressure relief is put forward; that is, presplitting drilling holes inclined to the solid coal side are drilled in the coal seam roof, explosives are installed in the drilling holes, and presplitting slits are formed in the lower part key stratum of the coal seam roof by explosive blasting, and the lower part key stratum is cut off so that it cannot transmit side abutment pressure caused by mining in the working face. In the process of mining in the working face, the gravity from the lower part key stratum of the coal seam roof to the surface rock layer is transferred from the thick and hard part key stratum above the lower part key stratum to the solid coal, as shown in Figure 2, so that the small coal pillars and gob-side entry retained are under lower supporting pressure, which is beneficial to the bearing stability of the small coal pillars and the maintenance of the gob-side entry retained.

3. Geological Conditions

3.1. Overview of No. 2 Panel. Gaojiapu Coalfield is located in the northwest of Binchang mining area in Shaanxi Province, China. The test working faces (No. 201 and No. 202) are in the second panel. The average thickness of coal seam is about 6.48 m, and the buried depth of working face is about 1000 m. The coal seam structure is relatively simple. The immediate roof is mainly composed of mudstone, with an average thickness of 3.66 m; the main roof is composed of fine sandstone, with an average thickness of 9.06 m. The rock conditions are shown in Table 1.

3.2. Overview of Gob-Side Retained in Working Face. Due to the large mining depth of Gaojiapu Coal Mine, the district entry arrangement is adopted in the way of double entry layout, but the entry protection with wide coal pillars easily induce rock burst. In order to solve the above technical problems, it is necessary to adopt the layout of gob-side
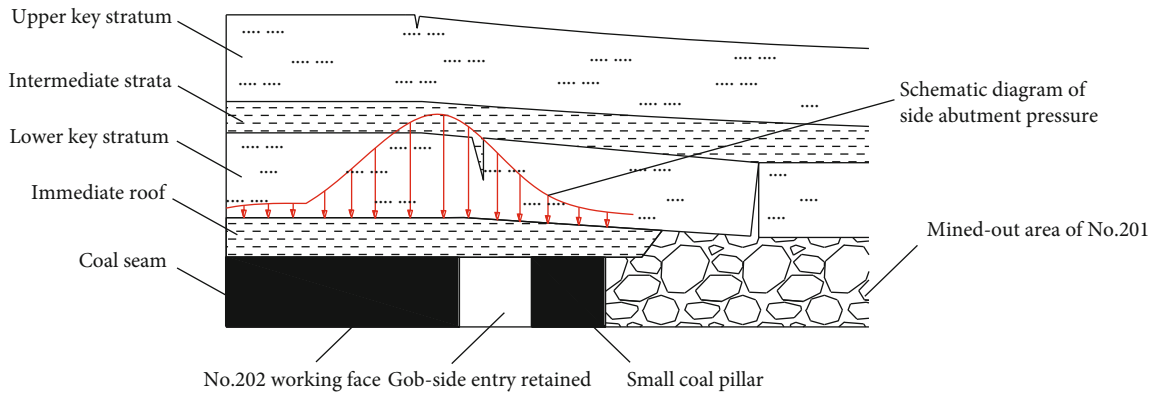
FIGURE 1: Distribution giagram of abutment pressure before roof cutting.
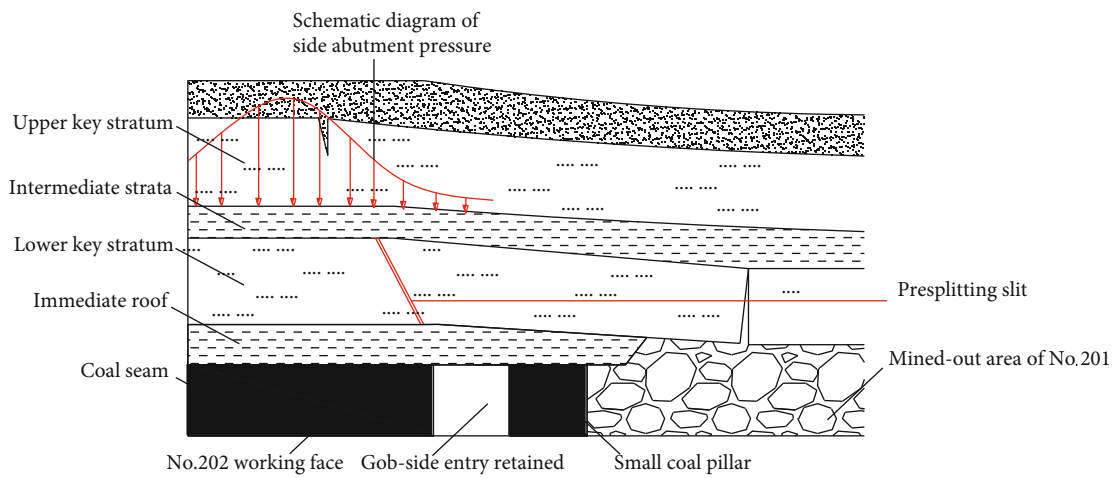
FIGURE 2: Distribution giagram of abutment pressure after roof cutting.

TABLE 1: Illustrative table of support sections of the gob-side entry retained.

Cross section	17.88 m^2	Anchor name	Rebar resin anchors	Quantity of anchor rods	16.9 (m)
Net cross section	16.69 m^2	Specification for roof anchors	MSGLW-500 22/2200 mm	Anchor ropes	SKP18 − 1/1860 mm × 7000 mm Spacing: 1900 mm
Shape	Trapezoidal	Gang anchor specifications	MSGLD-500 20/2200 mm	Anchor ropes pallets	250 mm × 250 mm × 20 mm
Slope	Design slope	Row spacing	950 mm	Roof metal mesh	LW50/4-SZ
Steel belts	T-shaped	Anchor rods pallets	150 mm × 150 mm × 10 mm	Anchoring agent	Roof: MSCKb2350, MSCK2370 Gangs: MSCKb2370 Top anchor cable: MSCKb2350, MSCK2370

entry. The headentry and the tailentry of No. 201 working face were excavated in solid coal. The tailentry excavation of No. 202 working face lags behind the small coal pillar during the mining of No. 201 working face. The construction layout diagram is shown in Figure 3.

3.3. Determination of the Support Method for the Test Section of Roadway. The original 201 working face headentry and tailentry were designed as trapezoidal roadways. The width of the trapezoidal roadways is 4.4 m at the top and 5.0 m at the bottom, with a clear height of 3.5 m and a net area of 16.45 m^2. Therefore, the test section of the gob-side entry retained (202 working face tailentry) in this manuscript took the same roadway shape and dimensions and used the same support parameters. The aim of this manuscript is to highlight the comparison of channel deformation variables before and after top cutting, so the same support parameters are used both before and after the roof cutting. The test
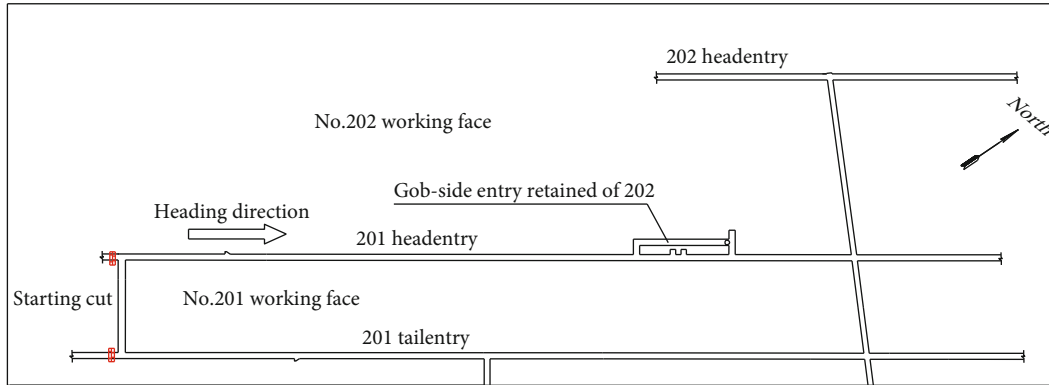
FIGURE 3: Schematic diagram of 202 gob-side entry retained test section.
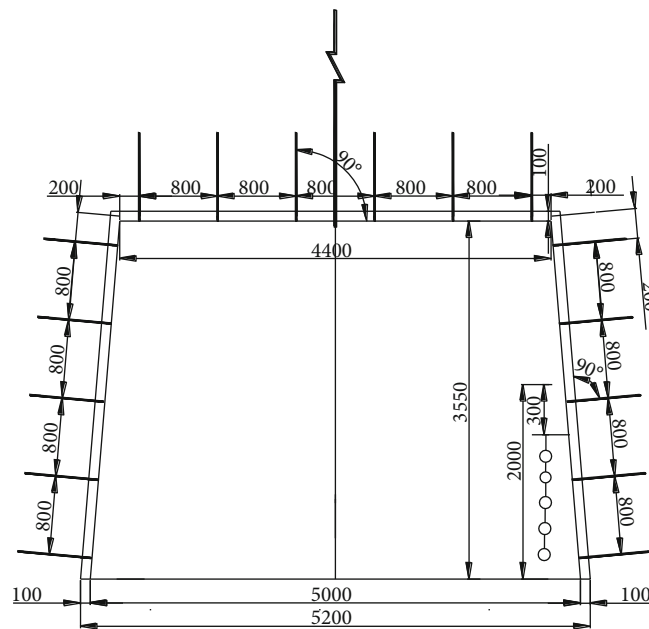
FIGURE 4: Roadway cross sections of the gob-side entry retained.

control variable is only whether or not the roof is broken, which is used to determine the effectiveness of the pressure relief from the broken roof. The roadway cross section is shown in Figure 4, and the support parameters are shown in Table 1.

3.4. Coal Seam Roof Conditions. It is very important for the technology to analyze the roof conditions of coal seam and determine the key stratum closest to the coal seam in the roof, namely, the lower key stratum. The lower key stratum is the rock layer with large thickness and hard rock that is closest to the immediate roof above the immediate roof and can transmit the stress of the overlying strata. According to Table 2, the immediate roof of No. 4 coal seam is mudstone (3.66 m), and the main roof is fine sandstone (9.9 m). There are two layers of thick mudstone and coarse sandstone above the main roof, and the position of the key stratum is not obvious. Therefore, according to the geological data of Gaojiapu Coal Mine, the FLAC^{3D} numerical calculation

model is established. The numerical calculation model takes 345 m in the x direction (dip), 300 m in the y direction (strike), and 72 m in the z direction. The simulation direction of the coal seam is horizontal, and the buried depth is 800 m. The horizontal displacement constraint is applied to the four boundaries, and the vertical displacement of the bottom is limited. The equivalent uniform load of the average 800 m buried depth is applied to the top boundary of the model by 20 MPa. The Mohr-Coulomb constitutive model is used for the contact model. The numerical model is shown in Figure 5, and the physical and mechanical parameters of each rock layer are shown in Table 2.

The calculation process of the numerical model is as follows: model establishment ⟶ parameter assignment and initial balance calculation ⟶ No. 201 working face headentry excavation and gob-side entry retained test simulation ⟶ calculation result output and analysis. After the above procedures, the distribution law and range of side

TABLE 2: Rock mechanics parameters.

No.	Lithology	Bulk modulus GPa	Shear modulus GPa	Cohesion MPa	Internal friction angle °	Tension strength MPa	Density kg·m^{-3}	Height m
1	Mudstone	0.3	0.35	0.8	30	0.1	2400	14
2	Aluminous argillite	0.8	1.62	3.8	35	0.4	2450	2
3	4# coal seam	0.3	0.39	3.64	31	0.9	1390	8
4	Mudstone	0.3	0.35	0.8	30	0.1	2400	4
5	Fine sandstone	4.84	3.26	7.8	32	6.5	2650	10
6	Mudstone	0.3	0.35	0.8	30	0.1	2400	17
7	Coarse sandstone	6.28	5.09	9.9	34	5.6	2600	17
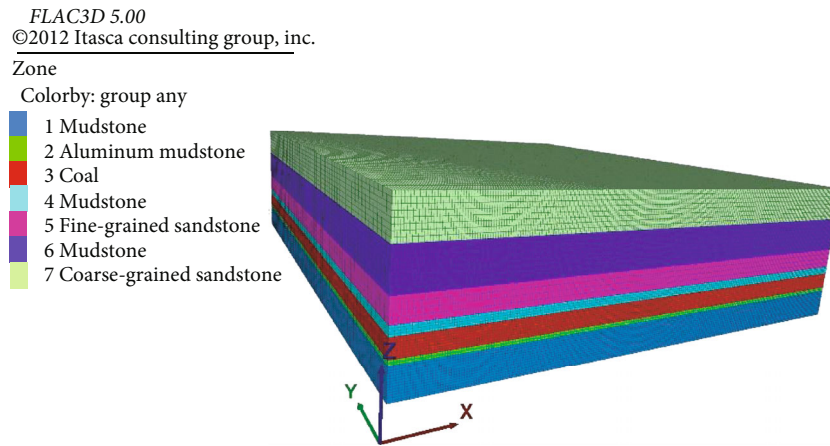
FIGURE 5: Numerical model diagram.
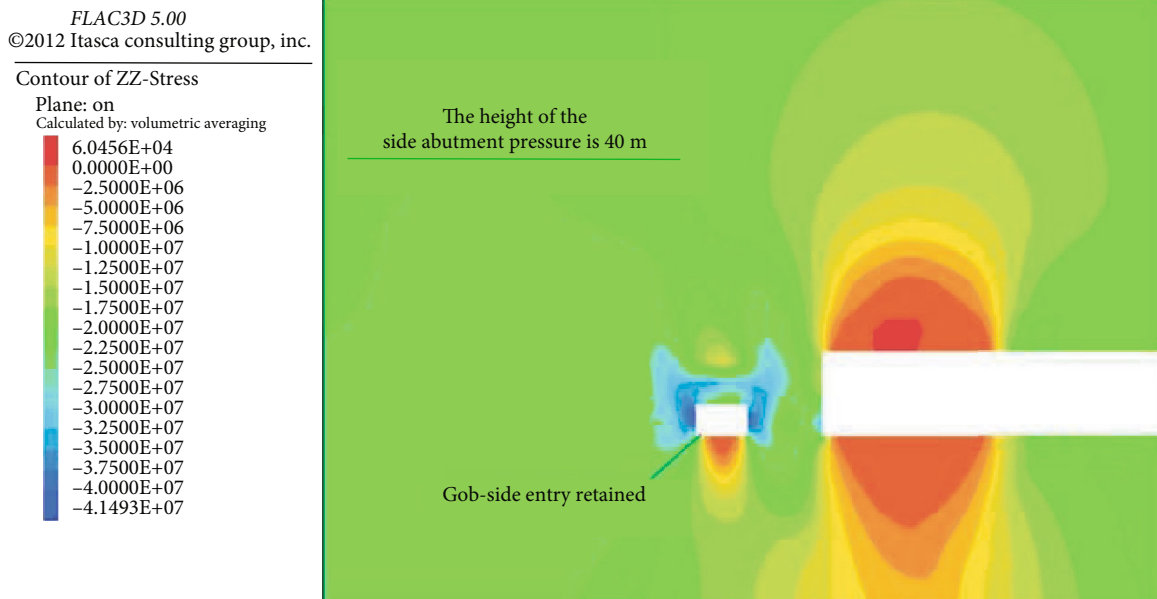
FIGURE 6: Nephogram of side abutment pressure distribution in the working face.

abutment pressure after mining in the No. 201 working face are analyzed to determine the position of the lower key stratum. Numerical simulation results are shown in Figure 6.

It can be seen from Figure 6 that the side abutment pressure generated after the mining of the No. 201 working face has obvious stress concentration phenomenon in the test

Contour of ZZ-Stress
Plane: on
Calculated by: volumetric averaging

0.0000E+00
−2.5000E+06
−5.0000E+06
−7.5000E+06
−1.0000E+07
−1.2500E+07
−1.5000E+07
−1.7500E+07
−2.0000E+07
−2.2500E+07
−2.5000E+07
−2.7500E+07
−3.0000E+07
−3.2500E+07
−3.5000E+07
−3.6935E+07

(a) 5 m coal pillar

Contour of ZZ-Stress
Plane: on
Calculated by: volumetric averaging

0.0000E+00
−2.5000E+06
−5.0000E+06
−7.5000E+06
−1.0000E+07
−1.2500E+07
−1.5000E+07
−1.7500E+07
−2.0000E+07
−2.2500E+07
−2.5000E+07
−2.7500E+07
−3.0000E+07
−3.2500E+07
−3.5000E+07
−3.7000E+07
−3.7516E+07
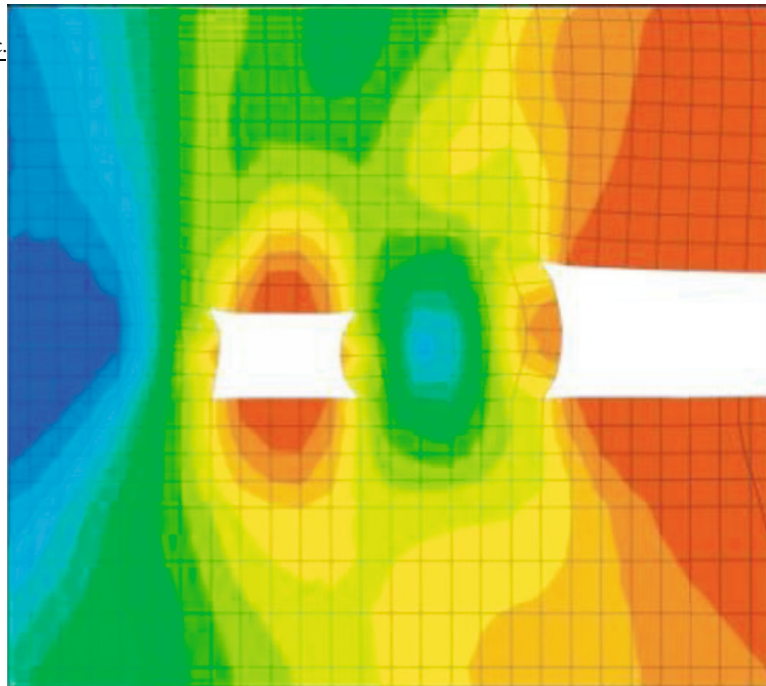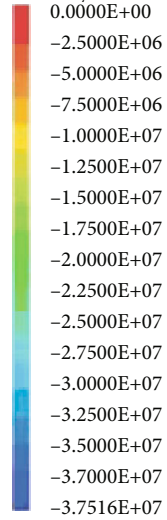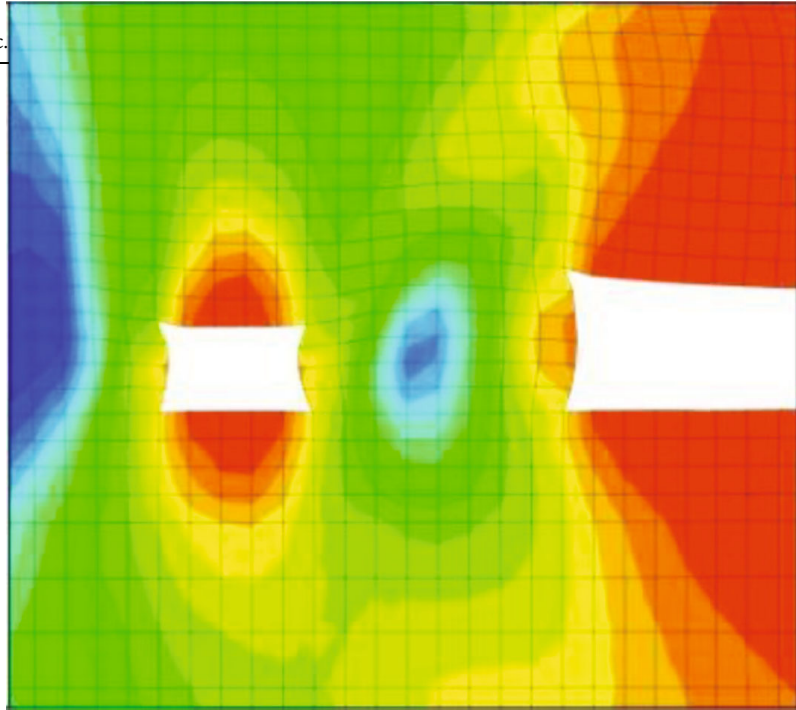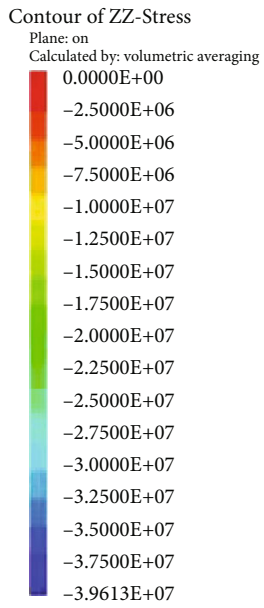
(b) 6 m coal pillar

Figure 7: Continued.

(c) 7 m coal pillar

(d) 8 m coal pillar

Figure 7: Continued.
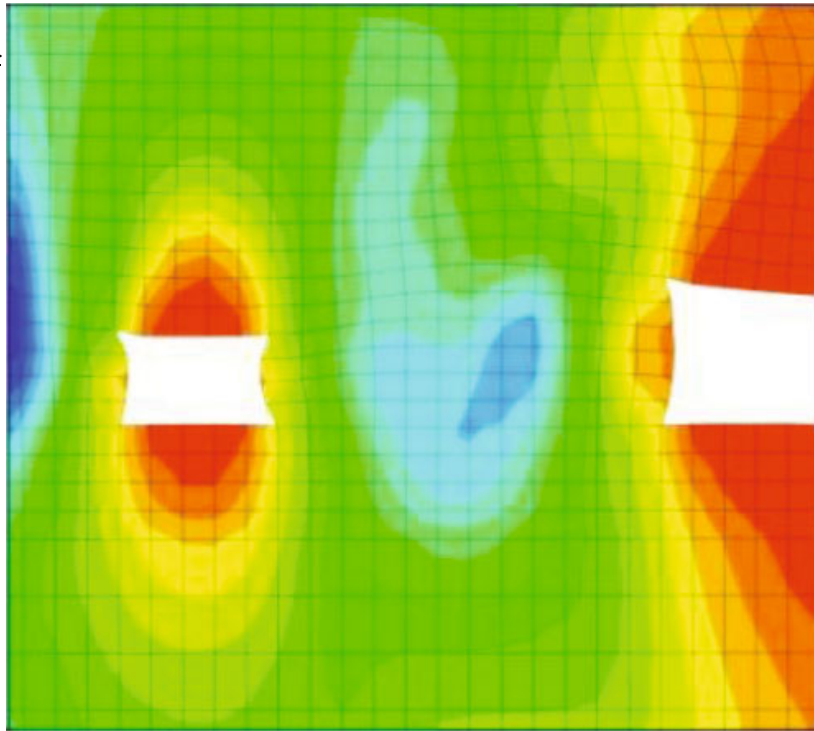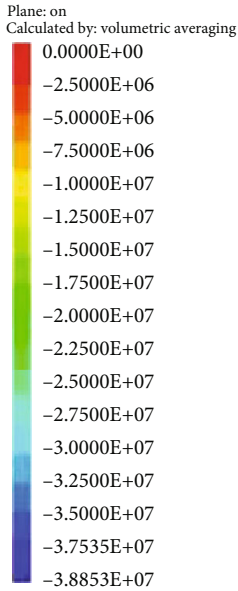
(e) 10 m coal pillar

(f) 12 m coal pillar

FIGURE 7: Cloud map of vertical stress distribution of different coal pillar widths under the effect of one mining.

gob-side entry retained section, and the vertical stress is butterfly-shaped distribution. The maximum influence height of the abutment pressure on the left side of the gob-side entry retained is 40 m. From Figure 6 and Table 2, it can be seen that the height of the fifth group of fine sand-stone in the model is about 38 m, and the fine sandstone with a thickness of 10 m can still transfer stress after the mining of the No. 201 working face. Therefore, the key stratum at the bottom of the entry roof is the fine sandstone with a thickness of 10 m.

3.5. Determination of Reasonable Size of Small Coal Pillar.

Determining the reasonable width of small coal pillar is one of the key factors to ensure the success of gob-side entry retained. For Gaojiapu Coal Mine, in view of the problems of large mining depth, obvious impact tendency, and serious connection tension, the reasonable position and width of small coal pillar are determined. The entry arrangement in the low stress area can ensure that the coal pillar has a stable bearing area, which is an important condition to ensure the success of the gob-side entry test.

According to the limit equilibrium theory, the yield zone width R of near-horizontal coal seam [16, 17] is

$$R = \frac{mA}{2 \tan \phi_0} \ln \left[\frac{\lambda \gamma H + (C_0/\tan \phi_0)}{(C_0/\tan \phi_0) + (P_x/A)} \right]. \quad (1)$$

In these equations, m is coal pillar height (m); A is lateral pressure coefficient; φ_0 is internal friction angle (°); C_0 is cohesion (MPa); λ is stress concentration coefficient; γ is average rock bulk density (kN/m³); H is coal pillar depth (m); and P_x is the support resistance of P_x-support to the entry side (kN).

Substituting the data into equation (1), the yield width of coal pillar is 4.32 m.

The above analysis shows that the reasonable position of gob-side entry retained driving is to arrange the gob-side entry in the "internal stress field," so that it is in a low stress environment, which is conducive to maintaining the overall stability of the entry. Therefore, it is necessary to calculate the distribution range of the abutment pressure "internal stress field" on the coal side of the working face in theory. According to the theory of "internal stress field," the vertical abutment pressure distributed in the range of internal stress field around the gob is equal to the weight of the main roof rock beam before the first weighting of the working face [18]:

$$\frac{1}{2} S_0 \frac{k\gamma h S_0}{S_3} = \frac{LC \sum_1^n M_i \gamma}{2(L+C)}. \quad (2)$$

In these equations, S_0 is internal stress field width (m); M_i is the main roof rock beam thickness (m); C is first weighting interval of main roof (m); L is length of the working face (m); S_3 is bearing pressure which has obvious influence range (m); k is 2.2~2.8; γ is density (kN/m³); and n is number of main roof rock beams.

Substituting the data into equation (2), $S_0 = 12.86$ m can be obtained.

According to the above equation (1), the yield width of coal pillar is 4.32 m, so the entry should be arranged within 4.32~12.86 m from the working face in theory. In order to ensure that the coal pillar is arranged in the low stress zone, so as to reduce the deformation of the coal pillar and ensure the internal integrity of the coal pillar, which is helpful for the bolt to effectively play a supporting role, so as to maintain the overall stability of the entry, six numerical simulation schemes with different coal pillar sizes are proposed: 5 m, 6 m, 7 m, 8 m, 10 m, and 12 m, and the numerical simu-
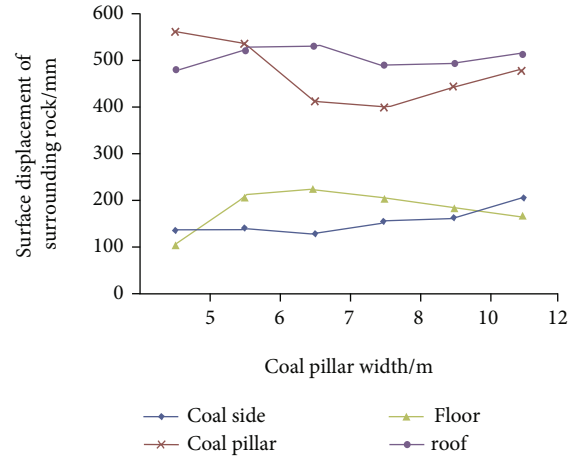
Figure 8: Deformation curve of surrounding rock of coal pillar with different widths.

lation comparative analysis of coal pillars with different sizes during a mining period is carried out; the numerical simulation results are shown in Figure 7.

From the numerical simulation results and Figure 8, during the working face mining, due to the roof rotation and subsidence of the roof, the stress of the surrounding rock of the entry is redistributed, and the peak value of the vertical stress in the coal pillar increases first and then decreases. When the coal pillar size is 5~7 m, it has good bearing capacity, and the side abutment pressure affected by mining is small, the stress concentration coefficient is small, and the entry is in a safe environment. When the coal pillar size is 7~12 m, the peak stress begins to decrease, and the coal pillar still maintains good bearing capacity. However, the peak stress of the side coal seam is higher, and the stress concentration coefficient is large, which is not conducive to the stability and maintenance of the entry. After comprehensive consideration, under the specific geological conditions of Gaojiapu Coal Mine, the reasonable coal pillar size of the test section of small coal pillar gob-side entry retained should be 7 m.

3.6. Analysis of the Mechanical State of the Coal Pillar Gob-Side Entry Retained.

The second rock layer (fine-grained sandstone) above the coal seam is identified from Subsection 3.4 as the lower key layer. According to the Academician Qian Minggao's "critical stratum theory," after the working face was mined, a small structure consisting of key blocks A, B, and C was formed together, as shown in Figure 9.

A mechanical analysis of the coal pillars of god-side entry retained was performed. With reference to literature [19], we analyze the coal pillars to obtain the following equation:

$$u = (m + n - kn) \frac{(l_1 + l_2 + l_3)}{l}. \quad (3)$$

In these equations, u is the amount of sinking of key block B (m); m is the thickness of the coal seam (m); n is the thickness of the immediate roof (m); k is the immediate
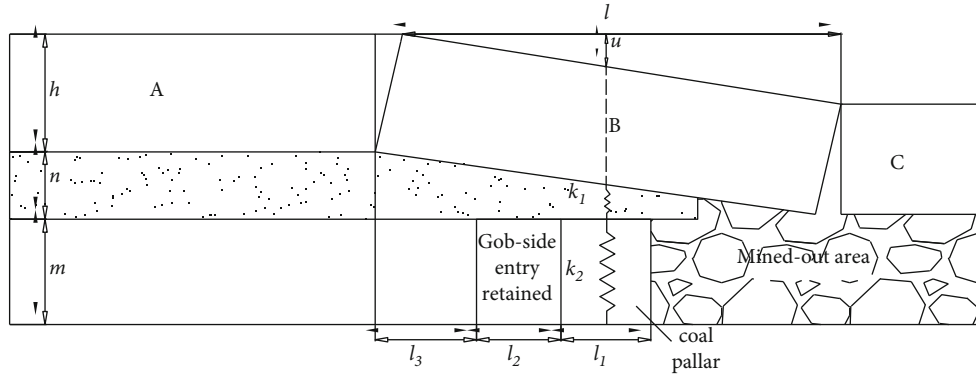
Figure 9: Mechanical model diagram of coal pillar.

roof breaking expansion factor; l_1 is the width of the coal pillar (m); l_2 is the width of the gob-side entry retained (m); l_3 is the length of the key block B fracture location from the roadway (m); and l is the length of the key block B (m), where the key block B length l is equal to the distance of periodic roof weightings.

The l_3 is obtained from the following equation:

$$l_3 = \frac{MA}{2 \tan \varphi} \ln \frac{k\gamma H + (C_0/2 \tan \varphi)}{(C_0/\tan \varphi) + (P_x/A)}. \tag{4}$$

In these equations, A is the lateral pressure coefficient; φ is the angle of internal friction; γ is the gravitational density of the rock formation (kN/m^3); H is the mining depth (m); C_0 is the cohesion of the coal seam at the junction with the roof and floor; P_x is the preload force of the anchor against

the roof (kN); and M is the mining height (m). In this manuscript, the coal thickness is equal to the mining height ($M = m$).

The pressure p acting on the coal column is given by the following equation:

$$p = \frac{k_1 k_2}{k_1 + k_2} u = \frac{E_1 E_2 l_1}{E_1 m + E_2 n} u. \tag{5}$$

In these equations, p is the pressure acting on the coal pillar (MPa); k_1 and k_2 are the stiffness factor in the vertical direction of the direct roof and coal pillar; and E_1 and E_2 are the modulus of elasticity of the direct top and coal pillar, respectively (MPa). Substituting equation (4) into equation (3) yields u; then, substitute u in equation (5) to obtain p as follows:

$$p = \frac{(m + n - kn)(E_1 E_2 l_1)(l_1 + l_2 + (mA/2 \tan \varphi) \ln ((k\gamma H + (C_0/2 \tan \varphi))/((C_0/\tan \varphi) + (P_x/A))))}{l(E_1 m + E_2 n)}. \tag{6}$$

In this manuscript, the pressure p before and after the top break is related to the location of the key block B break, l3, and the amount of sinking of key block B-u. When the tops are manually forced off, the l_3 decreases and the u follows, resulting in fewer p.

3.7. Determination of Roof Breaking Method and Parameters

3.7.1. Determination of Roof Breaking Method. In the past 20 years, in order to solve the occurrence of rock burst in deep mining, many researchers have developed a series of pressure relief methods, among which hydraulic fracturing and blasting pressure relief are the most common. The hydraulic fracturing method was originally used for the development and utilization of natural gas and petroleum gas and then was used for the pressure relief method in deep mining. However, the hydraulic fracturing itself is greatly affected by the rock strata, and the rock hardness

and fracture development degree affect the effect of hydraulic fracturing to a large extent. Therefore, this paper adopts the blasting pressure relief method of D-type [20] polymer tube, which is more commonly used in the pressure relief method.

As shown in Figure 10, the conventional explosive is loaded into the D-type-shaped tube in the predrilling. When the charge explosive explodes in the device, the explosion energy is collected to form an energy flow. The energy flow is released along the D-tube structure, and the release direction is the planned crack direction. The initial crack is first caused by explosion shock wave and stress wave. Because the rock is a brittle material, the subsequent local failure is easily caused by the stress concentration in the damaged area. When the borehole is arranged in a straight line at a certain interval and the charge in the energy gathering pipe is reasonably designed, the rock roof can be cut along the direction of energy accumulation, while the rock in other

(a) D-shaped energy collecting groove
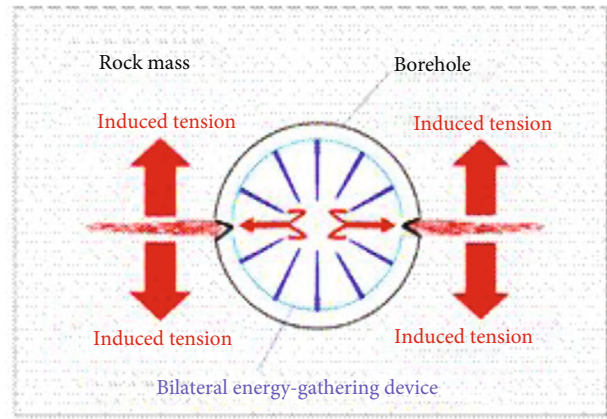
(b) The mechanical effect of energy accumulation

FIGURE 10: Mechanical model of double-sided energy-accumulating tension blasting.

directions is intact due to the protection of the energy gathering pipe.

3.7.2. Determination of Blasting Parameters. The factors affecting the presplitting blasting effect involve the charge mass, charge structure, sealing length, and borehole spacing.

(1) Charge mass. The charge mass determines the cohesive blasting energy produced by single hole charge explosion, which affects the cutting effect. Small charge mass and insufficient crack propagation cannot effectively cut off the key stratum. When the charge mass is large, the energy generated by blasting will destroy the roof and other supporting materials. Especially in this technical research, the purpose is to cut off the lower key stratum and protect the integrity of the immediate roof as far as possible. Therefore, the charge should be based on the strength of rock mass

(2) Charge structure. There are many charging methods in the hole in the roof presplitting blasting, but in order to facilitate the charging or meet the needs of the blasting engineering in the actual blasting engineering, no matter the radial and axial direction, the noncoupling charging method is adopted, which is mainly divided into two ways: one section of the air column and several sections of the air column, as shown in Figure 11

(3) Sealing length. When doing column explosive blasting, the antiexplosion ability of rock mass increases with the increase of hole depth, and the blasting ability of explosive is related to the length of sealing hole and the antiexplosion strength of rock mass

(4) Borehole spacing. When the roof is presplitting blasting by deep hole blasting, the rock is around the explosive explosion, and there is no free surface. The stress wave generated by blasting can be seen as

FIGURE 11: Axial decoupling charge method.
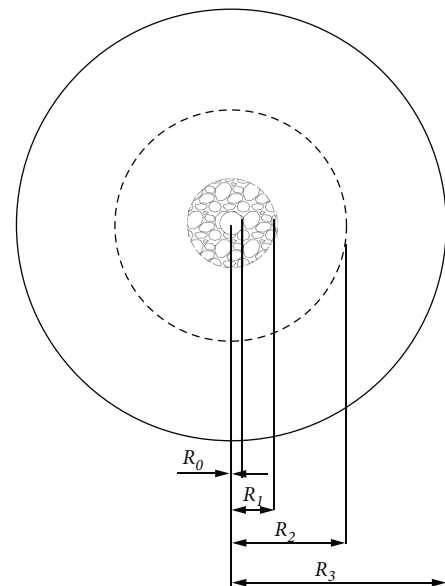
FIGURE 12: Internal effect of blasting.

uniform diffusion around the rock mass. After explosion, the borehole radius of R_0, the crushing zone of R_1, the rupture zone of R_2, and the vibration zone of R_3 will be generated with the borehole as the center in the rock mass, as shown in Figure 12

After the explosive is detonated in the borehole, the resulting stress wave causes the rock mass to be crushed
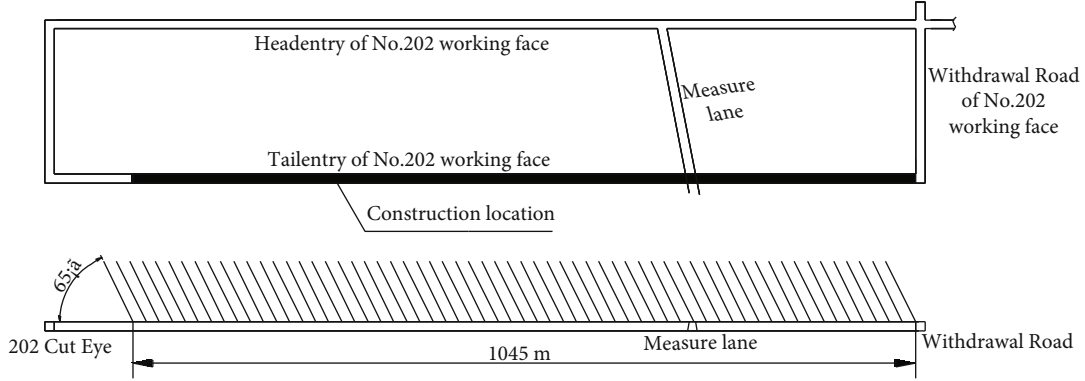
Figure 13: Drilling plan layout.

and destroyed, thus forming the crushed zone. The radius calculation formula of the crushed zone can be used in the following equation:

$$R_1 = \left(\frac{\rho_m C_p^2}{5\sigma_c}\right)^{1/2} R_k. \tag{7}$$

In these equations, R_1 is radius of crushing zone; ρ_m is rock initial density (kg/m³); C_p is wave velocity of rock mass (m/s); R_K is cavity radius limit value is calculated by equation (4); and Σ_c is rock uniaxial compressive strength (MPa).

$$R_k = \left(\frac{p_1}{\sigma_0}\right)^{1/4} r_b. \tag{8}$$

In these equations, r_b is drilling radius (mm); P_1 is explosive explosion pressure (MPa); it can be calculated by equation (9); σ_0 is rock strength under multidirectional stress (MPa); it can be calculated by equation (10).

$$P_1 = \frac{1}{8}\rho_0 D^2, \tag{9}$$

$$\sigma_0 = \sigma_c \left(\frac{\rho_m C_p^2}{\sigma_c}\right)^{1/4}. \tag{10}$$

Since the explosion of explosives, the force time of the shock wave on the coal is very short, and its effect is rapidly attenuated, and the radius of the crushing zone is relatively small. Therefore, the radius calculation of the fracture zone is crucial to the study of the borehole layout parameters. At present, the radius of the fracture zone is mainly determined by the stress wave, so the radius of the fracture zone is solved by equation (11) of the stress wave:

$$R_2 = \left[\frac{bp_2}{S_T}\right]^{1/\alpha} r_b. \tag{11}$$

In these equations, R_2 is rupture radius (mm); b is the ratio of radial stress to tangential stress which can be calculated by equation (12); α is the attenuation coefficient of

α-stress wave which can be calculated by equation (13); P_2 is the peak shock wave stress under the uncoupled charge factor, which can be calculated by equation (14); r_b is drilling radius (mm); and S_T is rock uniaxial tensile strength (MPa).

$$b = \frac{\mu}{1-\mu}. \tag{12}$$

In these equations, μ is the Poisson ratio.

$$\alpha = 2 - b, \tag{13}$$

$$P_2 = \frac{1}{8}\rho_0 D^2 \left(\frac{r_c}{r_b}\right)^6 n. \tag{14}$$

In these equations, ρ_0 is explosive density (kg/m³); D is explosion velocity (m/s); r_c is charge radius (mm); and n is stress increase multiple, generally 8~11.

The rock mechanics data of Gaojiapu are substituted into the above equation and coupled with the explosive charge to calculate and solve radius of crushing zone R_1 is 0.7 m, and the radius of fracture zone R_2 is 5.3 m. The lower key stratum thickness is 10 m. Through theoretical analysis and field investigation, it is known that when the coal seam conditions are certain, the smaller the borehole spacing is, the more conducive to the formation of precracking surface of fracture propagation, and the better the unloading effect is. However, with the decrease of borehole spacing, the amount of field engineering increases and the construction cost increases. Therefore, according to the specific geological conditions and construction conditions of Gaojiapu No. 202 working face, the borehole spacing is determined to be 2 m.

3.7.3. Layout of Boreholes for Roof Breaking Presplitting Blasting. The arrangement of blasting boreholes is based on the thickness of the main roof, the degree of joint fracture development, the first weighting and periodic weighting interval of the working face, the explosive performance of explosives, and other factors. The drilling arrangement of presplitting blasting in advance broken roof is divided into a unidirectional drilling method and bidirectional drilling method. The one-way drilling method is to drill a deep hole at the other end of the tailentry or headentry to ensure the overall stability of the roadway. The two-way drilling
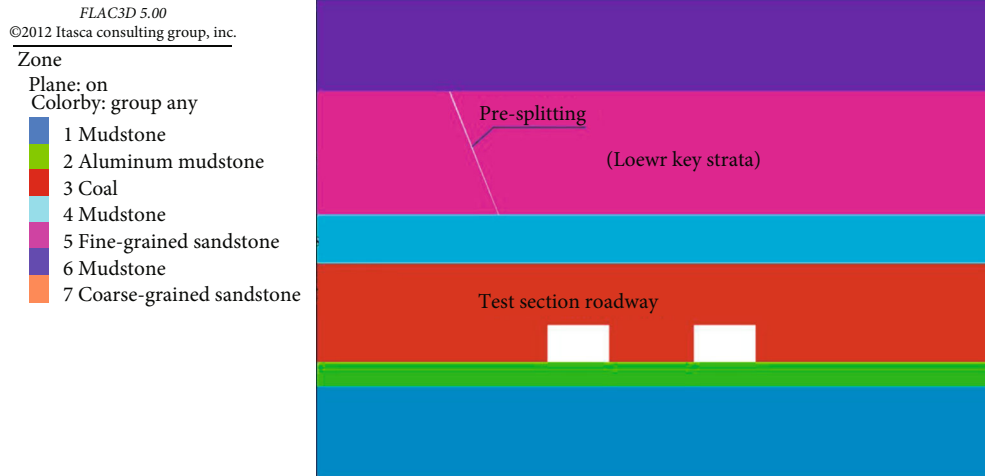
FIGURE 14: Simulated diagram of roof-breaking presplitting blasting.

(a) 20 m from the working face

(b) 0 m from the working face

(c) 40 m behind the working face
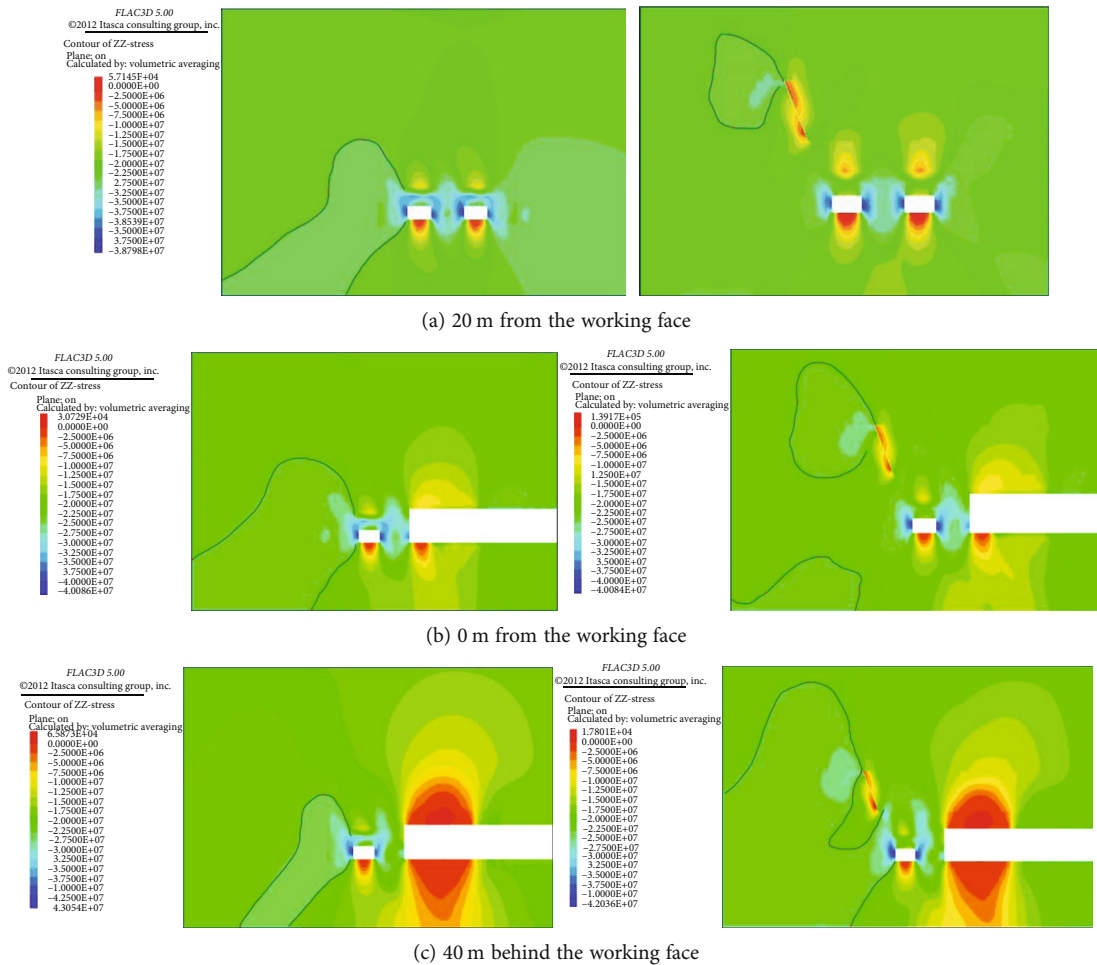
FIGURE 15: Vertical stress distribution nephogram.

method is to simultaneously drill deep and oblique holes into the coal body in the tailentry or headentry [21, 22].

Through the above theoretical calculation and field investigation and analysis, in view of the characteristics of high ground stress in the No. 202 working face of Gaojiapu

Coal Mine, the layout mode of unidirectional roof breaking presplitting blasting boreholes with 75 mm borehole diameter, 60 mm charge diameter, 1.25 uncoupling coefficient, 65° borehole inclination angle, 20 m borehole depth, 2 m borehole spacing, and 6 m sealing length is proposed. The

(a) 20 m from the working face

(b) 0 m from the working face

(c) 40 m behind the working face
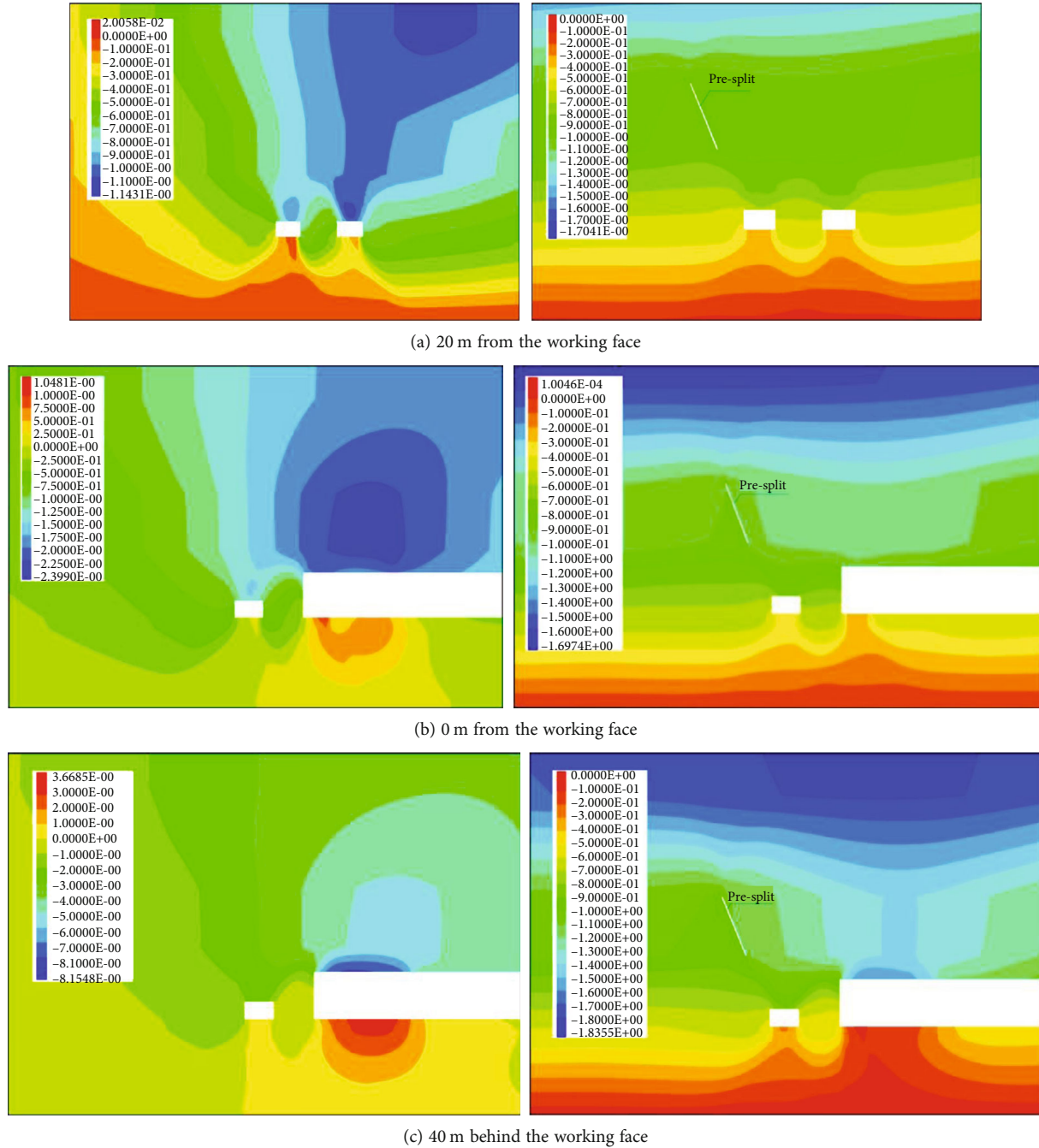
Figure 16: Horizontal displacement nephogram of entry.

presplitting blasting time of roof breaking in the No. 202 working face is set before the mining after the breakthrough of tailentry, and the scheme layout diagram is shown in Figure 13.

4. Numerical Simulation Analysis of Presplit Blasting of Broken Roof

In order to facilitate the overall coherence analysis and simulation, this chapter used the numerical simulation of mechanical model mentioned above, to continue using FLAC^{3D} finite difference software to continue the simula-

tion, and analyzed the roof cutting and pressure releasing and not roof cutting and pressure releasing under the condition of two kinds of working condition of small coal pillar along the gob-side entry retained for the surrounding rock stress variation of the arrangement. The deformation of surrounding rock along the test section of the gob-side entry retained is monitored under two working conditions. Through the method of comparative analysis, it is verified that the parameters designed by the presplitting blasting of interrupted roof in the stopping process of the No. 202 working face can achieve good results in maintaining the gob-side entry retained.

According to the above theoretical calculation, it can be concluded that the lower key stratum is the fine-grained sandstone directly above the immediate roof of the coal seam, with a thickness of 10 m. In this section, fine-grained sandstone 10 m above the entry in the test section is simulated to simulate the unloading effect of top-breaking presplitting blasting, and then, the deformation amount of the remaining small coal pillar and the transfer law of surrounding rock stress are analyzed through numerical simulation calculation. The blasting area is shown in Figure 14.

4.1. Comparative Analysis of Surrounding Rock Vertical Stress. Through numerical simulation under two working conditions before and after the roof cutting of 202 tailentrye, we compare and analyze the law of stress change of small coal pillars of gob-side entry retained when excavating 202 working face. We intercepted three sections (20 m, 0 m, and 40 m from the working face) to reflect the comparative changes of stresses under the two working conditions from near to far from the working face. Final comprehensive evaluation of the vertical stress distribution law before and after interruption of top decompression by top precracking blasting in the mining process of thick coal seams in deep wells was performed. The vertical stress distribution cloud diagram is shown in Figure 15.

Through comparative analysis of the stress distribution law of the three sections, it is found that without the roof off the top handling pressure state, The side abutment pressure concentration zone of the roadway was always in the position close to the roadway during the retrieval process of the 202 working face. The maximum stress value reached 43 MPa, and the stress concentration factor reached 1.9. During this period, the roadway is always under the influence of high bearing pressure, which can easily lead to coal wall flakes, serious deformation of the roadway, and even instability. And the maximum range of side abutment pressure is about 40 m above the left side of the entry, indicating that the side abutment pressure is transmitted by 10 m fine-grained sandstone at this time. After the roof cutting and pressure relief, the precracking surface setup during the simulation calculation cuts off the stress transfer path between the lower key stratum. And it can be seen from Figures 15(a) and 15(b) that there is an obvious unloading pressure zone in a certain range above the roadway, and the lateral support pressure side abutment pressure range above the roadway is located above the cut, and the height is about 55 m. And the abutment pressure increases in the left side of the fracture line after the roof cutting, forming a stress concentration area. This indicates that the lower key layer is not transferring pressure and that pressure is being transferred farther up the line from the higher rock stratum. As can be seen from the previous section, the abutment pressure is transferred in the mudstone layer of 17 m above the fine-grained sandstone at this time. In this state, the entry itself is in the range of in situ stress zone, which is conducive to the stability of the entry itself and the performance of bolt support.

4.2. Comparative Analysis of Entry Roof Subsidence. Through the actual investigation of Gaojiapu Coal Mine, it is found
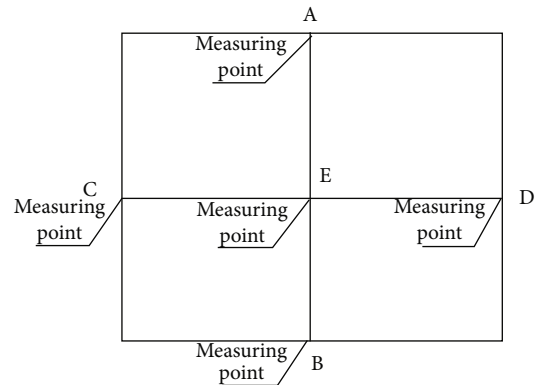
FIGURE 17: Schematic map of measuring point arrangement.

that the bolt (cable) support of mining entry in one panel area is not ideal, and the roof subsidence is serious, which is manifested as roof separation subsidence and support structure bending fracture. In order to ensure the effect of presplit blasting with broken roof and provide feasible suggestions for later support, the roof subsidence of mining entry under two working conditions of broken roof unloading and unbroken roof unloading was compared and analyzed.

According to the overall analysis of Figure 16, it can be seen that the maximum subsidence of entry is located in the middle of the roof, so the support design of the middle of the roof should be strengthened when considering entry support. After the implementation of top-breaking presplitting blasting on the working face, the amount of roof subsidence is significantly reduced in the range affected by advanced mining, and the final settlement value is reduced from 2000 mm to 1100 mm, 900 mm less. It can be seen that under the condition of roof breaking and presplitting blasting without considering the support, the roof subsidence of the test section becomes smaller as a whole because the concentrated stress zone in the coal body of the entry is obviously weakened and unloading zone appears in the entry roof.

In conclusion, the stress and vertical displacement of surrounding rock of the 202 tailentry have changed significantly after the roof presplitting blasting. It can be seen that the stress concentration area moves to a higher and farther place obviously after the presplitting blasting. The influence of vertical stress on entry is obviously reduced in the lateral coal body and the unloading zone appears at the top of entry. The roof subsidence of the entry in the test section is significantly reduced, the overall deformation of the entry in the test section is reduced, and the bearing capacity is increased, which is more conducive to the stability of the entry in the test section.

5. Actual Entry Ore Pressure Monitoring

5.1. Coal and Rock Surface Displacement Monitoring

5.1.1. Station Layout. The No. 1 station was selected as the measuring point to monitor the surrounding rock deformation
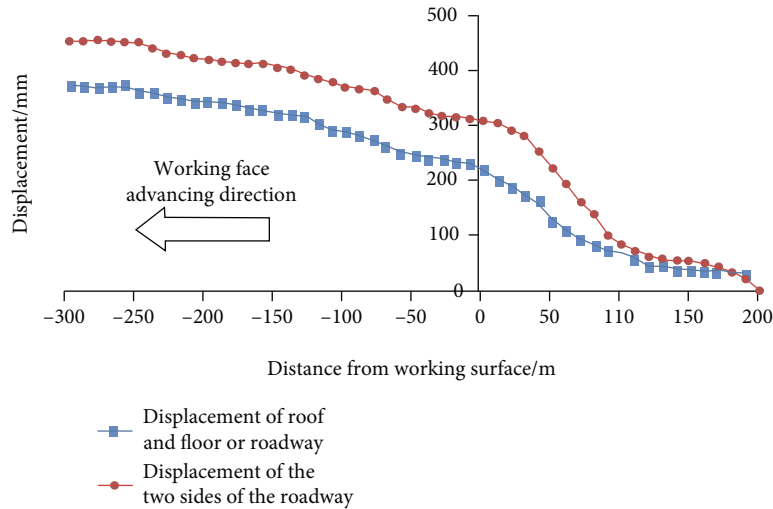
FIGURE 18: Approaching quantity of roof and floor and two sides of entry during the mining period of the No. 201 working face.

FIGURE 19: Effect picture of entry staying along goaf before and after roof failure pressure relief.

of the entry, mainly monitoring the surrounding rock deformation before and after the mining of the No. 201 working face. The monitoring data were sorted out, and the deformation curves of the roof and floor and two sides of the entry were drawn.

5.1.2. Layout and Monitoring Requirements of Artificial Observation Points for Surrounding Rock Deformation. The layout of measuring points of the monitoring section of entry deformation in the test section is shown in Figure 17. The stations are arranged by crosspoint method.

5.2. Monitoring of Entry Surrounding Rock Deformation during Mining of the No. 201 Working Face. During the stopping of working face 201, the deformation of surrounding rock of entry along the test section of goaf retaining entry was monitored. The change rule of entry surrounding rock surface displacement at the measuring station with the progress of stopping the working face is shown in Figure 18.

It can be seen from Figure 18 that when the station is 110 m away from the working face, the moving amount of the roof, floor, and two sides of the entry begins to increase, indicating that the influence range of advanced abutment pressure of working face 201 is 110 m in front of the working face. In the range of 50~80 m from the working face to the

station, the moving rate of the roof, floor, and two sides is accelerated, indicating that the leading abutment pressure has a severe influence on the surrounding rock of entry in this range. After the working face pushes over the measuring point, the deformation of surrounding rock of entry continues to increase under the influence of the movement of the basic roof rock beam. After 250 m stopping of the working face, the deformation of entry tends to be stable, indicating that the movement of the basic roof rock beam basically ends at this time and the entry will no longer have obvious deformation. The actual engineering effect is shown in Figure 19.

By comprehensive analysis of the above observation results, it can be seen that when small coal pillars are used in the goaf retaining test in No. 2 panel area of Gaojiapu Coal Mine, the supporting system can always play an active supporting effect and maintain the stability of entry surrounding rock under the action of a mining disturbance. From the analysis of surrounding rock deformation, the surrounding rock deformation of entry is always in a controllable range, and the overall deformation of entry is relatively small, which can meet the needs of safety production and continue to serve the mining of the No. 202 working face. It can be seen that the entry retention test was successful, but it is still necessary to continue monitoring the entry in

the test section during the stopping of the No. 202 working face to test the overall effect of entry retention in the test section.

6. Conclusion

In this paper, a method of roof cutting and pressure releasing of small coal pillar is proposed based on the lower key layer of coal seam roof. According to the characteristics of high in situ stress in Gaojiapu Coal Mine, the roof conditions of coal seam are analyzed through theoretical calculation and the lower key layer above the coal seam is determined through field investigation and actual construction conditions. The arrangement mode and blasting parameters of presplit blasting borehole for one-way roof breakage were designed to cut off the lower key stratum, and FLAC^{3D} software was used to simulate the unloading effect of the lower key stratum after fracture.

The results show that the presplitting surface formed by blasting can effectively cut off the transmission of raw rock stress between the lower key stratum, and the stress concentration area in the side coal body of entry is obviously transmitted to the higher and farther inside the solid coal, and part of the unloading area appears above. The gob-side retaining entry can adopt the same support parameters as the transport entry, so that superstrong support is no longer needed. Besides, the retention of small coal pillars reduces the consumption of the entry side retaining rod system, reduces the cost of coal mining, and improves the safety of coal mining.

Data Availability

The data used to support the findings of this study are included within the article.

Conflicts of Interest

We declare that we have no conflict of interest.

Acknowledgments

References

[1] A. J. Li, "Research and application of key technology of gob-side entry retained in deep mine," *Coal Science and Technology*, vol. 44, no. 11, pp. 12–17, 2016.

[2] F. R. Tang, Z. G. Ma, D. W. Yang, F. Z. Qi, J. Hu, and Y. H. Chen, "Study on key parameters of filling gob-side entry in the thick layer soft rock fault top," *Journal of Mining and Safety Engineering*, vol. 36, no. 6, pp. 1128–1136, 2019.

[3] G. Y. Hou, T. Hu, Z. X. Li, Z. H. Li, J. P. Chen, and Y. K. Cui, "Effect of cutting roof height on the stability of gob-side retain-ing entry with roadside support," *Journal of Mining and Safety Engineering*, vol. 36, no. 5, pp. 924–931, 2019.

[4] M. C. He, H. P. Xie, and S. P. Peng, "Study on rock mechanics in deep mining engineering," *Chinese Journal of Rock Mechanics and Engineering*, vol. 24, no. 16, pp. 2803–2813, 2005.

[5] F. T. Wang, S. H. Tu, Y. Yuan, Y. Feng, F. Chen, and H. Tu, "Deep-hole pre-split blasting mechanism and its application for controlled roof caving in shallow depth seams," *International Journal of Rock Mechanics and Mining Sciences*, vol. 64, no. 6, pp. 112–121, 2013.

[6] M. C. He, X. H. Zhang, and S. Zhao, "Directional destress with tension blasting in coal mines," *Procedia Engineering*, vol. 191, pp. 89–97, 2017.

[7] Y. B. Gao, Y. J. Wang, J. Yang, X. Zhang, and M. He, "Meso- and macroeffects of roof split blasting on the stability of gateroad surroundings in an innovative nonpillar mining method," *Tunnelling and Underground Space Technology*, vol. 90, pp. 99–118, 2019.

[8] S. Zhang, X. L. Wang, Z. Q. Wu, L. G. Zhao, J. K. Liu, and H. F. Liu, "Status analysis of the key parameters of blasting borehole and the retaining effect for gob-side entry retained by the way of roof cutting and pressure releasing," *Journal of Henan Polytechnic University*, vol. 38, no. 6, pp. 1–9, 2019.

[9] S. Y. Chen, M. C. He, and H. J. Wang, "Coordination control and stress evolution of surrounding rock of gob-side entry retaining cutting roof in deep mine," *Journal of Mining and Safety Engineering*, vol. 36, no. 4, pp. 661–669, 2019.

[10] P. Yang, H. X. Zhu, Y. F. Li, Q. J. Liu, and C. Yang, "Backfill horizontal stability analysis of gob-side entry retained with compound roof in deep mine," *Rock and Soil Mechanics*, vol. 39, pp. 405–411, 2018.

[11] J. K. Wu, J. G. Kan, F. X. Xie, and Z .Q. Yang, "Study on deformation and failure characteristics of deep gob-side entry retained roof and the controlling countermeasures," *Journal of Mining and Safety Engineering*, vol. 34, no. 1, pp. 16–23, 2019.

[12] N. Zhang, H. Chen, and Y. Chen, "An engineering case of gob-side entry retained in one kilometer-depth soft rock entry with high ground pressure," *Journal of China Coal Society*, vol. 40, no. 3, pp. 494–501, 2015.

[13] X. G. Zheng, N. Zhang, L. Yuan, and F. Xue, "Method and application of simultaneous pillar-less coal mining and gas extraction by staged gob-side entry retained," *Journal of China University of Mining and Technology*, vol. 41, no. 3, pp. 390–396, 2012.

[14] X. Z. Hua, M. Yang, Q. J. Liu, and P. Yang, "Model test on evolution mechanism of floor heave in gob-side retaining entry of deep mine," *Journal of Mining and Safety Engineering*, vol. 35, no. 1, pp. 1–9, 2018.

[15] M. Xingen, H. Manchao, W. Yajun, Z. Yong, Z. Jiabin, and L. Yuxing, "Study and application of roof cutting pressure releasing technology in retracement channel roof of Halagou 12201 working face," *Mathematical Problems in Engineering*, vol. 2018, Article ID 6568983, 15 pages, 2018.

[16] C. J. Hou and N. J. Ma, "Stress in in-seam entry sides and limit equilibrium zone," *Journal of China Coal Society*, vol. 12, no. 4, pp. 21–29, 1989.

[17] J. Bai, W. Wang, C. Hou, and H. Huang, "Control mechanism and support technique about gateway driven along goaf in fully mechanized top coal caving face," *Journal of China Coal Society*, vol. 5, no. 5, pp. 478–481, 2000.

[18] Y. K. Shi, Z. Q. Song, and C. G. Wang, "The supporting design of road driving along next goaf in soft seam with fully mechanized top-caving," *Rock and Soil Mechanics*, vol. 22, no. 4, pp. 509–512, 2001.

[19] X. G. Zheng, T. L. An, and Y. Guo, "Surrounding rock control mechanism and engineering application of in-situ coal pillar in gob-side entry retaining," *Journal of Mining and Safety Engineering*, vol. 35, no. 6, pp. 1091–1098, 2018.

[20] S. Zhang, X. L. Wang, W. F. Zhao, M. Wang, Z. Q. Wu, and L. G. Zhao, "Study on application of D-type energy gathering blasting tube on gob-side entry retaining," *Coal Science and Technology*, vol. 47, no. 10, pp. 175–181, 2019.

[21] J. P. Li, H. R. Ye, and X. Q. Hou, "Dynamic simulated model for the destress blast for the hard rock entry tunneling under the high geo-stress," *Journal of Safety and Environment*, vol. 18, no. 3, pp. 962–967, 2018.

[22] H. X. Wang, *The research of numerical modeling of destress blasting in a deep hard rock tunnel wall*, Xi'an University of Architecture and Technology, Xi'an, China, 2016.

WILEY | Hindawi

Research Article

Experimental Study on Vertical Propagation Behavior of Hydraulic Fracture Affected by Artificial Interlayer for Thick Oil Reservoirs

Beibei Chen,[1] Yingmin Qin,[2] Peng Xu,[1] Weijie Zheng,[1] Min Zhang [ID],[3] and Yan Peng[3]

[1]*Engineering Technology Research Institute of Xinjiang Oilfield Company, Karamay 834018, China*
[2]*Oil Testing Company, CNPC Western Drilling Engineering Co., Ltd., Karamay 834018, China*
[3]*College of Petroleum Engineering, China University of Petroleum, Beijing 102249, China*

Correspondence should be addressed to Min Zhang; 18601159662@163.com

Crude oil distribution in thick oil reservoirs is vertically heterogeneous; therefore, there is usually a dominant sublayer where oil resources are higher than that in other sublayers. The region of hydraulic fracture away from the dominant sublayer plays a negative role in production. In order to enhance efficiency of hydraulic fracturing, the hydraulic fracture height should be restricted around the dominant sublayer and the artificial interlayer is believed as an effective method. However, the propagation mechanism of fracture affected by artificial interlayer has been rarely investigated, which restricts the advance of optimization of artificial interlayer. In this paper, the impact of artificial interlayer on vertical propagation of hydraulic fracture is analyzed by hydraulic fracturing experiments and then the mechanism of artificial interlayer affecting propagation of hydraulic fracture is discussed. Based on the understanding of experimental observations and theory of fracture mechanics, the theoretical model of stress intensity factor for the fracture affected by artificial interlayer is proposed. The experimental data shows that the artificial interlayer can significantly decrease the hydraulic fracture height and the corresponding decrease magnitude of hydraulic fracture height depends on the thickness of artificial interlayer, proppant size, and fracture fluid pumping rate. The dominant mechanism of artificial interlayer restricting hydraulic fracture height is that the drop of fluid pressure induced by the artificial interlayer decreases the stress intensity factor at fracture tip. Based on the theory of fracture mechanics, the stress intensity factor at fracture tip is built and it can consider key factors shown by experimental observations. The fracture height solution from this model is consistent with experimental data, so this model can be used to optimize properties of artificial interlayer.

1. Introduction

In the process of oil and gas exploitation, the hydraulic fracturing is a commonly used reservoir stimulation method, which can sharply enhance oil and gas production rate. In Xinjiang oil field, the crude oil distribution is vertically heterogeneous and the top sublayer in thick oil reservoirs is the dominant sublayer where the oil resource is higher than that of other sublayers. If the hydraulic fracture height is much higher than the thickness of this dominant sublayer, the proppants injected into reservoirs usually flow down to the other sublayers. In this case, the fracture in the dominant

sublayer cannot gain enough proppants to remain its width after flow back of hydraulic fracturing fluids, which negatively affects oil production for thick oil reservoirs. In addition, excessive hydraulic fracture height can bring problems such as invalid water injection and casing damage, seriously affecting later production [1]. More seriously, hydraulic fractures may communicate with water layer and cause water channeling, which leads to sharp rise of water content in oil wells. Therefore, controlling the hydraulic fracture height is significantly important to improve oil and gas production.

At present, the method to generate an artificial interlay inside hydraulic fracture is the widely used technique to

TABLE 1: Mechanical properties of physical model specimens [15].

Density (g/cm^3)	UCS (MPa)	Tensile strength (MPa)	Poisson's ratio	Elastic modulus (GPa)
2.11	27.98	3.55	0.17	20.6

control hydraulic fracture height. Initially, the low pumping rate is used to generate a hydraulic fracture with short length and then proppants or diverting agents are carried into the hydraulic fracture by fracturing fluids. When these proppants or diverting agent place at the bottom of the hydraulic fracture, the artificial interlayer is generated. After that, common pumping schedule is used to generate hydraulic fractures. Because of the artificial interlayer, the hydraulic fracture height usually decreases. Research on how to generate the artificial interlayer and the mechanism of artificial interlayer restricting fracture height have been investigated. Mukherjee [2] recommended the use of low viscosity fracturing fluids with lighter proppant to seal the top fracture ends and successfully restricted hydraulic fracture height. Talbot et al. [3] proposed a hydraulic fracturing method to limit fracture height propagation by adding front fluid with sand for bottom-water and energy-depleted reservoirs. It is widely believed that the stress difference between vertical layers of reservoirs is the dominant factor to suppress the vertical propagation of hydraulic fractures. The artificial interlay technique increases the pressure drop inside hydraulic fracture and the pressure at fracture tip decreases as well, so the hydraulic fracture height can be restricted [4]. Dali et al. [5–10] studied the factors influencing fracture height propagation of hydraulic fractures by using theoretical model and numerical simulation and proposed that the use of artificial interlayer, variable displacement, and low-viscosity fracturing fluid can effectively control the fracture height. Barree and Mukherjee [11] studied the effects of pumping rate, fluid viscosity, proppant concentration, proppant size, and specific gravity on the effectiveness of the placement of artificial interlayers according to a theoretical model. Salah et al. [12] used artificial interlayer to control fracture height growth in the absence of in situ stress contrasts in Egypt's Western Desert. Another field applications showed that successful placement of artificial interlayer can control the fracture height and increasing the fracture half-length [13, 14]. Theoretical model, numerical simulation, and field application results all show that artificial interlayers can significantly control the height of hydraulic fractures. For mechanism research, both the numerical model and theoretical model simplify the formation conditions, and it is difficult to describe the true fracture propagation process. Based on the true triaxial physical simulation experiment, the hydraulic fracture propagation process under the interference of real artificial interlay is simulated, which is more in line with the actual construction of the oil field. However, the experimental research on the principle and influencing factors of artificial interlayer controlling hydraulic fracture height is rarely reported.

In this paper, hydraulic fracturing experiments are first conducted to illustrate the impact of artificial interlay on hydraulic fracture height. An artificial interlayer is generated in artificial rock samples before hydraulic fracturing experiments are conducted. The triaxial stress condition is applied at artificial rock samples to reflect the in-situ stress of thick oil reservoirs. Based on the theory of fracture mechanics and experimental observations, the main mechanics of artificial interlay controlling fracture height is discussed. Finally, the theoretical solution of stress intensity factor for fractures with artificial interlayer is proposed and it is validated by experimental data. Experiment results and theoretical model show that the thickness and pressure drop gradient are the main factors influencing artificial interlayer restricting fracture height.

2. Physical Simulation Experiment with Artificial Interlayer

The main influencing factors of artificial interlayer controlling fracture height include fracture pressure, fracture toughness, thickness, and pressure drop gradient of artificial interlayer. In the process of hydraulic fracturing, the fracture toughness and in situ stress are reservoirs' properties. Therefore, a true triaxial physical simulation experiment with artificial interlayer is carried out in this paper to study the influence of fracture pressure, thickness, and pressure drop gradient of artificial interlayer on hydraulic fracture height.

2.1. Experimental Design. The physical simulation test piece is mixed with PC32.5R composite Portland cement and 0.12~0.38 mm quartz sand in a certain proportion and cured for 24 days. Its mechanical properties are cited from Reference [15] and shown in Table 1. The size of the test piece is 300 mm × 300 mm × 300 mm.

Artificial fractures are prefabricated inside the prefabricated specimens in advance, and artificial interlayer made of ceramic particles is placed at the bottom of the prefabricated artificial fractures. Artificial interlayers generated by different sizes ceramic particles have different pressure drop gradients. The design and boundary conditions of specimens are shown in Figure 1. The prefabricated artificial fracture is in the middle of the artificial wellbore to simulate vertical well. The normal direction of prefabricated fractures is parallel to the minimum horizontal principal stress direction (as shown in Figure 1(a)). An artificial interlayer is formed at the bottom of the prefabricated fracture by sedimentation of proppant, and its thickness is half of the height of the prefabricated fracture (as shown in Figure 1(b)).

In reality, the permeability and fluid loss capacity of reservoir are limited and increasing the injection rate can increase the fracture pressure [7]. By changing the thickness h_a of the artificial interlayer, the particle size R of the proppant, and the fracturing fluid pumping rate v, the impacts of the thickness of the artificial interlayer, the pressure drop gradient, and the fracture pressure on fracture height are studied.

(a) Schematic diagram of physical simulation specimen   (b) Schematic diagram of prefabricated fracture and artificial interlayer
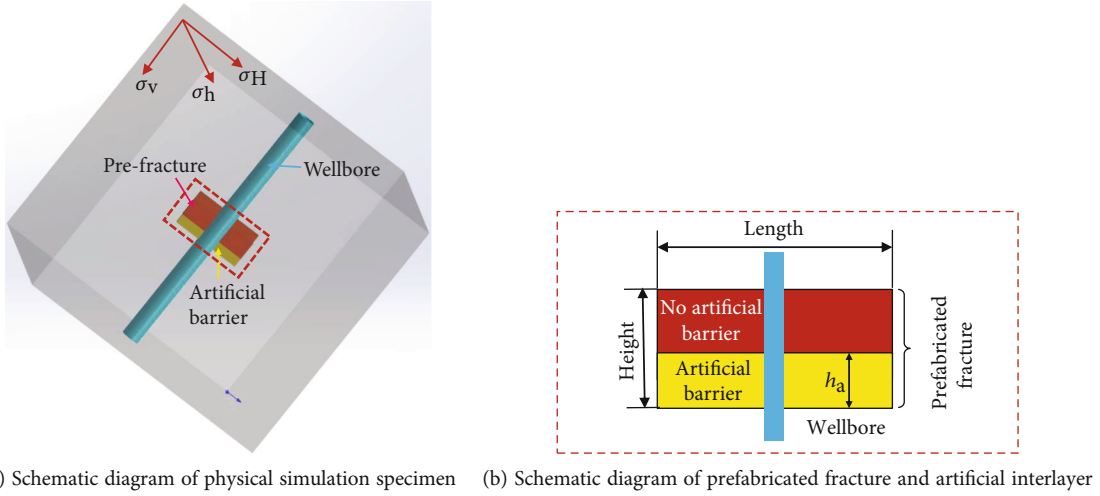
FIGURE 1: Sketch of experimental sample.

The 300R2 high temperature and high stress hydraulic fracturing simulation equipment (Figure 2) is used for this experiment, and it is designed and constructed by the Rock Mechanics Laboratory of China University of Petroleum (Beijing). The maximum load capacity of this equipment is 50 MPa, and the maximum temperature is 180°C; the required size of the specimen is 300 mm × 300 mm × 300 mm.

The specific experimental grouping design is shown in Table 2. In this paper, 5 physical simulation experiments are designed. In experiments 1-1, 1-2, and 1-3, the thickness (h_a) of artificial interlayer is 5, 15, and 20 mm, respectively, which is formed by 40/70 proppant (R). The fracture fluid pumping rate (v) is 6 ml/min in the above three experiments. For experiment 1-4, h_a is 15 mm, R is 40/70 mesh, and v is 12 ml/min. For experiment 1-5, h_a is 15 mm, R is 70/140 mesh, and v is 6 ml/min.

2.2. Experimental Results. The illustration of samples used in this experiment is shown in Figure 1. A prefabricated fracture and an artificial interlay are first prefabricated in the physical simulation test piece. The length of this fracture is 25 mm, and its height is 20 mm. The length of this artificial interlay is 25 mm. In order to investigate the impact of pressure drop on hydraulic fracture propagation, different height values of the artificial interlay are set, and they are 5 mm, 15 mm, and 20 mm in different cases. In addition, the triaxial stresses are applied at this sample and they are the vertical stress σ_v, the minimum horizontal stress σ_h, and the maximum horizontal stress σ_H. Their values are set the same in different cases, and they are 25 MPa, 10 MPa, and 15 MPa, respectively. The directions of these three stresses are set based on the theory of fracture mechanics. The value of minimum horizontal stress is the least among these three stress values, so its direction is parallel to the normal direction of prefabricated fracture. The direction of vertical stress is the same with the well direction. The value of vertical stress is the highest among these three stress values, so the hydraulic fracture generated in this experiment propagates vertically.

The experimental results are shown in Figure 3. In order to quantitatively analyze the effect of artificial interlayers,
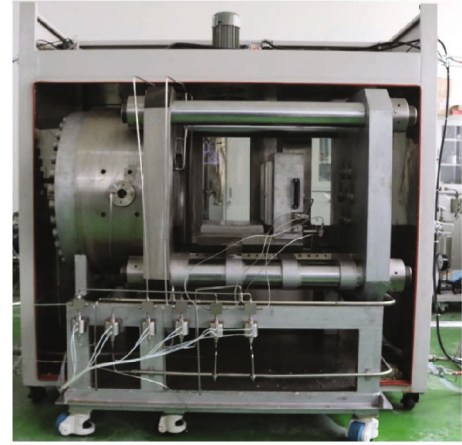
FIGURE 2: 300R2 high temperature and high stress hydraulic fracturing simulation equipment.

TABLE 2: Physical simulation experiment parameters.

Sample no.	h_a (mm)	v (ml/min)	R (mesh)
1-1	5		
1-2	15	6	
1-3	20		40/70
1-4	15	12	
1-5	15	6	70/140

the ratio of the height of fracture with the artificial interlayer $(H_L + h_a)$ to the height of fracture without the artificial interlayer $(H_U + h_a)$ is used to evaluate the effect of the artificial interlayer controlling fracture height. The high ratio value indicates a low magnitude of artificial interlayer restricting hydraulic fracture height. The ratio of the length of the hydraulic fracture to its height $(H_L/L_L$ or $H_U/L_U)$ is used to evaluate the influence of the artificial interlayer on the shape of the hydraulic fracture. The high ratio value
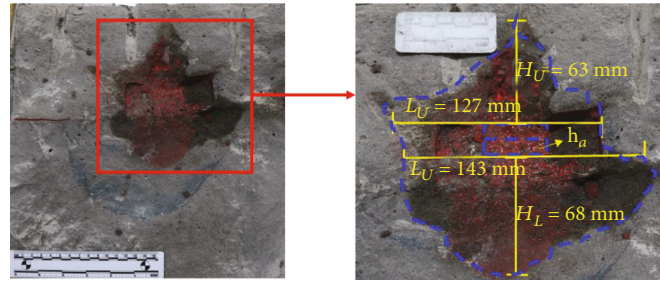
(a) Experiment 1-1
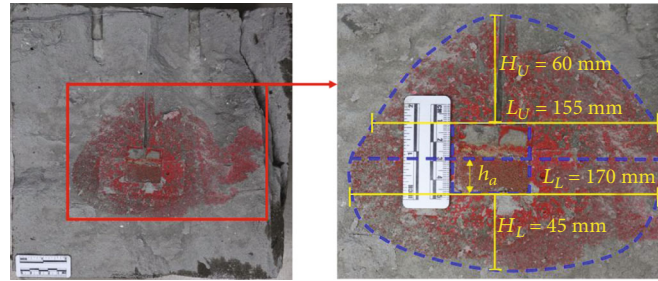
(b) Experiment 1-2
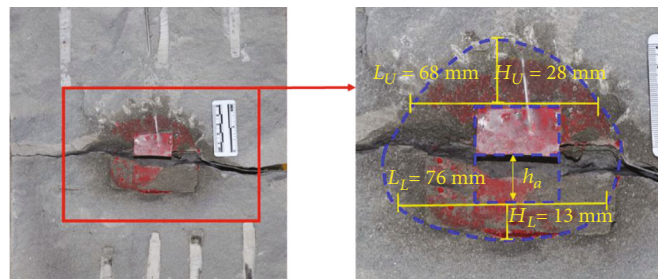
(c) Experiment 1-3
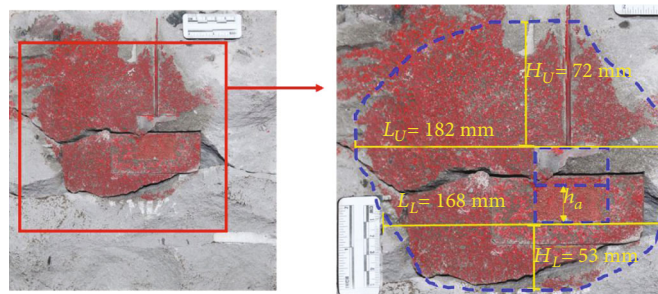
(d) Experiment 1-4
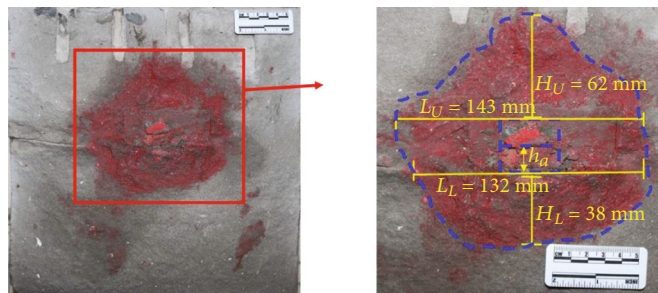
(e) Experiment 1-5

FIGURE 3: Experimental results of physical model with artificial interlayers.

TABLE 3: Experimental results of physical model with artificial interlayers.

Exp no.	$(H_L + h_a)/(H_U + h_a)$	H_L/L_L	H_U/L_U
1-1	0.92	68/143 = 0.48	63/127 = 0.50
1-2	0.8	45/170 = 0.26	60/155 = 0.39
1-3	0.69	13/76 = 0.17	28/68 = 0.41
1-4	0.78	53/168 = 0.30	72/182 = 0.38
1-5	0.69	38/132 = 0.29	62/143 = 0.43

TABLE 4: Factor normalization.

Factors	h_a (mm)			v (ml/min)		R (mesh)	
	5	15	20	6	12	40/70	70/140
Control effect	0	25%	53%	25%	26%	25%	38%
Normalized results	0	0.47	1	0.47	0.49	0.47	0.72

indicates a low magnitude of artificial interlayer restricting hydraulic fracture shape.

By comparing the results of experiments 1-1, 1-2, and 1-3 (seen in Figures 3(a)–3(c)), the thickness of artificial interlayer has a significant influence on the propagation morphology of hydraulic fracture. When the thickness of artificial interlayer is 5 mm, H_U/L_U and H_L/L_L are approximately equal (0.50 and 0.48). However, when the thickness is 15 mm and 20 mm, H_U/L_U is significantly greater than H_L/L_L (0.39 and 0.26; 0.41 and 0.17). When there is an artificial interlayer with a suitable thickness (>5 mm), the hydraulic fracture always preferentially expands in the horizontal direction and the fracture length increases sharply. At the same time, the artificial interlayer can effectively control the height of hydraulic fracture. When the thickness of artificial interlayer increases from 5 mm to 15 mm and 20 mm, $(H_L + h_a)/(H_U + h_a)$ decreases from 0.92 to 0.8 and 0.69, and the effect of artificial interlayer to control the height of the fracture is gradually increasing.

The fracture fluid pumping rates used in experiments 1-2 and 1-4 are 6 ml/min and 12 ml/min, respectively. By comparing Figures 3(b) and 3(d), as shown Table 3, H_U/L_U is greater than H_L/L_L for both of experiments 1-2 and 1-4. The interlayer can always influence the morphology of hydraulic fracture under different pumping rate. When the pumping rate increases from 6 ml/min to 12 ml/min, $(H_L + h_a)/(H_U + h_a)$ decreases from 0.8 to 0.78. It indicates that the pumping rate has no obvious impact on fracture height.

In experiments 1-2 and 1-5, artificial interlayer is fabricated with 40/70 and 70/140 proppant, respectively. The results of experiment 1-5 are the same as that of experiment 1-2; H_U/L_U is greater than H_L/L_L. When the proppant size decreases (the size of 40/70 proppant is larger than that of 70/140 proppant), $(H_L + h_a)/(H_U + h_a)$ decreases from 0.8 to 0.69. Therefore, the impact of artificial interlayer on restricting fracture height increases with the decrease of proppant size of artificial interlayer.

In order to analyze the influence degree of the thickness of artificial interlayer, pumping rates, and proppant sizes on

fracture height restriction induced by artificial interlayer, the experimental results in Table 3 are normalized by influencing factors, and the results of factor normalization are shown in Table 4. The control effect is defined as $(H_U - H_L)/H_U$ to describe the effect of artificial interlayer controlling the height of hydraulic fracture. The normalized results are between 0 and 1, which is calculated by the maximum and minimum value of control effect (normalized results = control effect − minimun/maximum − minimum).

It can be seen from Table 4 that the impact of the artificial interlayer on fracture height restriction can be significantly improved by increasing thickness of the artificial interlayer, decreasing pumping rate, and decreasing proppant size. The normalization results show that the thickness of artificial interlayer has the most significant impact on fracture height restriction by artificial interlayer, followed by the proppant size and the pumping rate.

2.3. Discussion. The artificial interlayer inside fracture affects fluid flow behavior and may induce pressure drop; therefore, the fluid pressure in fracture with artificial interlayer is less than that in fracture without artificial interlayer [16–18]. In order to show whether the pressure drop can be induced by artificial interlayer, the permeability of artificial interlayer is measured. According to Darcy's law, the pressure drop can be calculated if the velocity and viscosity of fluid flow and the permeability are known.

In this paper, FCS-842 equipment produced by Core-Lab is used to get permeability of artificial interlayer. In order to simulate the different closing pressure in hydraulic fractures, different confining pressure is applied on two rock slabs during this experiment. At the same time, pressure drop gradient can be calculated using the Darcy' law:

$$dp = \frac{v\mu}{kA}, \tag{1}$$

where v is pumping rate, μ is viscosity, k is permeability, A is cross-section area, and dp is pressure drop gradient. The pumping rate, viscosity, and cross-section area can be
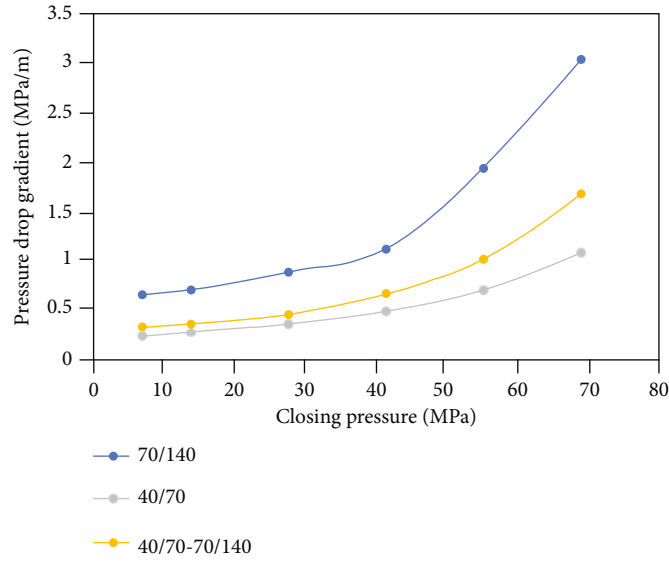
FIGURE 4: Pressure drop gradient of artificial interlayer.

recorded and measured in experiments. The permeability value can also be obtained by experiments. Therefore, the pressure drop gradient can be calculated. The proppant is statically placed in the rock slab to simulate the artificial interlayer formed in the hydraulic fracture. Short-term permeability tests of artificial interlayer with proppant sizes of 40/70 and 70/140 and mixed particle sizes (40/70 and 70/140; mass ratio 1 : 1) are carried out to calculate the pressure drop gradient of artificial interlayers, as shown in Figure 3.

As shown in Figure 4, by comparing the pressure drop gradient of artificial interlayer formed by different proppant sizes, the pressure drop gradient of 70/140 is about 50% higher than that of 40/70. At the same time, under the high closing pressure (>41 MPa), the pressure drop gradient of 70/140 artificial interlayer is significantly higher than that of 40/70. The above results indicate that artificial interlayer formed by small proppant size can increase the drop of fluid pressure inside hydraulic fracture to decrease stress intensity factor at fracture tip and restrict fracture height. In addition, the pressure drop of fluid pressure in hydraulic fracture increases with the increase of thickness of artificial interlayer. These conclusions can explain the phenomenon of physical simulation experiment in Section 2.3.

3. Theoretical Model

For thick reservoirs with less stress difference between vertical layers, hydraulic fracture propagation is less constrained by this stress difference between vertical layers, and the excessive fracture height is generated. The hydraulic fracture with large height can connect reservoirs with the water layer and reduce the efficiency of hydraulic fracturing stimulation. In order to predict the fracture height, a theoretical model of stress intensity factor for hydraulic fracture with artificial interlay is established. This model includes main factors affecting stress intensity factor. According to theory of frac-

ture mechanics, when the stress intensity factor exceeds the fracture toughness, the fracture can propagate. After fracture propagates, more in situ stress is applied at this fracture, so the stress intensity factor decreases. If the new stress intensity factor still exceeds the fracture toughness, the hydraulic fracture can continue propagating. When the stress intensity factor equals to the fracture toughness, the hydraulic fracture can stop to propagate. Therefore, making stress intensity factor equal to fracture toughness can obtain the hydraulic fracture height.

3.1. Illustration of Hydraulic Fracture with Artificial Interlayer. In order to simplify the model and calculation, the theory of fracture mechanics for elasticity material is used in this paper. Although the plastic region exists around fracture tip and affects the solution of stress intensity, the plastic region size is less than the size of hydraulic fracture so the impact of plastic region on stress intensity factor on hydraulic fracture is ignorable. Therefore, the theory of fracture mechanics for elasticity material is widely used to predict the propagation behavior of hydraulic fracture. In order to build the theoretical model of stress intensity factor for hydraulic fracture with artificial interlayer, the following assumptions are used:

(1) The stress difference between thick reservoir and up/down interlayer are large enough so the hydraulic fracture only propagates within the thick reservoir. This assumption is consistent with geology features of thick reservoirs in Xinjiang oil field

(2) The rock is an ideal linear elastic material. The shape of the reservoir and hydraulic fracture is axisymmetric

(3) The permeability of reservoir is low, and the period of hydraulic fracturing is short, so the loss of fracturing fluid into reservoir is ignored

(4) The pressure drop gradient in hydraulic fracture is much lower than that in artificial interlayer, so the pressure drop in hydraulic fracture is ignored

The conceptual illustration of hydraulic fracture with artificial interlayer is shown in Figure 5. The thick reservoir is divided into two regions. The top region is the region where the oil resource is high, and the bottom region is the region where the oil resource is low. The fracture height can be divided into three parts. The top part is the fracture in top region of reservoir (h_r) and is the fracture beneficial to production. The bottom part is the fracture in bottom region of reservoir (h_b). The third part of fracture is the one filled by artificial interlayer (h_a). If there is no artificial interlayer, this hydraulic fracture can go through the whole reservoir. If the artificial interlayer exists, the hydraulic fracture stops at some position in bottom region of reservoir. The minimum horizontal stress values between top and bottom regions are also different and are represented by symbols σ_r and σ_b. The artificial interlayer is a porous medium. According to Darcy's law, the hydraulic fracturing fluid flows through this artificial interlayer can experience an additional pressure drop and the pressure gradient of pressure drop is represented by K_a.

3.2. Fracture Propagation Model considering Impact of Artificial Interlayer.
Based on the theory of linear elastic fracture mechanics, the stress intensity factor generated by the stress acting on the fracture surface at the upper and lower tips of the fracture is [19]

$$K_{It} = \frac{1}{\sqrt{\pi H}} \int_0^H p(y) \sqrt{\frac{H+y}{H-y}} dy, \tag{2}$$

$$K_{Ib} = -\frac{1}{\sqrt{\pi H}} \int_H^0 p(y) \sqrt{\frac{H-y}{H+y}} dy, \tag{3}$$

where K_{It} and K_{Ib} are the stress intensity factor at the top and bottom tips of the fracture; H is the height of fracture; and $p(y)$ is the net pressure inside hydraulic fracture.

According to the stress condition shown in Figure 5, the net pressure inside hydraulic fracture ($p(y)$) is

$$p(y) = \begin{cases} p_f - \sigma_r & 0 < y < h_r, \\ p_f - \sigma_b & h_r < y < H. \end{cases} \tag{4}$$

Substituting the above equation into Equation (2), the stress intensity factor at lower tip of fracture (K_{Ib}^1) is

$$K_{Ib}^1 = \frac{1}{\sqrt{\pi H}} \left(\int_0^{h_r} \left(p_f - \sigma_r\right) \sqrt{\frac{H+y}{H-y}} dy + \int_{h_r}^H \left(p_f - \sigma_b\right) \sqrt{\frac{H+y}{H-y}} dy \right). \tag{5}$$

The thickness of the artificial interlayer is $y = h_a$, and the pressure drop gradient of this interlayer is K_a. According to Darcy's law, the pressure drop is [20]
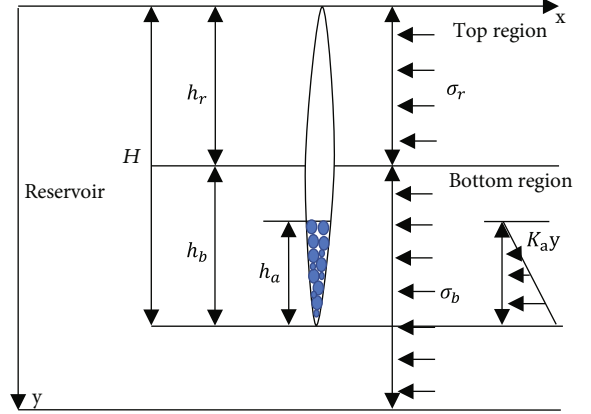
FIGURE 5: Stress distribution on fracture surface with artificial interlayer.

$$p(y) = K_a y. \tag{6}$$

Substituting the above equation into Equation (2), the stress intensity factor induced by pressure drop (K_{Ib}^2) is

$$K_{Ib}^2 = -\frac{1}{\sqrt{\pi H}} \int_0^{h_a} K_a y \sqrt{\frac{H+y}{H-y}} dy. \tag{7}$$

The stress intensity factor at lower fracture tip equals the sum of values of stress intensity factors shown in Equations (5) and (7):

$$K_{Ib} = \frac{1}{\sqrt{\pi H}} \left(\int_0^{h_r} \left(p_f - \sigma_r\right) \sqrt{\frac{H+y}{H-y}} dy \right.$$
$$\left. + \int_{h_r}^H \left(p_f - \sigma_b\right) \sqrt{\frac{H+y}{H-y}} dy - \int_{H-h_a}^H K_a y \sqrt{\frac{H+y}{H-y}} dy \right). \tag{8}$$

When the stress intensity factor at lower fracture tip equals to fracture toughness, the vertical propagation of hydraulic fracture will stop. This critical condition is

$$K_{Ib} = K_{Ic}. \tag{9}$$

By combining Equations (8) and (9), the model to solve hydraulic fracture height is

$$\frac{K_{Ic}}{\sqrt{\pi(h_b + h_r)(\sigma_b - \sigma_r)}} = \arcsin\left(\frac{h_r - h_b}{h_r + h_b}\right) + \frac{p_f - \sigma_b}{\sigma_b - \sigma_r}\left(\frac{\pi + 2}{2}\right)$$
$$+ \frac{K_a\left(\frac{h_a - 3(h_r + h_b)}{2}\sqrt{(h_b + h_r)^2 - (h_a - h_b + h_r)^2}\right)}{2\pi(h_b + h_r)(\sigma_b - \sigma_r)}$$
$$+ \frac{K_a(h_r + h_b)^2}{4\pi(h_b + h_r)(\sigma_b - \sigma_r)} \arcsin\frac{h_r}{h_r + h_b} - \frac{K_a}{4(h_b + h_r)(\sigma_b - \sigma_r)}. \tag{10}$$
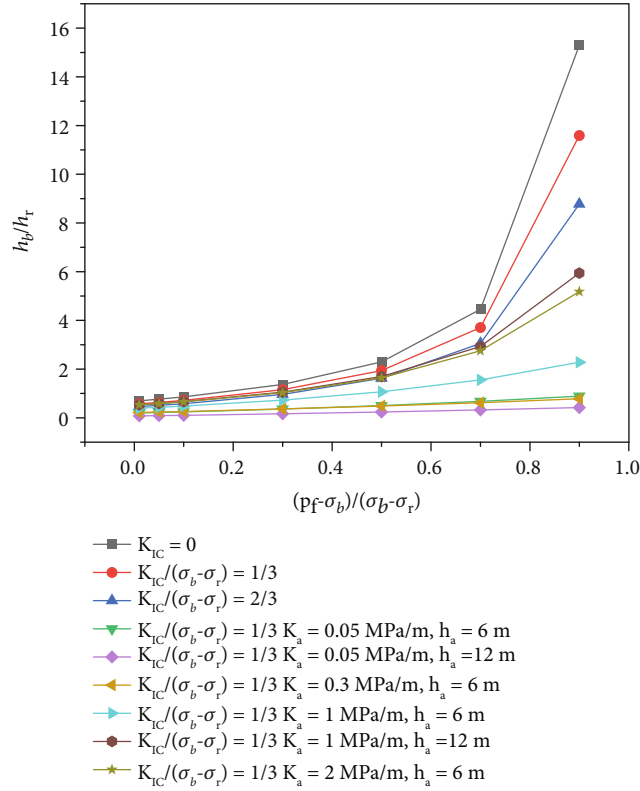
FIGURE 6: The ratio of the fracture height in the reservoir and the interlayer (h_b/h_r) under different conditions (hr equals to 10 m).

TABLE 5: Experimental results of physical model and solution results of theoretical model.

Sample no.	1-2	1-3	1-4	1-5
h_a (mm)	15	20	15	15
σ_b, σ_r (MPa)	5	5	5	5
K_a (MPa/m)	0.32	0.32	0.32	0.65
h_r (mm)	60	28	72	62
h_b (mm)	45	13	53	38
P_f (MPa)*	4	4	4	5
K_{Ic} (MPa $\sqrt{m}$)	1.8	1.75	1.9	1.15
Experimental results	0.80	0.69	0.78	0.69
Theoretical results	0.92	0.81	0.89	0.83
Error	15%	17%	14%	20%

*P_f is from fracture fluid injection pressure curve of physical model experiments.

In the above equation, h_r is the height of top region of reservoir; K_{IC} denotes fracture toughness of rocks; σ_r, σ_b are stress values within the reservoir layer and bottom layer, respectively; K_a and h_a are properties of artificial interlayer; and P_f is fracture pressure. If these parameters are known, the unknown h_b can be solved by this equation. Several sensitivity study results are shown in Figure 6. The ratio of h_b to h_r increases with P_f. In order to restrict hydraulic fracture height, the P_f cannot be too large. When the fracture pressure is large enough $((p_f - \sigma_b)/(\sigma_b - \sigma_r) > 0.6)$, the h_b starts
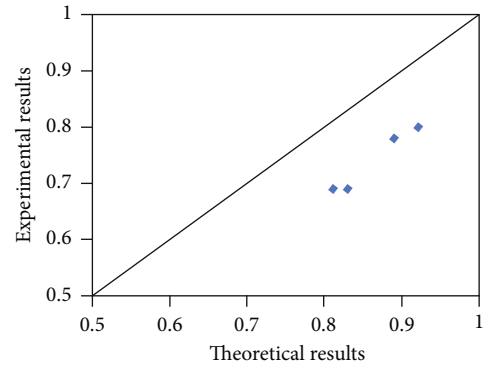
FIGURE 7: Comparison between theoretical solutions and experimental results.

to increase sharply. The increase of fracture toughness is beneficial to restrict the fracture height. The artificial interlayer can also significantly decrease fracture height because it induces more pressure drop inside fracture and makes fracture pressure at fracture tip decrease. The impact of pressure drop induced by artificial interlayer on decrease of fracture height is obviously higher than that of fracture toughness increase. When the fracture toughness becomes two times of its initial value, the ratio of h_b to h_r decreases from 15 (last point in red line with rhombus) to 10 (last point in blue line with circle). When the K_a is very few (only 0.05 MPa/m), the ratio of h_b to h_r decreases from 15 (last point in red line with rhombus) to 7 (last point in green line
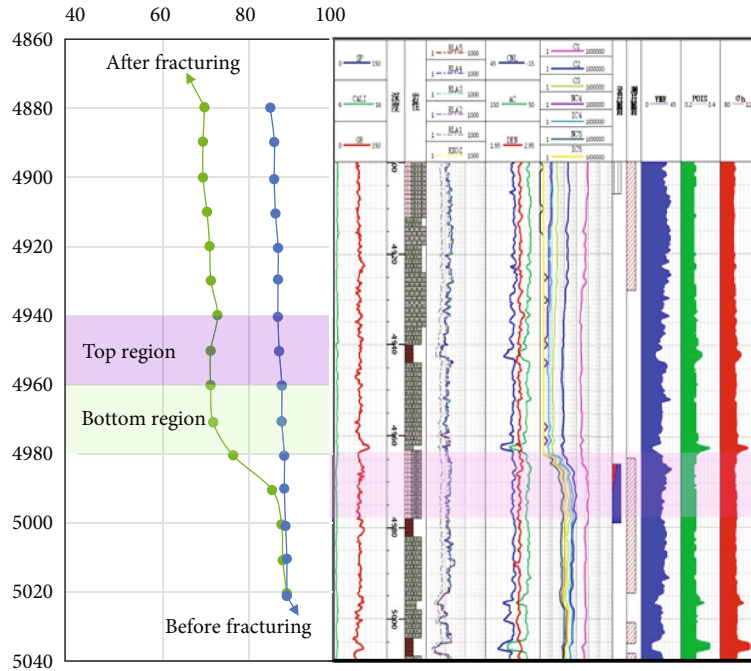
FIGURE 8: Well temperature monitoring curve of a well in Mahu before and after fracturing.

with cross). When K_a is over 1 MPa/m, the performance of artificial interlayer to restrict hydraulic fracture height is good enough. In this case, the ratio of h_b to h_r is less than 1.

4. Model Verification and Application

In order to validate the theoretical model proposed in Section 1, the conditions and parameters used in experiments completed in Section 2 are substituted into this theoretical model proposed in Section 3. The theoretical solutions are shown in Table 5. Since the artificial interlayer in experiment 1-1 does not restrict fracture propagation, the experimental results from experiments 1-2 to 1-5 are compared with the theoretical solution (shown in Figure 7). The maximum error between theoretical solution and the experimental data is less than 20%. Therefore, this theoretical model has a high accuracy.

Based on the above analysis, the theoretical model proposed in this study is accurate so it can be used to optimize the design of artificial interlayer. For a certain reservoir, the in situ stress values, the reservoir thickness, and fracture toughness are known by well-logging or experiments. The pressure drop gradient of artificial interlayer can be determined by permeability experiments and Darcy's law. Therefore, in this model, only three parameters are unknown, and they are fracture pressure (p_f), thickness of artificial interlayer (h_a) and fracture height in bottom reservoir (h_b). The fracture pressure (p_f) and thickness of artificial interlayer (h_b) can be variables. In this case, only h_b is unknown so it can be solved by the theoretical model. Figure 8 shows solutions of h_b/h_r for different cases. If engineers set a reasonable h_b/h_r, from these curves, the optimization parameters of artificial interlayer, such as h_a and K_a, can be determined.

Use the theoretical model derived in Section 3.2 to optimize the hydraulic fracture design for a well in the Mahu area in Xinjiang province. The reservoir thickness is 20 m, and the top 6 m is the target. The stress difference in vertical direction is only 2~3 MPa, and artificial interlayers are needed to control the bottom during hydraulic fracturing. Based on the theoretical model obtained in this paper, the design of the interlay height is 1 m, the pressure drop gradient is 1 MPa/m, and 40/70 mesh proppant is selected. The formation of the artificial interlay consumes a total of 4 m³ of sand-carrying liquid with a viscosity of 30 mPa·s and a sand ratio of 6%, 7%, 8%, and 9%. According to the design parameters, the construction displacement is 4-5 m³/min, the total guar gum fracturing fluid is 444 m³, and the total sand is 45 m³. From the well temperature monitoring curve, the lower fracture height is about 20 m, which has achieved the effect of height control by artificial interlayers (Figure 8).

5. Conclusion

In this paper, in order to illustrate the impact of artificial interlayer on fracture propagation, several physical simulation experiments are conducted and several factors affecting fracture height are shown. The mechanism of artificial interlayer restricting fracture height is discussed. Based on the theory of fracture mechanics and experimental observations, theory model for fracture height affected by artificial interlayer is proposed. The main findings are as follows:

(1) Experimental observations show that artificial interlayer can effectively restrict fracture height. The main factors include thickness of artificial interlayer, proppant size, and pumping rate

(2) The main mechanism of artificial interlayer restricting fracture height is that artificial interlayer can decrease fluid pressure inside fracture and then decrease stress intensity factor at fracture tip. In order to effectively restrict fracture height, the size of proppant generating artificial interlayer should be small enough and the artificial interlayer should be thick enough. The smaller proppant size and thicker artificial interlayer can induce more pressure drop

(3) The theoretical model proposed in this study is consistent with experimental data, and it can be used to optimize parameters of artificial interlayer, such as its thickness, proppant size, and fluid pressure inside fracture

Data Availability

All data, models, and code generated or used during the study appear in the submitted article.

Conflicts of Interest

The authors declare that they have no known competing financial interests or personal relationships that could have appeared to influence the work reported in this paper.

Acknowledgments

References

[1] M. I. Qiangbo, *Mechanism and Technology of Fracture Height Control in Low Stress Reservoir of Carbonate Rocks [Ph. D. Thesis]*, Chengdu University of Technology, Chongqing, 2017.

[2] H. Mukherjee, B. F. Paoli, T. McDonald, H. Cartaya, and J. A. Anderson, "Successful control of fracture height growth by placement of artificial barrier," *SPE Production & Facilities*, vol. 10, no. 2, pp. 89–95, 1995.

[3] D. M. Talbot, K. A. Hemke, and T. H. Leshchyshyn, "Stimulation fracture height control above water or depleted zones," in *SPE Rocky Mountain Regional/Low-Permeability Reservoirs Symposium and Exhibition*, Denver, Colorado, 2000.

[4] X. Lu, F. Liu, and Z. Han, "Manual control technology for vertical extension of fracturing fractures," *Oil Drilling & Production Technology*, vol. 1, pp. 82–89, 1995.

[5] G. U. O. Dali, J. I. Lujun, and Z. H. A. O. Jinzhou, "Research on three-dimensional simulation of coal seam crack extension and production forecast," *Applied Mathematics and Mechanics*, vol. 4, pp. 337–344, 2001.

[6] Y. Hu and S. Ren, "Analysis on the control of fracture height in hydraulic fracturing," *Petroleum Geology & Oilfield Development in Daqing*, vol. 2, pp. 55–58, 1996.

[7] X. Zhou, S. Zhang, X. Ma, and M. Liu, "Research on fracture height containment in thin and poor pay zones," *Journal of Shaanxi University of Science and Technology (Natural Science Edition)*, vol. 33, no. 4, pp. 94–99, 2015.

[8] W. Gu, Y. Pei, A. Zhao, T. Wang, J. Cai, and K. Wu, "Application of artificial barrier technology to fracture height control in fracturing wells," *Oil Drilling & Production Technology*, vol. 39, no. 5, pp. 646–651, 2017.

[9] X. Zhu, "Influential factors and propagation laws of hydraulic fracture height in the Hangjinqi block," *Oil Drilling & Production Technology*, vol. 42, no. 1, pp. 114–119, 2020.

[10] Z. Song, Z. Zhang, and J. Mao, "Study on the acid fracturing method for fracture height control based on micellar soft barrier suitable for the Tahe Oilfield," *Oil Drilling & Production Technology*, vol. 41, no. 3, pp. 382–386, 2019.

[11] R. D. Barree and H. Mukherjee, "Design guidelines for artificial barrier placement and their impact on fracture geometry," in *SPE Production Operations Symposium*, Oklahoma City, Oklahoma, 1995.

[12] M. Salah, M. A. Gabry, M. ElSebaee, and N. Mohamed, "Control of hydraulic fracture height growth above water zone by inducing artificial barrier in Western Desert, Egypt," in *Abu Dhabi International Petroleum Exhibition & Conference*, Abu Dhabi, UAE, 2016.

[13] P. Zhang, W. Zhao, and J. Wang, "Research and application of new down-diverting agent for fracturing treatment," *Fault-Block Oil Gas Field*, vol. 17, pp. 112–115, 2010.

[14] Z. H. Li, P. Sun, and B. Ma, "Fracture technology controlled by fracture length in bottom water reservoir with low permeability and its application for Ansaioilfield," *Petroleum Geology and Engineering*, vol. 24, pp. 82–84, 2010.

[15] G. Zhang, D. Zhou, J. Dou, Y. Nie, and H. Dong, "Experiments on hydraulic fracture propagation under actionof natural fractures and crustal stress difference," *Journal of China University of Petroleum (Edition of Natural Science)*, vol. 43, no. 5, pp. 157–162, 2019.

[16] G. D. Zhang, M. Z. Li, and M. Gutierrez, "Numerical simulation of proppant distribution in hydraulic fractures in horizontal wells," *Journal of Natural Gas Science and Engineering*, vol. 48, no. 157–168, pp. 157–168, 2017.

[17] C. N. Fredd, S. B. McConnell, and C. L. Boney, "Experimental study of fracture conductivity for water-fracturing and conventional fracturing applications," *SPE Journal*, vol. 6, no. 3, pp. 288–298, 2001.

[18] M. M. Mollanouri, S. F. Nia, and K. Jessen, "Dynamic conductivity of proppant-filled fractures," *Journal of Petroleum Science and Engineering*, vol. 151, pp. 183–193, 2017.

[19] L. P. Pook, *Linear Elastic Fracture Mechanics for Engineers: Theory and Applications, [M.S. Thesis]*, WIT press, 2000.

[20] L. Banks-Sills, "Application of the finite element method to linear elastic fracture mechanics," *Applied Mechanics Reviews*, vol. 44, no. 10, pp. 447–461, 1991.

WILEY | Hindawi

Research Article

Experimental Investigation on the Hydraulic Characteristics of the Two-Phase Flow in the Intersecting Rock Fractures

Chen Wang [ID],[1,2] Lujie Zhou [ID],[1,3] Yujing Jiang [ID],[2] Xuepeng Zhang [ID],[1,4]
and Jiankang Liu [ID][4]

[1]*State Key Laboratory of Mining Disaster Prevention and Control Co-Founded by Shandong Province and the Ministry of Science and Technology, Shandong University of Science and Technology, Qingdao 266590, China*
[2]*Graduate School of Engineering, Nagasaki University, Nagasaki 8528521, Japan*
[3]*College of Safety and Environmental Engineering, Shandong University of Science and Technology, Qingdao 266590, China*
[4]*College of Energy and Mining Engineering, Shandong University of Science and Technology, Qingdao 266590, China*

Correspondence should be addressed to Lujie Zhou; skd995954@sdust.edu.cn

An appropriate understanding of the hydraulic characteristics of the two-phase flow in the rock fracture network is important in many engineering applications. To investigate the two-phase flow in the fracture network, a study on the two-phase flow characteristics in the intersecting fractures is necessary. In order to describe the two-phase flow in the intersecting fractures quantitatively, in this study, a gas-water two-phase flow experiment was conducted in a smooth 3D model with intersecting fractures. The results in this specific 3D model show that the flow structures in the intersecting fractures were similar to those of the stratified wavy flow in pipes. The nonlinearity induced by inertial force and turbulence in the intersecting fractures cannot be neglected in the two-phase flow, and the Martinelli-Lockhart model is effective for the two-phase flow in intersecting fractures. Delhaye's model can be adapted for the cases in this experiment. The turbulence of the flow can be indicated by the values of C in Delhaye's model, but resetting the appropriate range of the values of C is necessary.

1. Introduction

In the subsurface space, multiple phases exist in the rock fracture network, such as geothermal energy reservoirs, natural gas-oil reservoirs, coal seams, and shale gas reservoirs [1–5]. The fluid-conducting capacity of the fracture network is the main concern in such engineering applications. Since the hydraulic properties of one phase of fluid in fractures will be totally different in the presence of another phase [6], a comprehensive understanding of the two-phase flow in fractures is necessary. Different from the single-phase flow, the two-phase flow in the fracture is influenced not only by the intrinsic properties of fractures, such as the fracture roughness and aperture, but also by the interactions between two phases [7–10]. The two-phase flow in a single fracture is the first step to understanding the flow characteristics in the fracture network [11–14]. The conventional approach to predict the two-phase flow in a single fracture is to extend Darcy's law for the single-phase flow to a generalized Darcy's equation for the two-phase flow [15–17], in which relative permeability is an important parameter. Relative permeability is defined as the ratio of the effective permeability of a certain phase in the two-phase flow to the permeability in the single-phase flow. It is the parameter to indicate the flow interference between two phases. With an exact model of relative permeability and permeability, the relationship between the pressure field and the velocity field in the two-phase flow can be established. The main concern of the researchers is how the relative permeability evolves, and different models are proposed to describe its evolution [7, 18–22].

In the subsurface, single fractures intersect with each other and constitute the fracture network. Besides the hydraulic characteristics of fluid in single fractures, insight into that of fracture intersections is also essential. Studies on the single-phase flow indicate that the fluid flow in the

intersecting fractures shows quite different characteristics from that in a single fracture due to the energy loss and interference induced by the fracture intersection [23, 24]. Wilson and Withspoon [25] studied the nonlinearity of fluid transport at the intersection of circular tubes with experiment, and their results indicate that the head loss induced by the intersection is about five times of the tube diameter when the Reynolds number is 100. Kosakowski and Berkowitz [26] numerically investigated the hydraulic properties of the intersecting fractures with Navier-Stokes equation, and their results indicate that when the Reynolds number is within 1 to 100, the inertial effect occurs and leads to a nonlinear flow. Su and Zhan [27] conducted water flow tests in crossed fractures and established the theoretical model for local loss of head at the intersection, and they proposed the correction factor for the theoretical model. All the abovementioned studies indicate that the hydraulic properties in the intersecting fractures have a nonlinearity and additional pressure drop and Darcy's law is generally not effective in such situations. However, the two-phase flow characteristics in the intersecting fractures are still not well understood. The generalized Darcy's equation is usually used to describe the two-phase flow, in which the relative permeability is the parameter to account for the flow interference between two phases, but the relative permeability does not account for the nonlinearity of the flow induced by the inertial effect or turbulence [10, 28], which cannot be neglected in the intersecting fractures.

With a developed system, an experiment is conducted to investigate the two-phase flow characteristics in a 3D fracture model with smooth intersecting fractures. The transparency of the 3D fracture model makes it possible to capture the flow structures. The pressure drop characteristics are analyzed with the Lockhart-Martinelli model and Delhaye's model, which is initially proposed for the two-phase flow in pipes. This study presents a basis for further studies to understand the two-phase flow properties in the rock fracture network and the mechanism of groundwater inflow in engineering applications.

2. Experiment in the Intersecting Fractures

2.1. Experiment System. The experimental system is shown in Figure 1, which is composed of four subsystems, as introduced in the following:

(1) The water supply subsystem. In this subsystem, the peristaltic pump is used for injecting water at a specified flow rate within 0–2000 mL/min. Since the pressure and flow rate of the injected water is always fluctuating, a pulse damper is connected to the pump to decrease the pulse in order to uniformly inject water into the 3D fracture model

(2) The gas supply subsystem. In this subsystem, nitrogen is supplied from a gas cylinder. The gas pressure in the cylinder is as large as 10 MPa, so a pressure regulator is connected to the cylinder to decrease the gas pressure to be under 0.3 MPa in order to protect the mass flow controller. The mass flow controller can control the gas flow rate to be a constant value within 0–5000 mL/min

(3) The 3D fracture model. This model is made of acrylic material and transparent, as shown in Figure 2. The schematic of the model from a vertical view (indicated by the blue arrow in Figure 2) is shown in Figure 3. The model has five smooth fractures: the apertures of fractures 1–5 are 0.6 mm, 0.3 mm, 0.3 mm, 0.6 mm, and 1 mm, respectively. The length of fracture 5 is 10 cm and the length of other four fractures is 5.78 cm. The model has two inlets connected to fracture 1 and fracture 2 and two outlets connected to fracture 3 and fracture 4. By opening or closing different inlets and outlets, different combinations of fractures can be established. In this experiment, two cases are adopted for testing, as shown in Figure 3, in which the red lines indicate the activated fractures, meaning that the flow of fluids only happens in these fractures, while the black lines indicate the fractures where inlets or outlets are closed, meaning that no flow occurs. The red arrow in Figure 2 shows the direction from which the photos were taken. The presented configuration of fractures in this 3D fracture model is a simplified configuration of the real ones. In real cases, the fractures are with roughness and may be continuous after the intersection. These multiple factors influence the two-phase flow in complicated ways. In order to avoid the effect of multiple factors and quantitatively study the effect of intersecting fractures, this simplified model is used for experiment

(4) The measurement subsystem. This subsystem includes a camera, three pressure sensors, a separation bottle, an electronic balance, and a flowmeter. The flow structures are captured by the camera. One pressure sensor is connected to the gas inlet, one is connected to the water inlet, and one is connected to the outlet. Pressure data are recorded by a digital recorder (not shown in Figure 1). The separation bottle, which is put on the electronic balance, is used to separate water and gas. Gas flows out of the separation bottle and water remains in the bottle. The water mass is recorded by the electronic balance in real time, and the data are transmitted to the computer simultaneously to calculate the flow rate of water

It should be noted that the water flow rate can be indicated in the peristaltic water pump, but without enough accuracy. That is why we set up an electronic balance to measure the water flow rate. The gas flow rate can be indicated by both the mass flow controller and the flowmeter. It shows that the gas flow rate indicated by the mass flow controller is identical to that of the flowmeter. Since the gas flow rate displayed by the mass flow controller is accurate enough, the flowmeter can be removed.
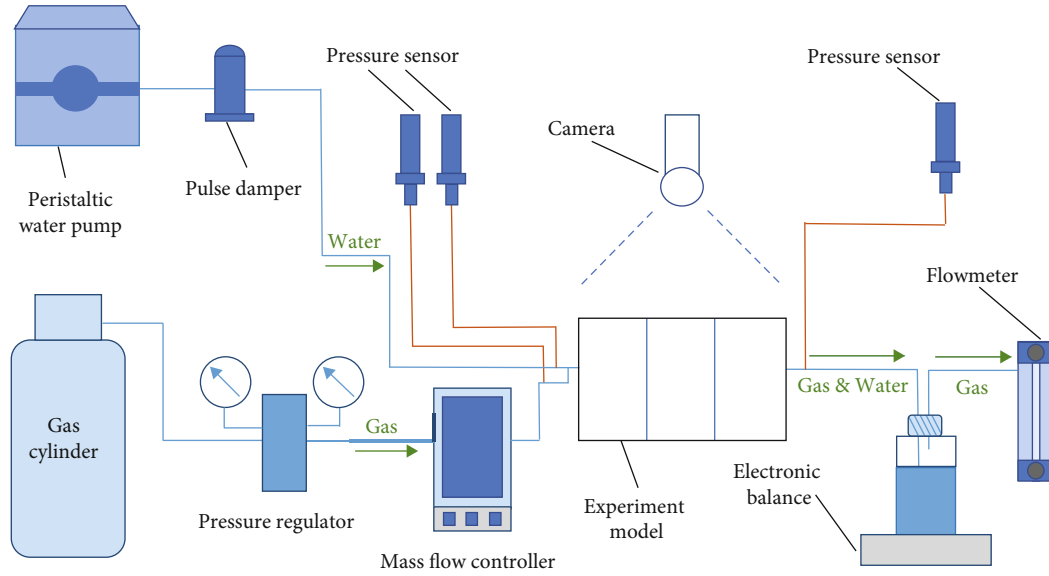
FIGURE 1: Schematic of the experimental system.
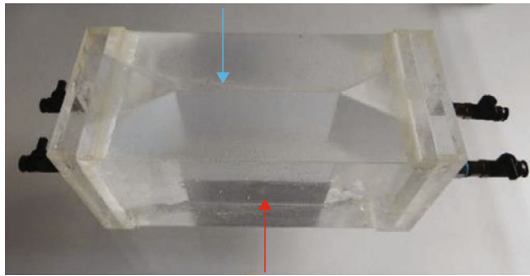
FIGURE 2: The 3D fracture model [23].

2.2. Experiment Procedures. As mentioned above, this experiment was conducted with two cases. In each case, the tests were conducted in the following procedures:

(1) Connect all the units in the experiment system and adjust the levelness of the 3D fracture model with a level gauge

(2) Conduct the preliminary test to check the tightness of the system and the accuracy of the measurement subsystem. The flowmeter connected to the separation bottle is used to check the accuracy of the gas flow rate displayed by the mass flow controller, and the electronic balance is used to check the accuracy of the water flow rate displayed by the peristaltic pump. The test results show that the accuracy of the peristaltic pump is not good, but the gas flow rate indicated by the flowmeter is identical to that displayed by the mass flow controller. However, we found that the flowmeter brought a large resistance to the flow of fluids. Since this would increase burden to the pump, the flowmeter was removed in the formal experiment in steps (3) and (4)

(3) Conduct a single-phase flow test of water to obtain the single-phase hydraulic properties of the 3D

model. Water was injected at different flow rates within 0–600 mL/min

(4) Conduct the two-phase flow test. In each case, five groups of two-phase flow tests were conducted. In each group, the water flow rate was kept constant while the gas flow rate was increased step by step. In each test, when the injection of water and gas started, wait for five minutes for the flow to reach a stable state. Then, the pressure and the water mass in the separation bottle were recorded with the pressure sensors and electronic balance. At the same time, the flow structures were captured by the camera. Since the pressure and the flow rates were always fluctuating, in each test, the data recording lasted one minute in order to obtain the average values; ten photos were taken to acquire the flow structures and average saturation in each test round

3. Model for Describing the Two-Phase Flow in Intersecting Fractures

As is known, in the single-phase flow, Darcy's law is not effective if the flow nonlinearity exists. This nonlinearity is caused by the inertial effect or turbulence, which can be induced by the fracture roughness or fracture intersection [23]. Consequently, revised laws such as Forchheimer's law are proposed to account for the nonlinearity [29–31]. Forchheimer's law can be described as equation (1):

$$\Delta P = aQ + bQ^2, \tag{1}$$

in which a is the parameter related to the aperture of the fracture and b is a parameter that indicates the nonlinearity of the flow. The equation is found to be applicable to the flow in porous media [32, 33] and in rough fractures [34, 35]. It has been demonstrated by literature [23] that
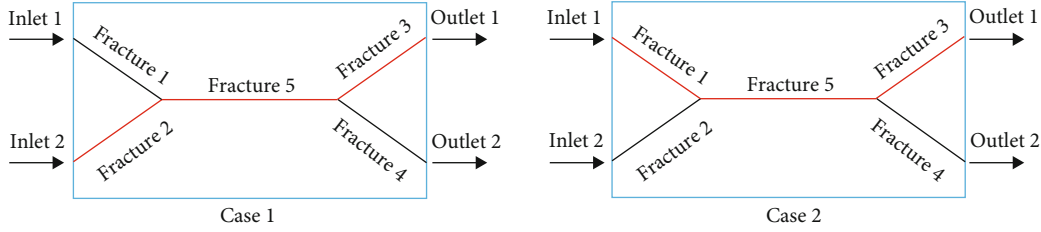
Figure 3: Schematic of the 3D fracture model (vertical view).

the single-phase flow in this 3D model used in our experiment is nonlinear and can be described by Forchheimer's law.

As for the two-phase flow, the Lockhart-Martinelli model considers the flow nonlinearity. This model is originally established to describe the two-phase flow in pipes [36]. It introduced two important parameters: the multiplier of water phase Φ_w and the multiplier of gas phase Φ_g, in order to assess the flow resistivity induced by two-phase interactions. They are defined as equations (2) and (3), respectively:

$$\Phi_w = \frac{dP/dx}{(dP/dx)_w}, \tag{2}$$

$$\Phi_g = \frac{dP/dx}{(dP/dx)_g}, \tag{3}$$

$$\chi = \frac{(dP/dx)_w}{(dP/dx)_g}, \tag{4}$$

in which dP/dx refers to the two-phase pressure gradient of both fluids, $(dP/dx)_w$ refers to the pressure gradient in the virtual single-phase flow of water with a same flow rate as the water flow rate in the two-phase flow, and $(dP/dx)_g$ refers to that of gas. The Martinelli parameter χ is used to analyze the evolution of the phase multipliers. It is defined as equation (4), which represents the fractions of two fluids, namely, the relative importance of the flow of water to gas. If χ is 0, it indicates the single-phase flow of gas; when χ increases, it means the increase of the fraction of water and the decrease of the fraction of gas; when χ approaches infinity, it means that the fraction of gas approaches 0 and the two-phase flow approaches the single-phase flow of water. It should be noted that Φ_w and Φ_g are originally defined as the square root of the ratio between the two-phase pressure gradient and the single-phase one. For the convenience of comparison with the definition of relative permeability, Fourar and Bories [37] redefined them as equations (2) and (3). In this paper, we followed this revised definition by Fourar and Bories.

It should be noted that the stratified flow has formed due to the difference of density between gas and water, meaning that gas and water flowed in separate layers. In this situation, the capillary pressure does not contribute to the total pressure drop, so the gas pressure drop and the water pressure
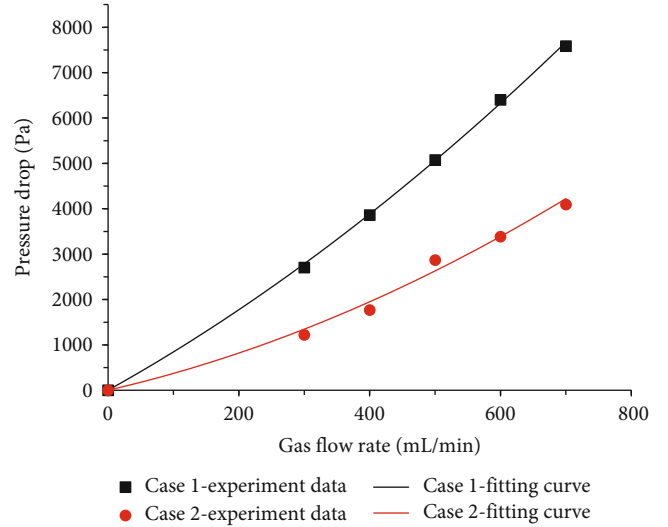
Figure 4: Test results of the single-phase flow.

drop in the two-phase flow are assumed to be equal to each other.

As shown in Figure 1, two pressure sensors are connected to the water injection tube and gas injection tube. The water injection tube and gas injection tube are both connected to the inlet (the black parts of the 3D model). Theoretically, they should be identical but there are small differences between the gas pressure and the water pressure at the inlet. This may be induced by the compressibility of gas, which led to severe fluctuation of the pressure. The adopted inlet pressure for calculation is the average of the inlet pressure of water and that of gas. Both water and gas flows out from the same outlet, and one pressure sensor is connected to the outlet and its average value is adopted as the pressure of water and gas at the outlet. The two-phase pressure drop dP is calculated as the difference between the pressure at the inlet and the pressure at the outlet.

With the Lockhart-Martinelli model, the two-phase pressure field can be calculated by the following steps in engineering applications (assuming that in a two-phase flow case, the flow rate of gas Q_g and the flow rate of water Q_w are given):

(1) Based on Forchheimer's law, the corresponding pressure gradient in the virtual single-phase flow of gas (which has the same flow rate as the gas flow rate in the two-phase flow) can be calculated as $\Delta P_g = a Q_g + bQ_g{}^2$, $(dP/dx)_g = \Delta P_g/\Delta x$
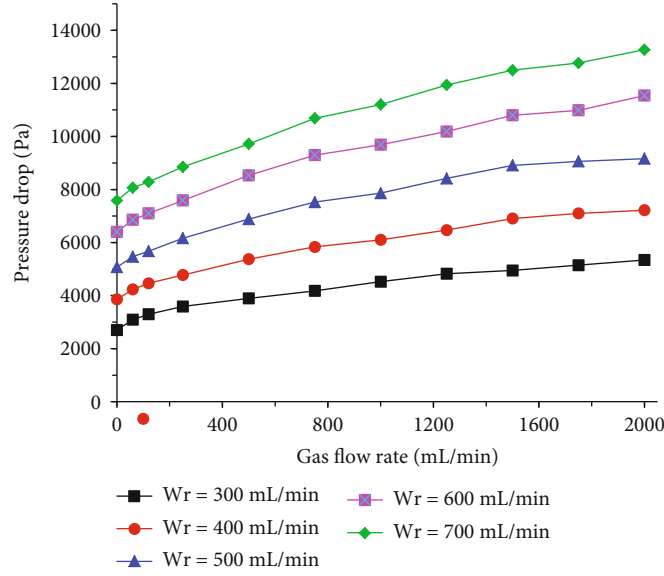
FIGURE 5: Evolution of the two-phase pressure drop with respect to the water flow rate and gas flow rate in case 1.

(2) With the same method, the corresponding pressure gradient in the virtual single-phase flow of water (which has the same flow rate as the water flow rate in the two-phase flow) can be calculated: $\Delta P_w = a Q_w + b Q_w^2$, $(dP/dx)_w = \Delta P_w / \Delta x$

(3) The Martinelli parameter is calculated as $\chi = (dP/dx)_w / (dP/dx)_g$

(4) With an appropriate model which describes the relationship between Φ_w, Φ_g, and χ (such as Delhaye's model), Φ_w and Φ_g can be calculated

(5) With the Lockhart-Martinelli model (equations (2) and (3)), the two-phase pressure gradient dP/dx can be calculated as $(dP/dx) = \Phi_w \cdot (dP/dx)_w$ or $(dP/dx) = \Phi_g \cdot (dP/dx)_g$

The Lockhart-Martinelli model evaluates the two-phase flow by tracing the evolution of Φ_w and Φ_g with respect to χ. Since at the same flow rate, the pressure drop of each phase in the two-phase flow is always larger than that in the single-phase flow; these two parameters represent the extra resistivity induced by the two-phase interference. Actually, the Martinelli-Lockhart model is similar to the generalized Darcy's law, because $1/\Phi_w$ is similar to k_{rw} (the relative permeability of water in generalized Darcy's law): $1/\Phi_w$ can be expressed as $(dP/dx)_w/(dP/dx) = [(dP/dx)_w/Q_w]/[(dP/dx)/Q_w] = $ (the two − phase conductivity of water)/ (the single − phase conductivity of water), while k_{rw} is defined as the ratio of effect permeability of water in the two-phase flow and the permeability in the single-phase flow. The difference lies in that the relative permeability does not consider the nonlinearity of flow but the Martinelli-Lockhart model does (the pressure gradients of the single-phase flow $(dP/dx)_w$ and $(dP/dx)_g$ are calculated by Forchheimer's law). Consequently, the Lockhart-Martinelli model can be

seen as a generalization of the two-phase Darcy's law in order to make it fit the non-Darcy two-phase flow [37].

The Lockhart-Martinelli model and Delhaye's model are initially proposed for describing the two-phase flow in pipes. Since these two models consider the flow nonlinearity, they have the potential to be effective for describing the two-phase flow in intersecting fractures. In this study, it is investigated whether the experiment data of the two-phase flow in the intersecting fractures can fit these models by the following steps:

(1) In the single-phase flow test of water, the pressure drop and flow rate are measured. The parameters a and b in Forchheimer's law are calculated

(2) In the two-phase flow test, the pressure drop ΔP and the flow rates of both phases Q_w and Q_g are measured. It is investigated whether the data are in accordance with Delhaye's model by the following steps:

(a) The corresponding pressure gradient in the virtual single-phase flow of gas (which has the same flow rate as the gas flow rate in the two-phase flow) can be expressed as $(dP/dx)_g = \Delta P_g / \Delta x = (aQ_g + bQ_g^2)/\Delta x$. Here, Δx is the total length of the fractures (in each case, $\Delta x = 5.78 + 10 + 5.78 = 20.78$ cm)

(b) The corresponding pressure gradient in the virtual single-phase flow of water (which has the same flow rate as the water flow rate in the two-phase flow) can be calculated as $(dP/dx)_w = \Delta P_w / \Delta x = (aQ_w + bQ_w^2)/\Delta x$

(c) The Martinelli parameter is calculated as $\chi = (dP/dx)_w/(dP/dx)_g = [\Delta P_w/\Delta x]/[\Delta P_g/\Delta x] = \Delta P_w /\Delta P_g$
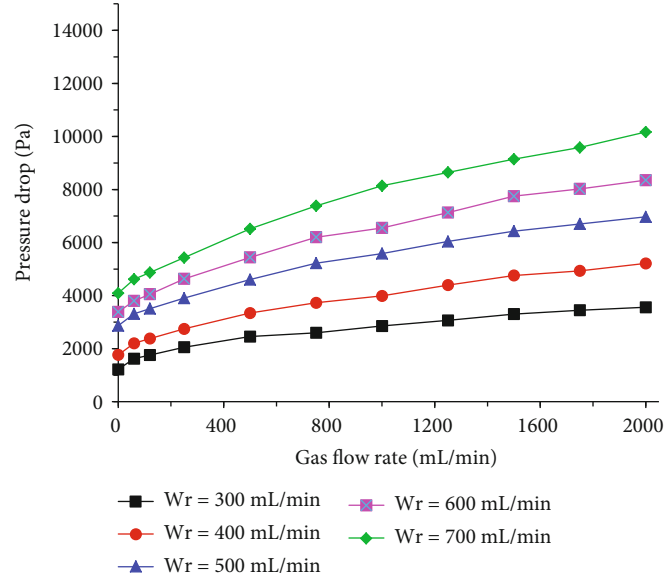
FIGURE 6: Evolution of the two-phase pressure drop with respect to the water flow rate and gas flow rate in case 2.
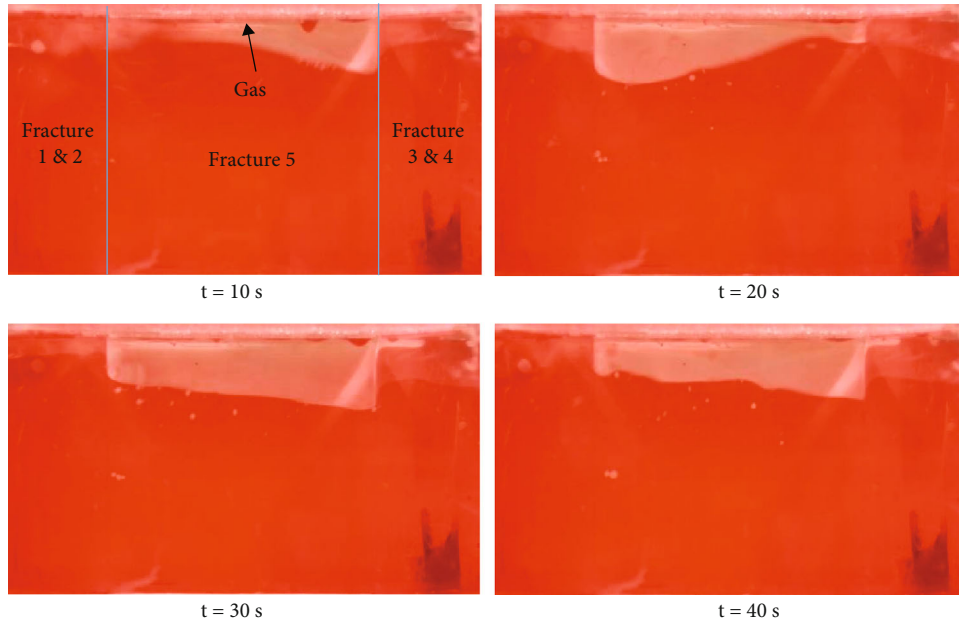
FIGURE 7: The flow structures at $W_r = 600$ mL/min and $G_r = 1500$ mL/min in case 1.

(d) The multiplier of the gas phase is calculated as $\Phi_g = (dP/dx)/(dP/dx)_g = [\Delta P/\Delta x]/[\Delta P_g/\Delta x] = \Delta P/\Delta P_g$

(e) The multiplier of the water phase is calculated as $\Phi_w = (dP/dx)/(dP/dx)_w = [\Delta P/\Delta x]/[\Delta P_w/\Delta x] = \Delta P/\Delta P_w$

It should be noticed that in the single-phase flow mentioned in step (1), the pressure drop and flow rate are the measured data in order to calculate the parameters of Forchheimer's law (a and b). The single-phase flow of water or gas mentioned in step (2)-(a) and step (2)-(b) is the vir-

tual single-phase flows defined by the Lockhart-Martinelli model.

If the calculated Φ_w, Φ_g, and χ prove to be in accordance with Delhaye's model, the pressure field of the two-phase flow in intersecting fractures can be calculated with the five steps mentioned above in engineering applications.

4. Hydraulic Characteristics of the Two-Phase Flow in the Intersecting Fractures

4.1. Results of the Single-Phase Flow Test. In the single-phase flow test of water, the relationship between the flow rate Q

Original photo   Binarized photo   Original photo   Binarized photo

(a) t = 5 s, S_w = 0.903   (b) t = 10 s, S_w = 0.894

(c) t = 15 s, S_w = 0.899   (d) t = 20 s, S_w = 0.897

(e) t = 25 s, S_w = 0.899   (f) t = 30 s, S_w = 0.894

(g) t = 35 s, S_w = 0.868   (h) t = 40 s, S_w = 0.881

(i) t = 45 s, S_w = 0.815   (j) t = 50 s, S_w = 0.903
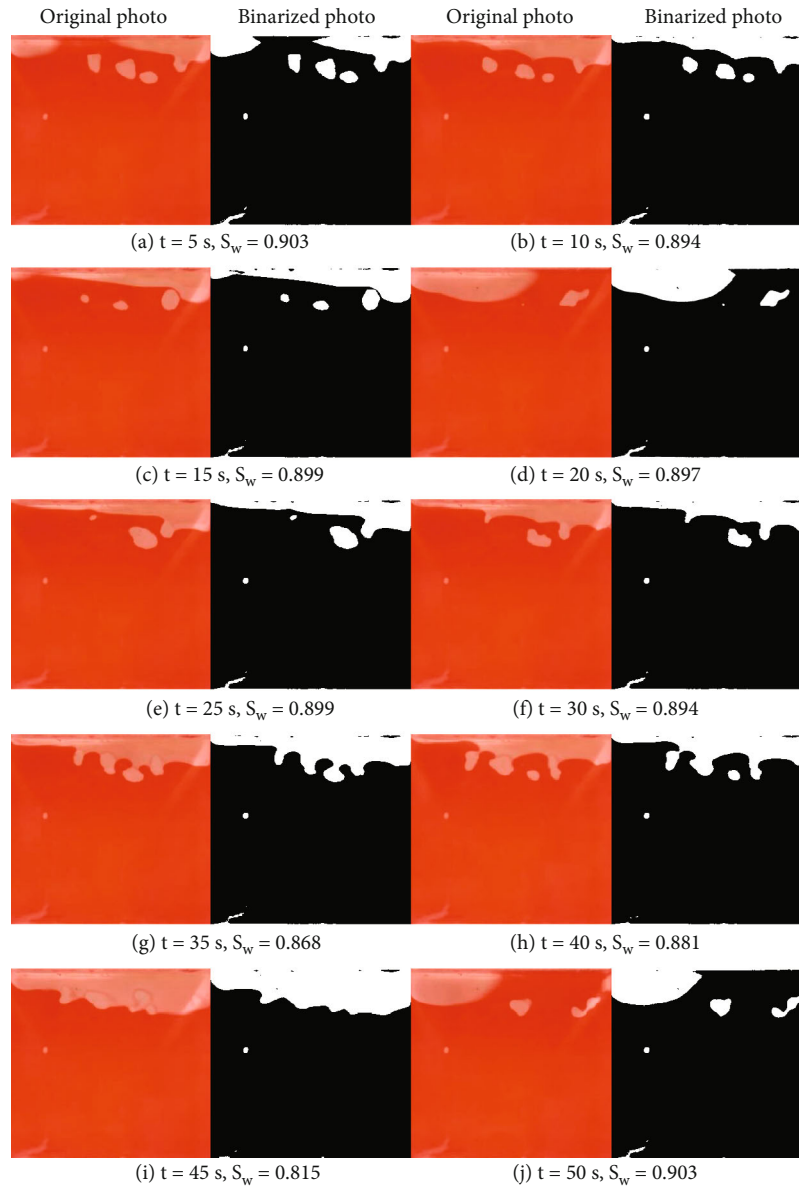
FIGURE 8: Saturations in fracture 5 at different moments when W_r = 500 mL/min and G_r = 500 mL/min in case 1.

and pressure drop ΔP is shown in Figure 4. Here the pressure drop ΔP is the pressure difference between the inlet and outlet. The results show that the pressure drop increases nonlinearly with respect to the flow rate, which is in accordance with the Forchheimer's law, which means that the flow nonlinearity cannot be neglected. Based on the results of single-phase flow test, the two-phase flow hydraulic characteristics can be calculated, as introduced in the next section.

4.2. Hydraulic Characteristics of the Two-Phase Flow in the Intersecting Fractures

4.2.1. The Pressure Drop Characteristics and Evolution of Flow Structures. Figures 5 and 6 show the evolution of the two-phase pressure drop with respect to the gas flow rate of case 1 and case 2, respectively. Each curve represents

the tests with a constant water flow rate. The pressure drop refers to the pressure difference between the inlet and outlet. Case 1 is composed of fractures 2, 5, and 3, with an aperture of 0.3 mm-1 mm-0.3 mm; case 2 is composed of fractures 1, 5, and 3, with an aperture of 0.6 mm-1 mm-0.3 mm. Case 1 has a smaller hydraulic aperture, and consequently, the pressure drop of case 1 is larger than that of case 2.

In the two-phase flow in pipes, there are usually sharp variations in the $P - Q$ (pressure drop-flow rate) curves if the flow structure changes. In our test, no sharp variations are observed in Figures 5 and 6. The reason can be sought from the flow structures. In our tests, the fractures in the 3D model were vertical to the horizontal plane, so gas and water flowed in separate layers and gas flowed above the water due to gravity, consequently forming a stratified flow. In the stratified flow, there is not an obvious transfer of flow

Original photo   Binarized photo   Original photo   Binarized photo

(a) t = 5 s, S$_w$ = 0.785   (b) t = 10 s, S$_w$ = 0.848

(c) t = 15 s, S$_w$ = 0.873   (d) t = 20 s, S$_w$ = 0.724

(e) t = 25 s, S$_w$ = 0.834   (f) t = 30 s, S$_w$ = 0.754

(g) t = 35 s, S$_w$ = 0.743   (h) t = 40 s, S$_w$ = 0.876

(i) t = 45 s, S$_w$ = 0.726   (j) t = 50 s, S$_w$ = 0.788
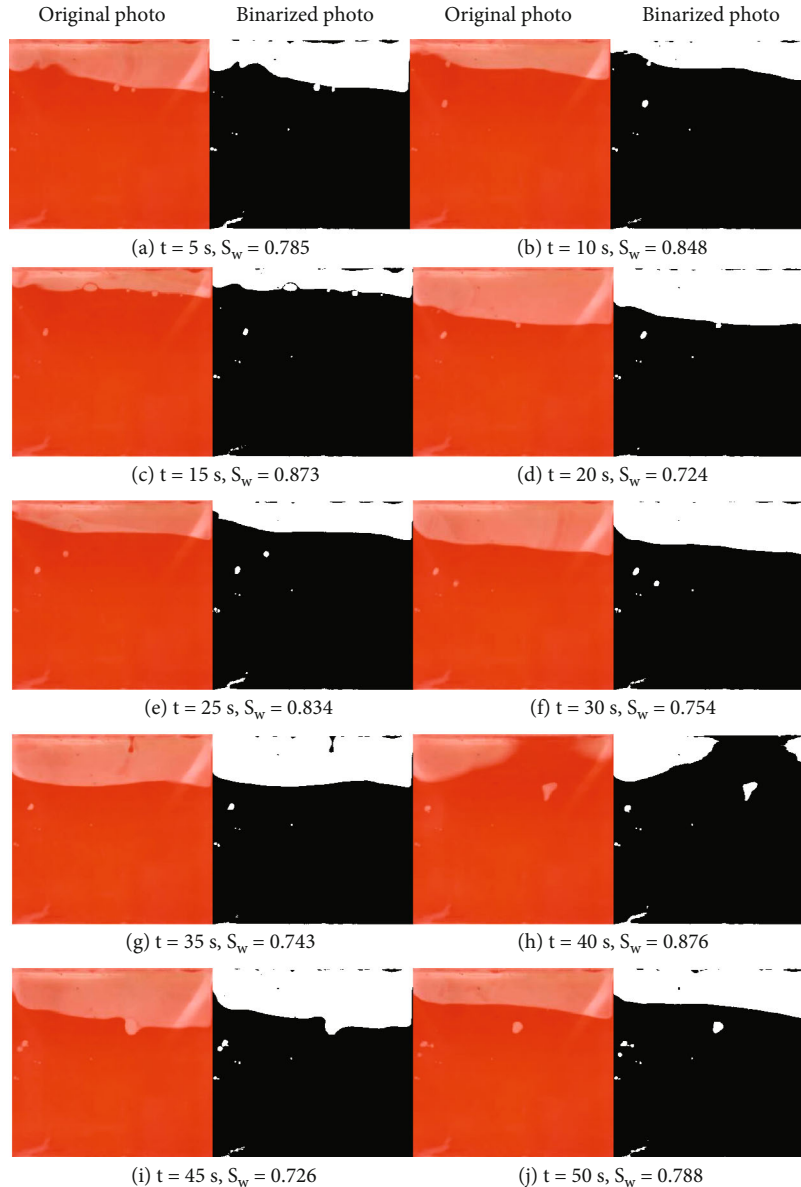
Figure 9: Saturations in fracture 5 at different moments when $Wr = 500$ mL/min and $Gr = 1000$ mL/min in case 1.

structures from the bubble flow to the continuous flow, so there are no sharp variations in the $P - Q$ curves.

As is indicated earlier, the single-phase flow in this 3D model used in our experiment is nonlinear and can be described by Forchheimer's law. As for the two-phase flow, the generalized Darcy's law does not account for the nonlinearity, either. Due to the existence of the fracture intersections in this 3D fracture model, which will contribute to flow nonlinearity, the generalized Darcy's law is not expected to fit the pressure drop data very well. However, we still analyzed the flow structures and measured the saturation as a reference.

Figure 7 shows the flow structures of case 1 at $W_r =$ 600 mL/min (water flow rate) and $G_r = 1500$ mL/min (gas flow rate). The photos were taken from the lateral direction, as indicated by the red arrow in Figure 2. In the photos, the

dark color represents water and the light color represents gas. It shows that the saturation of gas was fluctuating with respect to time, which is similar to the stratified wavy flow in pipes. Since fractures 1–4 were not vertical to the camera, to avoid refraction in taking photos, only the flow structures in fracture 5 are analyzed and the saturations are calculated.

The photos of fracture 5 are extracted from the original photos, as shown in Figures 8 and 9. Figure 8 shows the flow structures at $W_r = 500$ mL/min and $G_r = 500$ mL/min in case 1, while Figure 9 shows the flow structures at $W_r = 500$ mL /min and $G_r = 1000$ mL/min in case 1. The red pictures are the original photos taken by the camera, and the black-white pictures were converted from the original photos by binarization in order to calculate the water saturation S_w. It shows that the saturation was fluctuating with respect to time, though the flow rates of water and gas were kept
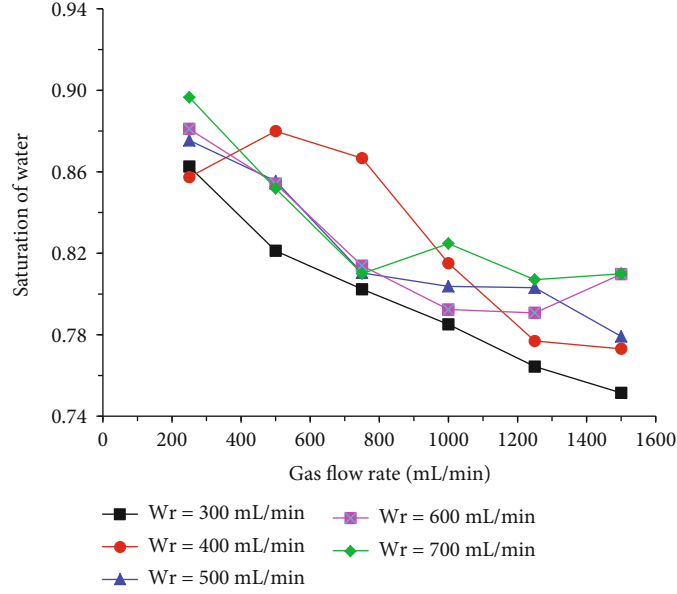
FIGURE 10: The evolution of water saturation.

constant. When the gas flow rate increased from 500 mL/min to 1000 mL/min, there was not an obvious variation in the flow structures.

Figure 10 shows the evolution of water saturation in case 2. Each saturation value is the average of ten pictures. It shows that the water saturation tends to decrease with respect to the gas flow rate but some exceptions exist, for example, in the curve of $W_r = 400$ mL/min, when G_r increases from 250 mL/min to 500 mL/min, the saturation increases. In addition, the variation of water saturation is not obvious. When W_r is 700 mL/min, G_r increases from 250 mL/min to 1500 mL/min, the water saturation decreased only by 10%. Besides, the curves at different water flow rates may intersect with each other. This also indicates that the generalized Darcy's law may not work well in describing the two-phase flow pressure drop in the intersecting fractures since the saturation cannot indicate the fractions of the two fluids very well.

4.2.2. Interpretation Model. Since the nonlinearity of the flow is confirmed in Figure 4, the Lockhart-Martinelli model is adopted to analyze the hydraulic characteristics of the two-phase flow in this experiment. The evolution of $1/\Phi_w$ and $1/\Phi_g$ in the two cases is shown in Figures 11 and 12. $\chi(1 + \chi)$ is selected as the x-axis instead of χ for convenience, since in this way, the x-axis varies from 0 to unity. As shown in Figures 11 and 12, the sum of $1/\Phi_w$ and $1/\Phi_g$ are less than 1, indicating a quite significant interference between two phases. When $\chi/(1 + \chi)$ approaches 1, it means that χ approaches infinity and the fraction of gas approaches 0, meaning that the two-phase flow approaches the single-phase flow of water. Consequently, in this condition, $1/\Phi_w$ approaches 1 and $1/\Phi_g$ approaches 0. All the experiment data approximately fall on the same curve, indicating that

$1/\Phi_w$ and $1/\Phi_g$ are independent of the flow rates to some extent, but dependent on χ.

It should be noted that in Figures 11 and 12, $1/\Phi_g$ seems to be decreasing linearly and $1/\Phi_w$ is increasing nonlinearly. This is induced by the physical property difference between two phases. $1/\Phi_w$ and $1/\Phi_g$ are defined as $(dP/dx)_w/(dP/dx)$ and $(dP/dx)_g/(dP/dx)$, respectively, in which the two-phase pressure gradients (dP/dx) are the same for either gas or water, but the single-phase pressure gradient of $(dP/dx)_g$ is much less than that of $(dP/dx)_w$ due to the difference of density. Therefore, the value range of $1/\Phi_g$ is also very small (within 0–0.1) and the nonlinearity cannot be well indicated in Figures 11 and 12. In Figures 13 and 14, the nonlinearity of both $1/\Phi_w$ and $1/\Phi_g$ can be well indicated.

As mentioned in the previous section, in order to predict the pressure field of the two-phase flow, an appropriate model between Φ_w, Φ_g, and χ is necessary. Delhaye et al. [38] proposed an empirical relationship, as shown in equations (5) and (6):

$$\Phi_w = 1 + \frac{C}{\sqrt{\chi}} + \frac{1}{\chi}, \tag{5}$$

$$\Phi_g = 1 + C\sqrt{\chi} + \chi, \tag{6}$$

in which C is a parameter that indicates the flow regime of each phase. When C is 5, both water and gas flow are laminar; when C is 10, water is turbulent and gas is laminar; when C is 12, liquid is laminar and gas is turbulent; when C is 20, both water and gas flow are turbulent. However, this method is initially proposed for describing the two-phase flow in pipes. Fourar and Bories [37] used this method to
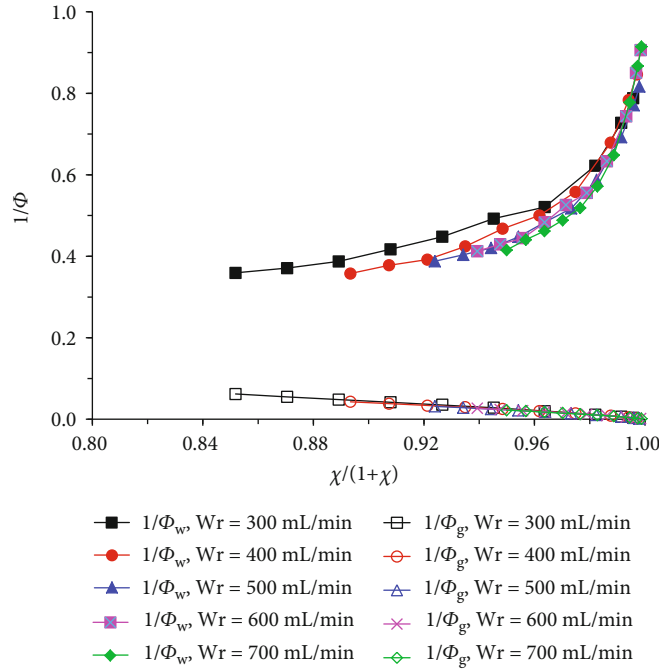
FIGURE 11: The relationship between Φ_w, Φ_g, and $\chi(1 + \chi)$ in case 1.
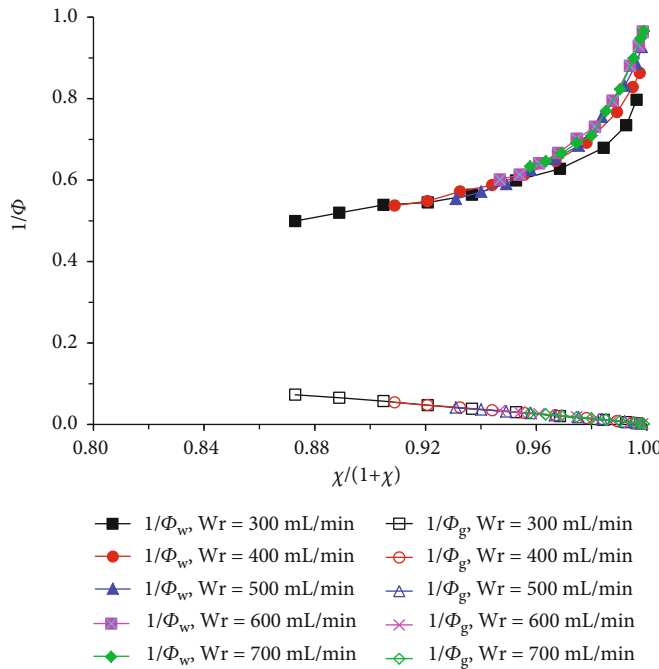
FIGURE 12: The relationship between Φ_w, Φ_g, and $\chi(1 + \chi)$ in case 2.

fit two-phase flow data in single fractures, and they found that this model can work well for approximate calculations. Since the two-phase flow in intersecting fractures has similarity to that in the rough single fracture in the aspect that the flow has nonlinearity induced by the inertial force, it is believed that this model may be also effective for the intersecting fractures. Therefore, the experiment data are fit with these two equations.

Figures 13 and 14 show the evolution of Φ_w and Φ_g with respect to Sqrt (χ) in case 1 and the corresponding fitting values of C. The curves of equations (5) and (6) are also plotted for reference. The five experiment curves approximately fall on the same curve, and they are close to $C = 5$, namely, the water laminar-gas laminar flow state. The flow rate has some weak impact on the values of C. To be accurate, when the water flow rates are 300 mL/min, 400 mL/min, 500 mL/
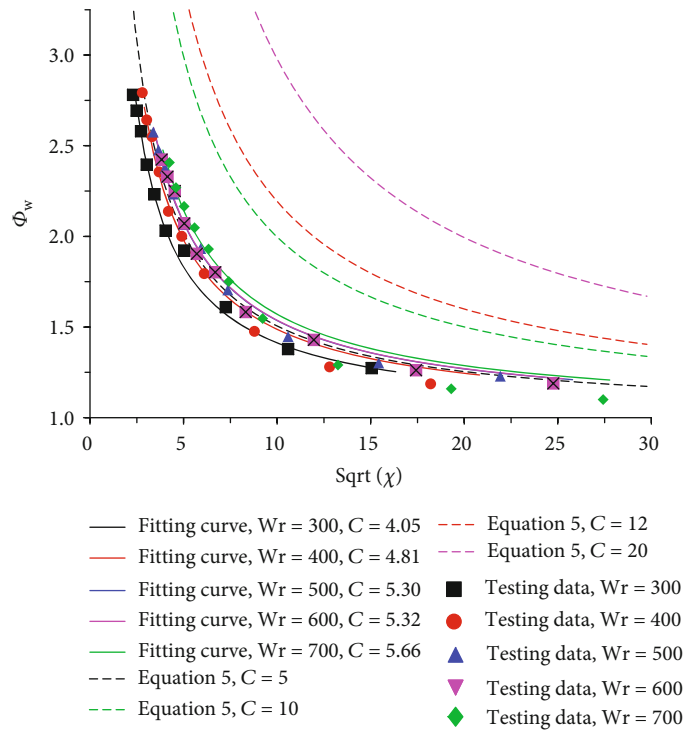
FIGURE 13: The relationship between Φ_w and Sqrt (χ) in case 1.
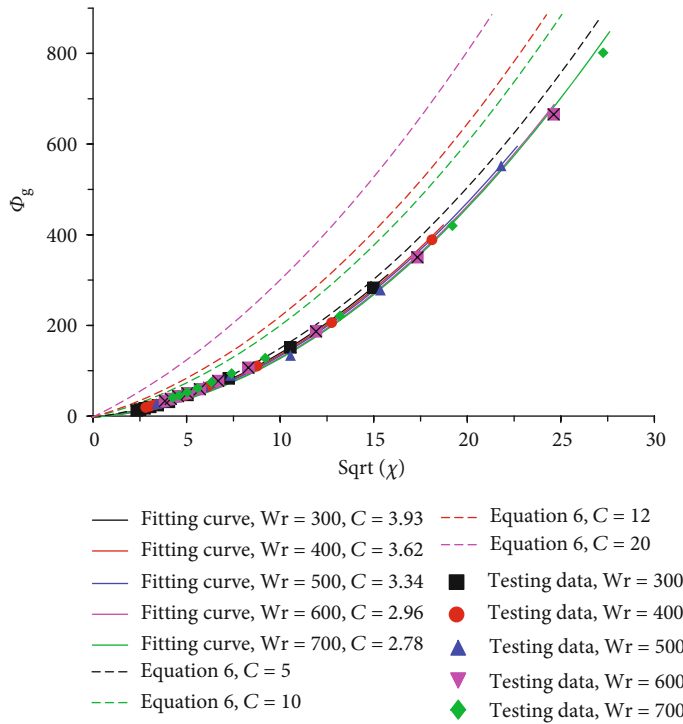
FIGURE 14: The relationship between Φ_g and Sqrt (χ) in case 1.

min, 600 mL/min, and 700 mL/min, the corresponding C values are 4.05, 4.81, 5.30, 5.32, and 5.66, respectively. With the increase of the water flow rate, the value of C increases, which indicates an increase of turbulence of the flow.

By fitting the test data to equation (6), the corresponding C values are 3.93, 3.62, 3.34, 2.96, and 2.78. The fitted values of C in Figure 14 are also close to $C = 5$, which is consistent with the fitting values of C with equation (5) to some extent.
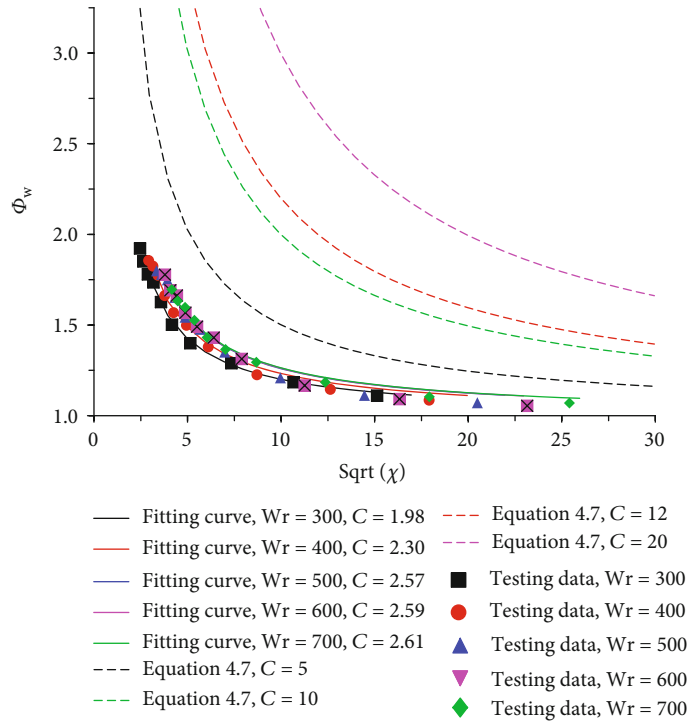
FIGURE 15: The relationship between Φ_w and Sqrt (χ) in case 2.
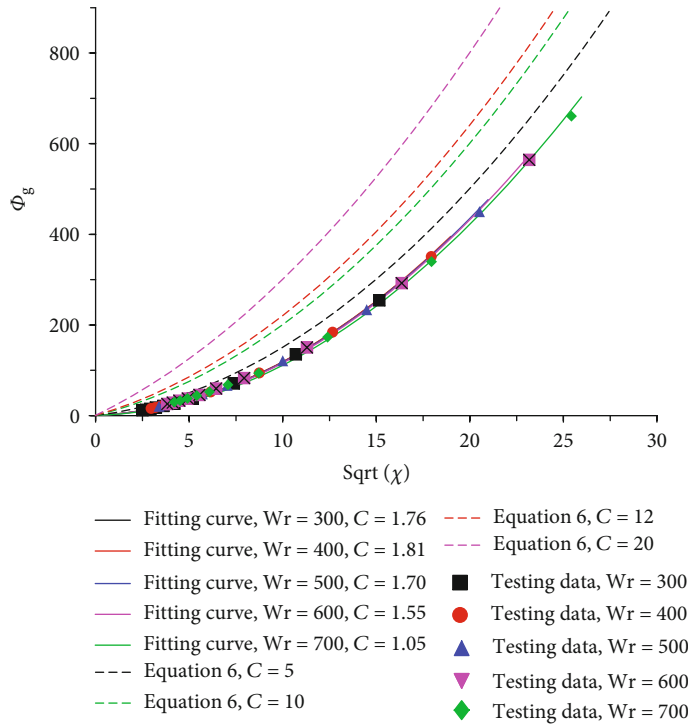
FIGURE 16: The relationship between Φ_g and Sqrt (χ) in case 2.

This indicates that Delhaye's model is approximately applicable to the two-phase flow in intersecting fractures but the values of C in the intersecting fractures seem to be different from those in the pipe two-phase flow. If Delhaye's model is modified, it can better fit the two-phase flow data in intersecting fractures.

Figures 15 and 16 show the fitting results of case 2. When the water flow rates are 300 mL/min, 400 mL/min,

500 mL/min, 600 mL/min, and 700 mL/min, the fitted values of C with equation (5) are 1.98, 2.30, 2.57, 2.59, and 2.61; the fitted values of C with equation (6) are 1.76, 1.81, 1.70, 1.55, and 1.05. Both groups of fitted values of C indicated that the turbulence in case 2 is smaller than that in case 1. This is reasonable since case 1 is composed of three fractures with an aperture of 0.3 mm-1 mm-0.3 mm, while case 2 is composed of three fractures with an aperture of 0.6 mm-1 mm-0.3 mm. The average fracture aperture of case 2 is larger than that of case 1, and in case 2, the superficial velocity is smaller, and consequently, the turbulence is small. In addition, the aperture change at the first intersection of case 2 (from 0.6 mm to 1 mm) is smaller than that of case 1 (from 0.3 mm to 1 mm), so in case 1, the turbulence induced by the aperture change at the fracture intersection is also serious.

To summarize, further studies should be conducted in the following aspects: (1) the values of C, which indicate different flow regimes, should be modified for the two-phase flow in intersecting fractures, to be different from those of the two-phase flow in pipes. (2) The relationship between C and the fracture configurations, such as the intersecting angle and the aperture variation, should be established. (3) The dependency of C on the fluid flow rate should be clarified. (4) In Delhaye's study, the values of C in equation (5) and C in equation (6) should be identical, but in our test, there is a little difference between the values of C calculated by these two equations. This means that equations (5) and (6) should be modified such as by multiplying a factor.

5. Summary

In this paper, a two-phase flow experiment is conducted in a 3D fracture model with smooth intersecting fractures to investigate its hydraulic characteristics. The following conclusions are supported by the results:

(1) The flow structures in the intersecting fractures show more similarity to those of the stratified wavy flow in pipes. The saturation kept fluctuating with respect to time, and it cannot reflect the fraction of two fluids very well. In addition, the nonlinearity induced by inertial force and turbulence in the intersecting fractures cannot be neglected in the two-phase flow. Due to these reasons, the generalized Darcy's law cannot well describe the hydraulic characteristics of the intersecting fractures; but the Lockhart-Martinelli model can fit the experiment data

(2) For an approximate calculation of the two-phase flow pressure drop in the intersecting fractures, Delhaye's model is effective since the experimental data approximately tend to fall on the same curve; but C increases with respect to the water flow rate to some extent, indicating an increase of flow turbulence. By comparing different cases, the degrees of turbulence in different cases can be well indicated by the average values of the parameter C. Due to the significant aperture change in case 1, it showed more significant turbulence by the value of C

(3) Delhaye's model can be used for approximate calculations of the two-phase pressure drop in the intersecting fractures, but not completely suitable. It should be modified for better fit. The phase multipliers Φ_w and Φ_g are believed to be related to the configuration of the intersecting fractures, such as the intersecting angle and the aperture change of the fractures. The range of values for C in Delhaye's model also needs to be reset. These aspects should be further investigated in future studies

Data Availability

The data used to support the findings of this study are included within the article.

Disclosure

This paper is part of a dissertation, which has previously been published [39].

Conflicts of Interest

The authors declare that there is no conflict of interest regarding the publication of this paper.

Acknowledgments

References

[1] R. L. Detwiler, H. Rajaram, and R. J. Glass, "Interphase mass transfer in variable aperture fractures: controlling parameters and proposed constitutive relationships," *Water Resources Research*, vol. 45, no. 8, 2009.

[2] S. Kimura, "Geothermal energy development and multiphase flows," *Japanese Journal of Multiphase Flow*, vol. 11, no. 1, pp. 11–14, 1997.

[3] P. Nuske, B. Faigle, R. Helmig, J. Niessner, and I. Neuweiler, "Modeling gas-water processes in fractures with fracture flow properties obtained through upscaling," *Water Resources Research*, vol. 46, no. 9, pp. 201–210, 2010.

[4] P. Persoff and K. Pruess, "Two-phase flow visualization and relative permeability measurement in natural rough-walled rock fractures," *Water Resources Research*, vol. 31, no. 5, pp. 1175–1186, 1995.

[5] W. Shen, X. Li, T. Ma, J. Cai, X. Lu, and S. Zhou, "High-pressure methane adsorption behavior on deep shales: experiments and modeling," *Physics of fluids*, vol. 33, no. 6, article 063103, 2021.

[6] J. Jarsjo, G. Destouni, and J. Gale, *Groundwater degassing and two-phase flow in fractured rock: Summary of results and conclusions achieved during the period 1994-2000 (No. SKB-TR–01-13).*, Swedish Nuchear Fuel and Waste Management Co, 2001.

[7] A. T. Corey, "The interrelation between gas and oil relative Permeabilities," *Producers Monthly*, vol. 19, no. 1, pp. 38–41, 1954.

[8] E. Dana and F. Skoczylas, "Gas relative permeability and pore structure of sandstones," *International Journal of Rock Mechanics and Mining Sciences*, vol. 36, no. 5, pp. 613–625, 1999.

[9] D. Yang and Y. Zhao, "Gas-liquid two-phase critical seepage law in single fracture and its random and compound mathematical model," *Chinese Journal of Rock Mechanics and Engineering*, vol. 27, pp. 84–89, 2008.

[10] G. Radilla, A. Nowamooz, and M. Fourar, "Modeling non-Darcian single- and two-phase flow in transparent replicas of rough-walled rock fractures," *Transport in Porous Media*, vol. 98, no. 2, pp. 401–426, 2013.

[11] T. Babadagli, X. Ren, and K. Develi, "Effects of fractal surface roughness and lithology on single and multiphase flow in a single fracture: an experimental investigation," *International Journal of Multiphase Flow*, vol. 68, pp. 40–58, 2015.

[12] A. Fumagalli and A. Scotti, "A numerical method for two-phase flow in fractured porous media with non- matching grids," *Advances in Water Resources*, vol. 62, pp. 454–464, 2013.

[13] K. Pruess and Y. W. Tsang, "On two-phase relative permeability and capillary pressure of rough-walled rock fractures," *Water Resources Research*, vol. 26, no. 9, pp. 1915–1926, 1990.

[14] M. Fourar and R. Lenormand, "A Viscous Coupling Model for Relative Permeabilities in a Fracture," in *SPE Annual Technical Conference and Exhibition*, New Orleans, Louisiana, USA, 1998.

[15] N. Watanabe, K. Sakurai, T. Ishibashi et al., "New v-type relative permeability curves for two-phase flows through subsurface fractures," *Water Resources Research*, vol. 51, no. 4, pp. 2807–2824, 2014.

[16] C. Y. Chen, *Liquid-Gas Relative Permeabilities in Fractures: Effects of Flow Structures, Phase Transformation and Surface Roughness*, Ph. D. Dissertation, Stanford University, Stanford, USA, 2005.

[17] A. E. Scheidegger, *The Physics of Flow through Porous Media (3rd Edition)*, University of Toronto Press, Toronto, Canada, 1974.

[18] E. S. Romm, *Fluid Flow in Fractured Rocks (in Russian)*, Nedra Publishing House, Moscow, Soviet Union, 1966.

[19] M. Fourar and S. Bories, "Experimental study of air-water two-phase flow through a fracture (Narrow Channel)," *International Journal of Multiphase Flow*, vol. 21, no. 4, pp. 621–637, 1995.

[20] D. Mahoney and K. Doggandt, "Multiphase Flow in Fractures," in *Proceedings of the Meanding of the Sociandy of Core Analysts*, Calgary, Canada, 1997.

[21] G. P. Diomampo, *Relative Permeability through Fractures*, Master Thesis, Stanford University, Stanford, USA, 2001.

[22] T. Ma, K. Zhang, W. Shen, C. Guo, and H. Xu, "Discontinuous and continuous Galerkin methods for compressible single-phase and two-phase flow in fractured porous media," *Advances in Water Resources*, vol. 156, article 104039, 2021.

[23] R. Liu, B. Li, Y. Jiang, and L. Yu, "Experimental and numerical study on hydraulic properties of 3-D crossed fractures," *Chinese Journal of Rock Mechanics and Engineering*, vol. A02, pp. 3813–3821, 2016.

[24] B. Li, R. Liu, and R. Y. Jiang, "Influences of hydraulic gradient, surface roughness, intersecting angle, and scale effect on nonlinear flow behavior at single fracture intersections," *Journal of Hydrology*, vol. 538, pp. 440–453, 2016.

[25] C. R. Wilson and P. A. Witherspoon, "Flow interference effects at fracture intersections," *Water Resources Research*, vol. 12, no. 1, pp. 102–104, 1976.

[26] G. Kosakowski and B. Berkowitz, "Flow pattern variability in natural fracture intersections," *Geophysical Research Letters*, vol. 26, no. 12, pp. 1765–1768, 1999.

[27] B. Su and M. Zhan, "Experimental study on fluid flow in crossed fractures," *Journal of Hydraulic Engineering*, vol. 5, pp. 1–6, 1997.

[28] M. Fourar and R. Lenormand, "Inertial effects in two-phase flow through fractures," *Oil & Gas Science and Technology*, vol. 55, no. 3, pp. 259–268, 2000.

[29] S. Irmay, "On the theoretical derivation of Darcy and Forchheimer formulas," *Transactions American Geophysical Union*, vol. 39, no. 4, pp. 702–707, 1958.

[30] D. Takhanov, "Forchheimer Model for Non-Darcy Flow in Porous Media and Fractures," in *Partial Fulfilment of the Requirements for the MSc and/or the DIC*, Imperial College London, London, UK, 2011.

[31] B. Rubin, *Accurate Simulation of Non-Darcy Flow in Stimulated Fractured Shale Reservoirs*, SPE Western Regional Meeting, Anaheim, California, USA, 2010.

[32] O. Temeng and R. Horne, "The Effect of High Pressure Gradients on Gas Flow," in *SPE 63rd Annual Technical Conference and Exhibition*, Houston, USA, 1988.

[33] J. Bear, *Dynamics of Fluids in Porous Media*, American Elsevier, New York, USA, 1972.

[34] W. Schrauf and D. Evans, "Laboratory studies of gas flow through a single natural fracture," *Water Resources Research*, vol. 22, no. 7, pp. 1038–1050, 1986.

[35] R. Zimmerman, A. al-Yaarubi, C. Pain, and C. Grattoni, "Nonlinear regimes of fluid flow in rock fractures," *International Journal of Rock Mechanics and Mining Sciences*, vol. 41, pp. 163–169, 2004.

[36] W. Lockhart and R. Martinelli, "Proposed correlation of data for isothermal two-phase, two-component flow in conduit," *Chemical Engineering Progress*, vol. 45, no. 1, pp. 39–48, 1949.

[37] M. Fourar, S. Bories, R. Lenormand, and P. Persoff, "Two-phase flow in smooth and rough fractures: measurement and correlation by porous-medium and pipe flow models," *Water Resources Research*, vol. 29, no. 11, pp. 3699–3708, 1993.

[38] J. M. Delhaye, M. Giot, and M. L. Riethmuller, *Thermohydraulics of Two-Phase Systems for Industrial Design and Nuclear Engineering*, McGraw-Hill, New York, USA, 1981.

[39] C. Wang, *Experimental and Numerical Investigations on the Hydraulic Characteristics of Two-Phase Flow in Rock Fractures*, Ph. D. Dissertation, Nagasaki University, Nagasaki, Japan, 2019.

WILEY | Hindawi

Research Article

Two-Phase Flow Model for Numerical Investigation of Impact of Water Retention on Shale Gas Production

Ershe Xu,[1,2,3] **Lingjie Yu,**[1,2,3] **Ming Fan,**[1,2,3] **Tianyu Chen** [ID],[4] **Zhejun Pan** [ID],[5] **Yuling Tan** [ID],[6,7] **and Guanglei Cui** [ID][4]

[1]*Wuxi Research Institute of Petroleum Geology, SINOPEC, Wuxi 214126, China*
[2]*SINOPEC Key Laboratory of Petroleum Accumulation Mechanism, Wuxi 214126, China*
[3]*State Key Laboratory of Shale Oil and Gas Enrichment Mechanisms and Effective Development, Wuxi 214126, China*
[4]*Key Laboratory of Ministry of Education on Safe Mining of Deep Metal Mines, Northeastern University, Shenyang 110004, China*
[5]*Key Laboratory of Continental Shale Hydrocarbon Accumulation and Efficient Development, Ministry of Education,*
 Northeast Petroleum University, Daqing, Heilongjiang 163318, China
[6]*Department of Engineering Mechanics, Shijiazhuang Tiedao University, Shijiazhuang 050043, China*
[7]*Hebei Key Laboratory of Mechanics of Intelligent Materials and Structures, Shijiazhuang Tiedao University,*
 Shijiazhuang 050043, China

Correspondence should be addressed to Guanglei Cui; cuiguanglei@mail.neu.edu.cn

In this work, a triple-porosity, two-phase flow model was established to fill the knowledge gap of previous models focusing on gas production characteristics while ignoring the impacts of water injection. The proposed model considers the water flow in the fracture systems and clay minerals and the gas flow in the organic matter, inorganic pore, and fracture systems. The proposed model is solved using a finite element approach with COMSOL Multiphysics (Version 5.6) and verified with field data. Then, the evolutions of the intrinsic and relative permeabilities during water injection and gas production are examined. Furthermore, the impacts of water injection time and pressure are investigated. Good verification results are obtained; the goodness-of-fit value is 0.92, indicating that the proposed model can replicate both the water stimulation and the gas production stages. The relative gas permeability declines during water injection but recovers in the gas depletion stage. Furthermore, the intrinsic permeability increases during the water injection stage but decreases during the gas production stage. A higher water injection pressure and longer injection time would enlarge the intrinsic permeability, thus improving flow capacity. However, it would reduce gas relative permeability, thereby hindering gas flow. The shale gas production characteristic is controlled by the two abovementioned competing mechanisms. There exists a perfect combination of water injection pressure and injection time for achieving the maximum profitability of a shale gas well. This work can give a better understanding of the two-phase flow process in shale reservoirs and shed light on the field application of hydraulic fracturing.

1. Introduction

Compared with other fossil fuels, shale gas plays an important role in the global energy mix with the exhaustion of conventional reservoirs [1, 2]. Owing to the extremely low permeability (nanodarcies, 10^{-21} m^2) and porosity (less than 5%) of shale gas [3], highly effective reservoir stimulation technologies are vital for the successful exploitation of shale gas reservoirs [4]. Hydraulic fracturing (HF), wherein large volumes of water are injected into shale reservoirs to induce gas production, is a mainstream method of stimulation (Figure 1(a)). Injected water flows into the hydraulic fractures and enters the shale matrix, thus occupying the gas flow channels and impairing the gas flowback process [5] (Figure 1(b)). Besides the injected water, abundant reserves of connate water are present in shale gas reservoirs [6, 7]; this is adsorbed on the surface of inorganic matter (clays) [8, 9] or trapped by capillary pressure in small inorganic pores [5, 10]. In general, connate water is initially immobile.
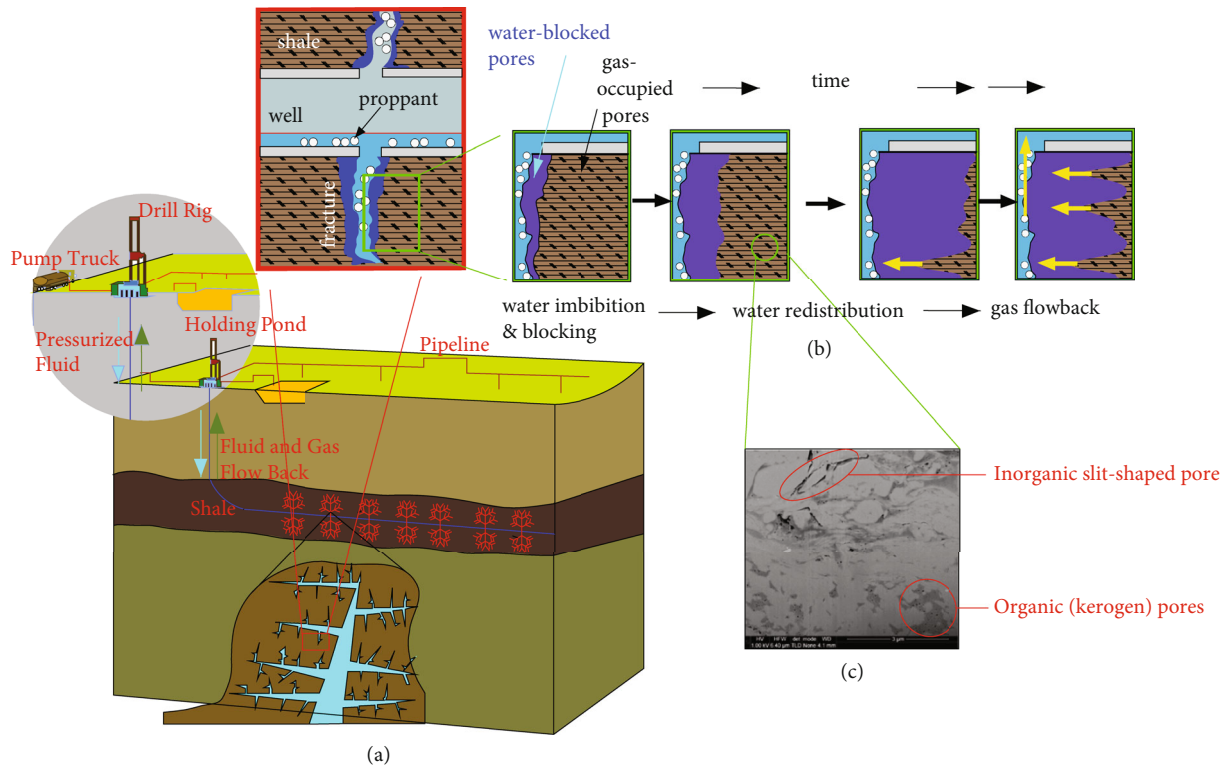
Figure 1: (a) Schematic illustration of shale gas HF. (b) Water imbibition process in a shale reservoir. (c) SEM image of the shale matrix.

However, during the water injection process, part of the penetrating water becomes residual water in the inorganic matrix, since it is filled to normal irreducible water saturation [11, 12]. In conclusion, both injected water and connate water can significantly impact gas production characteristics [13], yet most gas production models only consider the influence of gas pressure and effective stress or connate water [14]; there is no comprehensive investigation of the impacts of injected water.

Injected hydraulic water dramatically influences gas diffusivity and permeability [15, 16], thereby hindering gas transport in shale. According to experimental results for the Svalbard Shale, moisture content strongly decreases Ar and CO_2 permeability [17]. Increasing water saturation leads to an exponential decline in apparent effective He permeability; at a water saturation of approximately 30%, He permeability decreased strongly [18]. Further, the permeability of crushed shale samples exhibited exponential decline when saturated with water [19]. In addition, retained water can occupy void spaces and adsorption sites that were initially originally available for gas storage through two mechanisms [20]: (i) a part of void space would be occupied by injected water, directly decreasing the free gas content in shale [21, 22]. (ii) Moreover, pore surface sites originally intended for methane adsorption are partially occupied by water molecules through competitive adsorption, since condensed water is blocking the pore throat, resulting in a decline in gas adsorption capacity [21, 23–25].

The two-phase flow process during shale gas production has been widely investigated analytically and semianalytically with the influence of complexity and half-length of hydraulic fracture [26, 27], increased permeability, and frac-

ture conductivity in stimulated reservoir volume (SRV) [28, 29] considered. In Clarkson and Williams-Kovacs' work, the short-term flowback data was adopted to characterize water and gas production characteristics and flowing pressure [26]. In the later work, Williams-Kovacs and Clarkson [28] proposed a data-driven pseudoanalytical model in which the two-phase flowback process was investigated and the impacts of key frac properties were analyzed. However, the complex coupling mechanisms between reservoir deformation and gas-water two-phase flow are typically ignored in these previous approaches [30]. By countering this problem, numerical reservoir models are widely used to predict production [2, 14], improve profitability [31], and understand potential hazards [32]. Cao et al. [33] proposed a multiscale, multiphase model for gas-water two-phase flow within shale reservoirs. Based on an evaluation of shale gas recovery, the model can quantitatively differentiate these properties of fractured water. Later, a multidomain unstimulated reservoir volume (USRV) and stimulated reservoir volume (SRV), multiphysics model was proposed by Cui et al. [14] to represent two-phase flow within a heterogeneous shale gas reservoir. In Li et al.'s work [34, 35], a three-component solid system including organic kerogen, inorganic matrix, and hydraulic fracture (HF) was specified to characterize two-phase flow during the gas production stage. The dual-porosity, dual-permeability media was adapted to the first two components with a 1D cracked medium referred to as the last for simplification. Different properties in the so-called stimulated reservoir domain (SRD) and unstimulated reservoir domain (SRD) were assumed to simulate the influence of HF in the near-HF matrix.

As mentioned above, current gas production models are mostly focused on gas flow characteristics and ignore the impacts of the injection of hydraulic water. In other words, only the gas production stage is replicated in the simulation work, and the water injection process is seldom studied. In such approaches, the impacts of water injection pressure and injection time are not fully understood. To address these shortcomings, this study proposes a coupled two-phase flow model to comprehensively examine the effect of injected water on reservoir production. A group of partial differential equations governing the multiscale, two-phase flow in a shale gas reservoir is proposed, and both intrinsic and relative permeability evolutions are considered. The proposed model is elucidated via numerical simulations and sensitivity analyses and verified with field data.

This paper is organized as follows: the conceptual model and mathematical model are presented in Sections 2 and 3, respectively. Then, model verification is conducted in Section 4, and the results and discussion are shown in Section 5. Finally, the conclusions are explained in Section 6.

2. Conceptual Model

2.1. Triple-Porosity Model. A field emission scanning electron microscopy (FESEM) image (Figure 1(c)) [36–40] is selected to represent highly heterogeneous properties of shale matrix, such as mineral constituents, pore structure, and gas storage term. Based on these observations, a triple-porosity model was established in this study to probe the effect of hydraulic water and connate water on shale gas production characteristics. In this triple-porosity model, the shale reservoir is divided into the fracture system, inorganic matrix, and organic matter [41]. Free gas exists in the fracture system and inorganic matrix, whereas absorbed gas is present in the organic matter [42]. The hydraulic fluid enters the fracture system and inorganic matrix system, while connate water exists in the inorganic matrix and organic matter, impacting the gas storage amount.

2.2. Water Injection Process

(a) Initial equilibrium state and pressure rise stage

As shown in Figure 2(a), before HF, the water saturation is relatively low. As the injection process continues, the water injection volume increases linearly with time, and the water pressure in the wellbore rises continuously with continuous water injection. Water percolation in shale reservoir fractures can be described by Darcy's law [43]. When the water pressure reaches the fracture pressure, the shale reservoir is in a critical state, which manifests externally as hydraulic fractures.

(b) HF stage

Under the combined action of in situ stress and high-pressure water, the radial stress on the inner surface of the fracture hole is expressed as compressive stress and the tangential stress is expressed as tensile stress [44]. Because the compressive strength is much greater than the tensile

strength, the newly generated fractures in the shale reservoir are mostly initiated by tensile failure [45]. The fracture initiation and propagation mechanisms of HF are generally described by fracture mechanics failure criteria: the tensile strength criterion and the Mohr–Coulomb criterion [46]. As shown in Figure 2(b), after HF is initiated, the injection water flows into the main fracture network, and generally the Darcy equation is applied.

(c) Water imbibition stage

The water environment is shaped under the water pressure after the fracture penetrates, and the water imbibition process can be divided into three stages. First, water enters the fracture system (Darcy's law). Then, it diffuses into the inorganic matrix. In this work, only clay minerals are assumed to be highly hygroscopic. In the last stage, the water diffuses into the organic matter through a competitive adsorption behavior. When the injection water diffuses into the shale matrix from the hydraulic or natural fractures, as shown in Figure 2(c), the gas relative permeability of the shale reservoir changes impacting the gas flow characteristics.

(d) Final equilibrium state

During the fracturing process, a large amount of slick water is pumped into the reservoir for several days. A technique called soak-back was recently developed to boost production after HF; it sets a well shut-in period (soaking time) to soak the fracture fluids and thus increase productivity. During these two processes, the hydraulic fluid continues to diffuse until a new equilibrium state is reached. However, a new state may never be achieved, as thousands of years are needed [2].

2.3. Gas Production Process

(a) Bubble flow

The water flowback and gas production processes can be roughly split into four stages as shown in Figure 3. In the first stage (Figure 3(a)), water in the horizontal well and hydraulic fracture fluid flow back together with a small amount of free gas. This part is known as bubble flow.

(b) Water-dominant two-phase flow

In the later stage (Figure 3(b)), the water in the inorganic matrix is depleted, since the water saturation between the hydraulic fracture and inorganic matrix is different. In this stage, some free gas in the inorganic matrix flows back because of the pressure difference. In this stage, the water flow plays the dominant role. The water saturation is higher than the gas saturation, leading to a significant larger water relative permeability.

(c) Gas-dominant two-phase flow

In the middle and later stages of production (Figure 3(c)), the residual water on the fracture surfaces is

(a)

(b)

(c)

(d)
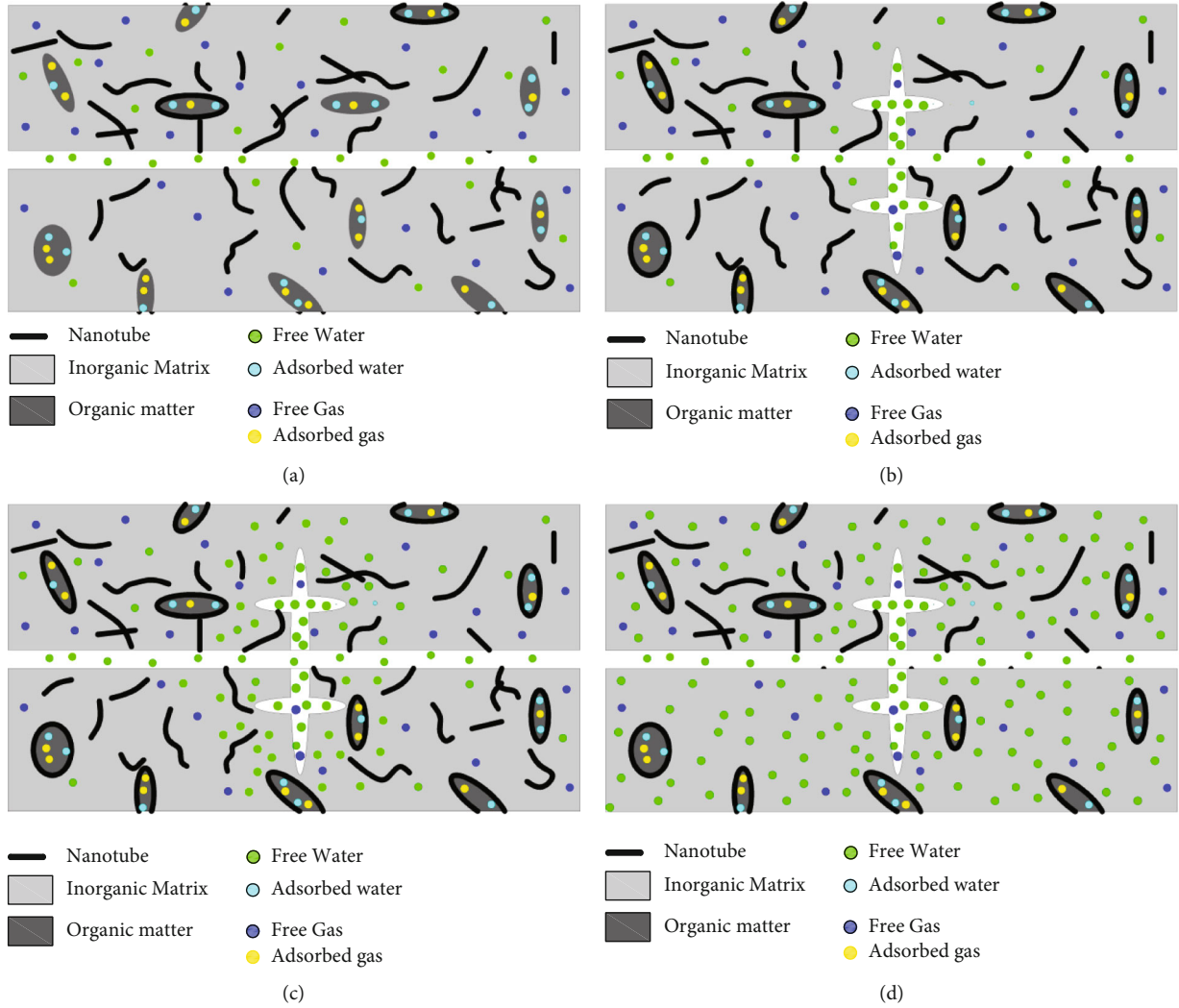
FIGURE 2: Schematic illustration of the water injection process: (a) initial and pressure rise stages, (b) HF stage, (c) water imbibition stage, and (d) final stage.

extracted through moisture transport. In the meantime, the fracture permeability is improved, since the gas flow channels in the fractures are widened by the evaporation of the water film, which also increases the gas output. Additionally, the adsorbed gas in the organic matter begins to diffuse because of the gas concentration gradient.

(d) Final equilibrium state

In the final state (Figure 3(d)), all the water and gas molecules are depleted, and a new equilibrium state is achieved. However, this state is difficult to achieve, as more than 3,000 years are needed to attain full equilibrium, as shown in a previous work [2].

2.4. Competitive Adsorption between Gas and Water. Shale gas adsorption under dry conditions plays a vital role in gas in place (GIP) estimation [47, 48]. Although a few studies have been conducted on methane adsorption in moisture-equilibrated shale [23, 49], the impact of water content has not been fully studied.

Figure 4 illustrates the microscopic differences between saturated shale (low/high moisture content) and dry shale. The adsorption sites in the shale matrix—the organic structure surfaces and the clay mineral surfaces—are fully occupied under dry conditions. However, these characteristics are quite different under moist conditions: (i) functional groups containing oxygen and nitrogen atoms are of stronger water absorption capacity and (ii) water molecules are easily adsorbed on clay minerals. Both conditions greatly reduce the shale gas adsorption capacity. Hence, a shale gas reservoir can achieve maximum adsorption capacity under dry conditions.

3. Mathematical Model

3.1. Gas-Water Two-Phase Flow in the Fracture System. The mass conservation equation of gas-water two-phase flow in a fracture system is given as [50]

$$\frac{\partial m_{fa}}{\partial t} + \nabla \cdot J_{fa} = Q_{fa},$$ (1)

(a)

(b)

(c)

(d)
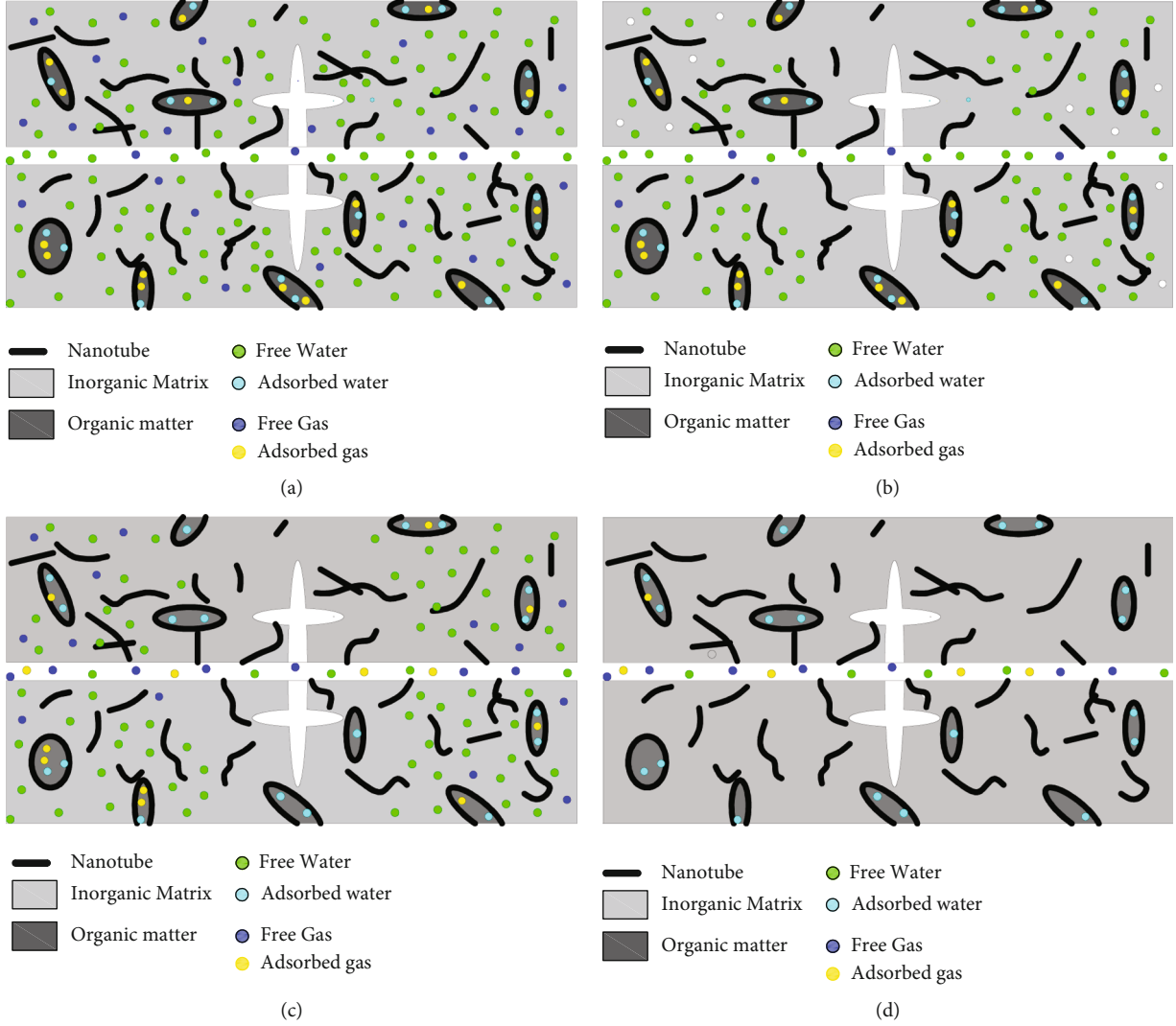
FIGURE 3: Schematic illustration of the gas production process: (a) bubble flow, (b) water-dominant two-phase flow, (c) gas-dominant two-phase flow, and (d) the new equilibrium state.

where subscript α refers to either water (w) or gas (g), subscript f denotes the fracture system, and $Q_{f\alpha}$ refers to the flow source or sink. With the consideration of gravity, the mass flux $J_{f\alpha}$ of the fluid can be calculated as [51]

$$J_{fa} = -\rho_{fa} \frac{k_f k_{fra}}{\mu_a} \left(\nabla p_{fa} + \rho_{fa} \mathbf{g} \right), \tag{2}$$

where k_f and k_{fra} are the intrinsic and relative permeabilities, respectively, of the fracture system, p_a represents the pore pressure, μ_α represents the viscosity, and $\mathbf{g}$ represents the acceleration due to gravity.

The water mass (m_{wf}) only contains free phase and is calculated as [52]

$$m_{wf} = s_{wf} \rho_{wf} \phi_f + Q_{wf}, \tag{3}$$

where s_{wf} refers to the water saturation, ρ_{wf} represents the

water density, φ_f refers to the porosity, and Q_{wf} refers to the water source term.

The gas mass (m_{gf}) is composed of free gas and mass resources provided by the inorganic pore system [53].

$$m_{gf} = s_{gf} \rho_{gf} \phi_f + Q_{\text{in}2f}, \tag{4}$$

where s_{gf} and ρ_{gf} represent the gas saturation and gas density, respectively.

The gas mass transfer term is proportional to the gas content difference between the fracture and inorganic matrix systems:

$$Q_{\text{in}2f} = \frac{\omega_{\text{in}} k_{\text{apin}}}{\mu} \rho_{\text{in}g} \left(p_f - p_{\text{in}} \right), \tag{5}$$

where ω_{in} is the shape factor.
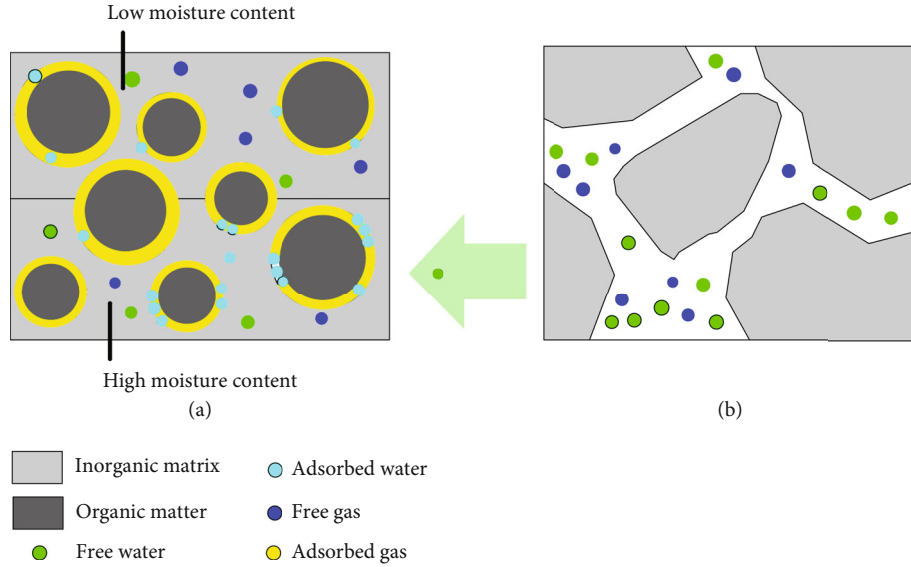
FIGURE 4: Schematic illustration of the effect of water content on the shale gas adsorption process: (a) shale matrix and (b) water injection process. The upper part of (a) represents the original state, and the lower part of (b) illustrates the changes induced by the water injection.

Therefore, the two-phase flow in a fracture system can be written as

$$\frac{\partial \left(s_{fw}\rho_{fw}\phi_f\right)}{\partial t} = \nabla \cdot \left(\rho_{fw}\frac{k_f k_{frw}}{\mu_w}\left(\nabla p_f + \rho_{fw}g\right)\right) + Q_{wf},$$

(6a)

$$\frac{\partial \left(s_{fg}\rho_{fg}\phi_f\right)}{\partial t} = \nabla \cdot \left(-\rho_{fg}\frac{k_f k_{frg}}{\mu_a}\left(\nabla p_{fg} + \rho_{fw}g\right)\right)$$
$$- \frac{\sigma_{in}k_{apin}}{\mu}\rho_{in}\left(p_f - p_{in}\right).$$

(6b)

3.2. Water Imbibition in the Inorganic Matrix. From microscopic images in some studies [54, 55], clay minerals in the shale matrix are usually embedded into nonclay minerals. Generally, a maximum water mass value exists, above which water mass remains constant, and the ratio of increase generally declines with the water mass content. Therefore, the rise in the water mass of clay minerals is determined by the disparity between the presented water mass (m_{cl}) and the maximum value (m_{max}) [50]:

$$\frac{\partial m_{cl}}{\partial t} = \begin{cases} R_a(m_{max} - m_d), & \text{if } m_{cl} < m_{max}, \\ 0, & \text{if } m_{cl} \geq m_{max}, \end{cases}$$

(7)

where R_a refers to the adsorption rate (1/s).

3.3. Gas Slippage Flow in the Inorganic Matrix. The mass conservation law of gas slippage flow in an inorganic pore can be represented as [14]

$$\frac{\partial m_{ing}}{\partial t} + \nabla \cdot J_{ing} = Q_s + Q_{in2f},$$

(8)

where subscript in represents inorganic minerals and J_{ing} refers to the gas mass flux.

Both the free-phase gas in inorganic pores and the gas mass source applied by the organic system contribute to the gas mass content m_{ing}:

$$m_{ing} = \rho_{ing}\phi_{in}S_{ing} + \rho_{ga}\rho_s m_{or},$$

(9)

where φ_{in} refers to the inorganic porosity and ρ_{ing} refers to the gas density. J_{ing} is described as the modified Darcy equation:

$$J_{ing} = -\frac{k_{apin}}{\mu}\rho_{ing}\nabla p_{in},$$

(10)

where k_{apin} refers to the apparent permeability and is written as [2]

$$k_{apin} = \left(1 + \frac{4\text{Kn}_{in}}{1 + \text{Kn}_{in}}\right)k_{ing}.$$

(11)

3.4. Diffusion of Gas in Organic Matter. The mass transfer rate between the inorganic and organic systems depends on the diffusion duration in the organic matter [56].

$$\frac{dm_{or}}{dt} = -\frac{1}{\tau_{or}}\left[m_{or} - m_{eq}(p_{wall})\right],$$

(12)

where $m_{eq}(p_{wall})$ represents the gas concentration at equipoise with the interface pressure p_{wall}. The diffusion time τ_{or} is represented as

$$\tau_{or} = \frac{1}{\omega_{or}D_{or}},$$

(13)

(a)

(b)
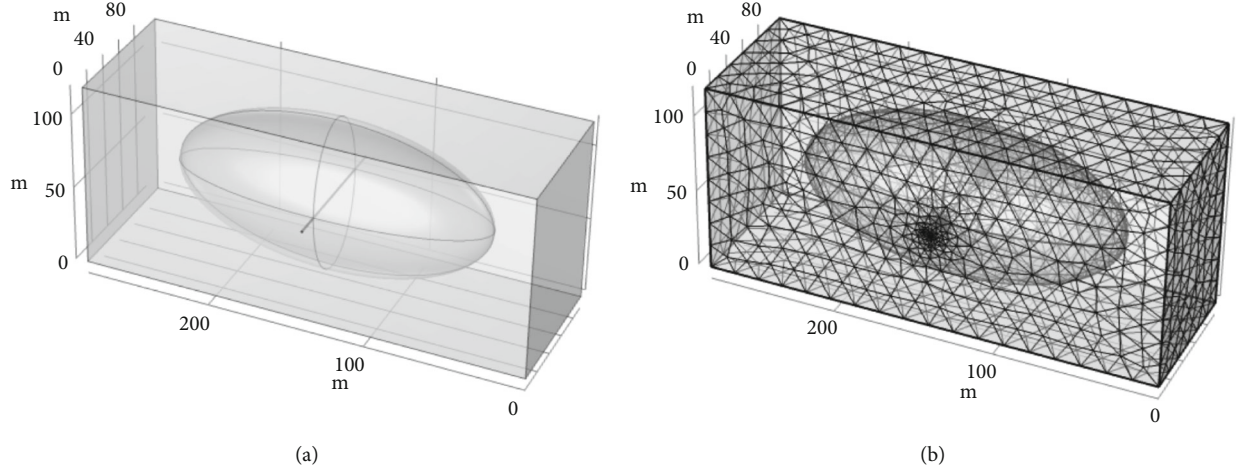
Figure 5: Illustration of the multiphysics, multidomain model: (a) geometric model and (b) meshing model.

where subscript or represents the organic matter, D (m^2/s) is the surface diffusion coefficient, and w_{or} is the shape factor.

3.5. Competitive Adsorption in Organic Matter.

We assumed a pseudosteady state in this work [31] and found that the interface pressure p_{wall} was equivalent to the inorganic matrix pressure p_{or}. Because of the presence of clay minerals, a water film exists on the surface of minerals in inorganic shale [21, 57] influencing the adsorption and desorption behavior of shale gas. The following equation is proposed [58]:

$$m_{or} = \beta \frac{V_H p_{or}}{p_{or} + P_H} + (1 - \beta) \frac{V_L p_{or}}{P_L + p_{or}}, \qquad (14)$$

where m_{or} is the gas adsorption volume in organic matter, V_L refers to the solid-gas (Langmuir) saturated adsorption volume, P_L is the Langmuir pressure constant, V_H refers to the liquid-gas saturated adsorption capacity, and β is the water molecular coverage ratio, defined as the rate of the wetting area of water molecules to the whole pore area. Moreover, the covering rate of the water molecules is relevant to irreducible water saturation, as shown by the following [59]:

$$S_{rw} = \left[1 - \left(1 - \frac{h}{r} \right)^2 \right] \beta, \qquad (15)$$

where S_w refers to the capillary water saturation (dimensionless), r refers to the pore radius, and h refers to the water molecular layer thickness.

3.6. Permeability Variation with Effective Stress and Water Saturation

3.6.1. Permeability Correction with Water Saturation.

The following supplementary equations for saturation and capillary pressure are necessary for solving the two-phase flow in a shale reservoir [60]:

$$s_{iw} + s_{ig} = 1,$$
$$p_{ic} = p_{ig} - p_{iw}, \qquad (16)$$

where p_{ic} is the capillary pressure and calculated with the Brooks and Corey formulation [61, 62]:

$$p_{ic} = p_{ie}(s_{iew})^{-1/\lambda_i}, \qquad (17)$$

where p_{ie} represents the nonwetting phase entry pressure, s_{iew} represents the effective saturation for the water phase, and λ_i represents a pore size distribution parameter. In our research, we assumed that the parameter λ_i was 2. Then, the effective water saturation can be expressed as

$$s_{ewi} = \frac{s_{wi} - s_{wri}}{1 - s_{wri} - s_{gri}}, \qquad (18)$$

where s_{wri} and s_{gri} represent the irreducible water and gas saturations in a fracture zone, respectively.

In this study, the relative permeability was governed by [63]

$$k_{irg} = (1 - s_{iew})^2 (1 - s_{iew}^2),$$
$$k_{irw} = \sqrt{s_{iew}} \left(1 - \left(1 - s_{iew}^{1/m} \right)^m \right)^2, \qquad (19)$$

where k_{irg} and k_{irw} refer to the relative permeabilities of gas and water, respectively.

Water saturation can be determined directly for the two-phase flow in a fracture system. The water saturation in clay minerals is related to the water mass and represented as

$$S_{wcl} = \frac{m_{cl}}{m_{max}} S_{w\,max}, \qquad (20)$$

where $S_{w\,max}$ denotes the maximum water saturation in clay minerals.

TABLE 1: Marcellus Shale property parameters [66, 67].

(a)

Reservoir parameter	Value
Reservoir temperature (°C)	79.4
Fracturing cluster spacing (m)	92
Size of the simulation area (rectangle, m)	$92 \times 280 \times 120$
Fracture permeability in SRV (k_{fx}, m²)	1.5×10^{-16}
Inorganic permeability in SRV (k_{inx}, m²)	1.5×10^{-18}
Fracture porosity in SRV	0.07
Inorganic porosity in SRV	0.03
Shape factor in the inorganic matrix (m⁻²)	15
Initial water saturation in SRV	0.05
Irreducible water saturation	0.06
Langmuir pressure constant (MPa)	4
Bottom-hole water saturation	0.1
General parameter	Value
Gas density (kg/m³)	0.714
Coefficient for relative permeability (m)	0.5
Universal gas constant (J/(mol·K))	8.314
Compressibility of methane (Pa⁻¹)	1.4×10^{-5}

(b)

Reservoir parameter	Value
Bottom-hole pressure (MPa)	3.45
Initial gas pressure (MPa)	32.6
Size of SRV (spheroid, m)	$30 \times 100 \times 50$
Fracture permeability in USRV (k_{fx}, m²)	1.3×10^{-18}
Inorganic permeability in USRV (k_{inx}, m²)	2×10^{-20}
Fracture porosity in USRV	0.04
Inorganic porosity in USRV	0.015
Surface diffusion coefficient (s)	4×10^{9}
Initial water saturation in USRV	0.05
Irreducible water saturation	0.04
Langmuir volume constant (m³/kg)	0.003
Biot's coefficient	0.8
General parameter	Value
Gas viscosity (Pa·s)	2×10^{-5}
Coefficient for capillary pressure (λ)	2
Molar mass of methane (kg/mol)	0.016
Compressibility of methane (Pa⁻¹)	3.8×10^{-10}

3.6.2. Permeability Correction with Effective Stress. The fracture permeability correlation for gas shale with effective stress can be written as

$$k = k_0 e^{-3c_f \left(\sigma_{ef} - \sigma_{ef0} \right)}, \tag{21}$$

where σ_{ef} refers to the effective stress and c_f refers to the
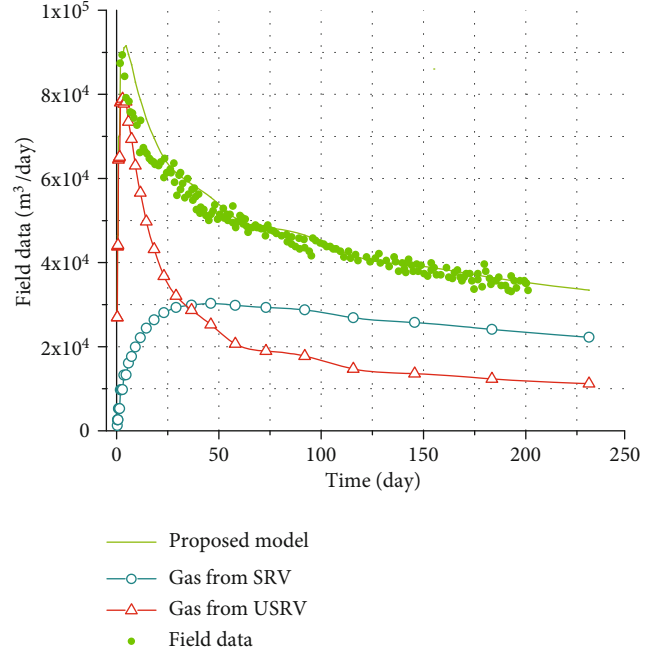
FIGURE 6: History matching results for field data gathered from the Marcellus Shale.

fracture compressibility. The effective stress, which represents the distinction between the formation stress and liquid pressure, can be formulated as

$$\sigma_{ef} = \sigma - p. \tag{22}$$

The liquid pressure is the combination of the gas and water pressures in the fracture system, which is defined as follows:

$$p = s_w p_{fw} + s_g p_{fg}, \tag{23}$$

and the inorganic system's gas pressure, which is defined as follows:

$$p = p_g. \tag{24}$$

4. Model Verification

4.1. Model Building. A testing well drilled into the lower sections of the Marcellus Shale [64] executed seven fracturing stages (each of which contained five perforation clusters) measuring over 630 m in the lateral section. Its completion design included 450,000 gallons of slick water per stage, and sand particles were used as proppants. Only 200 days of the production data were used for history matching. The distance between the different fracture stages far outweighed that between diverse perforation clusters in a special stage [29, 57]. Therefore, a computation domain including one fracture stage (five perforation clusters) and its adjacent area was selected.
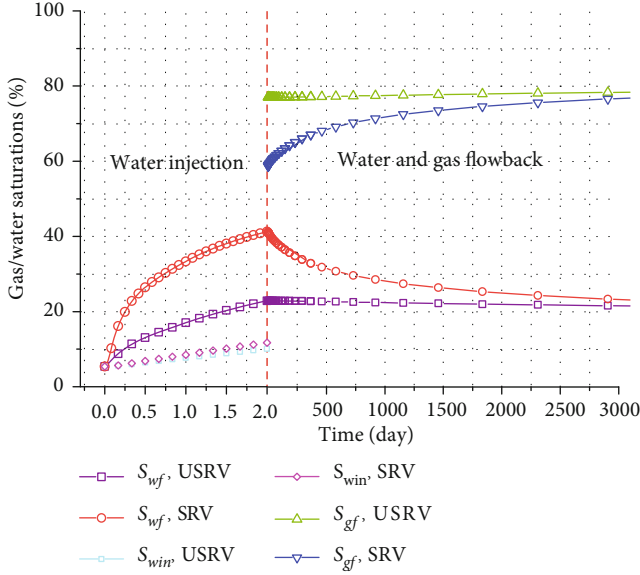
Figure 7: Evolution of average water saturation in the SRV and USRV regions.

Figure 8: Evolution of average water pressure in the SRV and USRV regions during water injection.

Figure 9: Gas/water relative permeability and intrinsic permeability of the SRV and USRV regions.

Similar to Cui et al. [14], we connected the SRV areas induced per perforation cluster and formed a spheroid-shaped volume. The nonimpacted area is the USRV. In the process of simulation model design, the research area was configured as a cuboid with a size of 92 m × 280 m × 120 m, while the SRV exhibits spheroid shape with the semiaxes defined as 35, 100, and 50 m (in the x, y, and z directions, respectively). The reservoir geometry and SRV are depicted in Figure 5(a). A highly refined mesh is required for the SRV region, while a relatively coarser mesh is suitable for the USRV. After meshing, there were a total of 113,895 elements with an average quantity of 0.85 as depicted in Figure 5(b).

Both the water injection, which lasted two days, and the gas production processes were replicated to fully verify the proposed model. For the water injection process, a constant water saturation value of 0.8 was used as the water flow boundary. For the gas production process, the bottom-hole pressure was obtained from Meyer [65]. For the gas flow model in the organic and inorganic matrixes, due to the lack of immediate engagement with hydraulically formed fractures, flow boundary conditions were not taken into consideration. The water saturation value applied to the well was 0.2. Information about the Marcellus Shale reservoir was gathered from the previous work [66–68] and is detailed in Table 1.

4.2. Verification Results. The matched gas production ratios are shown in Figure 6. The model perfectly matched the field data, with a goodness-of-fit value of 0.92. The gas sources were also examined. As the production time increased, the gas production rate increased and then decreased. The increase stage was mainly observed in the first two days. This is because a large amount of water was discharged during this stage, which increased the relative gas permeability.
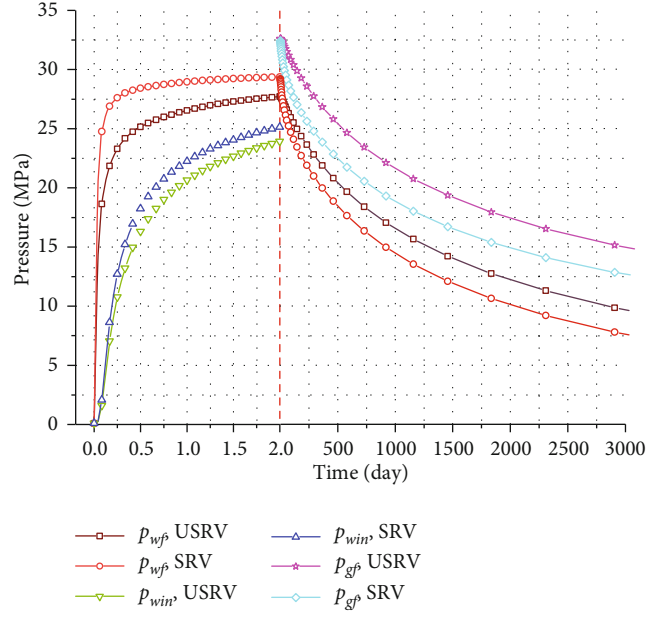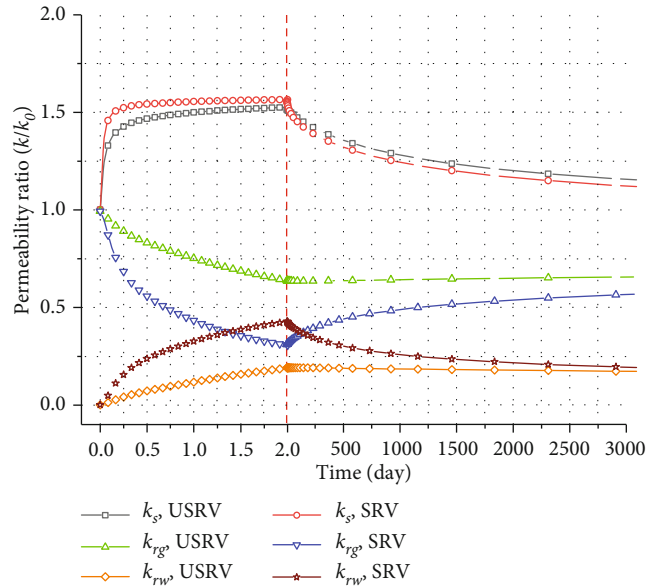
5. Results and Discussion

5.1. Water and Gas Transport Processes

5.1.1. Water and Gas Saturation Evolution. Changes in water and gas saturation directly affect gas and water relative permeabilities. In the water injection stage, the water pressure gradient forces the high-pressure water injected at the wellhead to migrate to the reservoir. Figure 7 shows the evolution of the s_{wf} and s_{wg} of the SRV and USRV regions. The average value of each domain is applied here. The
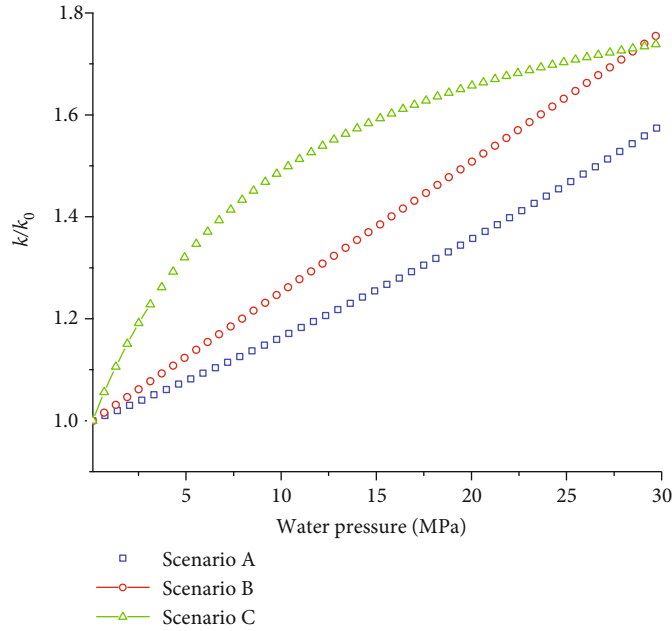
FIGURE 10: Intrinsic permeability variations with water pressure.

results show the following: (i) the values of s_{wf} in the SRV and USRV regions show significant discrepancies, while the values of $s_{w\text{in}}$ exhibit little differences. (ii) During the water flowback and gas production stage, the water in the fracture system first flows back, presenting a dramatic decrease in s_{wf}; by contrast, $s_{w\text{in}}$ shows little variation. (iii) As a result, the gas saturation (s_{gf}) in the fracture system spikes, but the value in the inorganic system shows only a small change.

5.1.2. Water and Gas Pressure Evolution. The water and gas pressures are further investigated to fully illustrate the water and gas transport processes in the shale reservoir. The average water and gas pressures of the fracture system in the SRV and USRV regions are shown in Figure 8. During the water injection stage, the water pressures of both systems significantly increase in not only the SRV region but also the USRV region; the values in the SRV system are larger than those in the USRV system. In the gas production process, the water and gas pressures drop sharply to the extraction pressure at the wellhead; the value in the SRV area is lower than that in the USRV area, leading to a pressure gradient. This pressure gradient causes the gas in the fracture to continuously migrate to the wellhead.

5.2. Permeability Evolution

5.2.1. Intrinsic Permeability Evolution. Permeability determines water and gas flow rates and therefore controls gas production characteristics. It is thus a significant parameter indicating the flow capacity in a reservoir. In this research, permeability is assumed as the combination of relative and intrinsic permeabilities, and their variations are examined.

Figure 9 shows the evolutions of intrinsic and relative permeabilities during the water injection and gas production stages. In the water injection stage, the effective stress increases, leading to an increment in intrinsic permeability. The value in the SRV area is larger than that in the USRV area due to the higher water pressure in the former region. During the water flowback and gas production stage, both intrinsic permeabilities in the SRV and USRV regions decline because of the decreased effective stress. On the contrary, the value in the SRV area is lower than that in the USRV area, but the difference is small because of the supporting effect of proppants.

5.2.2. Gas/Water Relative Permeability Evolution. Besides intrinsic permeability, the evolutions of relative permeabilities are illustrated. Gas and water relative permeabilities are directly related to water saturation, which is directly proportional to water relative permeability but inversely proportional to gas relative permeability. During the water injection process, water saturation continues to increase, leading to an increment in water relative permeability and a decline in gas relative permeability. In the water flowback and gas production stage, in the SRV region, the gas relative permeability rises as the water relative permeability is reduced. In the USRV area, the gas and water relative permeabilities do not change significantly. The gas relative permeability in the gas production stage is far below the original value, thereby hindering gas flow.

5.3. Impact of Water Pressure. As discussed above, gas production behavior is closely related to the evolution of intrinsic permeability and water injection pressure. This impact is further studied through three scenarios: (i) scenario A (benchmark model), where intrinsic permeability has an
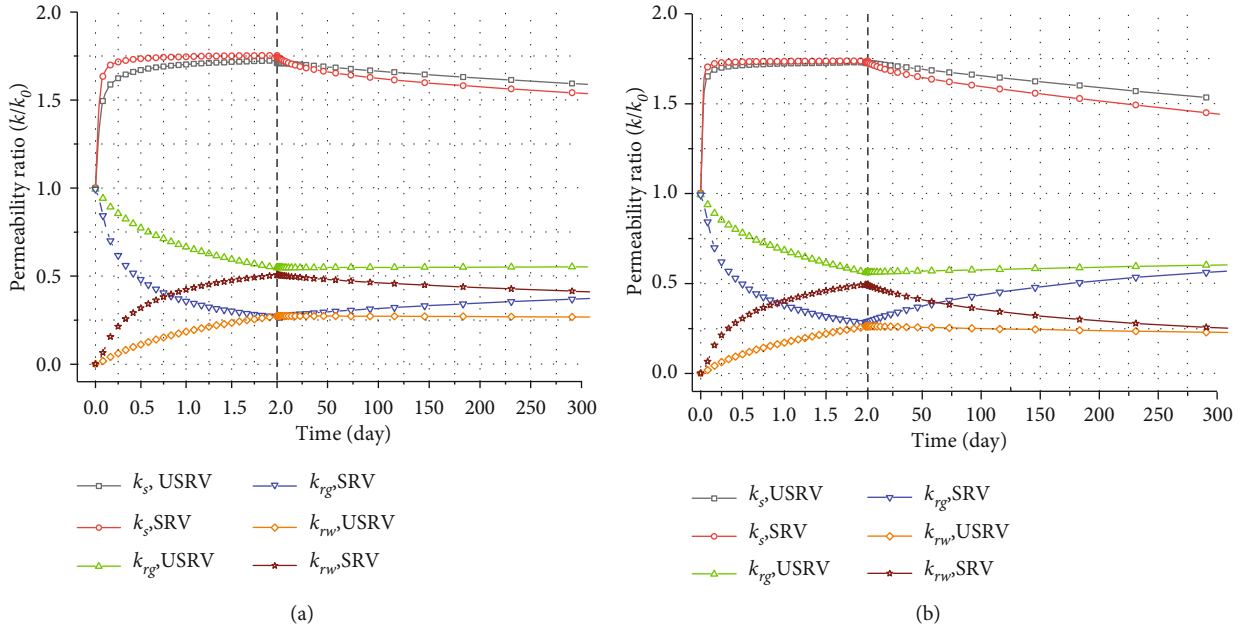
FIGURE 11: Gas/water relative permeability: (a) scenario B and (b) scenario C.

exponential relationship with water injection pressure; (ii) scenario B, where intrinsic permeability is linearly proportional to water injection pressure; and (iii) scenario C, where intrinsic permeability has a Langmuir function relationship with water injection pressure. The equations of the abovementioned three scenarios could be found in Appendix A with the relationship illustrated in Figure 10.

Figure 11 depicts the evolution of the intrinsic permeability and water/gas relative permeabilities of scenarios B and C. Comparison of Figures 9 and 11(a) shows that during water injection, the intrinsic permeability in scenario B is greater than that in scenario A; more water is injected into the fracture, thereby increasing the water saturation. Consequently, the water relative permeability rises, and the gas relative permeability declines. As seen in Figure 11(b), the intrinsic permeability obtained using the Langmuir function (scenario C) is greater than that acquired using the exponential function (scenario B), leading to a larger gas relative permeability and less water relative permeability. Comparing Figures 11(a) and 11(b), we find that the intrinsic permeability shows little difference between two scenarios, but its difference between the SRV and USRV regions is smaller in scenario C. In addition, the gas permeability of scenario C is significantly larger than that of scenario B.

Figure 12 illustrates the gas production rates of three scenarios. As observed in the figure, scenario C exhibits the highest production rate in the early production stage and then dramatically declines. This is because the intrinsic permeability obtained using the Langmuir function is significantly higher than that of the two other scenarios at the same downward pressure. Scenario B behaves most poorly during the whole production process. The main reason is that the linear growth of intrinsic permeability, which is greater than the exponential rise of permeability at the same water pressure, causes more water to be injected into
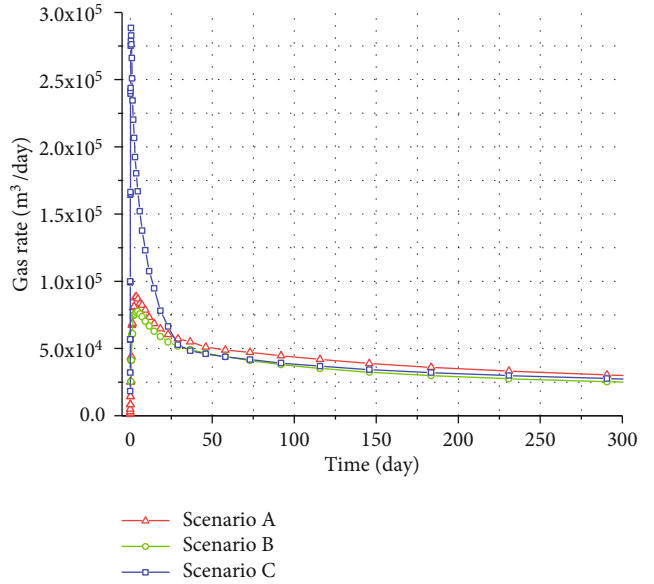
FIGURE 12: Gas production ratios of the three scenarios.

the fracture, which reduces the gas relative permeability. Under their combined effects, gas production is reduced.

5.4. Effect of Water Injection Time. The following scenarios are designed to sufficiently examine the effect of injection time on the gas production ratio: (i) scenario A (benchmark model), where intrinsic permeability is not affected by the water injection time; (ii) scenario B, where intrinsic permeability is linearly proportional to the water injection time; and (iii) scenario C, where intrinsic permeability has a Langmuir function relationship with the water injection time. The equations of the abovementioned three scenarios
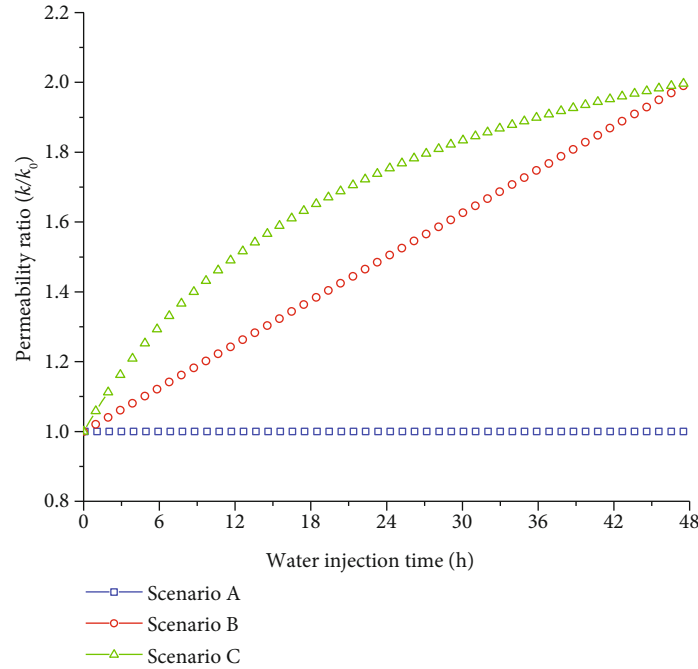
FIGURE 13: Intrinsic permeability variations with injection time.
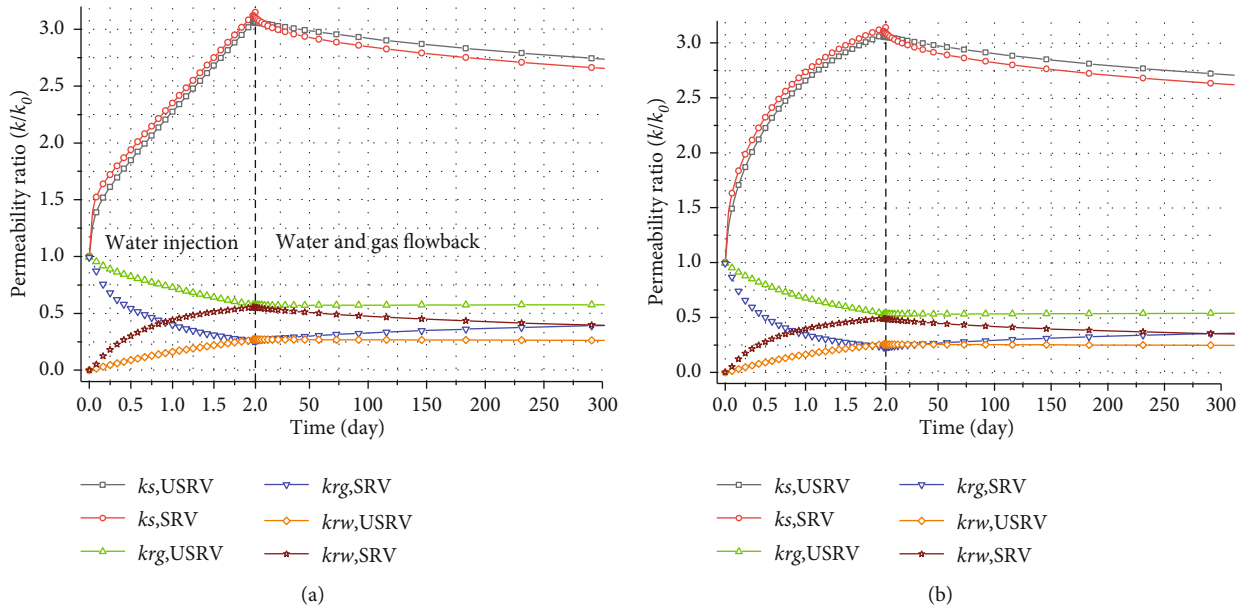
FIGURE 14: Gas/water relative permeability: (a) scenario B and (b) scenario C.

could be found in Appendix B with the relationship illustrated in Figure 13.

Figure 14 illustrates the evolutions of the intrinsic permeabilities and water/gas relative permeabilities of scenarios B and C. Comparison of Figures 9 and 14 indicate that during water injection, the intrinsic permeability of scenario B is almost twice that of scenario A. Therefore, after the water injection is completed, the water relative permeabilities in scenarios B and C are higher than that in scenario A.

Figure 15 illustrates the gas production rates of the three scenarios. From the figure, we can conclude that the production of scenarios B and C is significantly higher than that of scenario A. This is because the inherent intrinsic permeabilities of scenarios B and C are almost double that of scenario A after the water injection is completed. The gas production of scenario B is slightly higher than that of scenario C. The reason is that in scenario C, more water is injected, and the relative gas permeability is reduced.
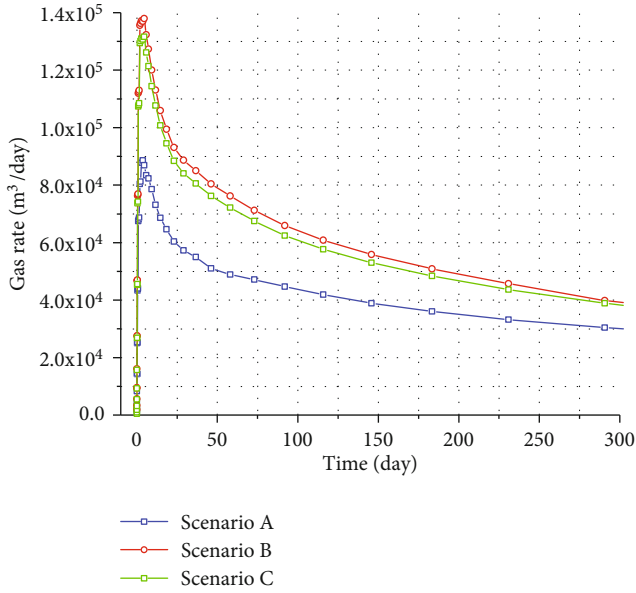
FIGURE 15: Gas production ratio of the three scenarios.

5.5. Comprehensive Effect of Water Injection Pressure and Time.

The comprehensive influences of water injection time and pressure on the gas depletion characteristic are examined by designing and solving nine computation scenarios. The water injection times are specified as 24, 48, and 72 h with the injection pressures defined as 20, 25, and 30 MPa. These two influencing factors are combined, and nine scenarios are obtained. In all scenarios, the intrinsic permeability has an exponential relationship with the water injection pressure and a linear relationship with the water injection time. The gas production ratios are shown in Figure 16. The gas production rate exhibits large differences between the scenarios, but no general variation laws can be identified. The scenario with 25 MPa and 48 h and the scenario with 30 MPa and 24 h show the largest gas production rates. The lowest values are observed in the scenario with 30 MPa and 48 h and the scenario with 30 MPa and 72 h. The performance of the rest of the scenarios is ranked randomly.

The nine scenarios are randomly arranged for the following reasons. As discussed above, both intrinsic and relative permeabilities affect gas production. In these nine scenarios, a larger injection pressure and longer injection time will result in a larger intrinsic permeability, thus enhancing gas flow. On the contrary, a higher intrinsic permeability will allow more water to flow into the reservoir, thereby decreasing gas relative permeability and hindering gas flow. Therefore, the gas production behavior is dominated by two competing mechanisms: increased intrinsic permeability and reduced gas relative permeability. Therefore, the impact of water injection pressure and water injection time on gas production should be considered systematically when designing HF and gas production processes. A higher water injection pressure and longer water injection time could improve reservoir intrinsic permeability to a greater extent; however, it would simultaneously cause more water to enter the reservoir and reduce the relative gas permeability, thereby dampening gas production.
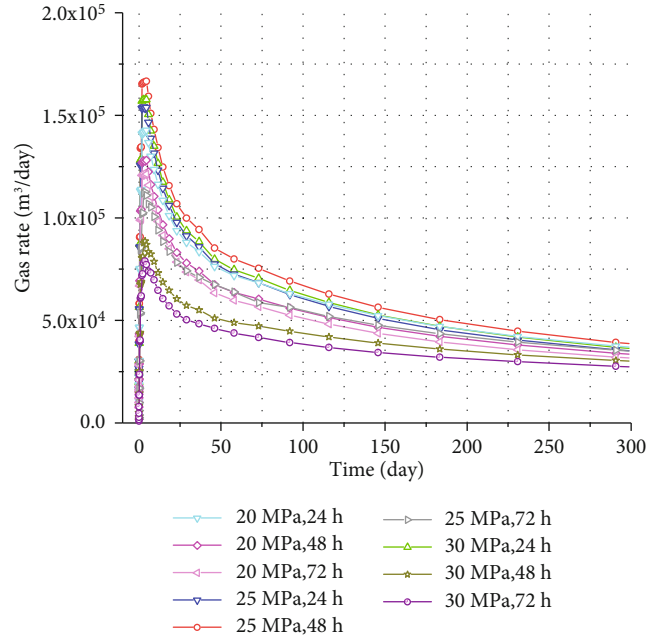
FIGURE 16: Evolution of the gas production ratio at different water injection pressures and water injection times.

5.6. Limitations

5.6.1. Assumed Permeability Relationships.

In this work, the relationships between reservoir intrinsic permeability, water injection pressure, and water injection time are artificially assumed and two different forms are proposed. Generally, the maximum tensile stress criterion or the Mohr–Coulomb criterion is applied to describe the permeability evolutions during the hydraulic fracturing process, while the main job of this work is to provide a feasible approach to investigate the impact of water injection or gas production. To achieve this goal, the complicated damage process is not considered.

5.6.2. Intrinsic Permeability Model.

In this work, a simple function (Eq. (22)) was adopted to describe the intrinsic permeability evolution in not only the water injection process but also the gas production process. This approach ignores the impacts of gas adsorption, interactions between matrix and fracture systems, and in situ geostress. This would certainly affect the determined gas production characteristics. Nonetheless, this impact is negligible for the following reasons: (i) compared with coalbed methane, the gas adsorption behavior is much smaller and has little impact on the gas permeability evolution. (ii) The interactions between matrix and fracture systems change the way permeability evolves but not its trend. (iii) In situ geostress changes due to water injection and gas production are not considered in this work. Only the change in effective stress created by pore pressure variations is studied. This work focuses on the effect of water injection pressure and time, instead of permeability laws, on gas production characteristics. Therefore, a convenient and widely used permeability model was applied.

6. Summary and Conclusions

A triple-porosity, two-phase flow model was established and applied in this paper to examine the impact of hydraulic water on shale gas production characteristics. Different from the previous works which only investigate the water injection process, we paid our attention to the whole shale gas exploration process—both water injection and gas depletion processes. In particular, the evolutions of both intrinsic and relative permeabilities were investigated. According to the results of the studied case and numeric simulations, the following conclusions were drawn:

(1) A shale reservoir can be divided into a fracture system, inorganic matrix, and organic matrix. HF fluid enters the fracture and inorganic matrix, with connate water existing in the inorganic matrix and organic matter. History matching with field gas production data verified that the proposed model can be applied to describe the evolution of physical quantities in not only the water injection stage but also the gas production stage in a shale reservoir

(2) The evolutions of both relative and intrinsic permeabilities in the hydraulic fracturing and gas depletion processes were studied. The water relative permeability increases in the reservoir stimulation process due to water imbibition and then declines in the gas production stage. On the contrary, the gas relative permeability is below the original value because of the water imbibition. The intrinsic permeability increases during water injection but decreases during gas production

(3) Gas production behavior is dominated by two competing mechanisms. Increasing the water injection pressure and prolonging the water injection time would produce more cracks, thereby increasing intrinsic permeability; more water will enter the cracks and inorganic matter, thus restricting gas production. For maximum efficiency of gas extraction, the perfect combination of an appropriate injection time and injection pressure was devised in the current simulation

(4) The relationships of intrinsic permeability with water injection pressure and water injection time were particularly specified. However, the details of these relationships remain debatable, and more work is required. Nonetheless, this work can shed light on the field application of HF

Appendix

A. Relationship of Permeability with Water Injection Pressure

The specific expressions and parameter values of scenarios B and C were as follows:

Scenario B: linear relationship

$$\frac{k}{k_0} = 1 + c_f \times (p_w - p_0), \tag{A.1}$$

where $p_0 = 0.1$ MPa and $c_f = 0.0255$ MPa^{-1}.

Scenario C: Langmuir function relationship

$$\frac{k}{k_0} = 1 + \left(\frac{p}{p + p_l} - \frac{p_0}{p_0 + p_l}\right) \tag{A.2}$$

where $p_l = 10$ MPa.

The intrinsic permeability variations with respect to the water injection pressure of the three scenarios are shown in Figure 10. As illustrated in the figure, the value of scenario C is the largest and that of scenario A is the smallest.

B. Relationship of Permeability with Water Injection Time

The specific expressions and parameter values were as follows:

Scenario B: linear relationship

$$\frac{k}{k_0} = 1 + \alpha \times t, \tag{B.1}$$

where $\alpha = 1/48$ h^{-1}.

Scenario C: Langmuir function relationship

$$\frac{k}{k_0} = 1 + \left(1.5 \times \frac{t}{t + \beta}\right), \tag{B.2}$$

where $\beta = 24$ h.

Nomenclature

m: Flow mass
p: Pressure
ρ: Density
S: Saturation
J: Mass flux
V_L: Solid-gas saturated adsorption volume
V_H: Liquid-gas saturated adsorption capacity
r: Pore radius
λ: Pore size distribution parameter
ω: Shape factor
$\mathbf{g}$: Gravitational acceleration
μ: Viscosity
φ: Porosity
Q: Flow source or sink
Kn: Knudsen number
P_L: Adsorption pressure constant
β: Water molecular coverage ratio
h: Water molecular layer thickness
σ: Stress
c_f: Fracture compressibility

Subscripts

w: Water
f: Fracture system
cl: Clay mineral
max: Maximum
c: Capillary pressure
r: Relative permeability
g: Gas
in: Inorganic matrix system
or: Organic matter system
eq: Equilibrium state
e: Nonwetting phase entry pressure
Ef: Effective stress.

Data Availability

All data included in this study are available upon request by contact with the corresponding author.

Conflicts of Interest

We declare that there are no commercial (or related) interests and any other conflict of interest regarding the submitted work.

Acknowledgments

References

[1] A. Vafaie, B. Habibnia, and S. A. Moallemi, "Experimental investigation of the pore structure characteristics of the Garau gas shale formation in the Lurestan Basin, Iran," *Journal of Natural Gas Science and Engineering*, vol. 27, pp. 432–442, 2015.

[2] G. Cui, J. Liu, M. Wei, X. Feng, and D. Elsworth, "Evolution of permeability during the process of shale gas extraction," *Journal of Natural Gas Science and Engineering*, vol. 49, pp. 94–109, 2018.

[3] G. Cui, J. Liu, M. Wei, R. Shi, and D. Elsworth, "Why shale permeability changes under variable effective stresses: new insights," *Fuel*, vol. 213, pp. 55–71, 2018.

[4] S. Wang, C. Qin, Q. Feng, F. Javadpour, and Z. Rui, "A framework for predicting the production performance of unconventional resources using deep learning," *Applied Energy*, vol. 295, article 117016, 2021.

[5] Y. Cheng, "Impact of water dynamics in fractures on the performance of hydraulically fractured wells in gas-shale reservoirs," *Journal of Canadian Petroleum Technology*, vol. 51, no. 2, pp. 143–151, 2012.

[6] J. Xu, L. Xu, and Y. Qin, "Two effective methods for calculating water saturations in shale-gas reservoirs," *Geophysics*, vol. 82, no. 3, pp. D187–D197, 2017.

[7] J. Li, Z. X. Chen, X. F. Li et al., "A quantitative research of water distribution characteristics inside shale and clay nanopores," *Scientia Sinica Technologica*, vol. 48, no. 11, pp. 1219–1233, 2018.

[8] H. Xiong, D. Devegowda, and L. Huang, "Water bridges in clay nanopores: mechanisms of formation and impact on hydrocarbon transport," *Langmuir*, vol. 36, no. 3, pp. 723–733, 2020.

[9] J. Li, X. Li, K. Wu et al., "Water sorption and distribution characteristics in clay and shale: effect of surface force," *Energy & Fuels*, vol. 30, no. 11, pp. 8863–8874, 2016.

[10] H. Yanagihara, K. Yamashita, A. Endo, and H. Daiguji, "Adsorption–desorption and transport of water in two-dimensional hexagonal mesoporous silica," *The Journal of Physical Chemistry C*, vol. 117, no. 42, pp. 21795–21802, 2013.

[11] F. P. Wang and R. M. Reed, "Pore networks and fluid flow in gas shales," in *SPE Annual Technical Conference and Exhibition*, p. 8, New Orleans, Louisiana, 2009.

[12] D. A. Handwerger, D. M. Willberg, M. Pagels, B. Rowland, and J. F. Keller, "Reconciling retort versus Dean Stark measurements on tight shales," in *SPE Annual Technical Conference and Exhibition*, p. 14, San Antonio, Texas, USA, 2012.

[13] L. Xinjing, H. Suyun, and C. Keming, "Suggestions from the development of fractured shale gas in North America," *Petroleum Exploration and Development*, vol. 34, p. 2, 2007.

[14] G. Cui, Y. Tan, T. Chen et al., "Multidomain two-phase flow model to study the impacts of hydraulic fracturing on shale gas production," *Energy & Fuels*, vol. 34, no. 4, pp. 4273–4288, 2020.

[15] W. Yuan, X. Li, Z. Pan, L. D. Connell, S. Li, and J. He, "Experimental investigation of interactions between water and a lower Silurian Chinese shale," *Energy & Fuels*, vol. 28, no. 8, pp. 4925–4933, 2014.

[16] T. Zhang, X. Li, Z. Sun et al., "An analytical model for relative permeability in water-wet nanoporous media," *Chemical Engineering Science*, vol. 174, pp. 1–12, 2017.

[17] R. van Noort and V. Yarushina, "Water, CO_2 and argon permeabilities of intact and fractured shale cores under stress," *Rock Mechanics and Rock Engineering*, vol. 52, no. 2, pp. 299–319, 2019.

[18] J. Gao and Z. Li, "Water saturation-driven evolution of helium permeability in Carboniferous shale from Qaidam Basin, China: an experimental study," *Marine and Petroleum Geology*, vol. 96, pp. 371–390, 2018.

[19] M. Achang, J. C. Pashin, and E. A. Atekwana, "The influence of moisture on the permeability of crushed shale samples," *Petroleum Science*, vol. 16, no. 3, pp. 492–501, 2019.

[20] J. Zhang, Q. Feng, X. Zhang, Q. Hu, J. Yang, and N. Wang, "A novel data-driven method to estimate methane adsorption isotherm on coals using the gradient boosting decision tree: a case study in the Qinshui Basin, China," *Energies*, vol. 13, no. 20, p. 5369, 2020.

[21] Z. Jin and A. Firoozabadi, "Effect of water on methane and carbon dioxide sorption in clay minerals by Monte Carlo simulations," *Fluid Phase Equilibria*, vol. 382, pp. 10–20, 2014.

[22] J. Li, S. Wang, S. Lu et al., "Microdistribution and mobility of water in gas shale: a theoretical and experimental study," *Marine and Petroleum Geology*, vol. 102, pp. 496–507, 2019.

[23] M. Gasparik, P. Bertier, Y. Gensterblum, A. Ghanizadeh, B. M. Krooss, and R. Littke, "Geological controls on the methane storage capacity in organic-rich shales," *International Journal of Coal Geology*, vol. 123, pp. 34–51, 2014.

[24] Z. Liu, D. Liu, Y. Cai, Y. Yao, Z. Pan, and Y. Zhou, "Application of nuclear magnetic resonance (NMR) in coalbed methane and shale reservoirs: A review," *International Journal of Coal Geology*, vol. 218, article 103261, 2020.

[25] L. Wang and Q. Yu, "The effect of moisture on the methane adsorption capacity of shales: a study case in the eastern Qaidam Basin in China," *Journal of Hydrology*, vol. 542, pp. 487–505, 2016.

[26] C. R. Clarkson and J. Williams-Kovacs, "Modeling two-phase flowback of multifractured horizontal wells completed in shale," *SPE Journal*, vol. 18, no. 4, pp. 795–812, 2013.

[27] J. Zhang, Q. Feng, X. Zhang et al., "Multi-fractured horizontal well for improved coalbed methane production in eastern Ordos basin, China: field observations and numerical simulations," *Journal of Petroleum Science and Engineering*, vol. 194, article 107488, 2020.

[28] J. Williams-Kovacs and C. Clarkson, "A modified approach for modelling 2-phase flowback from multi-fractured horizontal shale gas wells. Unconventional Resources Technology Conference," in *Unconventional Resources Technology Conference*, San Antonio, Texas, USA, 2015.

[29] R. Yang, Z. Huang, G. Li et al., "An innovative approach to model two-phase flowback of shale gas wells with complex fracture networks," in *SPE Annual Technical Conference and Exhibition*, Dubai, 2016.

[30] X. Shang, J. Wang, and Z. Zhang, "Iterative analytical solutions for nonlinear two-phase flow with gas solubility in shale gas reservoirs," *Geofluids*, vol. 2019, Article ID 4943582, 15 pages, 2019.

[31] G. Cui, F. Xia-Ting, Z. Pan et al., "Impact of shale matrix mechanical interactions on gas transport during production," *Journal of Petroleum Science and Engineering*, vol. 184, article 106524, 2020.

[32] Y. Luo and J.-P. Ampuero, "Stability of faults with heterogeneous friction properties and effective normal stress," *Tectonophysics*, vol. 733, pp. 257–272, 2018.

[33] P. Cao, J. Liu, and Y.-K. Leong, "A multiscale-multiphase simulation model for the evaluation of shale gas recovery coupled the effect of water flowback," *Fuel*, vol. 199, pp. 191–205, 2017.

[34] W. Li, J. Liu, J. Zeng, Y. K. Leong, and D. Elsworth, "A fully coupled multidomain and multiphysics model for shale gas production," in *5th ISRM Young Scholars' Symposium on Rock Mechanics and International Symposium on Rock Engineering for Innovative Future*, Okinawa, Japan, 2019.

[35] W. Li, J. Liu, J. Zeng et al., "A fully coupled multidomain and multiphysics model for evaluation of shale gas extraction," *Fuel*, vol. 278, article 118214, 2020.

[36] C. Chen, D. Hu, D. Westacott, and D. Loveless, "Nanometer-scale characterization of microscopic pores in shale kerogen by image analysis and pore-scale modeling," *Geochemistry Geophysics Geosystems*, vol. 14, no. 10, pp. 4066–4075, 2013.

[37] A. Mehmani, M. Prodanović, and F. Javadpour, "Multiscale, multiphysics network modeling of shale matrix gas flows," *Transport in Porous Media*, vol. 99, no. 2, pp. 377–390, 2013.

[38] R. J. Ambrose, R. C. Hartman, M. D. Campos, I. Y. Akkutlu, and C. Sondergeld, "New pore-scale considerations for shale gas in place calculations," in *SPE Unconventional Gas Conference*, Pittsburgh, Pennsylvania, USA, 2010.

[39] I. Y. Akkutlu and E. Fathi, "Multiscale gas transport in shales with local kerogen heterogeneities," *SPE Journal*, vol. 17, no. 4, pp. 1002–1011, 2012.

[40] A. Wasaki and I. Y. Akkutlu, "Permeability of organic-rich shale," in *SPE Annual Technical Conference and Exhibition*, Amsterdam, The Netherlands, 2014.

[41] S. Wang, Q. Feng, F. Javadpour, M. Zha, and R. Cui, "Multiscale modeling of gas transport in shale matrix: an integrated study of molecular dynamics and rigid-pore-network model," *SPE Journal*, vol. 25, no. 3, pp. 1416–1442, 2020.

[42] S. Wang, X. Yao, Q. Feng et al., "Molecular insights into carbon dioxide enhanced multi-component shale gas recovery and its sequestration in realistic kerogen," *Chemical Engineering Journal*, vol. 425, article 130292, 2021.

[43] J. G. Wang, Y. Ju, F. Gao, and J. Liu, "A simple approach for the estimation of CO_2 penetration depth into a caprock layer," *Journal of Rock Mechanics and Geotechnical Engineering*, vol. 8, no. 1, pp. 75–86, 2016.

[44] A. Millard, A. Bond, S. Nakama, C. Zhang, J.-D. Barnichon, and B. Garitte, "Accounting for anisotropic effects in the prediction of the hydro-mechanical response of a ventilated tunnel in an argillaceous rock," *Journal of Rock Mechanics and Geotechnical Engineering*, vol. 5, no. 2, pp. 97–109, 2013.

[45] P. Tan, Y. Jin, K. Han et al., "Analysis of hydraulic fracture initiation and vertical propagation behavior in laminated shale formation," *Fuel*, vol. 206, pp. 482–493, 2017.

[46] G. Cui, J. Wei, X.-T. Feng et al., "Preliminary study on the feasibility of co-exploitation of coal and uranium," *International Journal of Rock Mechanics and Mining Sciences*, vol. 123, article 104098, 2019.

[47] T. Y. Chen, X. T. Feng, and Z. J. Pan, "Experimental study of swelling of organic rich shale in methane," *International Journal of Coal Geology*, vol. 150-151, pp. 64–73, 2015.

[48] T. Chen, X.-T. Feng, and Z. Pan, "Experimental study on kinetic swelling of organic-rich shale in CO_2, CH_4 and N_2," *Journal of Natural Gas Science and Engineering*, vol. 55, pp. 406–417, 2018.

[49] F. Yang, C. Xie, Z. Ning, and B. M. Krooss, "High-pressure methane sorption on dry and moisture-equilibrated shales," *Energy & Fuels*, vol. 31, no. 1, pp. 482–492, 2017.

[50] T. Ma, K. Zhang, W. Shen, C. Guo, and H. Xu, "Discontinuous and continuous Galerkin methods for compressible single-phase and two-phase flow in fractured porous media," *Advances in Water Resources*, vol. 156, article 104039, 2021.

[51] T. Ma, J. Rutqvist, C. M. Oldenburg, W. Liu, and J. Chen, "Fully coupled two-phase flow and poromechanics modeling of coalbed methane recovery: impact of geomechanics on production rate," *Journal of Natural Gas Science and Engineering*, vol. 45, pp. 474–486, 2017.

[52] Z. Wei and D. Zhang, "A fully coupled multiphase multicomponent flow and geomechanics model for enhanced coalbed-methane recovery and CO2 storage," *SPE Journal*, vol. 18, no. 3, pp. 448–467, 2013.

[53] J. G. Wang and Y. Peng, "Numerical modeling for the combined effects of two-phase flow, deformation, gas diffusion and CO_2 sorption on caprock sealing efficiency," *Journal of Geochemical Exploration*, vol. 144, pp. 154–167, 2014.

[54] W. Yuan, Z. Pan, X. Li et al., "Experimental study and modelling of methane adsorption and diffusion in shale," *Fuel*, vol. 117, pp. 509–519, 2014.

[55] L. Wang, M. Bornert, E. Héripré, S. Chanchole, A. Pouya, and B. Halphen, "Microscale insight into the influence of humidity on the mechanical behavior of mudstones," *Journal of Geophysical Research: Solid Earth*, vol. 120, no. 5, pp. 3173–3186, 2015.

[56] J. G. Wang, A. Kabir, J. Liu, and Z. Chen, "Effects of non-Darcy flow on the performance of coal seam gas wells," *International Journal of Coal Geology*, vol. 93, pp. 62–74, 2012.

[57] R. Aringhieri, "Nanoporosity characteristics of some natural clay minerals and soils," *Clays and Clay Minerals*, vol. 52, no. 6, pp. 700–704, 2004.

[58] W. Shen, X. Li, T. Ma, J. Cai, X. Lu, and S. Zhou, "High-pressure methane adsorption behavior on deep shales: experiments and modeling," *Physics of Fluids*, vol. 33, no. 6, article 063103, 2021.

[59] J. Li, X. Li, X. Wang et al., "Water distribution characteristic and effect on methane adsorption capacity in shale clay," *International Journal of Coal Geology*, vol. 159, pp. 135–154, 2016.

[60] J. Zhang, B. Zhang, S. Xu, Q. Feng, X. Zhang, and D. Elsworth, "Interpretation of gas/water relative permeability of coal using the hybrid Bayesian-assisted history matching: new insights," *Energies*, vol. 14, no. 3, p. 626, 2021.

[61] R. H. Brooks and A. T. Corey, "Hydraulic properties of porous media and their relation to drainage design," *Transactions of the ASAE*, vol. 7, no. 1, pp. 0026–0028, 1964.

[62] M. T. Van Genuchten, "A closed-form equation for predicting the hydraulic conductivity of unsaturated soils," *Soil Science Society of America Journal*, vol. 44, no. 5, pp. 892–898, 1980.

[63] M. Leverett, "Capillary behavior in porous solids," *Transactions of the AIME*, vol. 142, no. 1, pp. 152–169, 1941.

[64] D. S. Lee, J. D. Herman, D. Elsworth, H. T. Kim, and H. S. Lee, "A critical evaluation of unconventional gas recovery from the Marcellus Shale, northeastern United States," *KSCE Journal of Civil Engineering*, vol. 15, no. 4, pp. 679–687, 2011.

[65] B. R. Meyer, L. W. Bazan, R. H. Jacot, and M. G. Lattibeaudiere, "Optimization of multiple transverse hydraulic fractures in horizontal wellbores," in *SPE Unconventional Gas Conference*, Pennsylvania, USA, 2010.

[66] W. Yu and K. Sepehrnoori, "Simulation of gas desorption and geomechanics effects for unconventional gas reservoirs," *Fuel*, vol. 116, pp. 455–464, 2014.

[67] W. Yu, T. T. Zhang, S. du, and K. Sepehrnoori, "Numerical study of the effect of uneven proppant distribution between multiple fractures on shale gas well performance," *Fuel*, vol. 142, pp. 189–198, 2015.

[68] Y. Tan, Z. Pan, J. Liu, X.-T. Feng, and L. D. Connell, "Laboratory study of proppant on shale fracture permeability and compressibility," *Fuel*, vol. 222, pp. 83–97, 2018.

WILEY | Hindawi

Research Article

Numerical Simulation of Coupled Thermal-Hydrological-Mechanical-Chemical Processes in the Spontaneous Combustion of Underground Coal Seams

Yuntao Liang (ID) **and Rui Zhou** (ID)

State Key Laboratory of Coal Mine Safety Technology, China Coal Technology & Engineering Group Shenyang Research Institute, Shenfu Demonstration Zone 113122, China

Correspondence should be addressed to Rui Zhou; zhouruicumt@126.com

In this study, we develop a fully coupled thermal-hydrological-mechanical-chemical (THMC) model to analyze the spontaneous combustion process of underground coal seams, focusing on investigating the influences of the pressure difference between oxygen and coal, the rate of coal-oxygen reaction heat, and the activation energy. The simulation results show that as oxygen propagates into the coal seams, the coal-oxygen reaction causes the spontaneous combustion of coal to heat. The consumption of oxygen leads to an increase in oxygen consumption along the way and a decrease in gas pressure. The permeability near the right boundary increases while significantly reducing the area far away from the right boundary as the predominant effect of spontaneous combustion. Additionally, a sensitivity study shows that a more considerable pressure difference and coal-oxygen reaction heat contribute to promoting the coal temperature, while the activation energy has a slight effect. Moreover, an increase in coal-oxygen reaction heat and activation energy accelerates the oxygen consumption rate and thus causes a lower oxygen concentration. Overall, the results provide a basis for the prediction and prevention of coal seam spontaneous combustion.

1. Introduction

The problem of coal seam spontaneous combustion is recognized as an urgent problem in coal production, which has the potential possibility leading to production accidents such as gas explosions, as well as severe economic and environmental problems [1–6]. In China, nearly 100-200 million tons of coal are lost to spontaneous combustion every year. Additionally, CO_2 content produced by spontaneous combustion accounts for 2-3% of global carbon emissions [7].

The process of coal spontaneous combustion is believed to be a complex physical and chemical process, including the contact and flow of coal and oxygen in the cracks of the coal seam, the accumulation and diffusion of heat when oxygen is sufficient, the distribution of temperature fields, and the transfer of energy [5, 6, 8]. Wu et al. [9] studied the influence of air and dust on the com-

bustion process near the spontaneous combustion point of coal by numerical analysis of the kinetic equation. Su et al. [10] analyzed the influence of coal seam inclination and airflow on coal spontaneous combustion by establishing a three-dimensional model. Xia et al. [11] showed a coupled modeling of coal seam heat flow solidification. The effect of gas expansion changes in pressure gradient on gas seepage and heat transfer is investigated. Zongqing [12] studied the competitive adsorption relationship among multicomponent gases in the spontaneous combustion process of underground coal seams and the influence of gas concentration on the development of coal pores. Xia et al. [13] studied the interaction of multiphysics coupling during the spontaneous combustion of methane-rich coal seams. The simulation results showed that the resolved methane gas dilutes the oxygen concentration and hinders oxygen migration in the porous medium. Liu and Qin [14] studied the mechanism of spontaneous combustion in the

coal seam from experiments, which demonstrates that the spontaneous combustion phenomenon is the interaction and coupling of the internal pressure, velocity, oxygen concentration field, gas, and coal solid temperature field in the coal seam. Hongfen et al. [15] considered coupling factors of the mechanical, temperature, seepage, mass transfer, and other multiphysical fields. They summarized the location and change law of both high temperature and high displacement areas in the process of coal spontaneous combustion.

In the combustion process, the rock mechanics simulation of underground spontaneous coal seams shows that the shrinkage of coal seams and changes in mechanical properties lead to the collapse of the overlying rock layer and larger fissures accelerating the combustion process [3, 16]. Based on the gas percolation and temperature diffusion in spontaneous combustion coal seams, Huang et al. [17] concluded that the coal seam permeability is greater than 10^{-9} m^2 in order for the gas to fully diffuse and circulate into the coal spontaneous combustion process. Meanwhile, the heat transfer method is dominated by heat convection in shallow coal seams. Heat transfer is dominated by heat conduction in the combustion of deep coal seams. Wen [18] established a super large-scale spontaneous combustion experiment platform, which considers the actual on-site situation and the critical value of the coal temperature change rate during the combustion process. Song and Kuenzer [19] considered the limited influence of oxygen convection and diffusion and mass transfer process on the reaction rate in coal fire oxidation and combustion and deduced the calculation formula of coal oxidation and combustion rate in the high-temperature stage of coal fire. Fusheng et al. [20] studied the influence of the pore structure characteristics of coal samples on the spontaneous combustion of coal by an experimental method. Wessling et al. [21] separated the spontaneous combustion process of coal into different stages. They performed a multiphysics coupling numerical simulation and investigated the influence of coal seam permeability anisotropy on coal spontaneous combustion. Wen et al. [22] used different gas flow equations to construct three coupling models. The influence of gas seepage on the temperature distribution in the natural process of coal is explored. Dudzińska and Cygankiewicz [23] analyzed the impact of the gas produced and the gas adsorbed by the coal body through experiments. Lu [24] established a mathematical model to investigate the influence of plastic deformation on porosity and combustion effect caused by coal spontaneous combustion, which is used to analyze the on-site examples.

Considering the coupling of multiphysics is an attractive and effective method for studying coal seam spontaneous combustion. However, due to the complexity of the theoretical equations, the differences in boundary conditions and initial conditions significantly cause variations in the process of each physics. In this paper, we establish a fully coupled thermal-hydrological-mechanical-chemical (THMC) model to study the spontaneous combustion process of coal seams. Then, we investigate the influences

of the pressure difference between oxygen and coal, the rate of coal-oxygen reaction heat, and the activation energy.

2. Governing Equations of Coupled THMC Model

The spontaneous combustion process of underground coal seams includes geomechanical deformation, gas seepage, oxygen component transmission, and heat energy transmission. The changes in temperature cause the deformation of coal and thus result in porosity and permeability evolution. The variation in porosity and permeability affects the behavior of flow and heat. This is a complicated two-way coupling relationship. The proposed model in this paper is derived based on the following assumptions:

(1) Coal is a homogeneous and isotropic elastic medium

(2) The deformation of coal satisfies the assumption of small deformation

(3) The influence of gas and moisture in coal on spontaneous combustion of coal is neglected

(4) The gas inside the pores and fractures of the coal is an ideal gas. The viscosity of gas keeps constant during the whole process

2.1. Coal Deformation Equations. Based on the constitutive relations of poroelasticity, the governing equation for coal deformation that considers desorption-induced strain and temperature-induced strain can be expressed as follows [25, 26]:

$$\sigma = \sigma' - \alpha \mathbf{I} p = \mathbf{C} : \varepsilon^e - \alpha \mathbf{I} p = D : (\varepsilon - \varepsilon_s - \varepsilon_T) - \alpha \mathbf{I} p, \quad (1)$$

where σ' and σ is effective and total stress, p is pore pressure, and $\mathbf{C}$ is the tangential stiffness matrix.

The relationship between total strain ε and displacement is shown as

$$\varepsilon = \frac{1}{2} \left(\nabla u + \nabla^T u \right). \quad (2)$$

The thermal strain and desorption-induced volumetric strain are calculated by

$$\varepsilon_T = \alpha_T \mathbf{I} \Delta T,$$
$$\varepsilon_s = \frac{\varepsilon_L p_m}{p_m + p_L} \exp \left\{ - \left[\frac{b_2 (T - T_0)}{1 + b_1 p_m} \right] \right\} \mathbf{I}, \quad (3)$$

where ΔT is the temperature change and α_T is the thermal expansion coefficient; ε_L and p_L represent Langmuir strain constant and Langmuir pressure constant, respectively; b_1 and b_2 are the pressure and temperature coefficients, respectively; and T_0 is the reference temperature.

2.2. Gas Flow Equations. In the dual-porosity and single permeability (DPSP) model, the mass conservation law of the
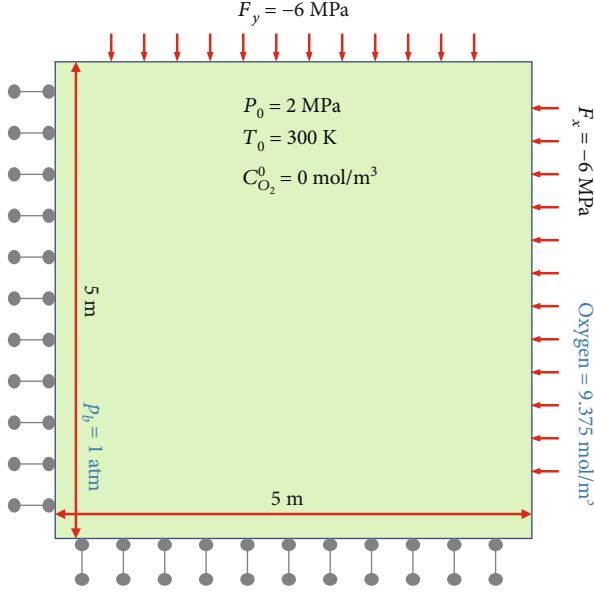
FIGURE 1: Geometric configurations with initial and boundary conditions.

FIGURE 2: Mesh discretization of the simulation domain.

coal matrix system can be described as the following:

$$\frac{\partial m_{\mathrm{m}}}{\partial t} = -Q(1 - \varphi_{\mathrm{f}}), \qquad (4)$$

where m_{m} represents the methane content per unit volume of the matrix, φ_{f} is the porosity of fracture, and Q is the mass exchange between coal matrix and fracture, which can be defined as

$$Q = D\chi \frac{M_{\mathrm{g}}}{RT}\left(p_m - p_f\right), \qquad (5)$$

where χ is the shape factor and M_{g} is molar mass of gas. In this study, we embed the new proposed nonlinear diffusion model into Equation (10), which depends on diffusion time, gas pressure, and temperature. The total methane content in the coal matrix consists of two components: free gas and adsorbed gas. Thus, the value of m_{m} can be given as follows:

$$m_{\mathrm{m}} = \varphi_{\mathrm{m}}\rho + \rho_a\rho_c V_{\mathrm{sg}}(1 - \varphi_{\mathrm{m}} - \varphi_{\mathrm{f}}), \qquad (6)$$

where φ_{m} is the porosity of matrix, ρ is gas density, ρ_a is the gas density under standard condition, ρ_c is coal density, and V_{sg} represent the adsorbed gas content in coal matrix, which is defined by Langmuir volume equation:

$$V_{\mathrm{sg}} = \frac{V_L p_m}{p_m + p_L} \exp\left\{-\left[\frac{b_2(T - T_0)}{1 + b_1 p_m}\right]\right\}, \qquad (7)$$

where V_L is the Langmuir volume constant.

TABLE 1: Parameters for the numerical simulation.

Parameter	Value	Unit
Young's modulus, E	3	GPa
Poisson's ratio, ν	0.30	1
Matrix porosity, φ_{m}	0.01	—
Fracture porosity, φ_{f}	0.03	—
The density of matrix, ρ_s	2300	kg/m³
Specific heat of matrix, C_s	1250	J/(kg·K)
Specific heat of gas, C_w	2160	J/(kg·K)
Thermal expansion coefficient, α_{T}	2.4×10^{-5}	K⁻¹
Langmuir pressure constant, p_{L}	2.7	MPa
Gas dynamic viscosity, μ	1.84×10^{-5}	Pa·s
Isosteric heat of adsorption, q_{st}	15000	J/mol
Langmuir strain constant, ε_{L}	0.005	—
Langmuir volume constant, V_{L}	0.045	m³/kg
Attenuation coefficient, λ	2×10^{-8}	—
Initial permeability, k_0	1×10^{-16}	m/s
Initial temperature, T_0	300	K
Thermal conductivity of coal, λ_s	0.2	W/(m·K)

Gas transport in fracture obeys Darcy's law and mass conservation law, so the governing equation for gas seepage in the fracture is expressed as [27]

$$\frac{\partial\left(\varphi_{\mathrm{f}}\rho + \rho_a\rho_c V_{\mathrm{sg}}(1 - \varphi_{\mathrm{m}} - \varphi_{\mathrm{f}})\right)}{\partial t} + \nabla \cdot \left(-\frac{k}{\mu}\rho\nabla p_f\right) = Q, \quad (8)$$

where k is cleat permeability, μ is the velocity of gas, and

(a) 1 day, temperature, T (K)

(b) 5 days, temperature, T (K)

(c) 10 days, temperature, T (K)

(d) 20 days, temperature, T (K)

FIGURE 3: The distributions of the temperature at t = 1, 5, 10, and 20 days.

Q is the source or sink of gas. In the model, the value of Q equals to the diffusion amount of gas in the matrix. Additionally, coal deformation has a significant impact on fracture porosity and permeability. Based on Reference [28] and cubic law, the porosity and permeability varying with mean effective stress are shown as Equations (9) and (10), respectively,

$$\varphi_f = \alpha_f + \left(\varphi_{f0} - \alpha_f\right) \exp\left(-\frac{\Delta\sigma'}{K}\right), \tag{9}$$

$$k = k_0 \left[\frac{\alpha_f}{\varphi_{f0}} + \frac{\left(\varphi_{f0} - \alpha_f\right)}{\varphi_{f0}} \exp\left(-\frac{\Delta\sigma'}{K}\right)\right]^3, \tag{10}$$

where σ' is effective stress and φ_{f0} and k_0 are the initial porosity of fracture and permeability, respectively. Substituting Equations (9) and (10) into Equation (8), we obtain

$$-\rho\frac{S}{K}\frac{\partial\sigma'}{\partial t} + \left(\frac{M_g\varphi_f}{RT} + \rho_a\rho_c V_{sg}(1 - \varphi_m - \varphi_f)\right)\frac{\partial p_f}{\partial t} \\ -\frac{\rho\varphi_f}{T}\frac{\partial T}{\partial t} + \nabla\cdot\left(-\frac{k}{\mu}\rho\nabla p_f\right) = Q, \tag{11}$$
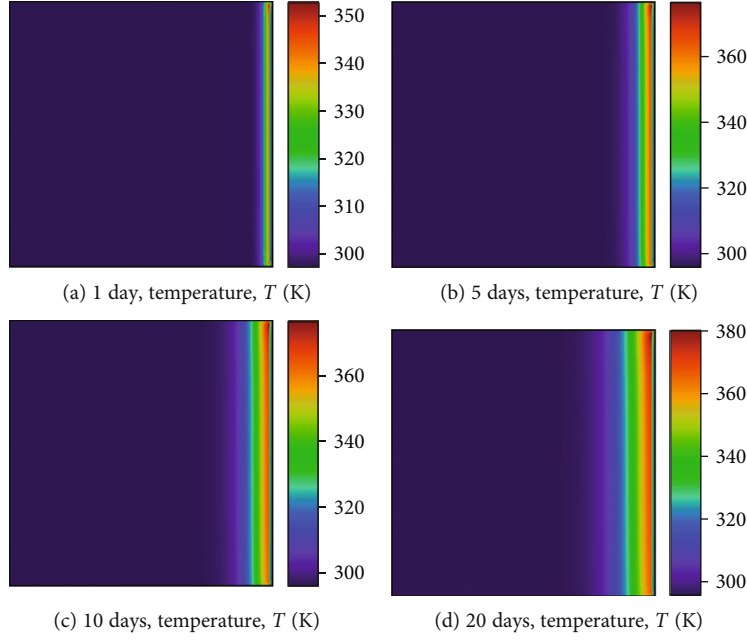
where $S = (\varphi_f - \alpha_f) \exp(-\Delta\sigma'/K)$.

2.3. Oxygen Transfer Equations. The mass conservation of oxygen component flow in porous media can be expressed

as [11, 13]

$$\varphi_f\frac{\partial c_k}{\partial t} + \nabla\cdot\left(-\varphi_f D_k\nabla c_k\right) + v_g\nabla c_k = -AC_{O_2}\exp\left(-\frac{E_a}{RT}\right), \tag{12}$$

where D_k is the gas diffusion coefficient, C_{O_2} are oxygen concentration and its reference value, A is preexponential factors, and E_a is the activation energy.

2.4. Heat Transfer Equations. Considering thermal dilatation of gas and coal, thermal convection, thermal conduction, and gas adsorption energy, the governing equation for heat transfer can be described as [29]

$$\frac{\partial[(\rho C)_M T]}{\partial t} + TK_g\alpha_g\nabla\cdot\left(-\frac{k}{\mu}\nabla p_f\right) + TK\alpha_T\frac{\partial\varepsilon_v}{\partial t}T + q_{st}\frac{\rho_c\rho_a}{M_g}\frac{\partial V_{sg}}{\partial t} \\ = -\nabla\left\{-\left[(1 - \varphi_f - \varphi_m)\lambda_s + (\varphi_f + \varphi_m)\lambda_g\right]\nabla T - \rho C_g\frac{k}{\mu}\nabla p_f T\right\} \\ + (1 - \phi)Q_h AC_{O_2}\exp\left(-\frac{E_a}{RT}\right), \tag{13}$$

where K_g is the bulk modulus of gas, $\alpha_g(\alpha_g = 1/T)$ is the thermal expansion coefficient of gas, Q_h is oxidation reaction heat, ε_v is volumetric strain, q_{st} is the isosteric heat of adsorption, C_g is gas-specific heat constant, λ_s and λ_g are thermal conductivities of coal and gas, respectively, and $(\rho C)_M$ represents specific heat capacity of gas-filled coal, which can be expressed as

$$(\rho C)_M = (\varphi_f + \varphi_m)\rho C_g + (1 - \varphi_f - \varphi_m)\rho_c C_s, \tag{14}$$
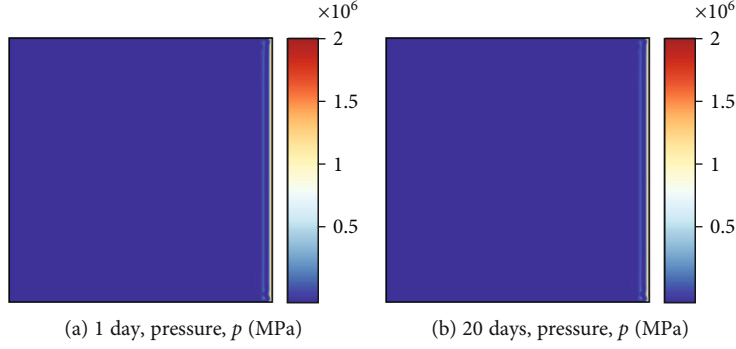
where C_s is the coal-specific heat constant.

(a) 1 day, pressure, p (MPa)

(b) 20 days, pressure, p (MPa)

FIGURE 4: The distributions of gas pressure at $t = 1$ and 20 days.

(a) 1 day, kk/k (-)

(b) 5 days, kk/k (-)

(c) 10 days, kk/k (-)

(d) 20 days, kk/k (-)
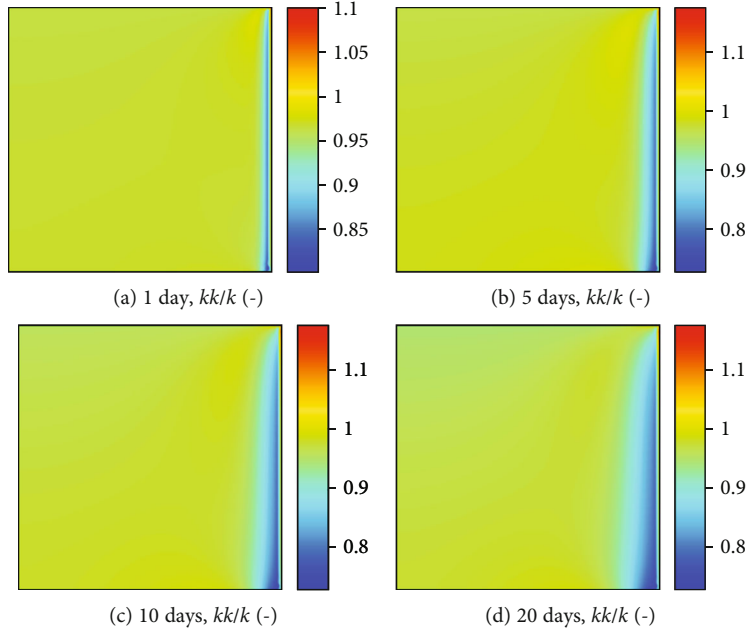
FIGURE 5: The distributions of permeability ratio at $t = 1$, 5, 10, and 20 days.

Assuming $(1 - \varphi_f - \varphi_m) \approx 1$, $(1 - \varphi_f - \varphi_m)\lambda_s \gg (\varphi_f + \varphi_m)\lambda_g$, and $K_g = p_f$ [30], Equation (13) evolves:

$$
\begin{aligned}
&\left[(\rho C)_M + \rho_c \rho_a \frac{q_{st}}{M} \frac{\partial V_{sg}}{\partial T} \right] \frac{\partial T}{\partial t} + \rho_c \rho_a \frac{q_{st}}{M} \frac{\partial V_{sg}}{\partial p_m} \frac{\partial p_m}{\partial t} \\
&+ TK\alpha_T \frac{\partial \varepsilon_v}{\partial t} + p_f \nabla \cdot \left(-\frac{k}{\mu} \nabla p_f \right) = \lambda_s \nabla^2 T \\
&+ \rho C_g \frac{k}{\mu} \nabla p_f \nabla T + + (1 - \phi) A C_{O_2} \exp\left(-\frac{E_a}{RT} \right).
\end{aligned}
\tag{15}
$$

3. Model Setup

In the proposed model, there are five variables $(p_m, p_f, c_k, T, \varepsilon_v, \text{or } \sigma')$ for the coupled mathematic model. All the variables are interactive, and all the governing equations are nonlinear partial differential equations (PDE). COMSOL Multiphysics software [31] is adopted to solve the complex problem, which provides a powerful PDE-based modeling environment. In this study, the coal deformation is calculated by the solid mechanics module with Equation (1). Four general PDE modules are utilized to address gas dynamic diffusion, gas flow, concentration transfer, and heat transfer with Equations (11), (12), and (15), respectively. We use the time-stepping method of the implicit backward differentiation formula (BDF), which is an implicit solver that adopts backward differentiation formulas with variable discretization order and automatic step-size selection. In the time step, the Newton-like method is used to solve the algebraic equations with automatic linearization. Then, the resulting linear equations are solved employing multifrontal massively parallel sparse (MUMPS) solvers.

The geometry of the two cases and mesh discretization of the simulation domain are shown in Figures 1 and 2, respectively. The size of the simulation domain is $5\,\text{m} \times 5\,\text{m}$. The simulation area is discretized into 6282 triangle elements and 200 edge elements. The initial temperature, pressure, and oxygen concentration are 300 K, 1 atm, and
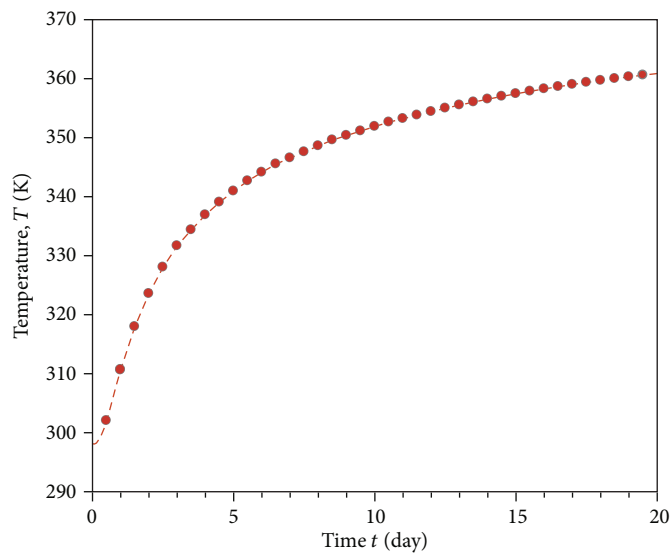
(a)
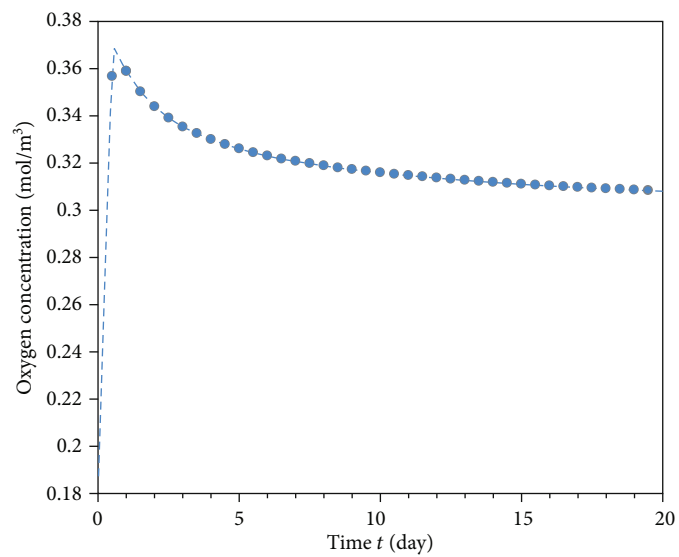
(b)

FIGURE 6: Continued.

(c)
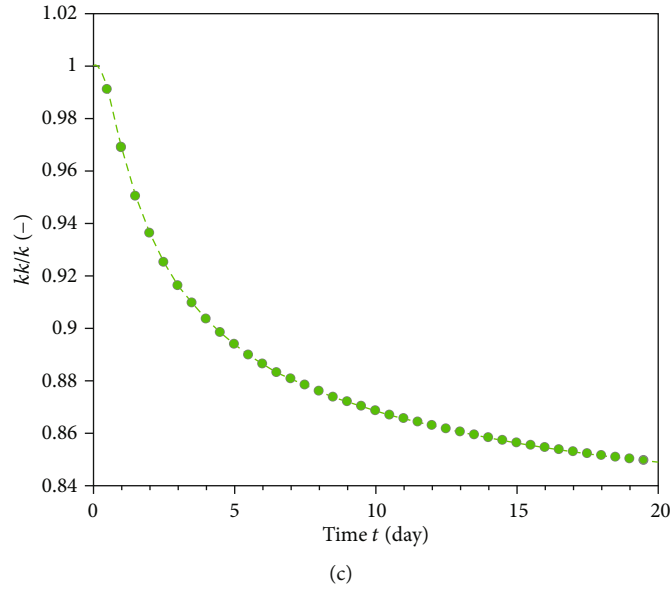
FIGURE 6: The evolution of temperature, oxygen concentration, and permeability ratio at monitoring point A.

$0 \, mol/m^3$. The right boundary is assigned as the oxygen injection boundary with $9.375 \, mol/m^3$. The pressure and temperature of the right-side boundary are 2 MPa and 300 K, while the left-side boundary has the same pressure and temperature values as the initial conditions. The remaining boundaries are imposed with thermal insulation and no-flow conditions. The domain has boundary loadings of 6 MPa on the left and upper boundaries for the mechanical boundaries. The lower and right boundaries are constrained with zero displacements. The numerical simulation is carried out in two steps. In the first step, we calculated the initial equilibrium state with a ramped loading under the in situ stress, pressure, and temperature conditions. In the second step, the above simulated results are obtained as the initial conditions for the second step. The loads and boundary conditions on a transient model are ramped up from values that are consistent with the initial values. The smoothed step functions are adopted to ramp the boundary condition. The specific simulation parameters are shown in Table 1.

4. Simulation Results

Figure 3 shows the spatial distributions of the temperature at $t = 1$, 5, 10, and 20 days. The simulated result shows that temperature increases with the continuous oxygen propagation into the coal seams. Moreover, the range of oxygen influence expands with the simulation time, which is about 1 meter far away from the right boundary after 20 days. Figure 4 shows the distributions of gas pressure at $t = 1$ and 20 days. The coal-oxygen reaction causes the spontaneous combustion of coal to heat up and oxygen consumption along the way. The heat-up of coal spontaneous combustion further aggravates the coal-oxygen reaction, resulting in an increase in oxygen consumption along

the way and a decrease in gas pressure. The high-temperature area is mainly concentrated in the area near the right boundary. Figure 5 shows the distributions of permeability ratio at $t = 1$, 5, 10, and 20 days. The expansion of the coal matrix caused by spontaneous combustion of coal causes the reduction of coal fracture opening. In contrast, the shrinkage of the coal matrix caused by gas dissociation results in the increase of the opening of coal fracture. The enhancement in permeability near the right boundary is observed, while the permeability in the area far away from the right boundary significantly reduces. Figure 6 shows the evolution of temperature, oxygen concentration, and permeability ratio at monitoring point A. After 20 days of spontaneous combustion of coal, the temperature generally increases up to about 360 K. The oxygen concentration at point A decreases with time after a short decrease. The maximum oxygen concentration inside the coal is about $3.65 \, kJ/mol^3$. The change of coal permeability is controlled by the combination of spontaneous combustion and shrinkage of the coal matrix. The permeability ratio reduced continually as the result of the predominated effect of spontaneous combustion of coal.

5. Sensitive Analysis

5.1. Effect of Pressure Difference. In this section, we investigate the influence of pressure difference between oxygen and coal. We perform three cases in which the right boundary is imposed with 2 MPa, 3 MPa, and 4 MPa, respectively. Figure 7 shows the evaluation of temperature and oxygen concentration with different pressure differences. It can be clearly seen that the greater the pressure difference causes, the higher the air leakage rate and greater oxidation heating rate of coal. The maximum temperature at point A increases from around 360 K to 480 K.

(a)

(b)
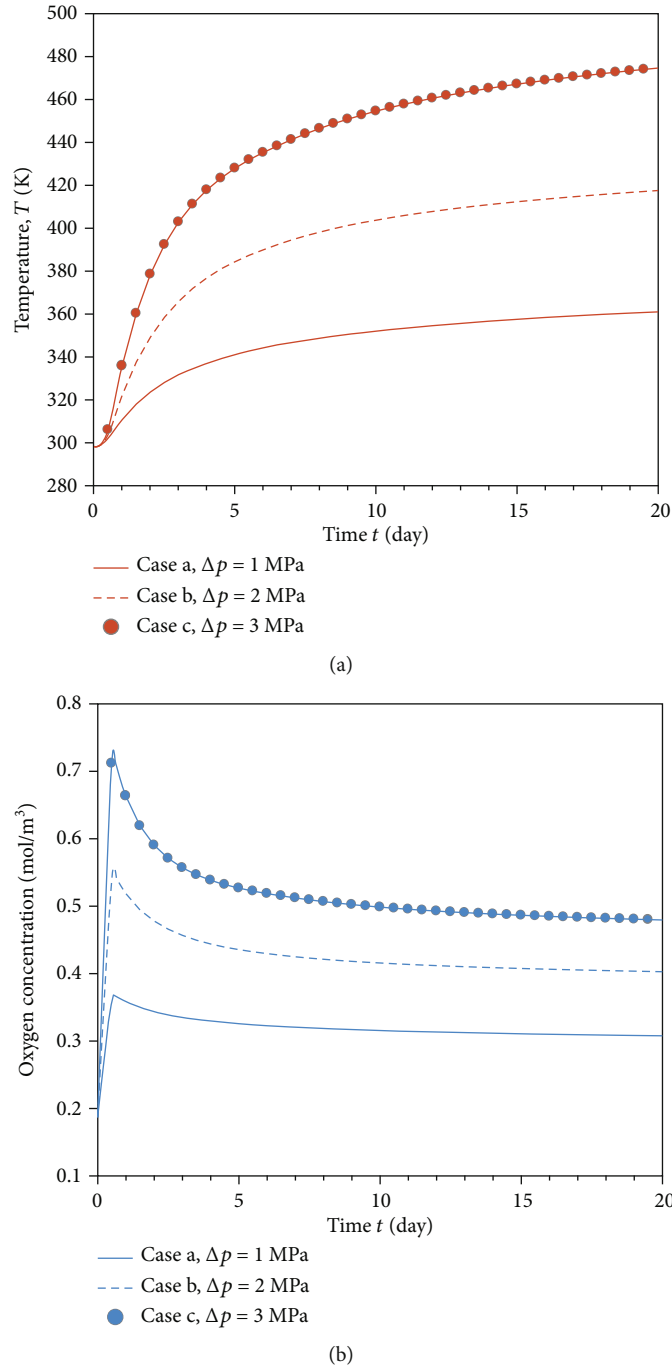
FIGURE 7: The evaluation of temperature and oxygen concentration with different pressure differences.

Case c has the largest oxygen concentration of 0.72 kJ/mol as more oxygen propagates inside the coal for the higher flow or transfer velocity.

5.2. Effect of Oxidation Reaction Heat. In this section, we carry out three cases of oxidation reaction heat $Q_n = 300$ kJ/mol, 350 kJ/mol, and 400 kJ/mol to the analysis of effect of heat released by coal oxidation. Figure 8 shows the evaluation of temperature and oxygen concentration with different values of coal-oxygen reaction heat. The temperatures in the three cases at point A are about 360 K, 370 K, and 380 K, respectively. The oxygen concentration is lower than the other two cases. It can be seen that the increase in the coal-oxygen reaction heat accelerates the oxygen consumption rate, thus resulting in a higher spontaneous combustion temperature.

5.3. Effect of Activation Energy. The influences of activation energy E_a are investigated in this section. Table 2 lists the activation energy E_a values for coal with low, medium, and high cases.

(a)

(b)
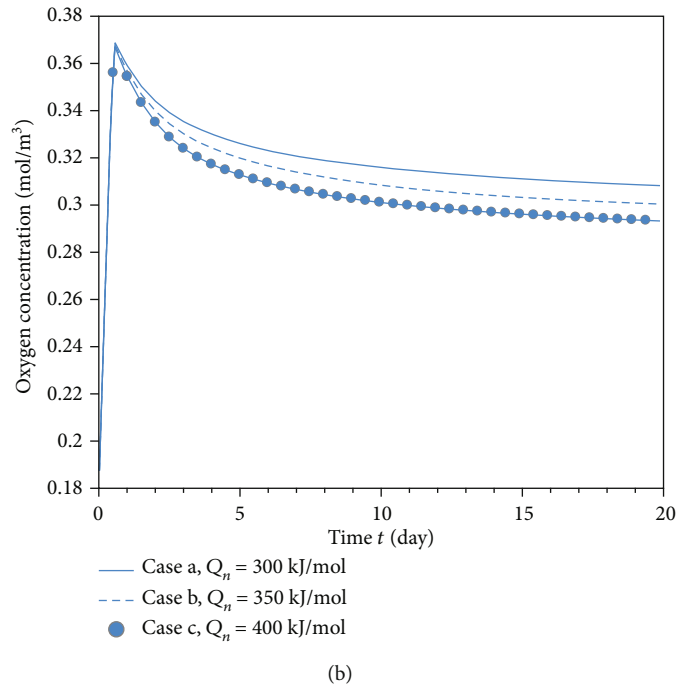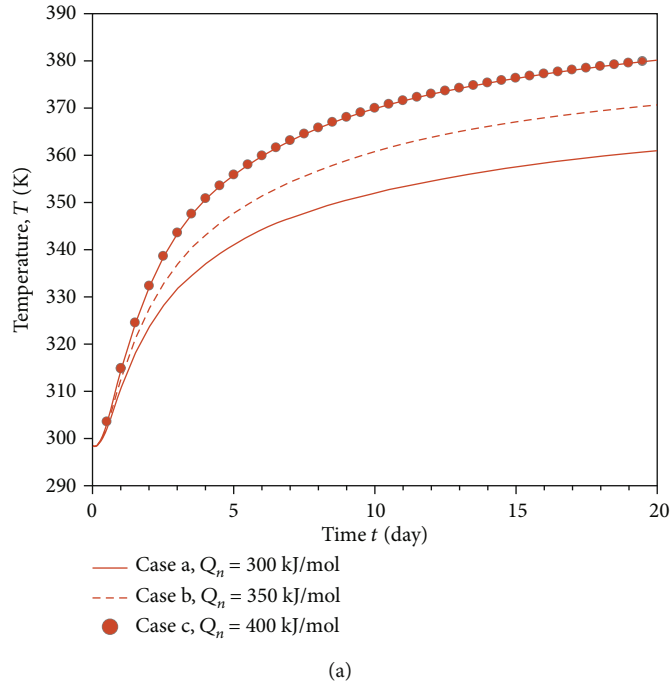
FIGURE 8: The evaluation of temperature and oxygen concentration with different values of coal-oxygen reaction heat.

TABLE 2: Different values of activation energy.

Cases	E_a	Unit
Low	3	kJ/mol
Medium	6	kJ/mol
High	12	kJ/mol

Figure 9 shows the evolution of oxygen concentration and coal spontaneous combustion temperature at monitoring point A in Cases a, b, and c. Comparing Figure 8 with Figure 9, it can be inferred that the rate of spontaneous combustion of coal is determined by both effects of the rate of coal oxidation and the activation energy E_a. The increase in activation energy E_a significantly promotes the oxygen consumption rate, while having a sight influence on temperature.

(a)

(b)
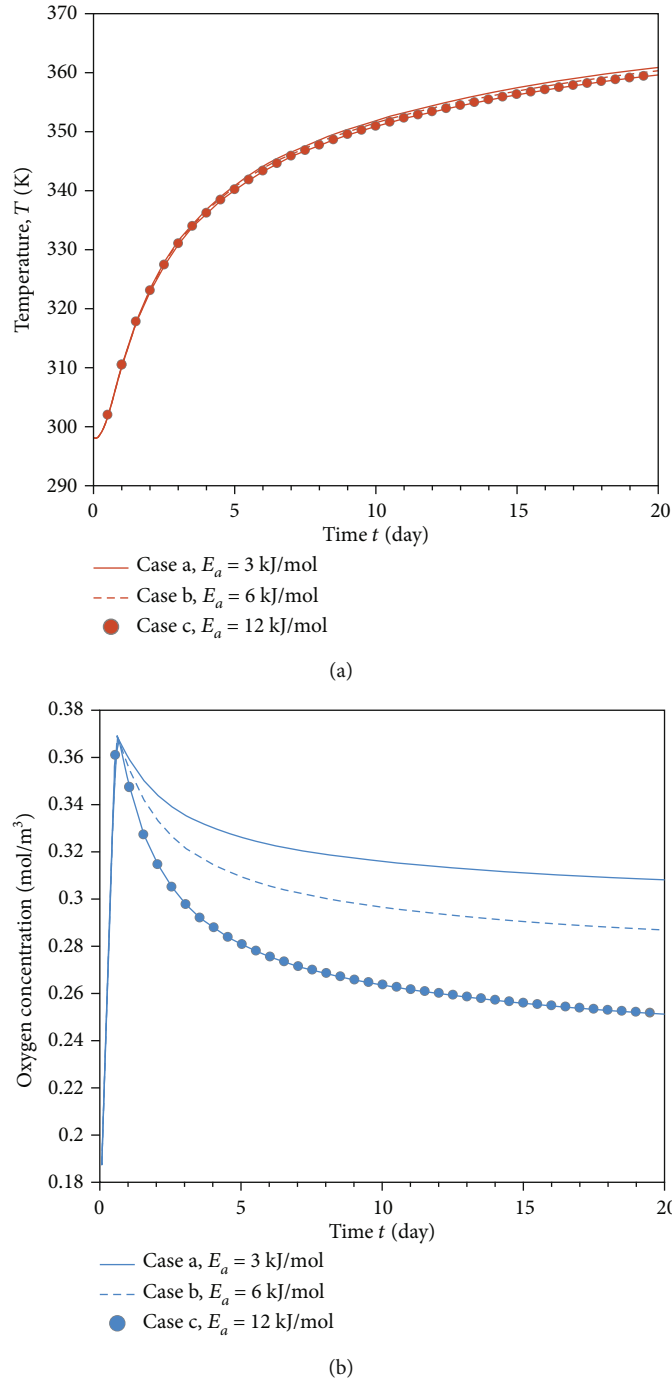
FIGURE 9: The evaluation of temperature and oxygen concentration with different values of activation energy.

6. Summary and Conclusions

In this study, we performed a fully coupled dual-porosity and single permeability (DPSP) thermal-hydrological-mechanical-chemical (THMC) modeling of the spontaneous combustion process of underground coal seams, emphasizing the investigation of the influence of pressure difference between oxygen and coal, the rate of coal oxidation, and the activation energy. The main conclusions are drawn based on the simulation results:

(1) The simulation results show that the temperature increases with the oxygen propagating into the coal that causes the spontaneous combustion, resulting in the consumption of oxygen along the way and a decrease in gas pressure

(2) The expansion of the coal matrix caused by spontaneous combustion of coal reduces the cleat aperture, while the strain induced by matrix shrinkage causes the increase of aperture. The permeability inside the

coal decreases as the result of the dominant effect of spontaneous combustion

(3) A sensitivity study shows that the increase in pressure difference and coal-oxygen reaction heat contributes to increasing the coal temperature. At the same time, the activation energy has a slight effect on the coal temperature. A more significant pressure difference causes a higher oxygen concentration. A higher value of coal-oxygen reaction heat and activation energy accelerates the oxygen consumption rate, leading to a lower oxygen concentration

Data Availability

The data used to support the findings of this study are available from the first author upon request.

Conflicts of Interest

The authors declare that they have no conflicts of interest.

Acknowledgments

References

[1] V. Fierro, J. Miranda, C. Romero et al., "Prevention of spontaneous combustion in coal stockpiles: experimental results in coal storage yard," *Fuel Processing Technology*, vol. 59, no. 1, pp. 23–34, 1999.

[2] E. KAYMAKÇI and V. Didari, "Relations between coal properties and spontaneous combustion parameters," *Turkish Journal of Engineering and Environmental Sciences*, vol. 26, no. 1, pp. 59–64, 2001.

[3] M. Onifade and B. Genc, "A review of research on spontaneous combustion of coal," *International Journal of Mining Science and Technology*, vol. 30, no. 3, pp. 303–311, 2020.

[4] J. D. N. Pone, K. A. Hein, G. B. Stracher et al., "The spontaneous combustion of coal and its by-products in the Witbank and Sasolburg coalfields of South Africa," *International Journal of Coal Geology*, vol. 72, no. 2, pp. 124–140, 2007.

[5] A. Rosema, H. Guan, and H. Veld, "Simulation of spontaneous combustion, to study the causes of coal fires in the Rujigou Basin," *Fuel*, vol. 80, no. 1, pp. 7–16, 2001.

[6] D. Szurgacz, M. Tutak, J. Brodny, L. Sobik, and O. Zhironkina, "The method of combating coal spontaneous combustion hazard in goafs—a case study," *Energies*, vol. 13, no. 17, p. 4538, 2020.

[7] S. Zeyang, *Thermogravimetric and Numerical Investigations on Couplings of Chemical Reaction, Hydraulic Field and Thermal Field of Coal Fires*, China University of Mining and Technology, Beijing, 2015.

[8] H. Wen, "Experiment simulaition of whole process on coal self-ignition and study of dynamical change rule in high-temperature zone," *Journal of China Coal Society*, vol. 29, pp. 689–693, 2004.

[9] D. Wu, F. Norman, M. Schmidt et al., "Numerical investigation on the self-ignition behaviour of coal dust accumulations: the roles of oxygen, diluent gas and dust volume," *Fuel*, vol. 188, pp. 500–510, 2017.

[10] H. Su, F. Zhou, X. Song, and Z. Qiang, "Risk analysis of spontaneous coal combustion in steeply inclined longwall gobs using a scaled-down experimental set-up," *Process Safety and Environmental Protection*, vol. 111, pp. 1–12, 2017.

[11] T. Xia, F. Zhou, J. Liu, J. Kang, and F. Gao, "A fully coupled hydro-thermo-mechanical model for the spontaneous combustion of underground coal seams," *Fuel*, vol. 125, pp. 106–115, 2014.

[12] T. Zongqing, *Pore Evolution during Coal Spontaneous Combustion: Mechanism and Its Effect on Multi-Gas Adsorption Characteristics*, China University of Mining and Technology, 2020.

[13] T. Xia, F. Zhou, F. Gao, J. Kang, J. Liu, and J. Wang, "Simulation of coal self-heating processes in underground methane-rich coal seams," *International Journal of Coal Geology*, vol. 141-142, pp. 1–12, 2015.

[14] W. Liu and Y. Qin, "Multi-physics coupling model of coal spontaneous combustion in longwall gob area based on moving coordinates," *Fuel*, vol. 188, pp. 553–566, 2017.

[15] Z. Hongfen, C. Wei, W. Baofu, and G. Erxin, "Hydrological-mechanical-thermal-chemical coupling numerical simulation of spontaneous combustion of loose top coal," *Journal of North China Institute of Science and Technology*, vol. 17, pp. 1–5, 2020.

[16] S. Wessling, W. Kessels, M. Schmidt, and U. Krause, "Investigating dynamic underground coal fires by means of numerical simulation," *Geophysical Journal International*, vol. 172, no. 1, pp. 439–454, 2008.

[17] J. Huang, J. Bruining, and K. Wolf, "Modeling of gas flow and temperature fields in underground coal fires," *Fire safety journal*, vol. 36, no. 5, pp. 477–489, 2001.

[18] H. Wen, *Study on Experimental and Numerical Simulation of Coal Self-Ignition Process*, Xi'an University of Science and Technology, 2003.

[19] Z. Song and C. Kuenzer, "Coal fires in China over the last decade: a comprehensive review," *International Journal of Coal Geology*, vol. 133, pp. 72–99, 2014.

[20] W. Fusheng, S. Chao, D. Xianwei, Y. Zhi, and H. Lingling, "Study on the pore structure change and spontaneous combustion characteristics of repeated coal seam," *Industrial Safety and Environmental Protection*, vol. 44, pp. 61–64, 2018.

[21] S. Wessling, C. Kuenzer, W. Kessels, and M. W. Wuttke, "Numerical modeling for analyzing thermal surface anomalies induced by underground coal fires," *International Journal of Coal Geology*, vol. 74, no. 3-4, pp. 175–184, 2008.

[22] H. Wen, Z. Yu, J. Deng, and X. Zhai, "Spontaneous ignition characteristics of coal in a large-scale furnace: an experimental and numerical investigation," *Applied Thermal Engineering*, vol. 114, pp. 583–592, 2017.

[23] A. Dudzińska and J. Cygankiewicz, "Analysis of adsorption tests of gases emitted in the coal self-heating process," *Fuel Processing Technology.*, vol. 137, pp. 109–116, 2015.

[24] Y. Lu, "Identification and control of spontaneous combustion of coal pillars: a case study in the Qianyingzi Mine, China," *Natural Hazards.*, vol. 75, no. 3, pp. 2683–2697, 2015.

[25] T. Ma, J. Rutqvist, C. M. Oldenburg, and W. Liu, "Coupled thermal-hydrological-mechanical modeling of CO_2-enhanced coalbed methane recovery," *International Journal of Coal Geology*, vol. 179, pp. 81–91, 2017.

[26] J. A. White, "Anisotropic damage of rock joints during cyclic loading: constitutive framework and numerical integration," *International Journal for Numerical and Analytical Methods in Geomechanics.*, vol. 38, no. 10, pp. 1036–1057, 2014.

[27] R. Yang, T. Ma, H. Xu, W. Liu, Y. Hu, and S. Sang, "A model of fully coupled two-phase flow and coal deformation under dynamic diffusion for coalbed methane extraction," *Journal of Natural Gas Science and Engineering*, vol. 72, article 103010, 2019.

[28] T. Ma, J. Rutqvist, C. M. Oldenburg, W. Liu, and J. Chen, "Fully coupled two-phase flow and poromechanics modeling of coalbed methane recovery: impact of geomechanics on production rate," *Journal of Natural Gas Science and Engineering*, vol. 45, pp. 474–486, 2017.

[29] Y. Wang, T. Li, Y. Chen, and G. Ma, "A three-dimensional thermo-hydro-mechanical coupled model for enhanced geothermal systems (EGS) embedded with discrete fracture networks," *Computer Methods in Applied Mechanics and Engineering*, vol. 356, pp. 465–489, 2019.

[30] F. G. Tong, L. R. Jing, and R. W. Zimmerman, "A fully coupled thermo-hydro-mechanical model for simulating multiphase flow, deformation and heat transfer in buffer material and rock masses," *International Journal of Rock Mechanics and Mining Sciences*, vol. 47, no. 2, pp. 205–217, 2010.

[31] A. Comsol, *COMSOL Multiphysics Reference Manual*, COMSOL AB., 2015.

WILEY | Hindawi

Research Article

An Experimental and Numerical Study on Acoustic Emission in the Process of Rock Damage at Different Stress Paths

Dongxu Liang ⓘ**, Nong Zhang** ⓘ**, and Haoyu Rong** ⓘ

Key Laboratory of Deep Coal Resource Mining, Ministry of Education of China, School of Mines, China University of Mining & Technology, Xuzhou, Jiangsu 221116, China

Correspondence should be addressed to Nong Zhang; zhangnong@cumt.edu.cn

The study of the damage process of rock under external loads is good guidance for geotechnical construction design. The differences in rock damage processes and damage modes under different stress paths are rarely reported. To explore the effects of stress paths on rock damage processes, uniaxial compression experiments under three stress paths were conducted. Numerical simulation is also used to simulate the rock acoustic emission (AE) and fracture process. The results of the study indicate that the maximum acoustic emission events are at the peak of stress, and fractures are mainly formed at this stage. The peak of AE energy occurs before the peak of AE events. The damage pattern and fragmentation size of the rock are related to the way the stresses are loaded. It is noticed that there is appearance of a quiet period of AE events prior to the production of significant cracks. Minor damage to the rock is accompanied by the generation of bright white spots in the specimen, which is due to the high tensile or shear stress in the units. When the stress in these units exceeds their strength, the units break down and tiny cracks appear. As the external load increased, the cracks developed and penetrated, and the specimen was damaged. Under cyclic loading and unloading, the number of AE events increased significantly compared with the controlled displacement and controlled stress loading methods, and the radius of the AE circle became larger and the energy also increased, which indicates a greater degree of destruction of the rock under cyclic loading and unloading. The results of the study are of reference significance for rock crack propagation and fracture mode influenced by stress conditions and provide some guidance for construction design under different working conditions.

1. Introduction

Destabilization damage to rock plays an important role in the field of engineering geology, such as underground mining, petroleum engineering, and slope engineering. At the same time, the cracks produced during rock fracture have a great influence on the permeability of the rock, causing a fluid flow in underground rock, especially for fluid flow in oil and gas reservoirs. Understanding the rock damage process and its damage mode is very informative for geotechnical and oil and gas extraction engineering.

Deformation and damage will occur when the rock is subjected to external loads, which is a process of the rock from the development of tiny damage in the intact medium to the formation of macroscopic cracks and eventually leading to global fracture. Many scholars have done a lot of

research on this. In order to investigate the complete stress-strain and damage evolution behavior of brittle rocks [1], acoustic emission experiments are widely used as an effective monitoring tool in laboratory experiments and field tests. Bruning et al. [2] conducted a series of triaxial compression tests on granite buried at depths greater than 1000 m to determine stress thresholds for crack initiation, coalescence, and damage. Xu et al. [3] conducted a series of uniaxial compression tests and cyclic loading tests on sandstone samples and the results showed that the ratio of maximum stress and stress amplitude to uniaxial compressive strength is the most important factor affecting the fatigue life of sandstone.

Liu et al. [4] used an acoustic emission localization technique and performed shear experiments to obtain the distribution mode and distribution characteristics of the cracks. Odegaard and Nilsen [5] proposed a simplified and cost-

effective method for measuring the minimum principal stress in the tunnel and using acoustic emission (AE) data to interpret fracture behavior and evaluate fracture normal stresses. With the aim of gaining a deeper understanding of the relationship between rock fracture and fracture scale, Shengxiang et al. [6] investigated the correlation between rock breakage mechanism and the characteristic parameters of acoustic emission (AE) signal under splitting load. The attempt of a CO_2 hydraulic fracturing acoustic emission monitoring experiment [7] provides implications for the use of carbon dioxide (CO_2) to recover geothermal energy and shale gas. Fluid penetration leads to rock dilatation and fracture. Zhou et al. [8] conducted several sets of cracking tests in different initial states using a self-made device, and the results of the study showed that the internal structure of the rock was damaged under the combined effect of swelling stress and softening effect, leading to the generation and development of cracks. The mechanical mechanism of crack generation and the shape of the generated cracks can be different due to different reasons for uneven swelling.

Cyclic loading [9] is often a common operating condition on engineering sites. Liang et al. [10] conducted laboratory experiments on sandstone with equal amplitude and graded cyclic loading and unloading under uniaxial compression and obtained damage evolution trends. Temperature also has a large effect on rock fracture. Wang et al. [11] studied the deterioration mechanism and fatigue fracture evolution of granite with two preexisting defects treated with freeze-thaw (FT). Sun et al. [12] used a combined infrared radiation (IR) and acoustic emission (AE) monitoring system for analyzing the acoustic and thermal effects during rock damage under uniaxial compression. The results showed that there were acoustic and thermal time-related effects during the damage to the rocks. It is well known that the creep properties of rocks are an unfavorable factor for the long-term stability of underground structures. Zhao et al. [13] carried out a series of creep tests to determine the relationship between the wave characteristics of acoustic emission signals and the length of microcracks in rock, and the wave characteristics of acoustic emission signals at different creep stages were considered from the perspective of elastic wave dynamics. The strength and damage characteristics of rocks under different stress paths are different. Lu et al. [14] studied the deformation, strength, and damage characteristics of soft sandstone and raw coal under two different true triaxial loading paths using a self-developed true triaxial test apparatus. Kharghani et al. [15] probed the effect of anisotropy on the Kaiser effect of rocks. Uniaxial compression tests and Brazilian tensile strength tests were performed on rock specimens with various anisotropic angles (0, 30, 60, and 90 degrees) to obtain their acoustic emission effects. The mechanical properties and fracturing behavior of coal bodies cannot be neglected for the safety and stability of underground mining. Li et al. [16] applied dynamic loading coupled to biaxial static and dynamic tests on coal specimens at five laminar directions and four impact velocities. A positive correlation was obtained between the velocity of coal injection and loading rate, and the average fragment size of coal samples was negatively correlated with impact velocity and energy absorp-

tion. Rock burst disasters and fluid-induced earthquakes occur frequently during coal mining, and microseismic monitoring is often used to monitor rock bursts or to provide early warning [17–21], showing good results. Fracture extension studies in rocks are important for assessing the ability of coal seams to form fracture networks by hydraulic fracturing for the development of coal bed methane (CBM) reservoirs [22] and drilling engineering for the petroleum industry [23]. To find out the determinants of hydraulic fracture extension and associated rock damage mechanisms, laboratory hydraulic fracturing experiments under triaxial stress were conducted to research this effect [24]. However, although there are many previous research results on rock fracture processes, the response of acoustic emission characteristics of rock damage under different stress paths and the influence of stress paths on damage modes have rarely been reported.

In the past decades, numerical computational methods have been widely used in rock mechanics problems. Nowadays, there are various numerical analysis methods that can be applied to rock mechanics, and the main methods include (1) finite element methods, such as Phase2D; (2) boundary element methods, such as Examine; and (3) discrete element methods, such as UDEC and PFC. However, the finite element method and the boundary element method are computational methods based on the mechanics of continuous media, which makes this method limited in its scope of application. The discrete element method highlights its advantages when analyzing the mechanics of rock fracture processes [25, 26]. So far, there is no mature simulation software that can better study the process of transforming rock masses from continuous to discontinuous media under the action of loads. In order to solve the problems of nonlinearity of geotechnical materials, the influence of fractures, joints in rock masses and discontinuous surfaces on calculation results, and the influence of stepwise excavation and filling construction operations on the stability of surrounding rock, Tang [27] proposed a new numerical simulation method "Realistic Failure Process Analysis (RFPA)" method, which takes into account the characteristics of nonhomogeneity, discontinuity, and anisotropy of rock media. The RFPA code can be used to analyze the deformation and damage to rock specimen loading, acoustic emission of rock, deformation and damage to brittle materials such as concrete, ground sinking, rock movement, damage to the roadway, roof fall, bottom slab sudden water, simulation and analysis of deformation and damage of ceramics and composite materials, gas-solid coupling analysis such as gas protrusion of coal and rock bodies, heat-solid coupling analysis in materials such as rock and concrete, slope stability simulation, and analysis. Rock rheology-solid coupling in hydraulic engineering, rock rheological characteristics' analysis, underground engineering excavation and support, and other issues for analysis and research were discussed. RFPA adopted a calculation method combining finite element theory and statistical damage theory. This calculation method takes into account the nonuniformity of the medium and the randomness of the defect distribution, takes the material properties into account using the knowledge of statistical distribution, and

combines the finite element numerical calculation method with the damage treatment of the unit body according to the set strength criterion to complete the numerical simulation of the damage process of nonuniform materials, which can solve the difficult problem of the fine rupture process in geotechnical engineering with the RFPA code.

In this paper, by conducting uniaxial compression acoustic emission experiments on sandstone with different stress paths, parameters such as the number of acoustic emission events and energy captured by acoustic emission combined with stress-strain curves were analyzed, and the phenomenon of the AE events quiet period was found. Subsequently, a numerical simulation method was used to simulate the acoustic emission localization and fracture damage process for uniaxial compression experiments under different stress paths, and the simulation results were in high agreement with the experimental results. Finally, the influence of stress paths on the final damage mode of the rock is discussed.

2. Laboratory Experiments

In order to study the characteristics of AE during uniaxial compression damage to rocks under different stress paths, laboratory experiments were conducted, and the stress-strain curves, the number of AE events, and the energy parameters under different paths were analyzed.

2.1. Preparation of Rock Specimens. The rock specimens were standard cylindrical specimens of 100 mm × 50 mm in size, which were prepared by drilling from the natural rock mass of sandstone in strict accordance with the method recommended by the International Society of Rock Mechanics [28]. A total of 14 rock specimens were made, as shown in Figure 1. Five of them were used for uniaxial compression experiments and shear experiments to obtain the basic mechanical parameters (including uniaxial compressive strength, modulus of elasticity, density, and angle of internal friction), and the basic physical-mechanical parameters obtained by averaging are shown in Table 1. Three experiments were conducted for each of the three different stress paths (described in detail in Section 2.2).

2.2. Experimental Apparatus and Loading Scheme. The uniaxial compression experiments were performed on the MTS-816 electrohydraulic servo tester, which can be programmed to control the displacement and stress loading, and the equipment automatically records the load and displacement and stores them on the computer. During the loading process, four acoustic emission probes were attached to the rock surface. The acoustic emission probes were connected to the acoustic emission signal acquisition device through an amplifier. The amplifier parameters were set to 40 dB, the acquisition frequency was set to 3 MHz, and the minimum amplitude was set to 20 mV. All the experimental equipment was connected as shown in Figure 2. The experimental system consists of two parts: the loading system and the AE monitoring system.

Figure 1: Rock samples.

Three experiments were conducted for each loading scheme under the three stress paths. The three loading scenarios are shown in Figure 3, respectively.

(1) Loading by means of controlled displacement loading, with axial loading at a displacement rate of 0.002 mm/s, and one loading until the specimen is destroyed (as shown in Figure 3(a))

(2) Loading by means of controlled stress loading, with a stress loading rate of 0.5 kN/s, once loaded until the specimen is destroyed (as shown in Figure 3(b))

(3) Cyclic loading and unloading by means of controlled stress loading, with a stress loading rate of 0.5 kN/s (as shown in Figure 3(c))

3. Experimental Results

In this work, to study the damage and destruction of rocks during uniaxial compression, the experimentally acquired stress-strain curves, AE events, and AE energies were statistically analyzed.

3.1. Acoustic Emission Law under Controlled Displacement Loading Conditions. As can be seen from Figure 4, the AE events of the sandstone reached a peak in the pressure-dense phase (near 0.08% strain) when the loading was carried out with controlled displacement. This was due to the dense structure of the sandstone, and after pressure loading, the original microfractures closed under the load and deformed, and the accumulated large amount of deformation energy was released to produce elastic waves. After entering the elastic stage, the AE events of the sandstone remained at a stable level, and the AE events were basically 0, indicating that there was no substantial damage to the rock at this stage. When the strain reached 0.28%, the sandstone entered the plastic stage, and the AE events increased abruptly and another peak (reaching 920) appeared. Accompanied by a small drop in stress, the AE event number decreased to close to 0, then increased sharply again, after which it stabilized at a smaller

TABLE 1: Basic physical and mechanical parameters of rock.

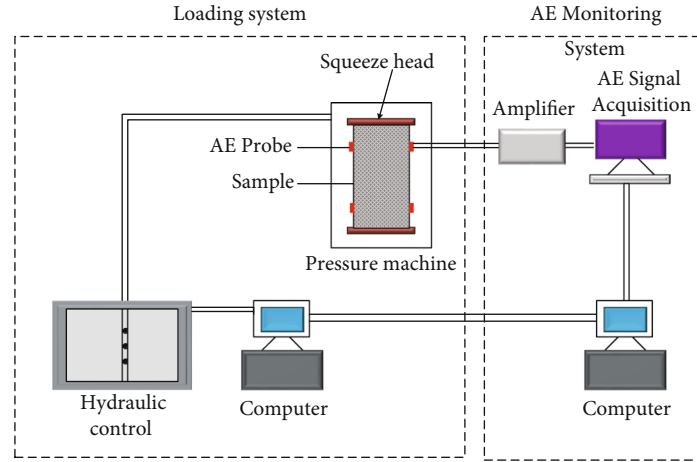| Sample name	Density $\rho\left(\text{g/cm}^3\right)$	Elastic modulus E (GPa)	Uniaxial compressive strength UCS (MPa)	Size (mm)
Sandstone	2.64	27.36	51	50×100

FIGURE 2: Experimental system connection diagram.
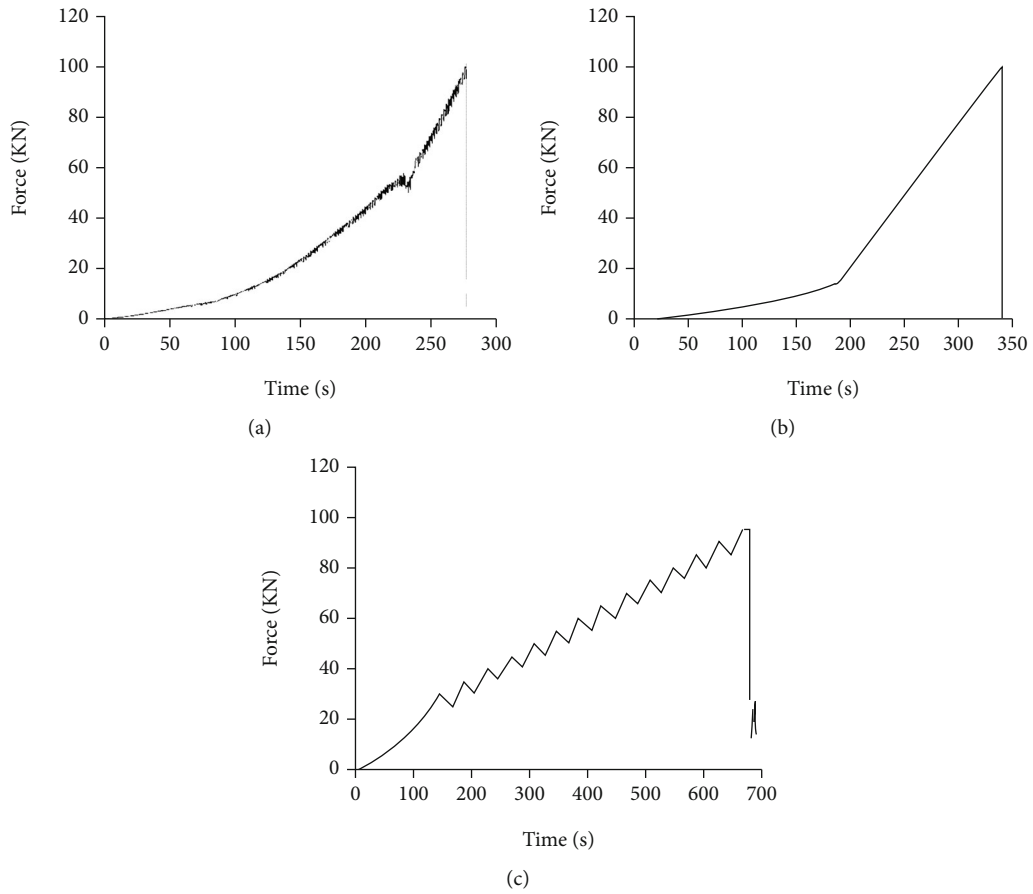

(a)

(b)

(c)

FIGURE 3: Loading scheme diagram: (a) controlled displacement loading, (b) controlled stress loading, and (c) controlled stress cyclic loading and unloading.
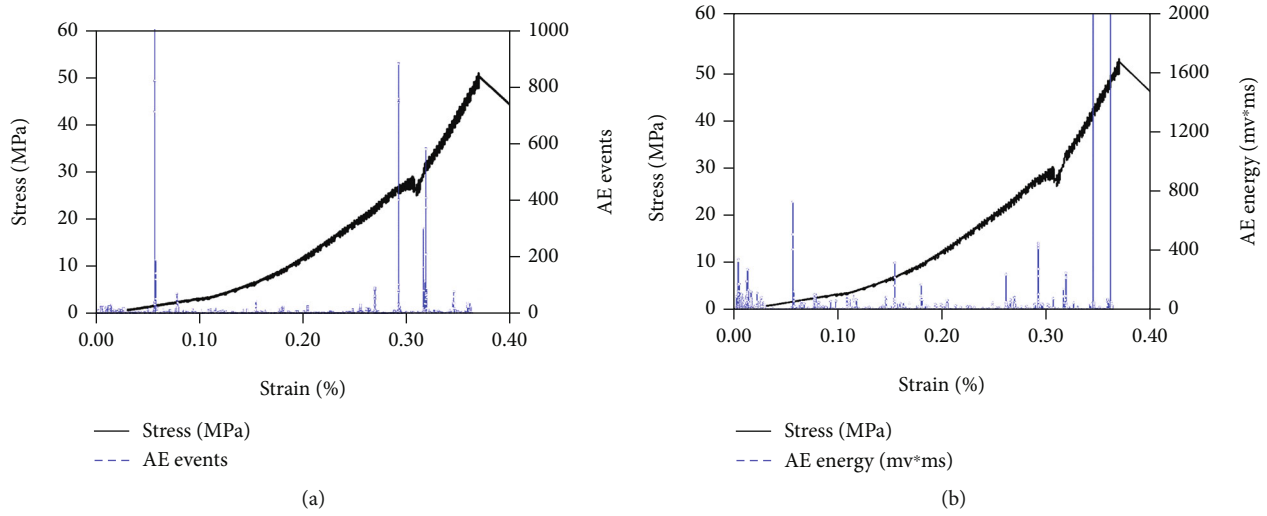
FIGURE 4: Diagram of AE parameters versus stress-strain for sandstone during controlled displacement loading: (a) AE events and (b) AE energy.
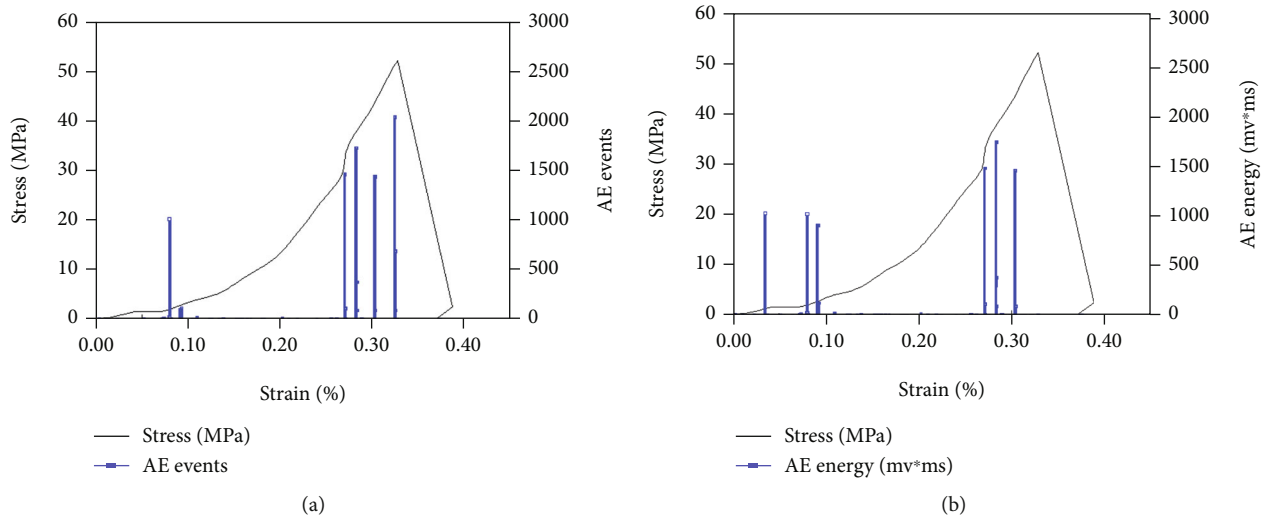

FIGURE 5: Diagram of AE parameters versus stress-strain for sandstone during controlled stress loading: (a) AE events and (b) AE energy.

value until a small increase before the peak stress. This indicates that the damage to sandstone was mainly in the plastic stage and completed most of the crack generation and expansion before the peak stress; i.e., the damage to the rock mainly occurred in the plastic stage, and the macroscopic damage after the peak stress was only a macroscopic presentation on the basis of the previous one. For the AE energy value, its trend was basically consistent with the AE events, but in the plastic stage, the AE energy value lagged relative to the AE events; i.e., the AE energy value was not maximum when the number of AE events was maximum.

3.2. Acoustic Emission Law under Controlled Stress Loading Conditions.
It can be seen from Figure 5 that the whole AE events and AE energy values of the sandstone vary distinctly. At the end of the compressional stage, the AE events reached a peak, and the AE energy values had a sudden and significant increase at the beginning and end of the compressional

stage. After entering the elastic stage, the AE events and AE energy values of the sandstone drop to zero, and the AE activity tends to calm down. At the boundary between elastic and plastic stages, AE events and AE energy values increase abruptly. Unlike the controlled displacement loading method, the AE events and AE energy values increased simultaneously after the rock entered the plastic stage when the controlled stress was loaded once, and there was no situation where the AE energy values lagged behind the increase in the number of AE events, so the AE events and AE energy values can be used as the precursor criterion for rock damage in this case.

3.3. Acoustic Emission Law under Controlled Stress Cyclic Loading and Unloading Conditions.
Under the uniaxial cyclic loading and unloading conditions, the variation pattern of AE events in sandstone was consistent with the stress-strain curve of the rock. In the compression-dense phase, the
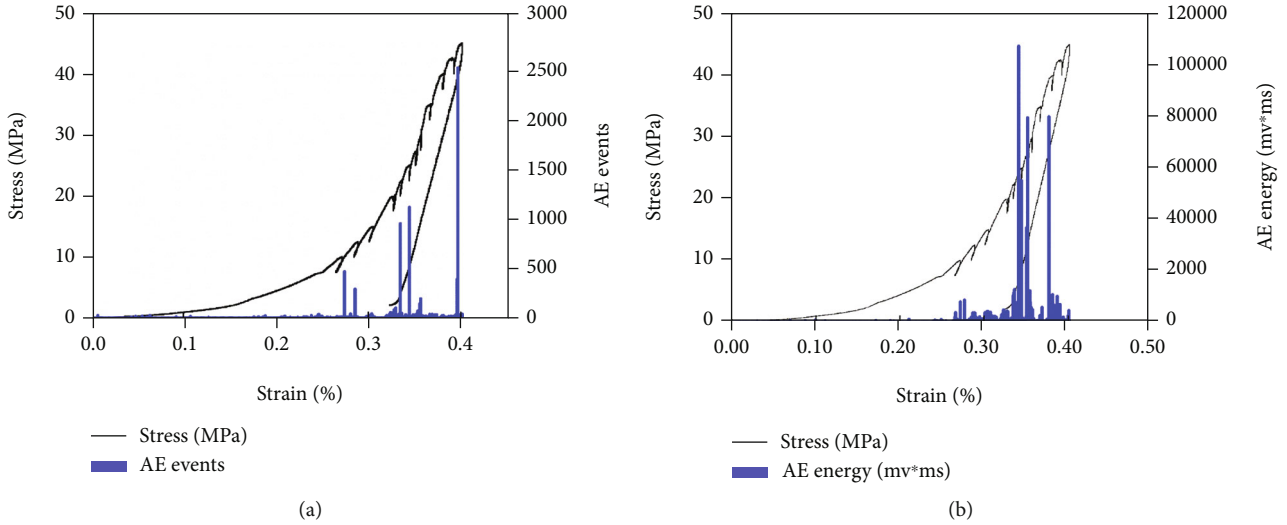
FIGURE 6: Diagram of AE parameters versus stress-strain for sandstone during controlled stress cyclic loading: (a) AE events and (b) AE energy.

sandstone was basically free of AE events as shown in Figure 6(a). When the stress increases, the sandstone lasts longer in the elastic phase, so the number of AE events tends to increase. In the late elastic stage, the AE events increased significantly. In the plastic stage, the cracks inside the rock gradually expanded and the damage intensified. The AE events increased significantly, the AE energy continued to grow, and the AE events increased abruptly when the peak stress was approached. This was due to the large number of new cracks generated at the peak stress, resulting in numerous acoustic emission points. From Figure 6(b), the peak energy of the sandstone was advanced compared to the peak AE events; i.e., the energy of the sandstone was not maximum when the AE activity was most intense. In the postpeak damage stage, after the peak stress, the sandstone showed fracture damage. The AE test ended. During the unloading process, the strain causes a rebound phenomenon. The AE event was basically 0, and the energy value decreased abruptly and gradually converged to 0.

4. Numerical Simulation

Numerical simulations were conducted using RFPA for sandstone with three different stress paths (displacement loading, stress loading, and cyclic loading and unloading) to compare with previous experiments and to study the acoustic emission characteristics under different stress paths.

4.1. Basic Theory of Simulating Acoustic Emission. In an effort to fully consider the deformation damage caused by the non-uniformity and discontinuity of the medium under external loading, three types of element were inserted into the RFPA system, namely, the matrix element, contact elements, and air element. The transformation of the three elements occurred when the strain reached a certain condition, which we called the phase transition, and the condition reached was called the phase transition point. So far, there is no unified understanding of how to properly select the phase transition

critical point. Since rock materials are similar to brittle materials and their tensile strength is much less than their compressive strength, the RFPA system used the modified Coulomb criterion as the phase transition critical point of the primitive element. It can be expressed mathematically as [29]

$$
\begin{cases}
\sigma_1 - \dfrac{(1+\sin\theta)}{(1-\sin\theta)} \cdot \sigma_3 \geq \sigma_c, \sigma_1 \geq \sigma_c\left(1 - \dfrac{1+\sin\theta}{1-\sin\theta} \cdot \dfrac{1}{\lambda}\right), \\
\sigma_3 \leq -\sigma_t, \sigma_1 \leq \sigma_c\left(1 - \dfrac{1+\sin\theta}{1-\sin\theta} \cdot \dfrac{1}{\lambda}\right),
\end{cases}
\tag{1}
$$

where σ_c is class I phase change threshold, σ_t is class II phase change threshold, and θ is friction angle of the rock.

$\sigma_c = \lambda|\sigma_t|$, λ is the ratio of tensile strength to compressive strength. It must be satisfied in this criterion that $\sigma \geq 0$, so only when

$$
\sigma_1 \geq \sigma_v\left(\left(\sigma_v = \sigma_c\left(1 - \dfrac{1+\sin\theta}{1-\sin\theta} \cdot \dfrac{1}{\lambda}\right)\right)\right).
\tag{2}
$$

The Coulomb criterion does not work, and the uniaxial tension criterion is applied in this case.

For discrete primitive bodies, their mechanical properties have a statistical distribution law, and the RFPA system uses the Weibull statistical distribution function to characterize the distribution law of the mechanical properties of the elements, which is expressed by the following equation.

$$
\varphi(\alpha) = \frac{m}{\alpha_0} \cdot \left(\frac{\alpha}{\alpha_0}\right)^{m-1} \cdot e^{-(\alpha/\alpha_0)^m},
\tag{3}
$$

where α is the mechanical parameter of the elements, α_0 is the mean value of the mechanical properties of the elements, m is

TABLE 2: The numerical simulation test parameters of rock.

Sample name	Homogeneity	Elastic modulus E (GPa)	Poisson's ratio μ	UCS σ_c (MPa)	Angle of internal friction ϕ (°)
Sandstone	3	27.36	0.3	51	35

the shape parameter of the distribution function, and $\varphi(\alpha)$ is the statistical distribution density of α.

There are only two states of the elements from the point of integrity, i.e., damaged and undamaged. In the undamaged state, the initial damage to the elements $D_0 = 0$. From Equation (3), the damage variable, expressed as a statistical distribution law of the strength of the material matrix, can be obtained as follows:

$$D = \int_0^\varepsilon \varphi(x)dx \int_0^\varepsilon \left[\frac{m}{\varepsilon_0} \cdot \left(\frac{x}{\varepsilon_0} \right)^{m-1} \cdot e^{(E/E_0)^m} \right] dx = 1 - e^{-(E/E_0)^m}, \tag{4}$$

where D is the damage variable of rock, E_0 is the average modulus of elasticity value of all elements of the matrix, and E is the value of the modulus of elasticity of the element.

A combination of the Monte-Carlo method and statistical theory was used in the element assignment, and the Weibull function integral of the elastic modulus based on Equation (3) can be expressed as

$$\phi(E) = \int_i^j \varphi(x)dx \int_i^j \left[\frac{m}{\varepsilon_0} \cdot \left(\frac{x}{\varepsilon_0} \right)^{m-1} \cdot e^{-(E/E_0)^m} \right] dx = 1 - e^{-(E/E_0)^m}, \tag{5}$$

where $\phi(E)$ is the value of the distribution of the elements with the modulus of elasticity E.

With the progress of damage mechanics research, research on the theory of acoustic emission techniques has made remarkable breakthroughs. In 1990, Tang [29] proposed the hypothesis that acoustic emission of rocks is consistent with the damage to rocks based on the principle of statistical microscopic damage mechanics and the principle of rock acoustic emission, also known as the following equation:

$$N \propto D, \tag{6}$$

where N is the number of AE events.

The rock contains different flaws within each unit, which leads to differences in the strength of the element. The units with low strength break earlier than the ones with higher strength. Also, due to the nonuniformity of the rock, the elastic modulus of the unit is not the same. Therefore, the inhomogeneity of the element leads to its rupture at different times one after another. Based on this characteristic of rocks, RFPA first takes into account the nonuniformity parameter of the material unitary in the simulation of rock acoustic emission and considers that this parameter obeys the statistical distribution law and then uses the assumption of Equation (6) to count the number of units destroyed at any time

FIGURE 7: Numerical simulation model.

in the calculation and uses this value as a measure of rock AE events, which is the principle of numerical simulation of rock acoustic emission using RFPA code.

4.2. Model Establishment. The physical and mechanical parameters of sandstone measured from uniaxial compression experiments are shown in Table 1, and the RFPA code was used to conduct numerical experimental studies of acoustic emission during uniaxial compression of rocks under different stress paths. The specimen's horizontal and vertical directions were divided into 100 to 200 grids. A step-in-step calculation method was used during the test. The advantage of this method is that it can describe the damage process of the specimen in more detail, and the system automatically destabilizes and stops after the damage to the specimen without the need to set the number of computing steps artificially. The parameters of the sandstone in the numerical simulation are set in Table 2, and the established model is shown in Figure 7.

Corresponding to the standard load loading method under static applied load in the RFPA code, the basic load was set to uniaxial compression, and the loading types were realized with displacement and force to control displacement loading and control stress at one-time loading and cyclic loading and unloading, respectively.

4.3. AE Characterization of Sandstone and Mudstone at Different Stress Paths. The RFPA code can present the changes of AE of rock specimens during loading in real time. The AE of sandstone under different stress paths is shown in Figures 8–10. Each image consists of five subplots from left to right, indicating the location and intensity of AE activity during loading. In the first to fourth pictures, red circles represent AE events generated by tensile damage, blue circles represent AE events generated by shear damage, and the size
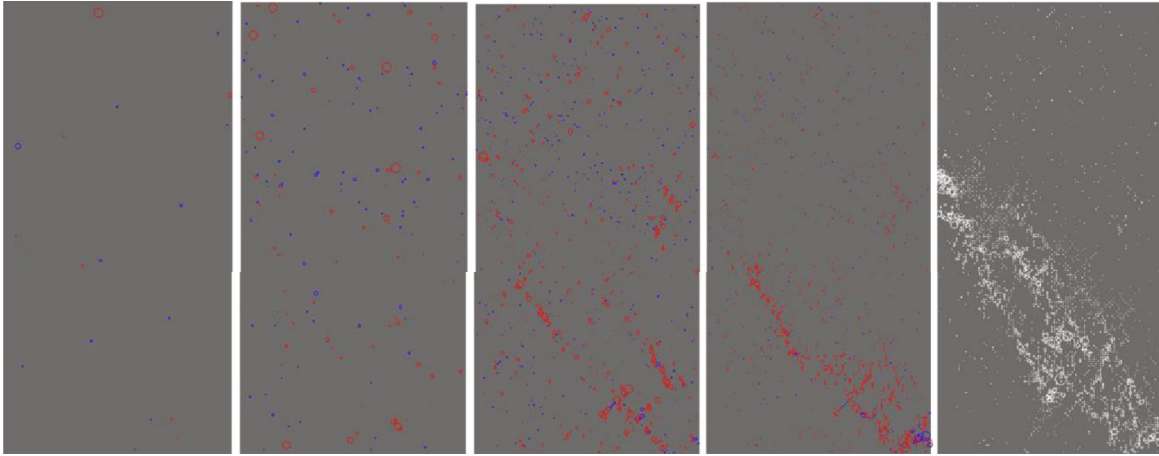
Figure 8: AE distribution of sandstone under controlling displacement.
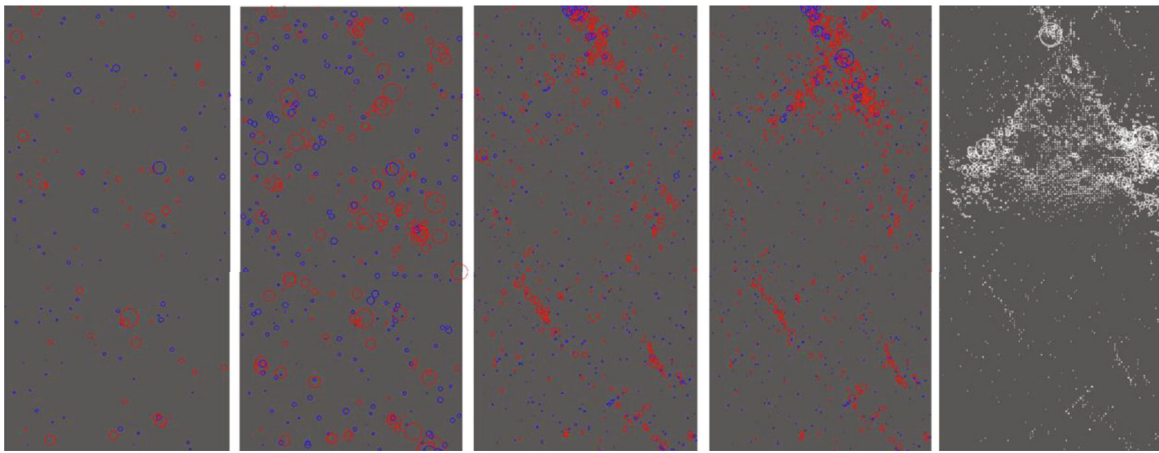
Figure 9: AE distribution of sandstone under controlling stress.
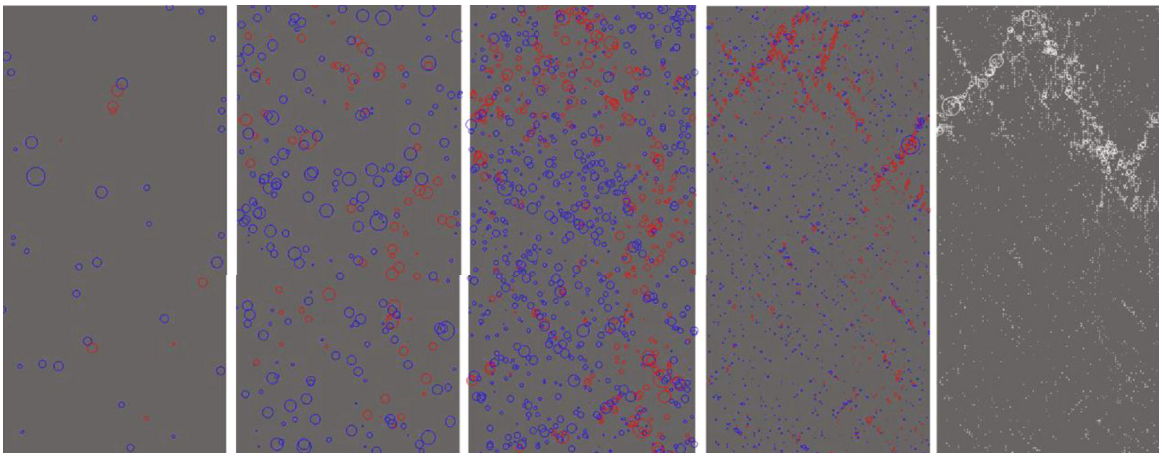
Figure 10: AE distribution of sandstone under cyclic loading and unloading.

of the circles indicates the magnitude of the AE energy, which also reflects the intensity of the AE event. In the fifth subplot, all the circles are changed to white to show more clearly the location where the rupture occurred.

As can be seen from Figures 8 and 9, at the early stage of loading (premid compression-dense stage and elastic stage), there were fewer AE events, but the AE energy values were relatively large, and after entering the plastic stage, there

Figure 11: Failure process of sandstone under controlled displacement loading.

was a substantial increase in both AE number and AE energy. However, as the AE number increases, the AE energy does not increase exactly simultan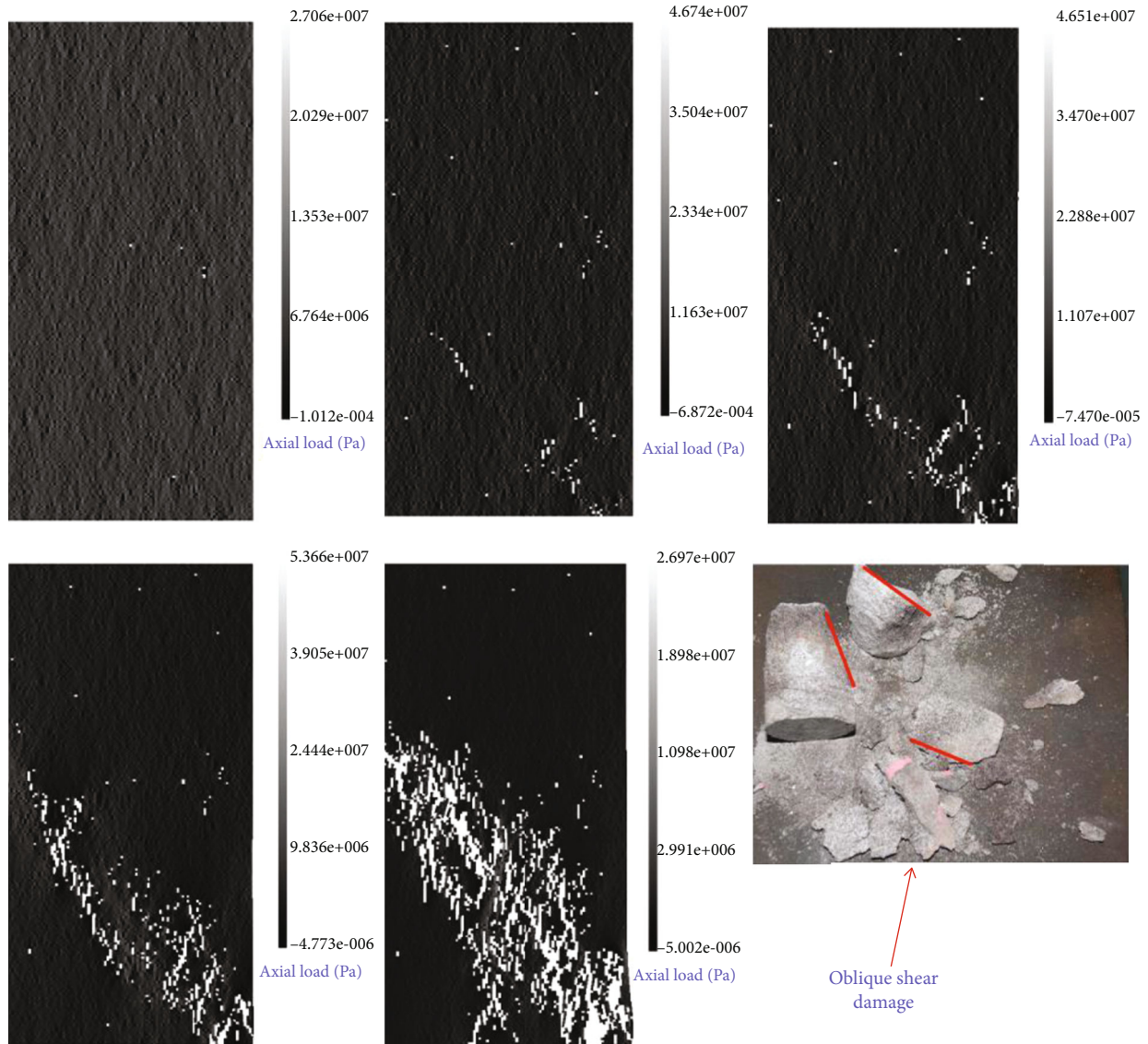eously but is significantly increased after it. The AE number jumped before the generation of macroscopic cracks and remains basically unchanged after the formation of fractures. As can be seen from Figure 9, there was a short period of calm where the AE number stopped increasing before a significant crack was produced. During this period, the AE number was essentially constant, which was consistent with the quiet period of acoustic emission found in the experiment. From Figure 10, it can be seen that the AE numbers of both rocks under cyclic loading and unloading were significantly higher than the first two loading methods, and the circle radius became larger and there was an increase in energy. This indicated a greater degree of damage to the sandstone under cyclic loading and unloading. From the last subplot of Figures 8–10, it showed that the AE numbers presented dense areas, which were consistent with the crack extension sites of the rocks, and the AE

numbers were the highest and brighter at the sites where fracture damage occurred in the rocks, and the bright white shape formed coincided with the damage shape of the rocks, revealing the law that the location of the acoustic emission event generation and the damage destruction of the rocks were consistent.

5. Discussion

Loading damage analysis of the rock specimens showed that the rock was significantly more homogeneous at the beginning of loading compared to the vicinity of the peak stress. The increase in stress in each cell can be seen from the change in cell color. In the vicinity of the peak stress, the color of the unit body was obviously brighter, which indicated that the damage to the rock was mainly concentrated in the vicinity of the peak stress. Therefore, to analyze and study the damage process of the rock, the study should focus on the area around the peak stress, which was consistent with the
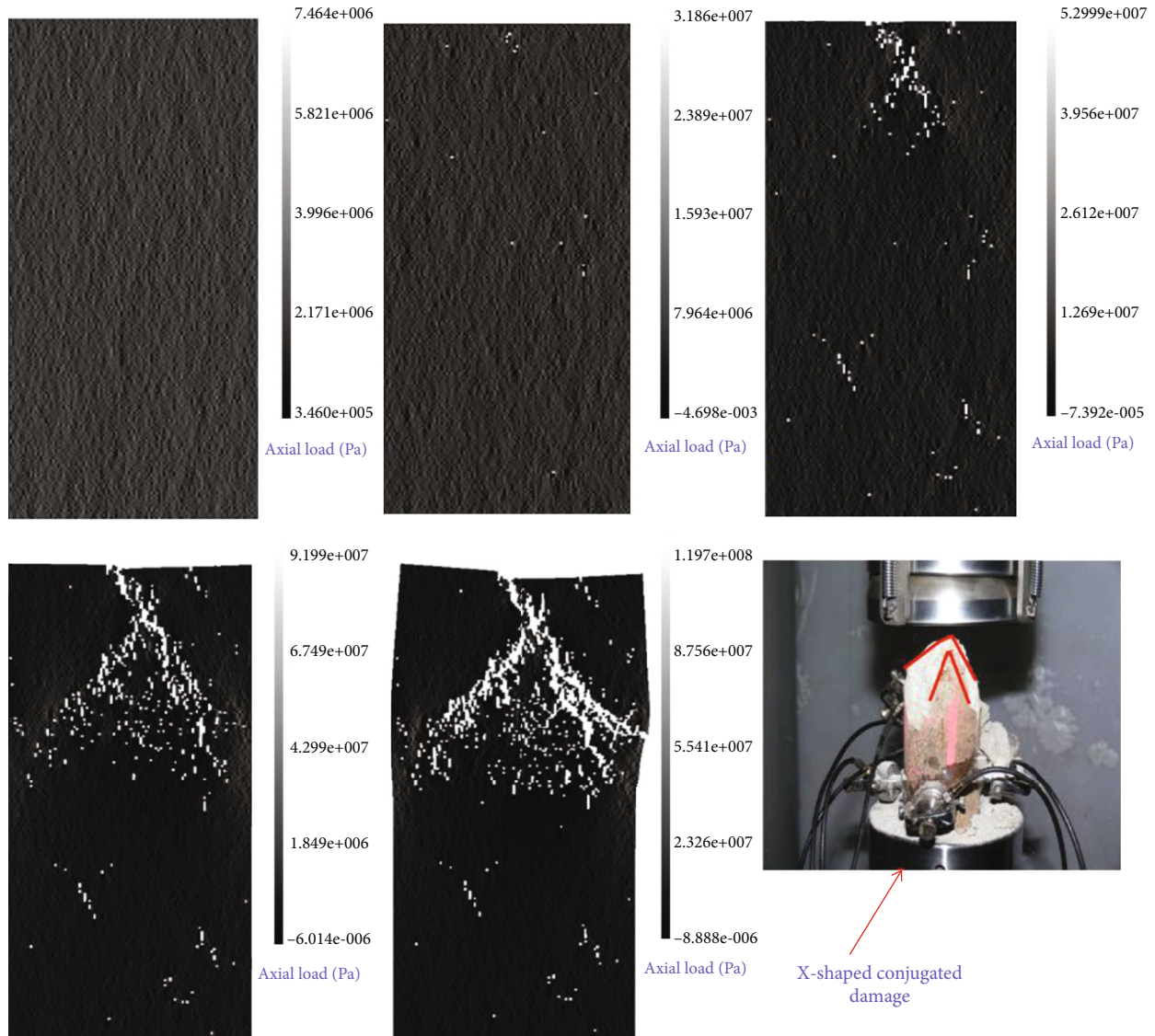
FIGURE 12: Failure process of sandstone under controlled stress loading.

conclusion that the damage to the rock under the uniaxial compression test mainly occurred in the plastic stage, as shown in Figures 11–13 for the numerical simulation of the damage process of sandstone under different stress paths.

As shown in Figure 11, when the sandstone was loaded by controlled displacement, the rock specimen initially had a more uniform color with an overall dark gray color, and then bright white spots began to be generated in the lower orientation of the rock specimen. This indicated that the tensile or shear stresses in the units near this location were high, and when the stresses in these units exceeded their strength, the units were damaged and tiny cracks appeared. With the increase in displacement, the cracks developed and diagonal cracks appeared below the specimen, and finally, an inclined damage surface was formed. That is, the sandstone occurs in an oblique shear fracture under controlled displacement for loading. From Figure 12, it can be seen that the sandstone was loaded under controlled stress for loading. The bright white spots appeared first at the upper and bottom, and with

the increase in stress, the crack expansion formed cracks first at the upper part of the rock specimen, and then the cracks penetrated and formed an X-shaped conjugate oblique fracture. That is, the sandstone under controlled stress for loading occurs in an X-shaped conjugate oblique damage. As observed in Figure 13, the sandstone showed more bright white spots at the beginning under cyclic loading and unloading, and the number was significantly higher than the first two loading methods, which indicated that the rock specimen was damaged to some extent at the beginning. After unloading and reloading, the bright white color tends to increase, and first, tiny bright white cracks are formed in the upper part of the rock mass. In the process of repeated loading and unloading, the top cracks developed and extended to the middle and lower parts and finally formed penetrating cracks, and the direction was parallel to the axial direction of the rock mass. That is, the sandstone under cyclic loading and unloading occurs vertical splitting tensile fracture.

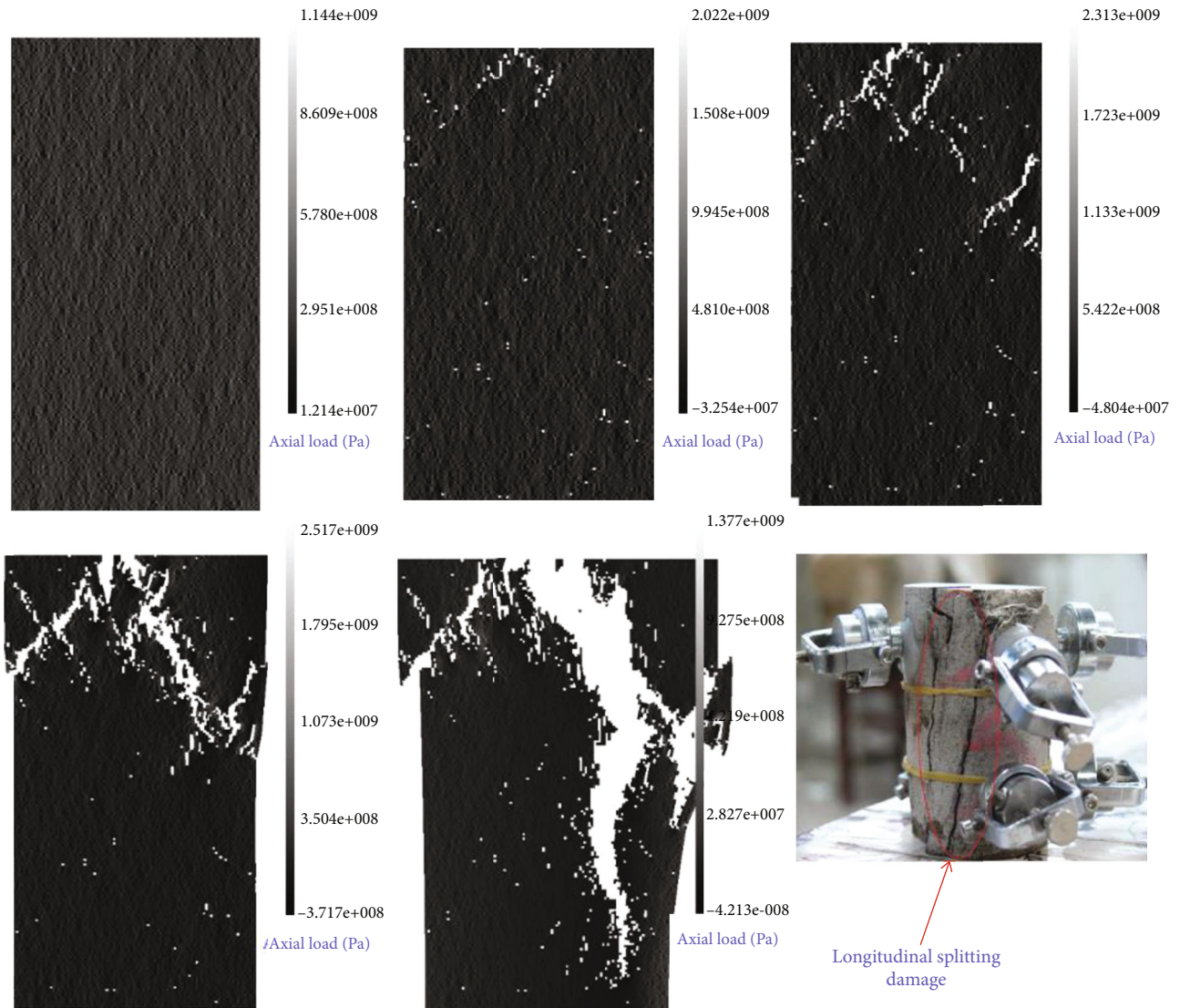FIGURE 13: Failure process of sandstone under the controlled stress cyclic loading and unloading.

(a)   (b)   (c)
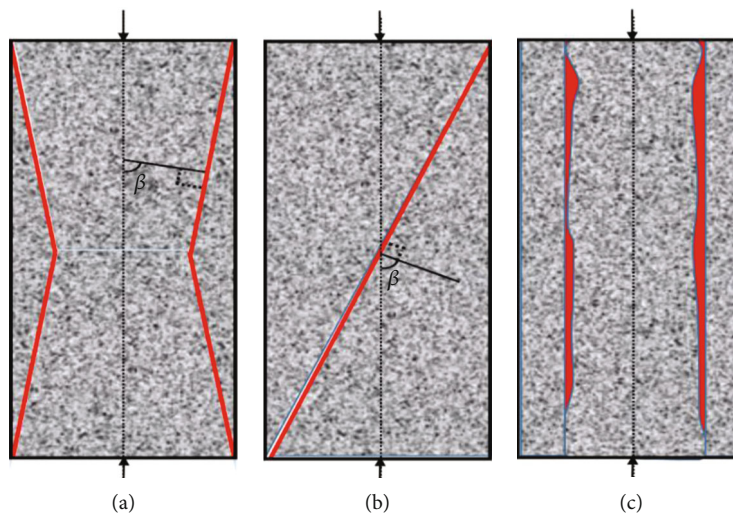
FIGURE 14: The failure modes of rock under uniaxial compression: (a) X-shaped conjugate oblique fracture, (b) oblique shear fracture, and (c) vertical splitting tensile fracture.

The damage modes of rock specimens under uniaxial compression can be classified into three categories, as shown in Figure 14.

X-shaped conjugate oblique shear breakage, as in Figure 14(a). The normal to the breaking surface and the axial load are at an angle of β. It can be expressed as

$$\beta = \frac{\pi}{4} + \frac{\varphi}{2}, \tag{7}$$

where β is the angle between the normal of the damage surface and the axial load and φ is the angle of internal friction of the rock.

This mode of damage was caused by the shear stress on the damaged surface exceeding the shear strength of the rock, resulting in shear damage to the rock. As shown in Figure 12, X-shaped conjugate oblique fracture occurred when controlled stress was applied. Single oblique shear damage is shown in Figure 14(b). This pattern of damage was also caused by the shear stress on the damaged surface exceeding the shear strength, but the maximum shear stress applied to the damaged surface before the specimen was damaged was related to the normal stress on the damage surface, so it is also called compression-shear damage. As in Figure 11, the specimen showed oblique fracture damage when the controlled displacement was loaded, which belongs to compression-shear damage. Longitudinal tensile fracture is shown in Figure 14(c). This mode of fracture was due to the axial load acting on the rock specimen. Owing to the Poisson effect, tensile stresses were generated in the lateral direction of the specimen, and when the lateral tensile stress was greater than the tensile limit of the rock, the specimen was damaged. As shown in Figure 13, under cyclic loading and unloading conditions, the specimen showed tensile damage with longitudinal splitting, and the acoustic emission point matched the rock crack damage shape.

6. Conclusions

The differences in acoustic emission characteristics and damage modes of sandstone during the damage process are analyzed by uniaxial compression failure experiments under different stress paths in the laboratory and numerical simulation studies using the RFPA code. The main conclusions are as follows:

(1) The maximum value of AE events in sandstones is at the peak of the rock, and AE activity is the most intense at the peak of stress. Peak AE energy is earlier than peak AE events

(2) When the sandstone is loaded with different stress loading methods, the rock specimens initially have a more uniform color with an overall dark gray color, and then bright white spots begin to be generated in the rock specimens. This is a result of the high shear stress in the units near this location, and when the shear stress in these units exceeds the shear strength, the units are damaged and tiny cracks appear. As the

displacement increases, the cracks develop and penetrate, and the specimen is fractured

(3) The damage pattern of the rock is related to the way the stress is loaded, and the fragmentation size is also influenced by the loading method. The fragmentation size of sandstone when loading is performed by controlled stress is much smaller than when loading by controlled displacement. Both experiments and numerical simulations found a momentary state of quiescence where the AE number of the sandstone stops increasing before significant cracking occurs, i.e., a period of AE calm

(4) Under cyclic loading and unloading, the number of AE events increases significantly compared with the controlled displacement and controlled stress loading methods, and the radius of the circle becomes larger and there is an increase in AE energy, which indicates a greater degree of destruction under cyclic loading and unloading. The place where the number of AE events shows a dense pattern indicates that the rock is cracked, concentrated, and prone to extensional fracture at that site. The maximum number of AE events and the brighter the color in the part of the rock where the fracture damage occurs, the more the bright white shape formed matches the shape of the damage to the rock

Data Availability

The data used to support the findings of this study are available from the corresponding author upon request.

Conflicts of Interest

The authors declare that they have no conflict of interest.

Acknowledgments

References

[1] Z. He, K. Zhao, Y. Yan, F. Ning, Y. Zhou, and Y. Song, "Mechanical response and acoustic emission characteristics of cement paste backfill and rock combination," *Construction and Building Materials*, vol. 288, p. 123119, 2021.

[2] T. Bruning, M. Karakus, G. D. Nguyen, and D. Goodchild, "Experimental study on the damage evolution of brittle rock under triaxial confinement with full circumferential strain control," *Rock Mechanics and Rock Engineering*, vol. 51, no. 11, pp. 3321–3341, 2018.

[3] T. Xu, M. Fu, S.-q. Yang, M. J. Heap, and G.-l. Zhou, "A numerical meso-scale elasto-plastic damage model for modeling the deformation and fracturing of sandstone under cyclic loading," *Rock Mechanics and Rock Engineering*, pp. 1–23, 2021.

[4] X. Liu, L. Wu, Y. Zhang, S. Wang, X. Yao, and X. Wu, "The characteristics of crack existence and development during rock

shear fracturing evolution," *Bulletin of Engineering Geology and the Environment*, vol. 80, no. 2, pp. 1671–1682, 2021.

[5] H. Odegaard and B. Nilsen, "Rock stress measurements for unlined pressure tunnels: a true triaxial laboratory experiment to investigate the ability of a simplified hydraulic jacking test to assess fracture normal stress," *Rock Mechanics and Rock Engineering*, vol. 54, no. 6, pp. 2995–3015, 2021.

[6] L. Shengxiang, X. Qin, L. Xiling, L. Xibing, L. Yu, and C. Daolong, "Study on the acoustic emission characteristics of different rock types and its fracture mechanism in Brazilian splitting test," *Frontiers in Physics*, vol. 9, 2021.

[7] T. Ishida, S. Desaki, Y. Kishimoto, M. Naoi, and H. Fujii, "Acoustic emission monitoring of hydraulic fracturing using carbon dioxide in a small-scale field experiment," *International Journal of Rock Mechanics and Mining Sciences*, vol. 141, p. 104712, 2021.

[8] Z. Zhou, S. Chen, Y. Wang, and Z. Dai, "Crack evolution characteristics and cracking mechanism of red beds in Central Sichuan during seepage and swelling," *Geofluids*, vol. 2021, Article ID 9981046, 19 pages, 2021.

[9] M. T. W. Schimmel, S. J. T. Hangx, and C. J. Spiers, "Impact of chemical environment on compaction behaviour of quartz sands during stress-cycling," *Rock Mechanics and Rock Engineering*, vol. 54, no. 3, pp. 981–1003, 2021.

[10] D. Liang, N. Zhang, L. Xie, G. Zhao, and D. Qian, "Damage and fractal evolution trends of sandstones under constant-amplitude and tiered cyclic loading and unloading based on acoustic emission," *International Journal of Distributed Sensor Networks*, vol. 15, no. 7, 2019.

[11] Y. Wang, J. Q. Han, and C. H. Li, "Acoustic emission and CT investigation on fracture evolution of granite containing two flaws subjected to freeze-thaw and cyclic uniaxial increasing-amplitude loading conditions," *Construction and Building Materials*, vol. 260, article 119769, 2020.

[12] H. Sun, L. Ma, W. Liu, A. J. S. Spearing, J. Han, and Y. Fu, "The response mechanism of acoustic and thermal effect when stress causes rock damage," *Applied Acoustics*, vol. 180, article 108093, 2021.

[13] K. Zhao, D. Yang, P. Zeng, C. Gong, X. Wang, and W. Zhong, "Accelerating creep stage of red sandstone expressed and quantitatively identified based on acoustic emission information," *Rock Mechanics and Rock Engineering*, 2021.

[14] J. Lu, G. Yin, D. Zhang, H. Gao, C. Li, and M. Li, "True triaxial strength and failure characteristics of cubic coal and sandstone under different loading paths," *International Journal of Rock Mechanics and Mining Sciences*, vol. 135, p. 104439, 2020.

[15] M. Kharghani, K. Goshtasbi, M. Nikkah, and K. Ahangari, "Investigation of the Kaiser effect in anisotropic rocks with different angles by acoustic emission method," *Applied Acoustics*, vol. 175, p. 107831, 2021.

[16] J. Li, J. Zhao, S. Y. Gong et al., "Mechanical anisotropy of coal under coupled biaxial static and dynamic loads," *International Journal of Rock Mechanics and Mining Sciences*, vol. 143, p. 104807, 2021.

[17] P. M. Benson, D. C. Austria, S. Gehne et al., "Laboratory simulations of fluid-induced seismicity, hydraulic fracture, and fluid flow," *Geomechanics for Energy and the Environment*, vol. 24, p. 100169, 2020.

[18] A. Butcher, A. L. Stork, J. P. Verdon et al., "Evaluating rock mass disturbance within open-pit excavations using seismic methods: a case study from the Hinkley point C nuclear power station," *Journal of Rock Mechanics and Geotechnical Engineering*, vol. 13, no. 3, pp. 500–512, 2021.

[19] W. Cai, L. Dou, M. Zhang, W. Cao, J. Q. Shi, and L. Feng, "A fuzzy comprehensive evaluation methodology for rock burst forecasting using microseismic monitoring," *Tunnelling and Underground Space Technology*, vol. 80, pp. 232–245, 2018.

[20] G. Dresen, G. Kwiatek, T. Goebel, and Y. Ben-Zion, "Seismic and aseismic preparatory processes before large stick-slip failure," *Pure and Applied Geophysics*, vol. 177, no. 12, pp. 5741–5760, 2020.

[21] Y. V. Marapulets and A. O. Shcherbina, "Assessing the orientation of the axis of maximum compression of rocks with a combined point receiver system," *Acoustical Physics*, vol. 64, no. 6, pp. 742–749, 2018.

[22] J. Zhang, C. Ai, Y. W. Li, M. G. Che, R. Gao, and J. Zeng, "Energy-based brittleness index and acoustic emission characteristics of anisotropic coal under triaxial stress condition," *Rock Mechanics and Rock Engineering*, vol. 51, no. 11, pp. 3343–3360, 2018.

[23] A. Davarpanah, R. Shirmohammadi, B. Mirshekari, and A. Aslani, "Analysis of hydraulic fracturing techniques: hybrid fuzzy approaches," *Arabian Journal of Geosciences*, vol. 12, no. 13, p. 402, 2019.

[24] A. Damani, C. H. Sondergeld, and C. S. Rai, "Experimental investigation of in situ and injection fluid effect on hydraulic fracture mechanism using acoustic emission in Tennessee sandstone," *Journal of Petroleum Science and Engineering*, vol. 171, pp. 315–324, 2018.

[25] D. Liang, N. Zhang, H. Rong, and Z. Xiang, "Experimental and numerical studies on crack initiation and coalescence in sandy mudstone with prefabricated cross-flaws under uniaxial compression," *Shock and Vibration*, vol. 2021, Article ID 6672913, 17 pages, 2021.

[26] D. Liang, N. Zhang, H. Liu, D. Fukuda, and H. Rong, "Hybrid finite-discrete element simulator based on GPGPU-parallelized computation for modelling crack initiation and coalescence in sandy mudstone with prefabricated cross-flaws under uniaxial compression," *Engineering Fracture Mechanics*, vol. 247, article 107658, 2021.

[27] C. Tang, "Numerical simulation of progressive rock failure and associated seismicity," *International Journal of Rock Mechanics and Mining Sciences*, vol. 34, no. 2, pp. 249–261, 1997.

[28] C. E. Fairhurst and J. A. Hudson, "Draft ISRM suggested method for the complete stress-strain curve for intact rock in uniaxial compression," *International Journal of Rock Mechanics & Mining Science & Geomechanics Abstracts*, vol. 36, no. 3, pp. 281–289, 1999.

[29] T. F. Wong, R. H. C. Wong, K. T. Chau, and C. A. Tang, "Microcrack statistics, Weibull distribution and micromechanical modeling of compressive failure in rock," *Mechanics of Materials*, vol. 38, no. 7, pp. 664–681, 2006.